



HAL
open science

Kinematics of spatial linkages and its applications to rigid origami

Huijuan Feng

► **To cite this version:**

Huijuan Feng. Kinematics of spatial linkages and its applications to rigid origami. Mechanical engineering [physics.class-ph]. Université Clermont Auvergne [2017-2020], 2018. English. NNT : 2018CLFAC014 . tel-01919775

HAL Id: tel-01919775

<https://theses.hal.science/tel-01919775>

Submitted on 12 Nov 2018

HAL is a multi-disciplinary open access archive for the deposit and dissemination of scientific research documents, whether they are published or not. The documents may come from teaching and research institutions in France or abroad, or from public or private research centers.

L'archive ouverte pluridisciplinaire **HAL**, est destinée au dépôt et à la diffusion de documents scientifiques de niveau recherche, publiés ou non, émanant des établissements d'enseignement et de recherche français ou étrangers, des laboratoires publics ou privés.

UNIVERSITE CLERMONT AUVERGNE

**ECOLE DOCTORALE
SCIENCES POUR L'INGENIEUR DE CLERMONT-FERRAND**

T h è s e

Présentée par

Huijuan FENG

pour obtenir le grade de

DOCTEUR D'UNIVERSITÉ

SPECIALITE : Génie Mécanique

**Kinematics of Spatial Linkages and Its Applications to Rigid
Origami**

Soutenue publiquement le 30 mai 2018 devant le jury :

M. Qinchuan LI, Professeur des universités, Zhejiang Sci-Tech University, Rapporteur et président

M. Damien CHABLAT, Directeur de recherche CNRS, LS2N, Rapporteur

M. Chedli B. BOUZGARROU, Maître de conférences, HDR, SIGMA Clermont, Examineur

M. Jian S. DAI, Professeur des universités, Tianjin University, Co-directeur de thèse

Mme. Yan CHEN, Professeur des universités, Tianjin University, Co-directeur de thèse

M. Grigore GOGU, Professeur des universités, SIGMA Clermont, Co-directeur de thèse

天津大学博士学位论文

空间机构运动学及其在刚性折纸中的
应用

**Kinematics of Spatial Linkages and Its
Applications to Rigid Origami**

学科专业：机械工程

研 究 生：冯慧娟

指导教师：戴建生 教授

陈焱 教授

Grigore Gogu 教授

天津大学机械工程学院

2018 年 06 月

ABSTRACT

This dissertation systematically explores the applications of spatial linkages into rigid origami. This is achieved by utilizing the kinematics of linkages to folding motion of rigid origami, where links and revolute joints are corresponded to paper facets and crease lines, respectively. Major findings of this dissertation are in three areas, and listed as follows.

First, rigid foldability and motion behaviour of simple origami geometry are investigated. A well-known *triangle twist* origami is used, and converted into a network of spherical $4R$ linkages based on their kinematic equivalence. The compatibility of this network is combined to discuss the rigid foldability and motion behaviour of the pattern. It is found that diverse mountain-valley crease assignments of the pattern exist, based on the flat-foldable conditions of four-crease vertex. The pattern is then altered into a new overconstrained $6R$ linkage by using the kirigami technique, and shows a good agreement to our proposed kinematic analysis method.

Secondly, kinematic bifurcation conditions for spatial overconstrained $6R$ linkages are considered by using a traditional D-H matrix method. A set of closure equations of plane-symmetric Bricard linkage are derived in explicit forms. This has allowed us to characterize various bifurcation behaviours and their corresponding geometric conditions, build up a connection between plane-symmetric Bricard and Bennett linkage families, and is ready to be applied in rigid origami geometries.

Thirdly, the analysis method is extended from zero-thickness to thick-panel origami forms. A multi-degree of freedom (DOF) pattern consisted with six-crease vertices is used, namely *waterbomb* origami. Its zero-thickness and thick-panel forms under symmetric folding are converted into networks of plane-symmetric spherical $6R$ linkages and plane-symmetric Bricard linkages, respectively, resulting in one-DOF systems with kinematic equivalence. The zero-thickness form is shown to have a bifurcation behaviour with two different folding paths. However, this behaviour can be eliminated in thick-panel form, as the thickness has provided additional geometric constraints. Finally, an investigation of closed cylindrical form of waterbomb origami is conducted through a parametric study. It is seen that the folded tube may undergo different behaviours, including uniform radius configuration, mechanism-structure-mechanism transition, wave-like configuration, and rigid twist motion. Nevertheless, the trigger condition of those behaviours can be determined by using the proposed kinematic analysis method of rigid origami with specified geometric conditions. The twist angle per axial strain and its relationship with geometrical parameters of the tube during the rigid twist motion are revealed. Experimental results show the enhancement in stiffness of the tube with occurrence of the continuous twist motion.

KEYWORDS: Kinematics; Rigid origami; Spherical linkage; Spatial overconstrained linkage; Plane-symmetric Bricard linkage; Bifurcation; Waterbomb origami; Thick-panel origami.

Contents

ABSTRACT	I
Contents.....	III
List of Figures	V
List of Tables.....	XIII
Notation.....	XV
Chapter 1 Introduction	1
1.1 Background and Significance	1
1.2 Aim and Scope	2
1.3 Outline of Dissertation	2
Chapter 2 Review of Previous Works.....	5
2.1 Kinematics of Spatial Linkages	5
2.1.1 Kinematic Analysis Approach.....	5
2.1.2 Singularity and Bifurcation	7
2.1.3 Spatial Overconstrained 6R Linkages	9
2.2 Rigid Origami.....	15
2.2.1 Origami Patterns.....	16
2.2.2 Flat Foldability and Rigid Foldability.....	19
2.2.3 Rigidly Foldable Origami Tubes.....	20
2.2.4 Thick-panel Origami	21
2.2.5 Kirigami	22
2.3 Spatial Linkages and Rigid Origami	24
2.3.1 Origami Analysis Based on Spatial Linkages	24
2.3.2 Origami-inspired Linkages.....	24
Chapter 3 Rigid Foldability of Triangle Twist Origami Pattern and Its Derived 6R Linkages	27
3.1 Introduction	27
3.2 Rigid Foldability	27
3.3 M-V Assignment and Its Effect on Rigid Foldability	33
3.4 Derived Overconstrained 6R Linkages	43
3.5 Conclusions	47
Chapter 4 Kinematic Study of Plane-symmetric Bricard Linkage and Its Bifurcation Variations	49
4.1 Introduction	49
4.2 Explicit Closure Equations and Kinematic Properties	49

4.3 Derived 5R/4R Linkages.....	56
4.4 Bifurcation between Plane-symmetric Bricard Linkage and Bennett Linkage	61
4.5 Other Bifurcation Behaviours.....	63
4.5.1 Bifurcation between Two 6R Motion Branches.....	63
4.5.2 Bifurcation between Kinematic Chains and a 4R Linkage.....	65
4.6 Conclusions.....	66
Chapter 5 Symmetric Flat-foldable Waterbomb Origami	69
5.1 Introduction.....	69
5.2 Geometry and Kinematic Setup.....	69
5.3 Symmetric Rigid Folding of Zero-thickness Waterbomb.....	71
5.4 Folding Thick Panels with the Waterbomb Pattern	79
5.5 Conclusions and Discussion	88
Chapter 6 Rigid Foldability of the Waterbomb Tube	91
6.1 Introduction.....	91
6.2 Contraction Motion.....	91
6.2.1 Kinematics of Linkages A, B, C	93
6.2.2 Contraction of a Tube with an Odd Number of Rows	95
6.2.3 Contraction of a Tube with an Even Number of Rows.....	111
6.3 Long and Truncated Tubes.....	117
6.3.1 Long Tubes	117
6.3.2 Truncated Tubes.....	120
6.4 Twist Motion.....	121
6.4.1 Rigid Twist Motion.....	121
6.4.2 Non-rigid Twist Motion	135
6.5 Conclusions.....	138
Chapter 7 Final Remarks	141
7.1 Main Achievements	141
7.2 Future Works.....	143
References.....	145
Appendix.....	161
Résumé	163
Publications and Research Projects during PhD's Study	185
Acknowledgements.....	187

List of Figures

Fig. 2-1	The D-H notation of adjacent links connected by revolute joints.....	6
Fig. 2-2	The D-H notation of a portion of a spherical linkage	7
Fig. 2-3	The Bennett linkage	10
Fig. 2-4	Construction of a serial Goldberg 6R linkage	10
Fig. 2-5	Bricard 6R linkages: (a) the general line-symmetric case, (b) the general plane-symmetric case, (c) the trihedral case, (d) the line-symmetric octahedral case, (e) the plane-symmetric octahedral case, and (f) the doubly collapsible octahedral case.	11
Fig. 2-6	Origami applications in aerospace engineering: (a) a foldable solar panel [137], (b) a deployable antenna [139], (c) a foldable telescopic lens [141]; in civil engineering: (d) a deployable origami tent [26], (e) a self-folding origami robot [14], (f) a modular origami robot [144]; and in biomedical engineering: (g) an origami stent [146], (h) an untethered miniature origami robot [147], (i) a four-DOF origami grasper [150].	16
Fig. 2-7	Three typical types of origami twist patterns: (a) triangle twist, (b) square twist, and (c) hexagon twist.	17
Fig. 2-8	(a) The eight-crease waterbomb base, (b) one of its tessellations forming the Resch pattern, (c) partially folded Resch pattern; (d) the six-crease waterbomb base, (e) its tessellation in unfolded and folded states, and (f) the tessellation can also be used to form a tube.	18
Fig. 2-9	Thickness accommodation methods: (a) tapered panel technique [196], (b) offset panel technique [197], (c) offset crease technique [198], and (d) hinge shift technique [29].	22
Fig. 2-10	Kirigami technique used in foldable structures: (a) a SILICOMB cellular structure [201], (b) a tapered honeycomb [202], (c) a kirigami auxetic pyramidal lattice core [203], (d) a cellular kirigami morphing wingbox [204], (e) a Kapton kirigami structure for solar tracking [205], (f) a paper-based triboelectric nanogenerator [206], (g) a paper pop-up RSSR mechanism [207], and (h) a kirigami-enabled parallel mechanism [16].	23
Fig. 3-1	(a) An art triangle twist, (b) a generalized triangle twist, where α_0 , β_0 , γ_0 , δ_0 and ε_0 is arbitrary within the domain $(0, \pi)$ and $\alpha_0 + \beta_0 \in (0, \pi)$	27
Fig. 3-2	A spherical 4R linkage	28
Fig. 3-3	Four-crease origami vertices with four schemes of M-V assignment: (a), (b) Vertex-I; and (c), (d) Vertex-II.	29
Fig. 3-4	The relationship between the kinematic variable and the dihedral angle for	

	(a) mountain crease, and (b) valley crease.....	29
Fig. 3-5	A generalized triangle twist origami pattern with a specific M-V assignment: (a) the general representation, and (b) the simplified one.	30
Fig. 3-6	Three types of the triangle twist pattern where (a) each crease-pair is intersected, or (b) only one crease-pair is parallel, or (c) each crease-pair is parallel.	32
Fig. 3-7	Four types of M-V assignment of one vertex in the generalized triangle twist where the minimum angle is (a) α_{12} or α_{23} for Type P, (b) α_{23} or α_{34} for Type Q, (c) α_{34} or α_{41} for Type R, and (d) α_{41} or α_{12} for Type S.	34
Fig. 3-8	All possible schemes of M-V assignment of a generalized triangle twist: No.1 PPP, No.2 PPQ, No.3 PQP, No.4 PQQ, No.5 PRR, No.6 PRS, No.7 PSR, No.8 PSS, No.9 QPP, No.10 QPQ, No.11 QQP, No.12 QQQ, No.13 QRR, No.14 QRS, No.15 QSR, No.16 QSS, No.17 RPR, No.18 RPS, No.19 RQR, No.20 RQS, No.21 RRP, No.22 RRQ, No.23 RSP, No.24 RSQ, No.25 SPR, No.26 SPS, No.27 SQR, No.28 SQS, No.29 SRP, No.30 SRQ, No.31 SSP, and No.32 SSQ.	35
Fig. 3-9	Duplicated M-V assignments: (a) the M-V assignment obtained by flipping the paper in Fig. 3-8 No.5, (b) the one obtained by rotating (a) along the centre of the triangle, and (c) the one copied from Fig. 3-8 No.17.	37
Fig. 3-10	Twelve unique schemes of M-V assignment of the generalized triangle twist pattern with vertex-types being (a) PPP, (b) PPQ, (c) PQQ, (d) PRR, (e) PRS, (f) PSS, (g)QQQ, (h) QRR, (i) QRS, (j) QSS, (k) PSR, and (l) QSR.....	38
Fig. 3-11	Physical triangle twist models with $\alpha = 55^\circ$, $\beta = 50^\circ$, $\gamma = 50^\circ$, $\delta = 45^\circ$ and $\varepsilon = 35.44^\circ$ for (a) origami pattern, and (b) kirigami pattern.	44
Fig. 3-12	Equivalent mechanisms of the generalized triangle twist: (a) the network of three spherical 4R linkages for the origami pattern, and (b) the derived overconstrained 6R linkage for the kirigami pattern.	44
Fig. 3-13	Schematic diagrams of the derived overconstrained 6R linkages when (a) $\gamma \neq \delta$, and (b) $\gamma = \delta$	46
Fig. 3-14	Kinematic paths of the derived overconstrained 6R linkages with $\alpha = 55^\circ$, $\beta = 50^\circ$, $\gamma = 50^\circ$, $\delta = 45^\circ$, $\varepsilon = 35.44^\circ$ as solid lines and $\alpha = 55^\circ$, $\beta = 50^\circ$, $\gamma = \delta = 45^\circ$, $\varepsilon = 33.52^\circ$ as dashed lines.....	46
Fig. 4-1	D-H parameters of the plane-symmetric Bricard linkage.....	50
Fig. 4-2	The degenerated plane-symmetric Bricard linkage: (a) when $\theta_1 = \pi$, (b) when $\theta_2 = \theta_6 = \pi$, (c) when $\theta_3 = \theta_5 = \pi$, and (d) when $\theta_4 = \pi$	57
Fig. 4-3	The plane-symmetric Bricard when $\theta_1 = \pi$: (a) the degenerated planar 5R	

- linkage with two joints 2 and 6 coincide, (b) the degenerated spherical 5R linkage with two joints 2 and 6 coincide, and (c) the degenerated serial kinematic chain with joints 2, 6 and 3, 5 both coincide.....58
- Fig. 4-4 Bifurcation between the plane-symmetric Bricard linkage and the Bennett linkage when $\theta_2 = \theta_6 = \pi$, where i-ii-iii-iv-v-vi-i correspond to configurations of the linkage along the plane-symmetric Bricard motion branch and i-vii-viii-iv-ix-x-i correspond to configurations of the linkage along the Bennett motion branch. Here the geometrical parameters of this linkage are $a = 3$, $b = 2$, $c = 1$, $\alpha = \pi/12$, $\beta = \pi/3$, $\gamma = \pi/4$ and $R_2 = R_3 = 0$61
- Fig. 4-5 Bifurcation between the plane-symmetric Bricard linkage and the Bennett linkage when $\theta_3 = \theta_5 = \pi$, where i-ii-iii-iv-v-vi-i correspond to configurations of the linkage along the plane-symmetric Bricard motion branch and i-vii-viii-iv-ix-x-i correspond to configurations of the linkage along the Bennett motion branch. Here the geometrical parameters of this linkage are $a = 1$, $b = 3$, $c = 2$, $\alpha = \pi/4$, $\beta = \pi/3$, $\gamma = 7\pi/12$ and $R_2 = R_3 = 0$62
- Fig. 4-6 Bifurcation between two 6R motion branches, where i-ii-iii-iv-i correspond to configurations of the linkage along *path I* and i-vi-iii-v-i correspond to configurations of the linkage along *path II*. Here the geometrical parameters of this linkage are $a = 2$, $b = 1$, $c = 1$, $\alpha = 2\pi/3$, $\beta = \pi/6$, $\gamma = -\pi/6$ and $R_2 = R_3 = 0$, which corresponds to Case 10 in Table 4-1.....64
- Fig. 4-7 A plane-symmetric Bricard linkage with two 6R motion branches where no collision happens.....64
- Fig. 4-8 Bifurcation of the plane-symmetric Bricard linkage: (a) between two equivalent single-revolute-joint branches and a serial kinematic chain with two revolute joints branch; (b) between two equivalent single-revolute-joint branches and a four-bar double-rocker linkage branch, where i-ii-iii-iv correspond to configurations of the linkage along *path I*, iv-v-vi correspond to configurations of the linkage along *path II*, vi-vii-viii-ix correspond to configurations of the linkage along *path III*, and viii-x-xi-xii-ii-xiii-xiv-xv correspond to configurations of the linkage along *path IV*.....66
- Fig. 5-1 (a) The six-crease waterbomb base, and (b) the waterbomb origami pattern formed by tessellating the waterbomb bases.....70
- Fig. 5-2 Kinematic modelling of the generalized waterbomb tube: (a), (b) and (c), spherical linkage A_i , B_i and C_i , respectively.....70
- Fig. 5-3 Set-up of coordinates and kinematic parameters for (a) zero-thickness, and (b) thick-panel origami according to the D-H notation.....71
- Fig. 5-4 Kinematic behaviour of the waterbomb origami pattern with $\alpha = 2\pi/9$, $\beta = 2\pi/9$. Kinematic relationships of vertices (a) B, and (b) A; and (c) two

	folding paths with configurations i-viii.	75
Fig. 5-5	Two-stage motion of <i>path I</i> with $\alpha = \pi/4$, $\beta = \pi/4$. (a) Folding paths with configurations i-xi, and (b) kinematic relationships of vertex B.	76
Fig. 5-6	Blockage of waterbomb origami pattern with $\alpha = 7\pi/36$, $\beta = \pi/4$. (a) Kinematic curve between ϕ_4 and ϕ_1 of vertex B, and (b) folding manners in which the framed configurations are with physical blockage.	77
Fig. 5-7	Two-stage motion and blockage during the folding manners of waterbomb origami pattern with $\alpha = \pi/6$, $\beta = \pi/3$ in which the framed configurations are with physical blockage.	78
Fig. 5-8	Fold lines around the vertices (a) A, and (b) B in thick panels	80
Fig. 5-9	The kinematic paths of thick-panel waterbomb when $\alpha = 7\pi/36$, $\beta = \pi/4$, $\mu = 0.5$. Kinematic relationships at vertices (a) A, and (b) B with ϕ_1' taken as input, where vertex B works as a plane-symmetric Bricard linkage while vertex A works as a line- and plane-symmetric Bricard linkage; (c) folding path of the Solidworks model of thick-panel waterbomb.	83
Fig. 5-10	Deployable sequences of physical models of the waterbomb pattern with zero-thickness sheets and thick panels when $\alpha = 7\pi/36$, $\beta = \pi/4$, $\mu = 0.5$	84
Fig. 5-11	Folding path of thick-panel waterbomb pattern with $\alpha = \pi/6$, $\beta = \pi/3$, $\mu = 0.7$, in which the framed configurations are with physical blockage.	85
Fig. 5-12	Folding path of thick-panel waterbomb pattern with $\alpha = 7\pi/36$, $\beta = \pi/4$ and $\mu = \cos(\alpha + \beta) \cdot \sin \alpha / \sin \beta = 0.14$	86
Fig. 5-13	Folding sequence for patterns with $\alpha = \beta = 2\pi/9$ and $\mu = 1$. (a) Two folding paths exist; physical models of zero- thickness sheet (top) and thick panels that fold along (b) <i>path I</i> , and (c) <i>path II</i>	87
Fig. 6-1	The generalized waterbomb tube with $m = 3$ and $n = 6$ formed by joining together two vertical sides of the waterbomb origami pattern in Fig. 5-1(b).	91
Fig. 6-2	Card model of a waterbomb tube from the expanded configuration (i) to the fully contracted configuration (vi). Additional twist is possible (vii and viii) that further shortens the model.	92
Fig. 6-3	(a) Top half of a longitudinal strip in a waterbomb tube. Vertices are marked as A, B and C. $E-E'$ is the equator of the tube. (b) A 3D view of a waterbomb tube with equatorial row (<i>Row 0</i>) and rows immediately adjacent to it. One of the base on <i>Row 0</i> is shown in blue. (c) The projection view of the waterbomb tube with only <i>Row 0</i> shown. O_0 is the centre of the tube. EP	

	is short for equatorial plane.....	96
Fig. 6-4	3D and projected views of a tube with $m=3$, $n=6$ and $\alpha=\beta=45^\circ$ deploying from configurations I to V. The corresponding folding angles θ are listed below the motion sequence.....	99
Fig. 6-5	Kinematic paths of a waterbomb tube when $n=6$, $m=3$ and $\alpha=\beta=45^\circ$ for (a) linkages \mathbf{A}_0 and \mathbf{A}_1 , and (b) linkages \mathbf{B}_0 and \mathbf{C}_0 . At configurations I: $\varphi_{0,1} = 60^\circ$, II: $\varphi_{0,1} = 65.88^\circ$, III: $\varphi_{0,1} = 120^\circ$, IV, $\varphi_{0,1} = 144^\circ$, V: $\varphi_{0,1} = 147.96^\circ$	100
Fig. 6-6	Variation of (a) radii of vertices A, B and C, and (b) the length of the tube with respect to θ when $n=6$, $m=3$ and $\alpha=\beta=45^\circ$	101
Fig. 6-7	3D and projected views of the tube with $n=6$, $m=7$ and $\alpha=\beta=45^\circ$ deploying from configurations I to V. The corresponding folding angles θ are listed below the motion sequence. The tube is completely concealed at configurations III _L and III _R at which the radii of vertices A on top and bottom rows reach 0.	102
Fig. 6-8	Kinematic paths of a waterbomb tube with $n=6$, $m=7$ and $\alpha=\beta=45^\circ$ for linkages \mathbf{A}_i . At configurations I: $\varphi_{0,1} = 60^\circ$, II: $\varphi_{0,1} = 65.88^\circ$, III _L : $\varphi_{0,1} = 90.72^\circ$, III: $\varphi_{0,1} = 120^\circ$, III _R : $\varphi_{0,1} = 128.52^\circ$, IV: $\varphi_{0,1} = 144^\circ$, V: $\varphi_{0,1} = 144.24^\circ$	103
Fig. 6-9	Kinematic paths of a waterbomb tube with $n=6$, $m=7$ and $\alpha=\beta=45^\circ$ for linkages (a) \mathbf{B}_i , and (b) \mathbf{C}_i . At configurations I: $\varphi_{0,1} = 60^\circ$, II: $\varphi_{0,1} = 65.88^\circ$, III _L : $\varphi_{0,1} = 90.72^\circ$, III: $\varphi_{0,1} = 120^\circ$, III _R : $\varphi_{0,1} = 128.52^\circ$, IV: $\varphi_{0,1} = 144^\circ$, V: $\varphi_{0,1} = 144.24^\circ$	104
Fig. 6-10	The radii of vertices A, B and C vs. θ of a waterbomb tube with $n=6$, $m=7$ and $\alpha=\beta=45^\circ$. The red curve shows $r_{A3} < 0$ between configurations III _L and III _R	105
Fig. 6-11	Relationship among r_{A3}/t , radius of vertices A_3 , θ and α . Some values of α are listed alongside their corresponding curves. The shaded plane is where $r_{A3} = 0$. Blue solid lines are for $r_{A3} > 0$ and the grey dashed line for $r_{A3} < 0$. Physical interference happens when $r_{A3} < 0$	107
Fig. 6-12	The configuration of tube with a uniform radius to be obtained by folding the flat origami pattern into the tube presenting with curve of $\varphi_{0,1}/2 - \phi_{B0,4}/2$ against $\varphi_{0,1}$ when $\alpha=\beta=45^\circ$	108
Fig. 6-13	Relationship among $\varphi_{0,1}/2 - \phi_{B0,4}/2$, $\varphi_{0,1}$ and α when $n=6$, $m=7$ and $\alpha + \beta = 90^\circ$	109

- Fig. 6-14 The curves of $\varphi_{0,1}/2 - \varphi_{B0,4}/2$ (blue lines), $180^\circ/n$ (black lines) and r_{A3}/t (red lines) against $\varphi_{0,1}$ when $n=6$, $m=7$, $\alpha+\beta=90^\circ$ and (a) $\alpha=50.9^\circ$, (b) $\alpha=51.5^\circ$, (c) $\alpha=47^\circ$, (d) $\alpha=44.8^\circ$, (e) $\alpha=44^\circ$, and (f) $\alpha=40^\circ$. 110
- Fig. 6-15 Projection of Row 1 of the waterbomb tube onto the EP when m is even: (a) 3D view, and (b) top view. 111
- Fig. 6-16 A waterbomb tube with $n=6$, $m=8$ and $\alpha=\beta=45^\circ$. (a) The kinematic path $\varphi_{B1,4}$ vs. $\varphi_{0,1}$ with $\varphi_{B4,4} < 0$ between configurations III_L and III_R marked as red line; (b) the radii of vertices A, B and C during the motion, where $r_{A4} < 0$ between configurations III_L and III_R highlighted with blue line in red shadow; (c) 3D and top views of the tube in the typical configurations I-V. 116
- Fig. 6-17 Radii of some vertices of the tube vs. θ when $n=6$ and $\alpha=\beta=45^\circ$. At I: $\theta=60^\circ$; II: $\theta=65.88^\circ$; III_L: $\theta=71.64^\circ$. (a) Radius of vertex on the equatorial row (r_{A0} , r_{B0} , r_{C0} , r_{B-1} , r_{C-1}) and the end row (r_{A6} , r_{B6} , r_{C6} , r_{B5} , r_{C5}) when $m=13$. (b) The radius of vertex A_i for a longer tube when $m=25$. 118
- Fig. 6-18 Three configurations of a long tube with $n=6$, $m=25$ and $\alpha=\beta=45^\circ$ when it undergoes rigid motion. 119
- Fig. 6-19 The changes of θ_I , θ_{II} and θ_{III} vs. (a) various n when $\alpha=\beta=45^\circ$, and (b) various α when $n=6$ and $\alpha+\beta=90^\circ$. 119
- Fig. 6-20 (a) Three configurations of an 8-row tube obtained by truncating a long tube. It keeps on the motion path of an odd row tube. (b) Three configurations of the same tube if it tracks the motion of an even-row tube (This is in fact a reproduction of first three configurations of Fig. 6-16(c)). 120
- Fig. 6-21 *The twist phase* of the waterbomb tube. (a) 3D view of a portion of tube when it completes the *the contraction phase*. Some of the representative vertices and dihedral angles are marked. Only three rows of the tube are shown: the equatorial row and two rows immediately adjacent to it. (b) Partially twist configuration of the tube. 121
- Fig. 6-22 The geometry of the line-symmetric linkage \mathbf{A}_0 on the equatorial row. 123
- Fig. 6-23 Twist motion on the equatorial row of a waterbomb tube with $n=6$ and $\alpha=\beta=45^\circ$. Kinematic paths of (a) linkages \mathbf{A}_0 and \mathbf{A}_1 , and (b) linkages \mathbf{B}_0 and \mathbf{C}_0 in *the twist phase* (blue) and in *the contraction phase* (grey). $\varphi_{0,2}$ is taken as input. The bifurcation points are marked by small grey circles. 126
- Fig. 6-24 Twist motion on the equatorial row of a waterbomb tube with $n=6$, $m=3$

- and $\alpha = \beta = 45^\circ$. (a) Length of the tube vs. $\varphi_{0,2}$. (b) Radii of vertices A, B, and C vs. $\varphi_{0,2}$127
- Fig. 6-25 The limitation of α obtained when the creases A_0C_0 and A_0B_{-1} coincide, where β is randomly chosen as 40°128
- Fig. 6-26 Limiting positions of the twisted case: (a) $\varphi_{0,2} = 0^\circ$, and (b) $\varphi_{0,3} = 0^\circ$130
- Fig. 6-27 Rigid twist of the waterbomb tube with $\alpha = \beta = 45^\circ$. (a) The twist angle between two ends of a tube, θ_t , vs. the number of bases in a row, n , when the number of rows $m = 3$. (b) The axial strain of the tube ε_t vs. n when $m = 3$. (c) The twist angle per axial strain θ_t / ε_t vs. n when $m = 3$. (d) θ_t / ε_t vs. m when $n = 6$. The twist angle here is calculated as the maximum rigid twist between two ends of a tube, and the axial strain is calculated as the strain when the maximum rigid twist is reached.132
- Fig. 6-28 Kinematic paths of the dihedral angles $\phi_{Bi,4}$ and $\phi_{Ci,4}$ against $\varphi_{0,2}$ during the twist motion on the equatorial row of a waterbomb tube in three cases with $m = 5$, $n = 6$, $\alpha_1 = 40^\circ$ (blue), $\alpha_2 = 45^\circ$ (red), $\alpha_3 = 50^\circ$ (grey) when (a) all $\beta = 40^\circ$, and (b) $\beta_1 = 42.01^\circ$, $\beta_2 = 45.59^\circ$, $\beta_3 = 49.17^\circ$133
- Fig. 6-29 Bifurcation behaviour during the twist motion of the fully squeezed waterbomb tube with uniform radius satisfying Eq. (6-49) where twist motion can occur from any row. Here the geometrical parameters are $m = 3$, $n = 6$, $\alpha = 40^\circ$ and $\beta = 42.01^\circ$134
- Fig. 6-30 Non-rigid twist of the waterbomb tube when $n = 6$. (a) 3D view of a waterbomb tube with $m = 3$ when twist starts from the not-fully-squeezed line- and plane-symmetric row (*Row 0*) with $\phi_{B0,4} \neq 0$. (b) Geometry of two adjacent bases on such not-fully-squeezed *Row 0*. (c) 3D view of a waterbomb tube with $m = 7$ where the *Row 3* is fully squeezed with only plane symmetry. (d) 3D view of a waterbomb tube when twist starts from a pair of rows, set as *Row 0* and *Row 1*. Only the twisted rows and those immediately adjacent to them are presented. EP is short for equatorial plane.136
- Fig. 6-31 Axial compression experiment of the waterbomb tube. (a) Compression process of the tube. (b) Reaction force of the tube vs. axial displacement curve. The tube in the experiment took a uniform radius with the following geometrical parameters: $\alpha = \beta = 45^\circ$, $n = 6$, $m = 8$, $a = 22.5\text{mm}$, and initial dihedral angle $\theta = 144^\circ$. ENDURO Ice material with 0.29mm in thickness was used to construct the tube. The compression test was conducted on an Instron machine at the loading rate of 5 mm/min.138

List of Tables

Table 3-1	Classification of M-V assignments for a generalized triangle twist	39
Table 4-1	The kinematic properties of the plane-symmetric Bricard linkage.....	54
Table 5-1	Kinematic behaviour of the general waterbomb tessellation of zero-thickness sheets and thick panels	88

Notation

Parameters

$a_{i(i+1)}$	Length of link $i(i+1)$ between joints i and $i+1$
$a_{i(i+1)}^A, a_{i(i+1)}^B$	Length of link $i(i+1)$ in the vertex A and B of the thick-panel waterbomb pattern, respectively
a, b, c	Link lengths of the linkages
a_i, b_i, c_i	Revolute joints in the equivalent spherical linkages of vertices A, B and C for the triangle twist pattern
$a_i a_{i(i+1)}, b_i b_{i(i+1)}, c_i c_{i(i+1)}$	Links in the equivalent spherical linkages of vertices A, B and C for the triangle twist pattern
a'	Thickness parameter for thick-panel waterbomb pattern, also the thickness of link 23 in the vertex B of the thick-panel waterbomb pattern
d	Length of edge AB in the central triangle of a triangle twist pattern
f_i	Number of degrees of freedom for the i th kinematic pair in a linkage
g	Number of kinematic pairs in a linkage
k	Number of links in a linkage
m	Number of waterbomb bases in the longitudinal direction of a waterbomb pattern
n	Number of waterbomb bases in the circumferential direction of a waterbomb pattern
n_M	Number of mountain creases for an origami vertex
n_V	Number of valley creases for an origami vertex
$r_{A_i}, r_{B_i}, r_{C_i}$	Radii of vertices A_i, B_i and C_i of a waterbomb tube
t	Half width of the six-crease waterbomb base
x_i, y_i, z_i	x, y, z coordinate axis of system i
z_i^j	Coordinate axis of crease i in vertex j for the triangle twist pattern
$z_{A_i}, z_{B_i}, z_{C_i}$	z coordinates of vertices A_i, B_i and C_i of a waterbomb tube
A_i, A'_i	Central vertices of waterbomb bases on Row i . A'_i is immediately adjacent to A_i
$A_i^p, A_i'^p$	Projection of vertices A_i and A'_i on the equatorial plane
B_i, B'_i	Corner vertices of waterbomb bases on Row i . B'_i is immediately adjacent to B_i
$B_i^p, B_i'^p$	Projection of vertices B_i and B'_i on the equatorial plane

C_i, C'_i	Middle vertices at the edges of waterbomb bases on Row i , C'_i is immediately adjacent to C_i
$C_i^p, C_i'^p$	Projection of vertices C_i and C'_i on the equatorial plane
E, E'	Midpoints at the vertical side edges of a waterbomb base on the equatorial row of an odd-row tube
I_i	Identity matrix of order i
L	Length of a waterbomb tube
M	Mobility of a linkage
N	Number of links in a linkage including the fixed one
$Q_{i(i+1)}$	3×3 transformation matrix between the coordinate system of link $(i-1)i$ and that of link $i(i+1)$ for spherical linkages
R_i	Offset of joint i
R_i^A, R_i^B	Offset of joint i in the vertex A and B of the thick-panel waterbomb pattern, respectively
$T_{i(i+1)}$	4×4 transformation matrix between the coordinate system of link $(i-1)i$ and that of link $i(i+1)$

Symbolic Variables

$\alpha_{i(i+1)}$	Twist angle of link $i(i+1)$ between joints i and $i+1$
$\alpha_{i(i+1)}^A, \alpha_{i(i+1)}^B$	Twist angle of link $i(i+1)$ in the vertex A and B of the thick-panel waterbomb pattern, respectively
$\alpha_{i(i+1)}^A, \alpha_{i(i+1)}^B, \alpha_{i(i+1)}^{B_0}$	Twist angle of link $i(i+1)$ of spherical $6R$ linkage $\mathbf{A}_i, \mathbf{B}_i$ and \mathbf{B}_0 of the waterbomb pattern
$\alpha_0, \beta_0, \gamma_0, \delta_0, \varepsilon_0$	Sector angles of the vertices in the triangle twist pattern
$\alpha_1, \alpha_2, \dots, \alpha_{2n}$	Consecutive sector angles of an origami pattern
$\alpha_{i(i+1)}^j$	Sector angles of the vertex j in the triangle twist pattern
$\alpha, \beta, \gamma, \delta, \varepsilon$	Sector angles of origami patterns or twist angles of spatial linkages
ε_t	Axial strain of the waterbomb tube during the rigid twist motion
η	Angle between the vertical crease $B'_0C'_{-1}$ of the waterbomb base and the coordinate axis z
θ	Dihedral angle between two largest triangular facets of a waterbomb base on the equatorial row of an odd-row waterbomb tube
θ_i	Angle of rotation from x_i to x_{i+1} about axis z_i , also known as kinematic variable of crease i or joint i

θ_t	Maximum twist angle of the waterbomb tube between two ends of <i>Row 0</i> along the tube axis
φ_i	Dihedral angle of crease <i>i</i> or revolute joint <i>i</i>
φ_i^j	Dihedral angle of crease <i>i</i> in vertex <i>j</i> for the triangle twist pattern
δ_i, ω_i	Kinematic variable of crease <i>i</i> in the vertex A and B of the zero-thickness waterbomb origami, respectively
δ'_i, ω'_i	Kinematic variable of crease <i>i</i> in the vertex A and B of the thick-panel waterbomb origami, respectively
$\delta_{i,j}, \omega_{B_i,j}, \omega_{C_i,j}$	Kinematic variable at <i>i</i> th joint of spherical 6 <i>R</i> linkage A_i , B_i and C_i in the waterbomb pattern, respectively, and $j=1, 2, \dots, 6$
φ_i, ϕ_i	Dihedral angle of crease <i>i</i> in the vertex A and B of the zero-thickness waterbomb origami, respectively
φ'_i, ϕ'_i	Dihedral angle of crease <i>i</i> in the vertex A and B of the thick-panel waterbomb origami, respectively
$\varphi_{i,j}, \phi_{B_i,j}, \phi_{C_i,j}$	Dihedral angle at <i>i</i> th joint of spherical 6 <i>R</i> linkage A_i , B_i and C_i in the waterbomb pattern, respectively, and $j=1, 2, \dots, 6$
μ	Proportion between the thickness of link 34 and link 23 in the vertex B of the thick-panel waterbomb pattern
μ^j	Relationship of the dihedral angles φ_1^j and φ_4^j in vertex <i>j</i> for the triangle twist pattern, and $j = a, b, c$
μ_k	Relationship of the dihedral angles φ_1 and φ_4 in Type <i>k</i> vertex for the triangle twist pattern, and $k = p, q, r, s$
μ_i^j	Relationship of the dihedral angles φ_1^j and φ_4^j in vertex <i>j</i> for the triangle twist pattern with different types of M-V assignment, and $i=1, 2, \dots, 12, j = a, b, c$

Abbreviations

D-H notation	Denavit-Hartenberg notation
DOF	Degree of freedom
SVD	Singular value decomposition
M-V assignment	Mountain-valley crease assignment
EP	Equatorial plane

Chapter 1 Introduction

1.1 Background and Significance

Mechanism is a core research field in mechanical engineering, where diverse mechanisms are designed as mechanical components to achieve desired movements. Spatial linkage is a unique type of mechanism, in which the motion is described in three dimensions [1]. As a subset of spatial linkage, the spherical linkage describes the linkage where all points in the moving links move along curves that lie on concentric spheres [2]. There is a special kind of linkage that does not comply with the Grübler-Kutzbach's mobility criterion [3], referred to as overconstrained linkage. It is mobile due to the geometric properties of joints and links. It has been widely utilized in the field of aerospace engineered structures, mainly because of its structural stiffness, simple construction and performance reliability. Kinematics is the study on the geometry of motion in mechanisms without regard to the forces acting on the mechanism [4]. The kinematics of spatial linkages is much more difficult than planar linkages since they produce more complicated motion. The study on it helps to better understand the motion of spatial linkages, which is the basis for the design, dynamic analysis and control of mechanisms.

On the other hand, origami, an ancient oriental art of producing 2D or 3D intricate structures through folding a flat sheet of paper, has recently seen surge in a variety of engineering fields. The highlights in the newly formed origami engineering include mechanical metamaterials [5-13], self-folding machine and robots [14-16], reconfigurable structure [17], shock-resistance device [18], packing [19, 20], and so on. Although the motion of origami structure is utilized in these fields, little work has been done on the kinematic property of the origami pattern itself due to the complexity and multi-degree-of-freedom in the origami motion. One exception is Miura-ori, whose motion is relatively simple and its kinematic analysis has been widely used to reveal the mechanical properties, such as Poisson's ratio and stiffness [6, 8, 21]. Since most engineering materials used to construct origami structures and metamaterials are relatively rigid, a subset of origami that permits continuous motion between folded and unfolded states along the pre-determined creases without stretching or bending of the facets, rigid origami, has drawn special attention.

In the mechanism perspective, the creases of rigid origami can be treated as rotation joints and the paper facets treated as links [22]. A single-vertex pattern with all creases intersected at the vertex is kinematically a spherical linkage [23, 24]. Then the multi-vertex crease pattern can be modelled as a network of spherical linkages, and its rigid foldability can be judged by kinematic approaches [25-27]. Yet, in most of the practical engineering applications, the thickness of the material cannot simply be

ignored. To fold these thick panels, an approach has been proposed recently, where the creases no longer intersect at one point, so the spherical linkage assembly for the origami of zero-thickness sheet is replaced by an assembly of spatial overconstrained linkages [28, 29]. Therefore, the work on the kinematics of spherical linkages and spatial overconstrained linkages contributes to the motion analysis of rigid origami, which further facilitates the engineering applications of origami patterns.

1.2 Aim and Scope

The aim of this dissertation is to conduct kinematic analysis of spatial linkages based on the D-H matrix method and apply it to explore the rigid foldability and motion behaviour of origami patterns.

In this process, the rigid foldability of triangle twist origami pattern is firstly examined based on the kinematics of spherical $4R$ linkage network and new overconstrained $6R$ linkages are derived by kirigami technique. Then the kinematics of the plane-symmetric Bricard $6R$ linkage is analyzed and its bifurcation variations are discussed. After that, the results are applied to study the symmetric folding of six-crease thick-panel waterbomb origami, which is modelled as a network of plane-symmetric Bricard $6R$ linkages. The motion behaviour of its corresponding tessellation of zero-thickness sheet is demonstrated by a network of spherical $6R$ linkages. Finally, the motion behaviour of the closed cylindrical form of waterbomb origami is investigated through a parametric study, by means of modelling it as a closed network of spherical $6R$ linkages.

1.3 Outline of Dissertation

This dissertation consists of seven chapters, which are outlined as follows.

Chapter 2 presents a bibliographic review of existing work related to our task, including the work on kinematics of spatial linkages, rigid origami and their cross-over study. Kinematic analysis approach, singularity and bifurcation of spatial linkages, and existing spatial overconstrained $6R$ linkages are summarized. In the rigid origami part, the review starts from engineering applications of origami patterns, then to origami patterns consisting of four-crease vertices and six-crease vertices. The flat foldability and rigid foldability are distinguished. Rigidly foldable origami tubes, thick-panel origami as well as the kirigami technique are reported. Finally, the survey on cross-over study of spatial linkages and rigid origami is conducted, including the origami analysis based on spatial linkages, and origami-inspired linkages.

Chapter 3 deals with the rigid foldability and motion behaviour of a generalized triangle twist origami pattern. Diverse mountain-valley crease (M-V) assignments of this pattern are enumerated based on the flat-foldable conditions for four-crease vertex. The effect of M-V assignment on the rigid foldability is discussed. A variant of doubly

collapsible octahedral Bricard and a novel overconstrained $6R$ linkage are derived by applying the kirigami technique to this pattern.

Chapter 4 is to conduct the kinematics and bifurcation analysis of the plane-symmetric Bricard $6R$ linkage based on the traditional D-H matrix method. The explicit closure equations of this linkage are derived by solving the highly nonlinear trigonometric functions. Accordingly, the kinematic properties of different plane-symmetric Bricard linkages are discussed. The degenerated $5R/4R$ linkages are obtained under certain geometric conditions. Various bifurcation behaviours of the plane-symmetric Bricard linkage and their corresponding geometric conditions are demonstrated.

Chapter 5 focuses on the symmetric folding behaviour of flat-foldable waterbomb pattern with both zero-thickness sheet and thick panels. Considering the compatible conditions, a general kinematics model of the waterbomb pattern is presented. The kinematic equivalence between the thick-panel origami and that of zero-thickness sheet is proved, where the plane-symmetric Bricard linkage is adopted to replace the spherical $6R$ linkage for the thick-panel waterbomb origami. The kinematic behaviours of the general waterbomb origami under different geometric conditions are presented for both zero-thickness and thick-panel origami forms.

Chapter 6 is devoted to seek the motion behaviour of a generalized waterbomb tube under both longitudinal and circumferential symmetry through a parametric study. The kinematics of the tube is setup by modelling it as a closed network of spherical $6R$ linkages. Considering the longitudinal symmetry, the motion is classified into two cases according to the number of rows being odd or even. Different behaviours of the tube are revealed, including the uniform radius configuration, mechanism-structure-mechanism transition, wave-like configuration and rigid twist motion. The trigger conditions of these behaviours are discussed based on the kinematics of the tube.

The main achievements of the research are summarized in Chapter 7, together with suggestions for future works, which conclude this dissertation.

Chapter 2 Review of Previous Works

2.1 Kinematics of Spatial Linkages

2.1.1 Kinematic Analysis Approach

The science of kinematics deals with the geometrical and time properties of a motion [2]. A detailed kinematic analysis of spherical mechanisms has been conducted by Chiang [30]. Several methods have been developed to analyze the kinematics of spatial linkages. Denavit and Hartenberg proposed a matrix method based on the use of four independent parameters, referred to as D-H notation [31]. Gogu systematically presented structural synthesis of various spatial parallel mechanisms by the theory of linear transformation [32]. Dai comprehensively presented the kinematics, mobility, mechanics and stiffness of various mechanisms, devices and robots based on the screw theory [33] after the theory being proposed by Ball [34] and developed by Hunt [3]. The theory has been further extended to finite screws for the kinematics of closed-loop linkages [35-37] based on the screw triangle [38]. Murray, Li and Sastry illustrated the kinematics of manipulators and multi-fingered hands by Lie group and Lie algebra theory [39]. This method was also adopted for the motion analysis of parallel mechanisms [40], such as the 3-PUP mechanism [33, 41]. Clifford algebra, also known as geometric algebra, has been adopted in the kinematics analysis of spatial linkages as well. Chai and Li derived the analytical expression of the motion space of Bennett linkage by this approach [42]. Dual quaternions, a kind of Clifford algebra, were used for the kinematic synthesis of constrained robotic systems [43] and inverse kinematics of general spatial $7R$ mechanism [44] as well as in neuroscience [45]. Based on dual quaternions, a new theory for the kinematic analysis of closed $5R$ linkages with revolute joints, termed as bond theory, was proposed by Hegedüs, Schicho and Schröcker [46, 47]. The theory was then extended to Stewart Gough platforms [48] as well as closed $6R$ linkages [49]. Chablat, Kong and Zhang dealt with a comprehensive kinematic study of a 3-DOF multi-mode parallel robot [50]. A comparative study on the three methods for robot kinematics based on the matrix transformation, Lie algebra and screw theory, has been conducted [33, 51]. The geometric methods in robotics including Lie groups and its subgroups, Lie algebra, line geometry, screw theory and Clifford algebra have also been reviewed by Selig [52]. Among all these methods, the matrix method based on D-H notation [31, 53] provides a straightforward way to reveal the motion of each joint and its relationship with any other joints, so it is adopted to conduct the kinematics of spatial linkages in this dissertation.

The setup of each coordinate system in a linkage is presented in Fig. 2-1, where the axis z_i is along the revolute joint i , x_i is the common normal from z_{i-1} to z_i , and y_i is determined by the right-hand rule. Thus the geometric parameters are

defined as the link length $a_{i(i+1)}$, the link twist $\alpha_{i(i+1)}$ and the joint offset R_i , where $a_{i(i+1)}$ is the normal distance between axes z_i and z_{i+1} , $\alpha_{i(i+1)}$ is the angle of rotation from z_i to z_{i+1} , positive along x_{i+1} , and R_i is the normal distance between axes x_i and x_{i+1} , positive along z_i . The kinematic variable θ_i is defined as the angle of rotation from x_i to x_{i+1} , positive along z_i , which measures the rotation between two links joined by the revolute joint z_i .

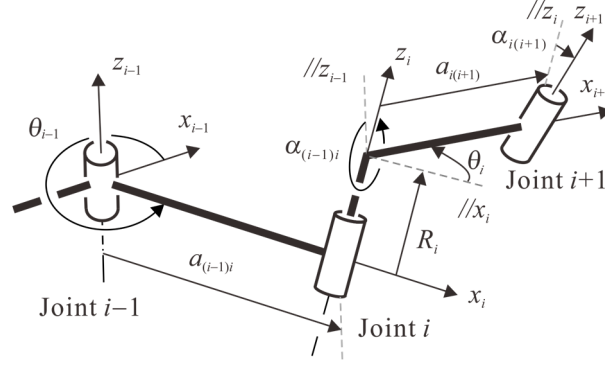


Fig. 2-1 The D-H notation of adjacent links connected by revolute joints

For a single-loop linkage consisting of k links, the closure equation is

$$\mathbf{T}_{21}\mathbf{T}_{32}\dots\mathbf{T}_{1k} = \mathbf{I}_4, \quad (2-1)$$

where the transformation matrix $\mathbf{T}_{(i+1)i}$ is

$$\mathbf{T}_{(i+1)i} = \begin{bmatrix} \cos \theta_i & -\cos \alpha_{i(i+1)} \sin \theta_i & \sin \alpha_{i(i+1)} \sin \theta_i & a_{i(i+1)} \cos \theta_i \\ \sin \theta_i & \cos \alpha_{i(i+1)} \cos \theta_i & -\sin \alpha_{i(i+1)} \cos \theta_i & a_{i(i+1)} \sin \theta_i \\ 0 & \sin \alpha_{i(i+1)} & \cos \alpha_{i(i+1)} & R_i \\ 0 & 0 & 0 & 1 \end{bmatrix}, \quad (2-2)$$

and when $i+1 > k$, it is replaced by 1. It transforms the expression in the $(i+1)$ th coordinate system to the i th coordinate system. The inverse transformation $\mathbf{T}_{i(i+1)}$ has the following property.

$$\mathbf{T}_{i(i+1)} = \mathbf{T}_{(i+1)i}^{-1} = \begin{bmatrix} \cos \theta_i & \sin \theta_i & 0 & -a_{i(i+1)} \\ -\cos \alpha_{i(i+1)} \sin \theta_i & \cos \alpha_{i(i+1)} \cos \theta_i & \sin \alpha_{i(i+1)} & -R_i \sin \alpha_{i(i+1)} \\ \sin \alpha_{i(i+1)} \sin \theta_i & -\sin \alpha_{i(i+1)} \cos \theta_i & \cos \alpha_{i(i+1)} & -R_i \cos \alpha_{i(i+1)} \\ 0 & 0 & 0 & 1 \end{bmatrix} \quad (2-3)$$

As for spherical linkages, the axes intersect at one point as shown in Fig. 2-2, which means the lengths and offsets of each links are zero and thus Eq. (2-1) reduces to

$$\mathbf{Q}_{21}\mathbf{Q}_{32}\dots\mathbf{Q}_{1k} = \mathbf{I}_3, \quad (2-4)$$

where

$$\mathbf{Q}_{(i+1)i} = \begin{bmatrix} \cos \theta_i & -\cos \alpha_{i(i+1)} \sin \theta_i & \sin \alpha_{i(i+1)} \sin \theta_i \\ \sin \theta_i & \cos \alpha_{i(i+1)} \cos \theta_i & -\sin \alpha_{i(i+1)} \cos \theta_i \\ 0 & \sin \alpha_{i(i+1)} & \cos \alpha_{i(i+1)} \end{bmatrix}, \quad (2-5)$$

and the inverse transformation is

$$\mathbf{Q}_{i(i+1)} = \begin{bmatrix} \cos \theta_i & \sin \theta_i & 0 \\ -\cos \alpha_{i(i+1)} \sin \theta_i & \cos \alpha_{i(i+1)} \cos \theta_i & \sin \alpha_{i(i+1)} \\ \sin \alpha_{i(i+1)} \sin \theta_i & -\sin \alpha_{i(i+1)} \cos \theta_i & \cos \alpha_{i(i+1)} \end{bmatrix}. \quad (2-6)$$

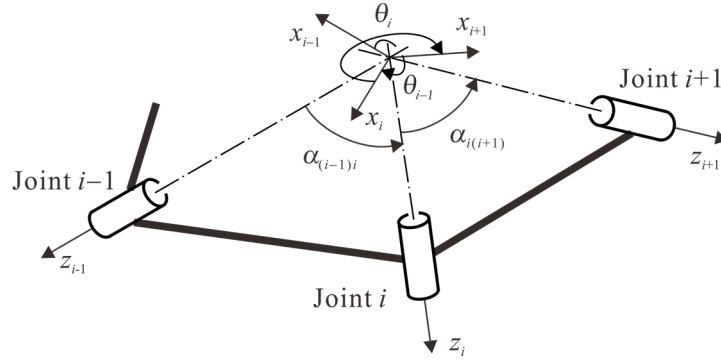


Fig. 2-2 The D-H notation of a portion of a spherical linkage

Therefore, the kinematics and motion behaviour of spatial linkages can be carried out based on the solutions of Eq. (2-1) or Eq. (2-4).

2.1.2 Singularity and Bifurcation

During the investigation on kinematics of spatial linkages, singularity should be taken into consideration. It is a configuration of a system in which the subsequent behaviour cannot be predicted [54]. Gosselin and Angeles defined singularity as a configuration in which the Jacobian matrices involved become rank deficient [55]. It is shown that singularities of closed-loop mechanisms can be classified into three types including inverse kinematic singularity, direct kinematic singularity and combined singularity. However, there exists a new family of singularity in parallel mechanisms where the Jacobian matrix of the input-output velocity equation is not singular, termed as constraint singularity by Zlatanov, Bonev and Gosselin [56]. This kind of singularity occurs at a configuration where the screw system of the constraint wrenches degenerates and the degree of freedom (DOF) of the mechanism instantaneously increases. Numerous approaches have been adopted to analyze the singularity of spatial mechanisms. For example, geometric algebra was used for the singularity analysis of 3-RPS [57], 3-RPR [58], and 3/6 Stewart parallel manipulators [59]. Jha et al. presented a descriptive singularity analysis of a Delta-like family by using algebraic tools [60]. SingLab, a graphical user interface for the singularity analysis of parallel robots based on the Grassmann-Cayley algebra, was developed by Ben-Horin et al. [61]. This

method was then extended to the singularity analysis of lower mobility parallel manipulators [62] and a 6-DOF parallel manipulator together with Gröbner bases [63].

Bifurcation is the phenomenon that the mechanism has two motion branches when it comes to the constraint singularity [64]. An algorithm for determining all the configuration branches and bifurcation points of symmetric Stewart platform was proposed by Wang and Wang [65]. It is believed by Lee and Hervé that bifurcation belongs to a special category of singularity, during the study of a 6R mechanism with a bifurcation towards two distinct single-DOF modes [66]. A parallel mechanism with bifurcation of Schönflies motion was designed by Li and Hervé [67]. Zhang, Dai and Fang investigated the bifurcated motion of the 3-PUP parallel mechanism when the platform is parallel to the base [33, 68]. Gogu discussed the nature of bifurcation in constraint singularities and demonstrated the relation between these singularities with the structural parameters of parallel mechanisms [54, 69].

For single-loop linkages, Chen and You stated a bifurcation of the extended Myard 6R linkage at two configurations where two states of self-stress exist and the DOF increases [70]. Song, Chen and Chen found a 6R linkage constructed by two Bennett linkages in an asymmetric configuration, which could bifurcate between Bennett linkage and general line-symmetric Bricard linkage [71]. Song and Chen presented the bifurcation of the double-subtractive-Goldberg 6R linkage [72] and Wohlhart's double-Goldberg 6R linkage [73]. Zhang and Dai proposed a metamorphic 8R linkage and investigated bifurcation and trifurcation of its two extracted overconstrained 6R linkages [33, 74]. They also presented an evolved Sarrus-motion linkage with trifurcation under specific parametric constraints [75]. Multifurcation was revealed by Qin, Dai and Gogu as a phenomenon that several states of a mechanism with different mobility would occur once a mechanism passes a constraint singularity [76] and was revealed by Aimedee et al. as a case for reconfiguration [77]. Zhang, Müller and Dai investigated the multifurcation of a reconfigurable 7R linkage, which can be transformed between the non-overconstrained 7R linkage and overconstrained 6R and 4R linkages [78]. He et al. developed a novel one-DOF single-loop reconfigurable 7R mechanism with multiple modes by insecting a revolute joint to the overconstrained Sarrus linkage [79].

Various tools have been used to study bifurcation of spatial overconstrained linkages. Pellegrino proposed a structural computation to determine the number of independent states of self-stress in the mechanism with singular value decomposition (SVD) of the equilibrium matrix [80], which was used to analyze the bifurcation of threefold-symmetric Bricard linkage [81]. Gan and Pellegrino introduced a numerical solution to a loop-closure equation for deployable structures forming a closed loop [82], which was adopted in the detection of bifurcation of double-subtractive-Goldberg 6R linkage [72] and Wohlhart's double-Goldberg 6R linkage [73]. Kumar and Pellegrino

developed a special algorithm to detect the existence of a bifurcation ahead of the current configuration [83]. The screw theory particularly the screw system approach [33, 84-86] has also been adopted in the bifurcation analysis of parallel mechanisms. Chen and Chai discovered the bifurcation of a special line and plane symmetric Bricard linkage from the motion paths based on closure equations [87]. Most of these methods help to identify the existence of bifurcation, but further work needs to be done on the specific bifurcated motion branches. Explicit solutions of closure equations contribute to reveal the detailed motion process of spatial linkages, therefore they will be derived based on the D-H notation in this dissertation.

2.1.3 Spatial Overconstrained 6R Linkages

For a spatial linkage, mobility, the number of independent coordinates needed to define the configuration of a kinematic chain or mechanism [88], can be determined by the Grübler-Kutzbach criterion [3]:

$$M = 6(N - g - 1) + \sum_{i=1}^g f_i, \quad (2-7)$$

where M is the number of DOFs, N is the number of links in the linkage including the fixed one, g is the number of kinematic pairs in the linkage, f_i is the number of DOFs for the i th kinematic pair.

However, some spatial linkages are mobile without satisfying the mobility criterion as Eq. (2-7), which are known as overconstrained linkages [84]. Here the focus is put on the overconstrained 6R linkages, which is a single closed-loop overconstrained linkage constructed by six revolute joints. These overconstrained 6R linkages are classified as followed.

(1) Bennett-based overconstrained 6R linkages

The Bennett linkage is a spatial overconstrained 4R linkage with zero offsets, in which alternative links have same lengths and twists, and the lengths are proportional to sine values of corresponding twists as shown in Fig. 2-3. The setup of the coordinate systems are in accordance with the D-H notation [31]. It is the only spatial overconstrained 4R linkage with joint axes neither concurrent nor parallel. Its geometry conditions are

$$a_{12} = a_{34} = a, \quad a_{23} = a_{41} = b, \quad (2-8a)$$

$$\alpha_{12} = \alpha_{34} = \alpha, \quad \alpha_{23} = \alpha_{41} = \beta, \quad (2-8b)$$

$$\sin \alpha/a = \sin \beta/b, \quad (2-8c)$$

$$R_i = 0 \quad (i = 1, 2, 3, 4). \quad (2-8d)$$

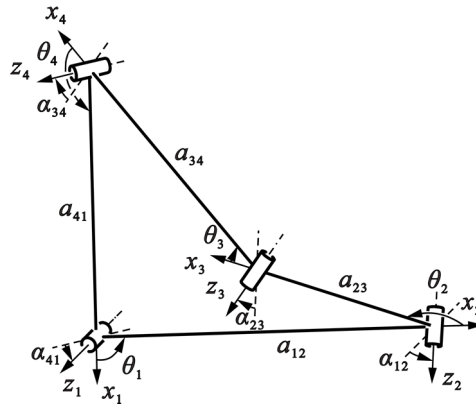


Fig. 2-3 The Bennett linkage

As a construction element, it can be combined together to generate different types of single-loop overconstrained 6R linkages with properly synthesis and construction methods. Baker defined the obtained linkages as Bennett-based overconstrained 6R linkages, on which a throughout and in-depth research was conducted [89]. These linkages include Myard's 6R linkage and its extension [90, 91], Goldberg's 6R linkages [92-94], Wohlhart's double-Goldberg 6R linkage [93], double-subtractive-Goldberg 6R linkage [94], back-to-back double-Goldberg 6R linkage [95], mixed double-Goldberg 6R linkages [96], Waldron's hybrid 6R linkage [97] and Yu and Baker's syncopated 6R linkage [98] etc. Figure 2-4 illustrates the construction of a serial Goldberg 6R linkage by combining three Bennett linkages where the common joints and links shown in dashed lines are removed. Since the Bennett linkage is the construction unit, its geometric condition should be satisfied for all Bennett-based overconstrained 6R linkages.

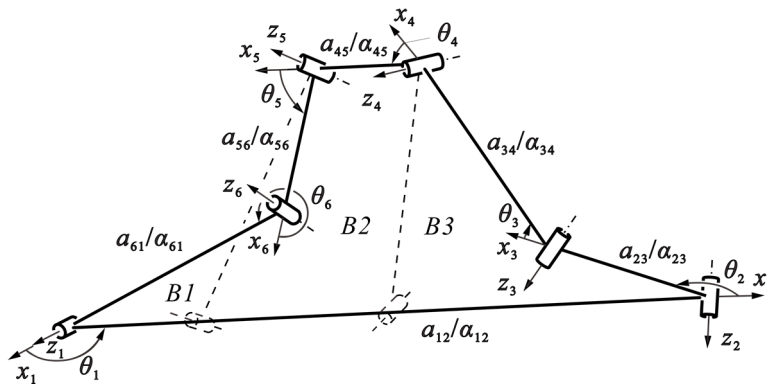


Fig. 2-4 Construction of a serial Goldberg 6R linkage

(2) Bricard 6R linkages

This family of overconstrained 6R linkages was proposed by Bricard consisting of three deformable octahedral cases [99] and three spatial-linkage cases [100], see Fig. 2-5, of which the mobility is due to the symmetric property. The geometric conditions of these linkages are listed below.

For the general line-symmetric case,

$$a_{12} = a_{45}, \quad a_{23} = a_{56}, \quad a_{34} = a_{61}, \quad (2-9a)$$

$$\alpha_{12} = \alpha_{45}, \quad \alpha_{23} = \alpha_{56}, \quad \alpha_{34} = \alpha_{61}, \quad (2-9b)$$

$$R_1 = R_4, \quad R_2 = R_5, \quad R_3 = R_6. \quad (2-9c)$$

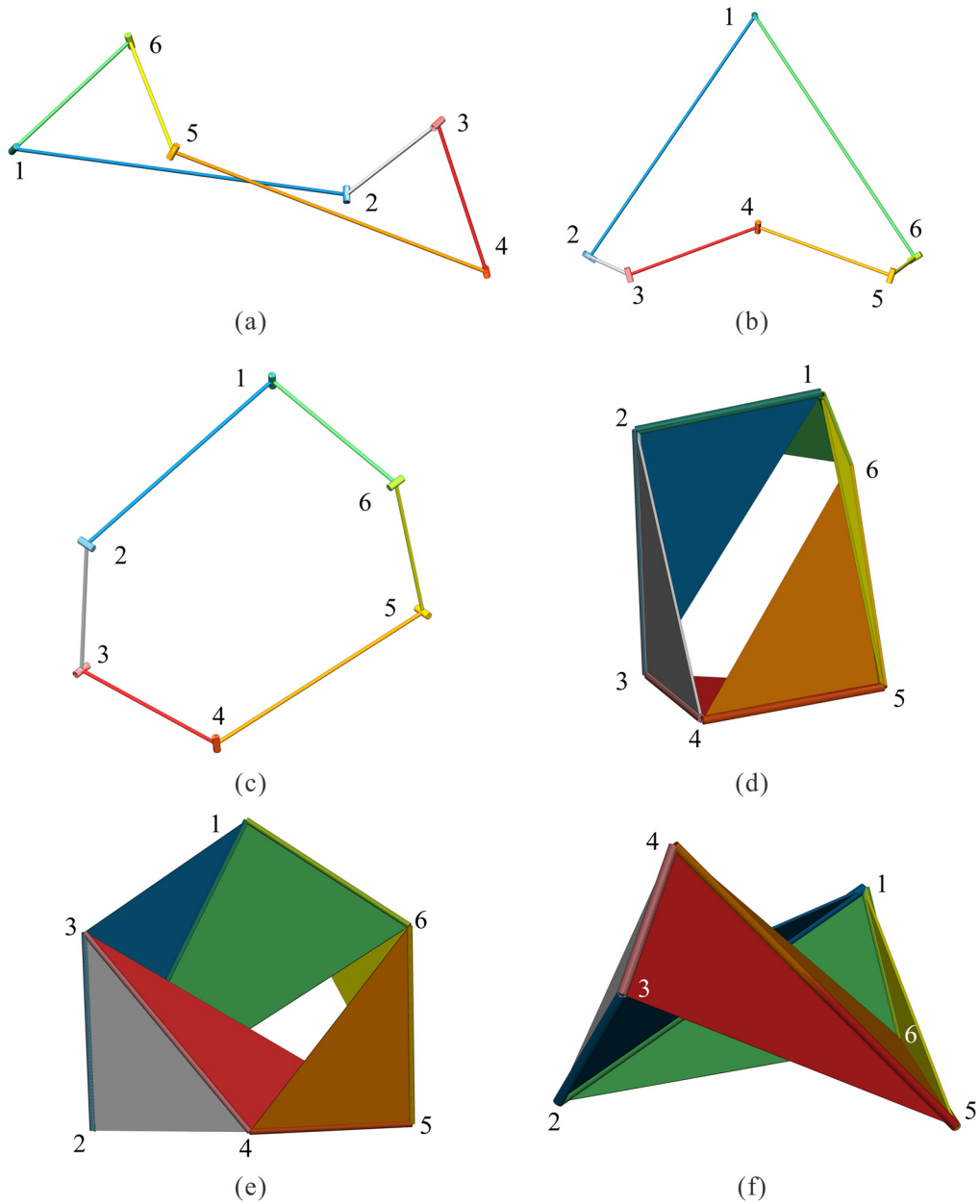


Fig. 2-5 Bricard 6R linkages: (a) the general line-symmetric case, (b) the general plane-symmetric case, (c) the trihedral case, (d) the line-symmetric octahedral case, (e) the plane-symmetric octahedral case, and (f) the doubly collapsible octahedral case.

For the general plane-symmetric case,

$$a_{12} = a_{61}, \quad a_{23} = a_{56}, \quad a_{34} = a_{45}, \quad (2-10a)$$

$$\alpha_{12} + \alpha_{61} = \pi, \quad \alpha_{23} + \alpha_{56} = \pi, \quad \alpha_{34} + \alpha_{45} = \pi, \quad (2-10b)$$

$$R_1 = R_4 = 0, \quad R_2 = R_6, \quad R_3 = R_5. \quad (2-10c)$$

For the trihedral case,

$$a_{12}^2 + a_{34}^2 + a_{56}^2 = a_{23}^2 + a_{45}^2 + a_{61}^2, \quad (2-11a)$$

$$\alpha_{12} = \alpha_{34} = \alpha_{56} = \frac{\pi}{2}, \quad \alpha_{23} = \alpha_{45} = \alpha_{61} = \frac{3\pi}{2}, \quad (2-11b)$$

$$R_i = 0 \quad (i = 1, 2, \dots, 6). \quad (2-11c)$$

For the line-symmetric octahedral case,

$$a_{12} = a_{23} = a_{34} = a_{45} = a_{56} = a_{61} = 0, \quad (2-12a)$$

$$R_1 + R_4 = R_2 + R_5 = R_3 + R_6 = 0. \quad (2-12b)$$

For the plane-symmetric octahedral case,

$$a_{12} = a_{23} = a_{34} = a_{45} = a_{56} = a_{61} = 0, \quad (2-13a)$$

$$R_4 = -R_1, \quad R_2 = -R_1 \frac{\sin \alpha_{34}}{\sin(\alpha_{12} + \alpha_{34})}, \quad R_3 = -R_1 \frac{\sin \alpha_{12}}{\sin(\alpha_{12} + \alpha_{34})},$$

$$R_5 = -R_1 \frac{\sin \alpha_{61}}{\sin(\alpha_{45} + \alpha_{61})}, \quad R_6 = -R_1 \frac{\sin \alpha_{45}}{\sin(\alpha_{45} + \alpha_{61})}. \quad (2-13b)$$

For the doubly collapsible octahedral case,

$$a_{12} = a_{23} = a_{34} = a_{45} = a_{56} = a_{61} = 0, \quad (2-14a)$$

$$R_1 R_3 R_5 + R_2 R_4 R_6 = 0. \quad (2-14b)$$

The study on the three Bricard octahedral cases began with Bennett who studied their geometry and kinematic properties [101]. Lee derived closure equations of the three octahedral cases with matrix transformation method [102]. Baker found that the stationary configurations of a special line-symmetric octahedral case are precisely equivalent to the minimum energy conformations of the flexing molecule [103]. Chai and Chen found a stationary structural configuration of the line-symmetric octahedral case with identical twists and offsets, which is independent of its mobile linkage form [104]. For the doubly collapsible octahedral case, Baker studied its planar, spherical and skew counterparts [105]. He also found out the connection between three six-bar linkage families synthesized from Bennett isograms and the skew network engendered by the doubly collapsible octahedral cases [106]. Lu et al. presented the construction of deployable quadrangles by the doubly collapsible octahedron together with a detailed parametric study [107]. They used this octahedron as the construction element to design one-DOF networks [108] as well as reconfigurable mechanisms [109].

As to the Bricard linkage cases, Goldberg made and analyzed a 6-plate linkage which is actually the trihedral Bricard linkage [110]. Yu studied the geometry of the

trihedral Bricard linkage with its circumscribed sphere and associated quadric surface [111]. Wohlhart studied the orthogonal Bricard linkage and revealed the two distinct trihedral cases [112]. For the general line-symmetric case, Baker analyzed it with the reciprocal screw system considering the special geometry constraint of the linkage [113]. Song, Chen and Chen found that it can bifurcate to the Bennett linkage under certain circumstance [71]. They also conducted kinematic study of the original and revised line-symmetric Bricard linkages [114]. Zhang and Dai extracted two special line-symmetric Bricard linkages from a metamorphic $8R$ linkage [74]. López-Custodio, Dai and Rico studied its branch reconfiguration based on toroid intersections [115].

Among them, the plane-symmetric Bricard linkage has been extensively studied. First of all, implicit closure equations of six Bricard linkages were derived by Baker [116]. Phillips reviewed the Bricard linkages and introduced their relationship with other overconstrained linkages [117]. Baker analyzed the general plane-symmetric six-screw linkage including the plane-symmetric Bricard linkage with the reciprocal screw system approach [118]. The movability of the plane-symmetric Bricard linkage was investigated by Li and Schicho based on the theory of bonds [119]. Deng et al. presented a geometric approach for design and synthesis of single loop mechanisms including the plane-symmetric Bricard linkage [120]. They also proposed a virtual chain approach for the mobility analysis of multi-loop deployable mechanisms with plane-symmetric Bricard linkage as basic element [121]. Kong conducted type synthesis of single-loop overconstrained $6R$ spatial mechanisms for circular translation in which the plane-symmetric Bricard linkage is taken as an example [122]. Even though various synthesis methods have been used to study the plane-symmetric Bricard linkage, there is no progress on the solution of explicit closure equations after Baker's implicit ones.

Recent research applies the plane-symmetric Bricard linkage to the design of deployable structures. For example, Chen, You and Tarnai proposed a threefold-symmetric Bricard linkage which is a special case of the plane-symmetric one to fold the triangular or hexagonal structures [81]. Viquerat, Hutt and Guest design a rectangular ring which can be folded into a compact bundle. Kinematically this is an alternative form of the plane-symmetric Bricard linkage [123]. A number of such retractable rectangular rings can form a family of large deployable mechanisms by synchronizing the motion of all linkages [124].

Because of the symmetry property, the plane-symmetric Bricard $6R$ linkage tends to have complicated bifurcation behaviours, which should be avoided in the application of deployable structures, but could be made use of in the design of reconfigurable mechanisms. The kinematics and bifurcation behaviour of a special line- and plane-symmetric Bricard linkage was analyzed using the SVD numerical method by Chen and Chai [87]. Zhang and Dai analyzed motion branch variations of the line- and plane-symmetric Bricard linkage based on reciprocal screw systems [33, 125]. López-

Custodio, Dai and Rico revealed a set of special plane-symmetric Bricard linkages with various branches of reconfiguration based on intersection of two generating toroids [126]. However, the current bifurcation analysis of the plane-symmetric Bricard linkage only focuses on special cases.

(3) Other overconstrained 6R linkages

There are several other overconstrained 6R linkages except for the two major linkage family, i.e., Bennett-based linkage family and Bricard linkage family. The Sarrus linkage is the first spatial overconstrained linkage, which has two set of hinges with different directions and each set consists of three parallel hinges [127]. Baker derived the closure equations of the double-Hooke's-joint linkage, which has been widely used as a transmission coupling [128]. Its geometric conditions are

$$a_{23} = a_{34} = a_{56} = a_{61} = 0, \quad \alpha_{23} = \alpha_{34} = \alpha_{56} = \alpha_{61} = \frac{\pi}{2}, \quad R_1 = R_2 = R_3 = R_6 = 0. \quad (2-15)$$

Bennett extended these two linkages to a general one, i.e., the Bennett plano-spherical hybrid 6R linkage, which can be regarded as a combination of two spherical 4R linkages with different centres [129]. The screw-system-variation enabled reconfiguration of this linkage and its evolved novel metamorphic parallel mechanism have been investigated by Zhang and Dai [130]. Altmann proposed an overconstrained 6R linkage, which was later identified as a special case of general line-symmetric Bricard linkage [131]. Its geometric conditions are

$$a_{12} = a_{45} = a, \quad a_{23} = a_{56} = 0, \quad a_{34} = a_{61}, \quad (2-16a)$$

$$\alpha_{12} = \alpha_{45} = \pi/2, \quad \alpha_{23} = \alpha_{56} = \pi/2, \quad \alpha_{34} = \alpha_{61} = 3\pi/2, \quad (2-16b)$$

$$R_i = 0 \quad (i = 1, 2, \dots, 6). \quad (2-16c)$$

Schatz derived a linkage from a special trihedral Bricard case, referred to as Schatz linkage, which was used as a Turbula machine for mixing fluids and powders [117]. Its geometric conditions are

$$a_{12} = a_{56} = 0, \quad a_{23} = a_{34} = a_{45} = a, \quad a_{61} = \sqrt{3}a, \quad (2-17a)$$

$$\alpha_{12} = \alpha_{23} = \alpha_{34} = \alpha_{45} = \alpha_{56} = \pi/2, \quad \alpha_{61} = 0, \quad (2-17b)$$

$$R_1 = -R_6, \quad R_2 = R_3 = R_4 = R_5 = 0. \quad (2-17c)$$

Wohlhart proposed an overconstrained 6R linkage with three partially plane-symmetric link-pairs, which is a generalisation of the trihedral Bricard linkage [132]. Its geometric conditions are

$$a_{12} = a_{23}, \quad a_{34} = a_{45}, \quad a_{56} = a_{61}, \quad (2-18a)$$

$$\alpha_{12} = -\alpha_{23}, \quad \alpha_{34} = -\alpha_{45}, \quad \alpha_{56} = -\alpha_{61}, \quad (2-18b)$$

$$R_1 = R_3 = R_5 = R_2 + R_4 + R_6 = 0. \quad (2-18c)$$

Mavroidis and Roth discovered the Bennett-joint $6R$ linkage when deriving the inverse kinematics for general $6R$ manipulators [133]. The geometric conditions of this overconstrained $6R$ linkage are

$$a_{12} = a_{34}, \quad a_{23} = a_{56}, \quad a_{45} = a_{61}, \quad (2-19a)$$

$$\alpha_{12} = \alpha_{34}, \quad \alpha_{23} = \alpha_{56}, \quad \alpha_{45} = \alpha_{61}, \quad (2-19b)$$

$$\sin \alpha_{12} / a_{12} = \sin \alpha_{23} / a_{23} = \sin \alpha_{45} / a_{45}, \quad (2-19c)$$

$$R_1 = R_4 = 0, \quad R_2 = R_5, \quad R_3 = R_6 \quad \text{or} \quad R_1 = R_4 = 0, \quad R_2 = R_6, \quad R_3 = R_5. \quad (2-19d)$$

Dietmaier found another overconstrained $6R$ linkage when solving the same inverse kinematics problem with a numerical method [134]. Its geometric conditions are

$$a_{23} = a_{56}, \quad (2-20a)$$

$$\alpha_{23} = \alpha_{56}, \quad (2-20b)$$

$$\begin{aligned} \sin \alpha_{12} / a_{12} &= \sin \alpha_{61} / a_{61}, \quad \sin \alpha_{34} / a_{34} = \sin \alpha_{45} / a_{45}, \\ \sin \alpha_{12} (\cos \alpha_{12} + \cos \alpha_{61}) / a_{12} &= \sin \alpha_{34} (\cos \alpha_{34} + \cos \alpha_{45}) / a_{34}, \end{aligned} \quad (2-20c)$$

$$R_1 = R_5, \quad R_2 = R_4, \quad R_3 = R_6 = 0. \quad (2-20d)$$

This section reviewed various spatial overconstrained $6R$ linkages. The emphasis was put on our object of study, Bricard linkages. For others, the geometric conditions are mainly summarized. Despite the extensive research on spatial overconstrained $6R$ linkages, the bifurcation behaviour of the plane-symmetric Bricard linkage as well as the inner relationship between the Bennett-based overconstrained linkages and the Bricard-related ones is to be revealed. In addition, novel mobile overconstrained $6R$ linkages remain to be discovered.

2.2 Rigid Origami

Origami has drawn increasing attention of mathematicians, scientists and engineers since the mid-1970s [135]. It has been widely adopted in aerospace engineering due to its superior efficiency of packaging large surface structures into smaller volumes for storage or transportation. These applications include solar arrays [136, 137], satellite antenna reflectors [138, 139] and space telescope [140, 141] etc. In civil engineering, the folding technique was used in the design of mobile facets [26, 142, 143], reconfigurable and multi-locomotive devices [14, 144, 145] and so on. In biomedical engineering, an origami stent graft was developed [146], several encapsulation origami robots [147-149] as well as origami surgical grippers [150, 151] were designed. Some of these applications are presented in Fig. 2-6.

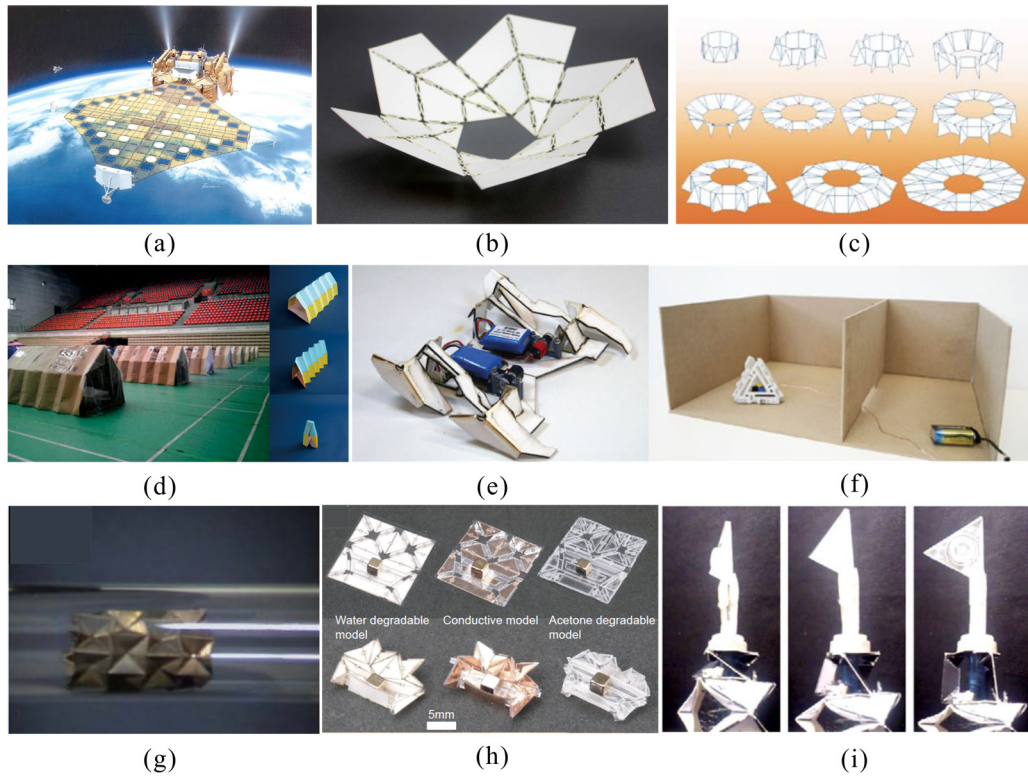


Fig. 2-6 Origami applications in aerospace engineering: (a) a foldable solar panel [137], (b) a deployable antenna [139], (c) a foldable telescopic lens [141]; in civil engineering: (d) a deployable origami tent [26], (e) a self-folding origami robot [14], (f) a modular origami robot [144]; and in biomedical engineering: (g) an origami stent [146], (h) an untethered miniature origami robot [147], (i) a four-DOF origami grasper [150].

2.2.1 Origami Patterns

In origami, there are two kinds of creases, i.e., mountain crease and valley crease. When you are looking at the paper, the mountain crease brings the moving part of the paper away from you, while the valley crease is opposite. The crease pattern refers to a mapping of all the creases in an origami form [152]. Even though there are numerous origami patterns, here my interests are limited in those consisting of four-crease vertices and six-crease vertices.

Among those origami patterns involving only four-crease vertices, the simplest one was presented by Huffman, which is called Huffman grid [153]. It consists of a single four-crease vertex, which is repeated continuously in rows and columns. Two sector angles of the vertex are equal to $\pi/2$ and the other two are equal to α and $\pi - \alpha$. By varying the angles of the generating vertex of Huffman grid, the chicken wire pattern was obtained by a mirror-symmetric vertex [154]. Barreto presented a pattern named Mars, which includes a single four-crease vertex and its inversion [155]. Miura invented an origami pattern comprised entirely of parallelograms for use in space

solar panels, referred to as Miura-ori [156]. The graded Miura-ori pattern was proposed by Xie, Li and Chen [157], and was used to design structure with graded stiffness by Ma, Song and Chen [21]. Tachi presented a quadrilateral mesh origami pattern consisting entirely of quadrilateral panels [158]. Evans et al. introduced origami gadgets to be used in modifying existing tessellations and creating new tessellations [159].

There is a family of origami twist among the four-crease-vertex origami patterns, which was often used for tessellation of origami patterns in art [160]. It is a crease pattern consisting of a central polygon with parallel crease-pairs radiating from each side of the central polygon [161]. Three typical origami twist patterns including triangle twist, square twist and hexagon twist are presented in Fig. 2-7.

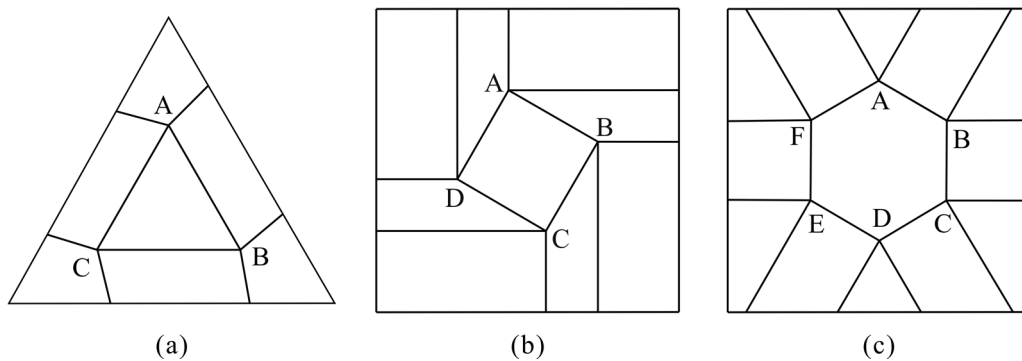


Fig. 2-7 Three typical types of origami twist patterns: (a) triangle twist, (b) square twist, and (c) hexagon twist.

For those origami patterns consisting of only six-crease vertices, there are three common patterns including Yoshimura pattern (also diamond pattern), waterbomb pattern and Resch pattern. The Yoshimura pattern was observed in the buckling pattern of longitudinally stressed cylinder by Yoshimura, which is a tessellation of six-crease diamonds with either all mountain or all valley folds along the diagonals [162, 163]. The Resch pattern is composed of many equivalent polygons [164], a special case of which is the one with only six-crease vertices. As to the waterbomb pattern, two terms are related to it: waterbomb bases and waterbomb tessellations. There are two types of waterbomb bases: the eight-crease base and the six-crease base. The former is made from a square sheet of paper consisting of eight alternating mountain and valley creases around a central vertex, Fig. 2-8(a). One of its typical tessellations is produced by four such bases tiling around a smaller square forming the square Resch pattern, Figs. 2-8(b) and (c). The latter, consisting of two mountain and four valley creases meet at a single vertex [165] shown in Fig. 2-8(d), is more commonly known, and its tessellations range from a flat-foldable surface to a deformable tube known as the magic origami ball, Figs. 2-8(e) and (f).

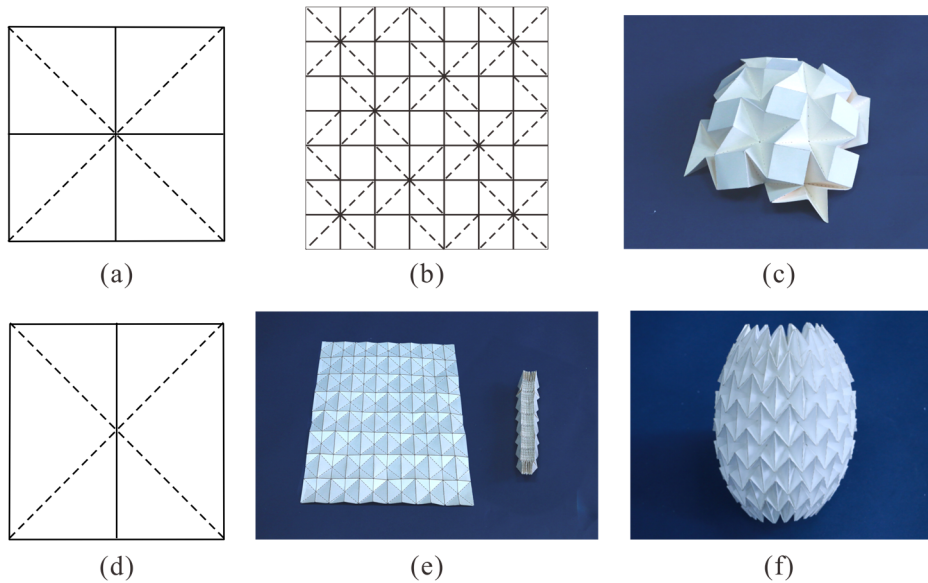


Fig. 2-8 (a) The eight-crease waterbomb base, (b) one of its tessellations forming the Resch pattern, (c) partially folded Resch pattern; (d) the six-crease waterbomb base, (e) its tessellation in unfolded and folded states, and (f) the tessellation can also be used to form a tube.

Among the vast pool of origami patterns, our particular interest are the triangle twist and the six-crease waterbomb pattern. For the triangle twist origami pattern, Evans et al. have analyzed its rigid foldability [161]. However, they did not tackle the one with non-parallel crease-pairs. Peng, Ma and Chen have considered all position relation of the crease-pairs, but the central triangle in the pattern was limited to an equilateral one [166]. For the six-crease waterbomb origami pattern, the motion of a single waterbomb base, analyzed as a spherical $6R$ linkage [30], has been shown to be rigidly foldable with three DOFs in general. When the base is tessellated, the DOF of the pattern could increase significantly if the pattern consists of a large number of waterbomb bases. Tachi, Masubuchi and Iwamoto have worked on the rigidity of its multi-DOF tessellation to achieve an adaptive freeform surface [167]. Although the waterbomb pattern is of multiple degrees of freedom, the symmetric folding is often preferred in most of research or art work, which is done by constraining it with symmetric conditions and then controlling the motion to reach an ideal flat-foldable state. Moreover, the modelling approach of the reaction force based on repelling screws has been implemented to the waterbomb base and the waterbomb-based integrated parallel mechanism [33, 168].

On the application side, the triangle twist could be adapted to design a surface linkage for large-scale deployable structures [169]. Single waterbomb bases have been applied as adaptive façades [170] and waterbomb tessellations have been applied in an extensible continuum robot [15] and an origami grasper [150]. The tubular configuration of the waterbomb is the most commonly-used form. For example, a self-deployable medical origami stent was proposed firstly with the structure being the

waterbomb tube [146]. A mobile robot with worm-like locomotion was designed later [171] and a novel earthworm-like locomotion robot was created incorporating with origami ball structures recently [172]. Besides, a deformable wheel robot [173] and highly efficient artificial muscles [174] were made using magic-ball origami structure. In all of the above-mentioned applications, the waterbomb tube undergoes only radial expansion/contraction, accompanied by the extending/shortening in the axial direction. In this folding motion, a rigorous synchronization of the waterbomb bases along a circumferential row is necessitated, which requires active motion control to realize.

Despite the wide application, the motion behaviour of the six-crease waterbomb origami has remained ambiguous as its kinematic behaviour changes drastically depending on the employed tessellation.

2.2.2 Flat Foldability and Rigid Foldability

For an origami pattern, flat foldability and rigid foldability are two important properties in both theory and practice. The flat foldability deals with the capacity of an origami pattern to be folded into flat sheets while the rigid foldability refers to the fact that panels do not stretch or bend during the folding process.

The flat foldability allows the origami pattern to achieve compact folding, which benefits the transportation and storage. Much work has been done on this aspect. Hull initiated a mathematical study on origami and gave the necessary and sufficient conditions of origami models with flat foldability [175, 176]. Bern and Hayes studied the flat foldability of a given crease and showed that assigning mountain and valley creases is non-deterministic polynomial hard [177]. Schneider gave the conditions for an arbitrary unsigned crease pattern to fold flat [178]. Tachi provided a design system to create new and complex 3D freeform origami patterns while preserving the flat foldability [179].

There are three conditions of flat foldability [152]. First, as indicated by the *Maekawa-Justin Condition*, for any flat-foldable vertex, the difference between the numbers of mountain creases and valley creases should be equal to two. That is,

$$n_M - n_V = \pm 2, \quad (2-21)$$

where n_M is the number of mountain creases and n_V is the number of valley creases. As a result, the number of creases for a flat-foldable vertex should be even.

Second, according to the *Kawasaki-Justin Condition*, let \mathcal{V} be a vertex of degree $2n$ in a single-vertex origami pattern, and let $\alpha_1, \alpha_2, \dots, \alpha_{2n}$ be the consecutive angles between the creases, the vertex \mathcal{V} is flat-foldable if and only if

$$\alpha_1 - \alpha_2 + \alpha_3 - \dots - \alpha_{2n} = 0. \quad (2-22)$$

Together with the developability that $\alpha_1 + \alpha_2 + \alpha_3 + \dots + \alpha_{2n} = 2\pi$, the sum of the

alternative angles about the flat-foldable vertex is π .

Third, as stated in the *Big-Little-Big Angle Condition*, if a smaller sector angle is bounded by two larger sector angles, the crease assignments of the two creases bounding the smaller angle are opposite to each other. It means that the two creases around the smallest angle must be of opposite assignment.

Rigid foldability allows an origami pattern to fold about crease lines without twisting or stretching component panels. It enables folding of rigid materials, facilitating the design of foldable structures. To achieve rigid foldability, motions around each vertex must be compatible with those around its neighbours, attained only under specific pattern geometries. Several approaches have been proposed to judge the rigid foldability of origami patterns. Diagram and numerical methods were proposed by Watanabe and Kawaguchi to check the rigid foldability of several known origami patterns [180]. Tachi used some numerical algorithms to find out a family of rigidly foldable origami with quadrilateral mesh [158]. Hull adopted spherical trigonometry to check the rigid foldability of some origami patterns with four-crease vertices [181]. Wu and You proposed the rotating vector model and employed quaternion and dual quaternion to study the rigid foldability of both single-vertex and multi-vertex origami patterns [182]. Cai et al. developed a new method to check the rigid foldability of cylindrical foldable structures by combining the quaternion rotation sequence method and the dual quaternion method [183, 184]. Recently, kinematic theories have been applied in the analysis and synthesis of rigid origami patterns [22-29, 185]. By setting up the kinematic model of the rigid origami pattern based on the assembly of spherical $4R$ linkages, four types of flat rigid origami patterns were obtained [185] as well as a family of deployable prismatic structures [26, 27].

Recent work shows that both the geometric conditions and mountain-valley crease (M-V) assignments affect the flat foldability and rigid foldability of origami patterns [153, 161, 186]. Hull examined the problem of counting the number of valid M-V assignments for a given crease pattern and developed recursive functions for single-vertex crease patterns [181]. For multi-vertex crease patterns, Evans et al. discussed the effect of M-V assignments on the rigid foldability for several origami twists including triangle twists, quadrilateral twists and regular polygon twists [161].

2.2.3 Rigidly Foldable Origami Tubes

The tubular structures with origami patterns have been adopted in various fields ranging from energy-absorbing devices [187] to medical devices [146]. Numerous origami patterns have been employed to generate tubular structures, such as the Yoshimura pattern [188], the Kresling pattern [189] and those proposed by Nojima [190]. However, these tubes can only be folded with deformation in surfaces. That is, they are not rigidly foldable. The emphasis is put on the rigidly foldable ones, especially

those with one DOF that are easy to be controlled.

Some efforts have been made to the rigidly foldable origami tubes. For example, Tachi invented a set of rigidly foldable origami tubes by a geometrical method [158, 191, 192]. A rigidly foldable cellular metamaterial was proposed based on a stack of the Miura-ori fold pattern [193]. The folding behaviour of Tachi-Miura polyhedron known as a rigidly foldable structure was examined [194]. Besides, the deployable prismatic structures with rigid origami pattern were analyzed in a kinematic approach [26]. Recently, new types of one-DOF rigidly foldable origami tubes have been constructed by either employing additional facets onto each modular unit or combining two joinable one-DOF tubes to a new configuration. These methods not only can be applied to multilayered vertical tubes, but also to a radially assembled arc form profiles [27]. For the tubular structure formed by waterbomb origami, it has multiple DOFs in general. It can be constrained to be rigidly foldable with one DOF under certain symmetric conditions [195].

2.2.4 Thick-panel Origami

Origami patterns are primarily created for zero-thickness sheets. However, the thickness of rigid materials cannot be ignored in practical applications. Hence, various methods have been proposed to fold thick panels as shown in Fig. 2-9. For instance, tapered surfaces have been used to fold a thick panel using the Miura-ori of zero-thickness sheet [196]. Offsets at the edge of the panels were introduced to implement folding of thick panels using the square-twist origami pattern [197]. A more recent research suggested to replace folds with two parallel ones to accommodate the thickness of materials [198]. In all of these methods, the fundamental kinematic model in which origami is treated as a series of interconnected spherical linkages remained. Different from the above-mentioned methods, an approach in which the fold lines were only allowed to be placed on top or bottom surfaces of flat thick panels has been proposed [29]. As a result, the spherical linkage assembly for the origami of zero-thickness sheet is replaced by an assembly of spatial linkages. It has been found that not only are the assemblies of such panels foldable, but they can be folded compactly under certain conditions. Lang et al. have made a thorough review on the thickness accommodation techniques in origami-inspired engineering [199]. They classified these techniques into seven cases, which include tapered panels technique, offset panel technique, hinge shift technique, doubled hinge technique, rolling contacts technique, membrane technique and strained joint technique. A detailed comparison of those techniques was conducted on several characteristics such as kinematics equivalency, motion preservability, surface flatness and design complexity. New hybrid approaches were also introduced by combining different thickness-accommodation techniques.

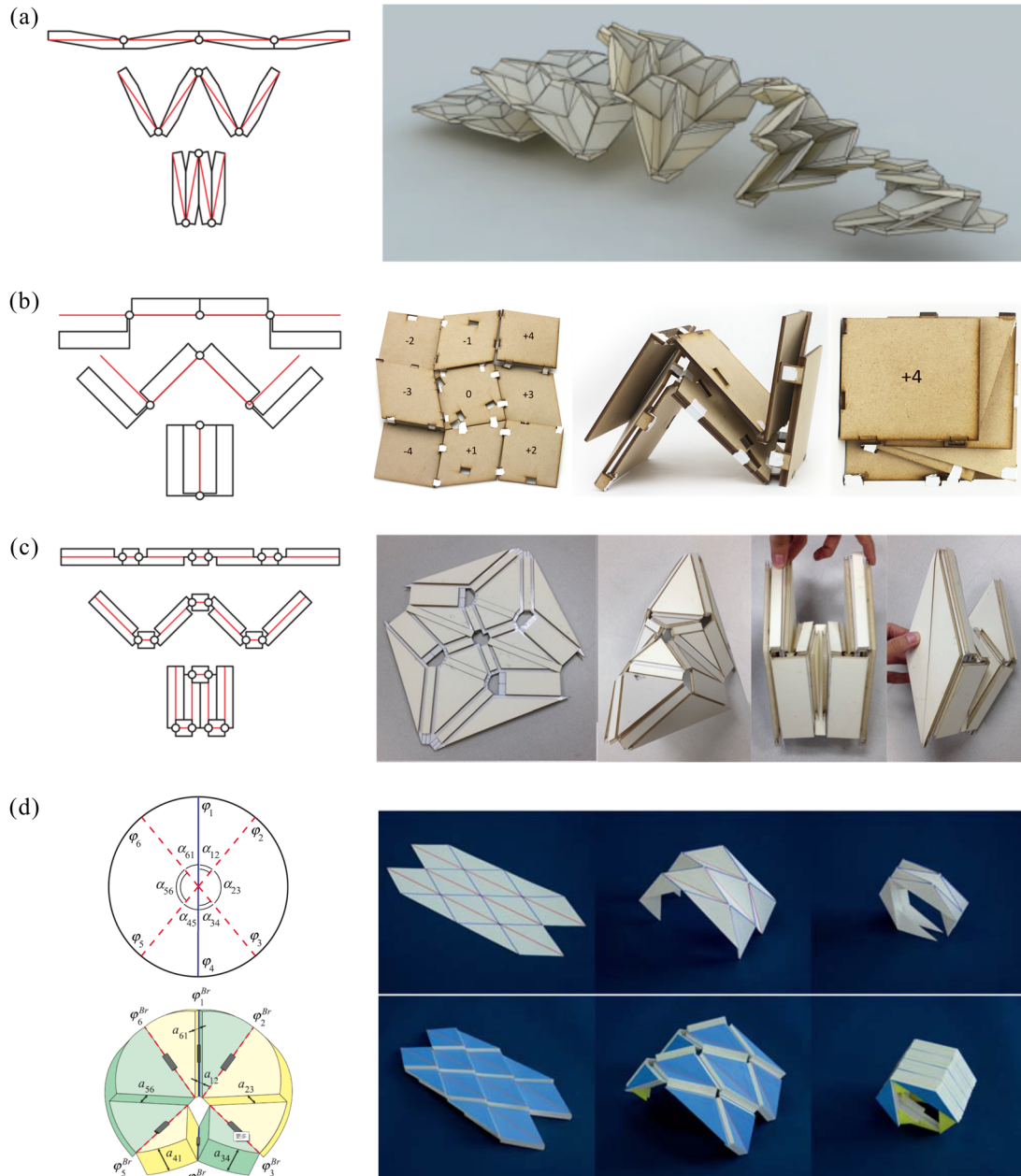


Fig. 2-9 Thickness accommodation methods: (a) tapered panel technique [196], (b) offset panel technique [197], (c) offset crease technique [198], and (d) hinge shift technique [29].

2.2.5 Kirigami

Unlike the traditional folding technique, kirigami is capable of folding discontinuous sheet materials as the cutting of paper is permitted [200]. There are three key features of kirigami, making it widely used in foldable structures as shown in Fig. 2-10. First, multiple materials can be joined by kirigami technique to create complex non-developable cellular patterns [201], such as 3D deployable honeycombs [202], auxetic pyramidal core [203] and hexagonal cellular morphing wingbox [204]. Second, the stiffness of a rigid sheet can be largely reduced, consequently raising flexibility for

solar trackers [205] and triboelectric nanogenerators [206]. Third, the weight over volume can be largely decreased since the sheets that make no contribution to the motion of the pattern are eliminated. The pop-up paper mechanism [207] and the kirigami-enabled parallel mechanism [16] where only the links and joints contributed to the motion of the mechanism are retained are two classic applications. The last feature will be utilized in this dissertation to derive new overconstrained linkages from triangle twist origami pattern.

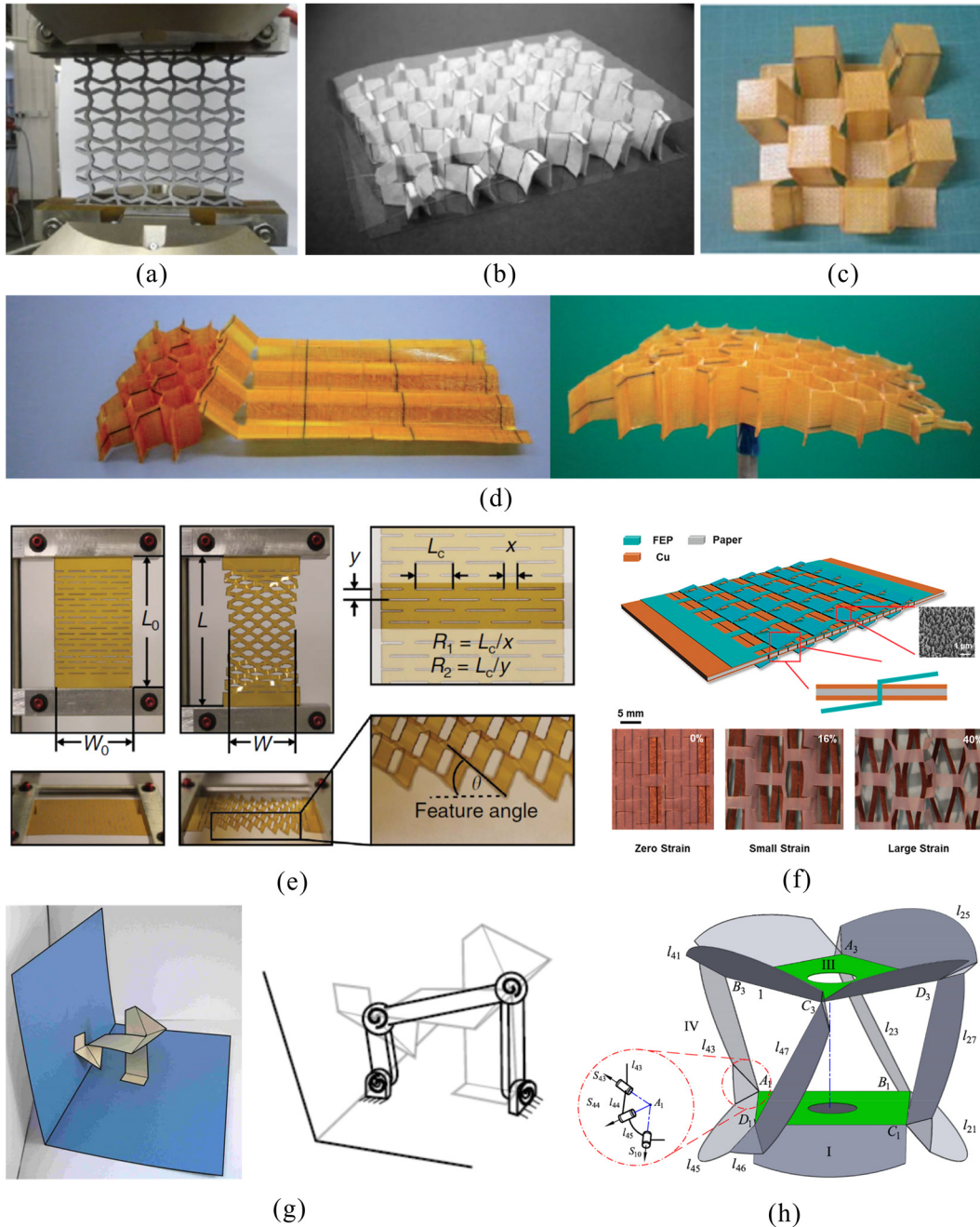


Fig. 2-10 Kirigami technique used in foldable structures: (a) a SILICOMB cellular structure [201], (b) a tapered honeycomb [202], (c) a kirigami auxetic pyramidal lattice core [203], (d) a cellular kirigami morphing wingbox [204], (e) a Kapton kirigami structure for solar tracking [205], (f) a paper-based triboelectric nanogenerator [206], (g) a paper pop-up RSSR mechanism [207], and (h) a kirigami-enabled parallel mechanism [16].

2.3 Spatial Linkages and Rigid Origami

2.3.1 Origami Analysis Based on Spatial Linkages

The motion behaviour of an existing origami pattern is desired for its engineering applications. Dai and Jones firstly modelled the paper folding by treating the creases as rotation joints and the facets as links [22, 23, 28, 33]. So the rigid origami around each vertex is treated as a spherical linkage in which the axes of all joints meet at a point [23, 24]. An origami pattern with multiple vertices is then regarded as an assembly with loops of spherical linkages. Therefore, the analysis of origami patterns can be conducted based on spherical linkages. The spherical trigonometry was adopted to judge the rigid foldability of a flat-foldable single-vertex pattern [181]. Streinu and Whiteley proved the rigid foldability of some single-vertex origami by linking it to spherical polygonal linkages [208]. Wu and You established the rotating vector model for single-vertex crease system based on origami-spherical linkage analogy [182]. Xi and Lien dealt with the foldability problem of origami patterns through a randomized method by modelling rigid origami as a kinematic system with closure constraints [209]. Wang and Chen modelled several origami patterns with equilateral trapezoids, general trapezoids and general quadrilaterals as spherical linkage assemblies for the design of closed patterned cylinder [210]. Moreover, the general condition for rigidly foldable prismatic structures was figured out by solving the kinematics and compatibility of the mobile assemblies of spherical $4R$ linkages [26]. With the proposal of thick panel origami [29], the analysis of origami also depends on the spatial overconstrained linkages. By treating the thick-panel origami as a network of spatial overconstrained linkages, Zhang and Chen have derived new mobile assemblies of Bennett linkages from four-crease origami patterns [211].

2.3.2 Origami-inspired Linkages

Inspired by rigid origami, several novel mechanisms have been developed. For instance, an equivalent overconstrained mechanism inspired and evolved from origami cartons with a crash-lock base has been proposed by screw-loop equations and spherical geometry. Accordingly, several planar-spherical overconstrained linkages were derived by altering the linkages at the diagonal corners [33, 212]. A parallel mechanism with three spherical kinematic chains has been designed based on a waterbomb origami pattern [213], of which the reaction force were analyzed based on the repelling-screw [33, 168]. This origami-inspired parallel mechanism has been used to design an extensible continuum robot [15] and an origami grasper for minimally invasive surgery [150]. By extension, Zhang and Dai designed a novel $8R$ linkage from a kirigami pattern with eight creases, which can evolve into overconstrained $6R$ linkages [74]. They also proposed a plane-symmetric double-spherical $6R$ linkage, which was extracted from a closed-loop origami [214].

Therefore, the interdisciplinary research on spatial linkages and rigid origami not only provides a way to analyze the motion behaviour of origami patterns, but also contributes to the discovery of novel mechanisms.

Chapter 3 Rigid Foldability of Triangle Twist Origami Pattern and Its Derived 6R Linkages

3.1 Introduction

A triangle twist in art is a crease pattern consisting of an equilateral triangle with parallel pleats radiating from its three sides [215], see Fig. 3-1(a). It has been proved that no triangle twist origami pattern with parallel pleats is rigidly foldable [161]. If we change the central equilateral triangle to a general one and remove the parallel constraint on the pleats, a generalized triangle twist as shown in Fig. 3-1(b) would be formed. Here a thorough analysis on rigid foldability and motion behaviour of the generalized triangle twist is to be conducted concerning all position relation of pleats and all schemes of mountain-valley crease (M-V) assignment. Meanwhile, the kirigami technique will be applied for the generation of new 6R linkages from the rigidly foldable triangle twist patterns.

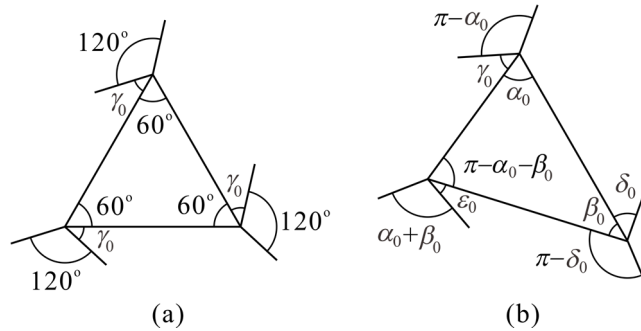


Fig. 3-1 (a) An art triangle twist, (b) a generalized triangle twist, where α_0 , β_0 , γ_0 , δ_0 and ε_0 is arbitrary within the domain $(0, \pi)$ and $\alpha_0 + \beta_0 \in (0, \pi)$.

The layout of this chapter is as follows. The kinematics and rigid foldability of a typical generalized triangle twist origami pattern are presented in section 3.2. Section 3.3 gives all schemes of M-V assignment for the generalized triangle twist and discusses their effect on rigid foldability. The type of derived 6R linkage inspired from the triangle twist kirigami pattern is identified and a new kind of overconstrained 6R linkage is proposed in section 3.4. Final part is the conclusion in section 3.5 which ends this chapter.

3.2 Rigid Foldability

The kinematics of the four-crease rigid origami vertex is studied firstly in order to analyze rigid foldability of the generalized triangle twist origami pattern. If a four-crease origami vertex is flat-foldable, its opposite sector angles should be supplementary [159]. Therefore, in its equivalent spherical 4R linkage (Fig. 3-2), following geometrical parameters can be defined in accordance with the D-H notation

shown in Fig. 2-2,

$$a_{12} = a_{23} = a_{34} = a_{41} = 0, \quad \alpha_{12} = \pi - \alpha_{34}, \quad \alpha_{23} = \pi - \alpha_{41}, \quad R_1 = R_2 = R_3 = R_4 = 0. \quad (3-1)$$

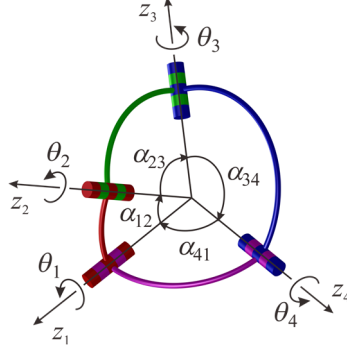


Fig. 3-2 A spherical 4R linkage

Substituting Eq. (3-1) to the closure equation of the spherical 4R linkage that

$$\mathbf{Q}_{21}\mathbf{Q}_{32}\mathbf{Q}_{43}\mathbf{Q}_{14} = \mathbf{I}_3, \quad (3-2)$$

and solving Eq. (3-2) by replacing $\sin\theta_i$, $\cos\theta_i$, $\sin\theta_{i+1}$ and $\cos\theta_{i+1}$ with the double angle formula, we can obtain two solutions,

$$\begin{aligned} \tan \frac{\theta_1}{2} &= -\frac{\sin \frac{\alpha_{23} - \alpha_{12}}{2}}{\sin \frac{\alpha_{23} + \alpha_{12}}{2}}, & \tan \frac{\theta_2}{2} &= \frac{\sin \frac{\alpha_{23} + \alpha_{12}}{2}}{\sin \frac{\alpha_{23} - \alpha_{12}}{2}}, \\ \tan \frac{\theta_3}{2} &= \frac{\sin \frac{\alpha_{23} - \alpha_{12}}{2}}{\sin \frac{\alpha_{23} + \alpha_{12}}{2}}, & \tan \frac{\theta_4}{2} &= -\frac{\sin \frac{\alpha_{23} + \alpha_{12}}{2}}{\sin \frac{\alpha_{23} - \alpha_{12}}{2}}, \end{aligned} \quad (3-3a)$$

and

$$\begin{aligned} \tan \frac{\theta_1}{2} &= -\frac{\cos \frac{\alpha_{23} - \alpha_{12}}{2}}{\cos \frac{\alpha_{23} + \alpha_{12}}{2}}, & \tan \frac{\theta_2}{2} &= -\frac{\cos \frac{\alpha_{23} + \alpha_{12}}{2}}{\cos \frac{\alpha_{23} - \alpha_{12}}{2}}, \\ \tan \frac{\theta_3}{2} &= \frac{\cos \frac{\alpha_{23} - \alpha_{12}}{2}}{\cos \frac{\alpha_{23} + \alpha_{12}}{2}}, & \tan \frac{\theta_4}{2} &= \frac{\cos \frac{\alpha_{23} + \alpha_{12}}{2}}{\cos \frac{\alpha_{23} - \alpha_{12}}{2}}. \end{aligned} \quad (3-3b)$$

It can be derived from Eq. (3-3a) that $\tan(\theta_1/2) = -\tan(\theta_3/2)$ while $\tan(\theta_2/2) = \tan(\theta_4/2)$, which means θ_1 and θ_3 are of opposite signs whereas θ_2 and θ_4 are of the same. Eq. (3-3b) is on the contrary. For a flat-foldable origami pattern, the two creases around the minimum sector angle should be of opposite assignment as a mountain or a valley crease, while the two creases around the maximum

sector angle are of the same assignment [159]. Assuming that α_{12} is the minimum angle, there are totally four schemes of M-V assignment of the four-crease origami vertex as shown in Fig. 3-3, where the mountain creases are illustrated by solid lines, the valley creases by dashed lines, and φ_i is the dihedral angle of the facets with a common crease z_i . If we flip the paper, the mountain creases become valley creases, and vice versa. Therefore, the schemes in Fig. 3-3(b) and (d) are duplicate cases of those in Fig. 3-3(a) and (c), respectively. The two solutions in Eqs. (3-3a) and (3-3b) correspond to the two schemes of M-V assignment in Fig. 3-3(a-b) and Fig. 3-3(c-d), respectively, which are named as Vertex-I and Vertex-II.

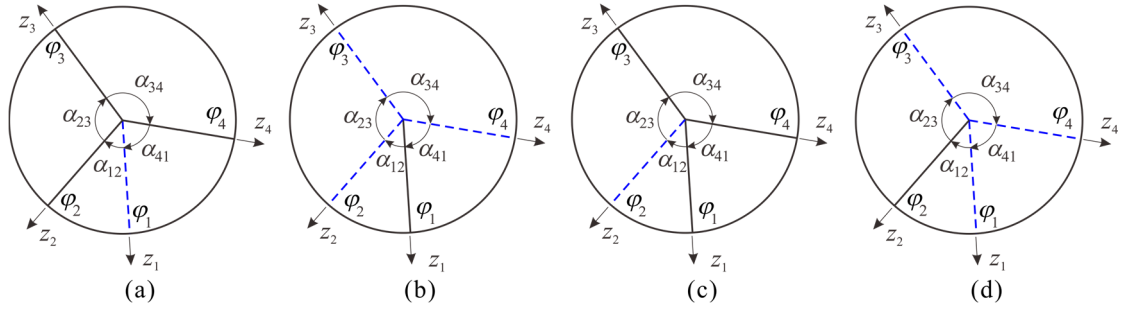


Fig. 3-3 Four-crease origami vertices with four schemes of M-V assignment: (a), (b) Vertex-I; and (c), (d) Vertex-II.

The relationship between the kinematic variable θ_i and the dihedral angle φ_i is presented in Fig. 3-4, where we can find out that for a mountain crease, $\varphi_i = \pi - \theta_i$, and for a valley crease, $\varphi_i = \theta_i - \pi$. So the relationship is $\varphi_1 = \theta_1 - \pi$, $\varphi_2 = \pi - \theta_2$, $\varphi_3 = \pi - \theta_3$, $\varphi_4 = \pi - \theta_4$ for Vertex-I and $\varphi_1 = \pi - \theta_1$, $\varphi_2 = \theta_2 - \pi$, $\varphi_3 = \pi - \theta_3$, $\varphi_4 = \pi - \theta_4$ for Vertex-II.

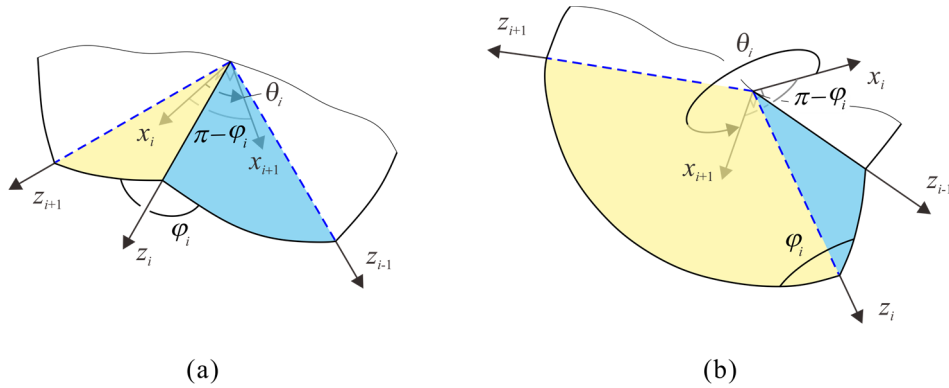


Fig. 3-4 The relationship between the kinematic variable and the dihedral angle for (a) mountain crease, and (b) valley crease.

Thus in Vertex-I we have,

$$\begin{aligned}
 \tan \frac{\varphi_1}{2} &= \frac{\sin \frac{\alpha_{23} + \alpha_{12}}{2}}{\sin \frac{\alpha_{23} - \alpha_{12}}{2}}, & \tan \frac{\varphi_2}{2} &= \frac{\sin \frac{\alpha_{23} - \alpha_{12}}{2}}{\sin \frac{\alpha_{23} + \alpha_{12}}{2}}, \\
 \tan \frac{\varphi_3}{2} &= \frac{\sin \frac{\alpha_{23} + \alpha_{12}}{2}}{\sin \frac{\alpha_{23} - \alpha_{12}}{2}}, & \tan \frac{\varphi_4}{2} &= \frac{\sin \frac{\alpha_{23} - \alpha_{12}}{2}}{\sin \frac{\alpha_{23} + \alpha_{12}}{2}},
 \end{aligned} \tag{3-4a}$$

and in Vertex-II

$$\begin{aligned}
 \tan \frac{\varphi_1}{2} &= \frac{\cos \frac{\alpha_{23} + \alpha_{12}}{2}}{\cos \frac{\alpha_{23} - \alpha_{12}}{2}}, & \tan \frac{\varphi_2}{2} &= \frac{\cos \frac{\alpha_{23} - \alpha_{12}}{2}}{\cos \frac{\alpha_{23} + \alpha_{12}}{2}}, \\
 \tan \frac{\varphi_3}{2} &= \frac{\cos \frac{\alpha_{23} + \alpha_{12}}{2}}{\cos \frac{\alpha_{23} - \alpha_{12}}{2}}, & \tan \frac{\varphi_4}{2} &= \frac{\cos \frac{\alpha_{23} - \alpha_{12}}{2}}{\cos \frac{\alpha_{23} + \alpha_{12}}{2}}.
 \end{aligned} \tag{3-4b}$$

Figure 3-5(a) shows a generalized triangle twist origami pattern with a specific M-V assignment. Since a four-crease vertex in rigid origami is kinematically equivalent to a spherical 4R linkage, the triangle twist origami pattern can be modelled as a network of three spherical 4R linkages. Assuming α_{12}^j ($j = a, b, c$) be the minimum angle of the four-crease vertex, following geometrical parameters of the triangle twist are setup,

$$\alpha_{41}^a = \pi - \alpha_{23}^a = \alpha, \quad \alpha_{12}^a = \pi - \alpha_{34}^a = \gamma, \quad 0 < \gamma \leq \min\{\alpha, \pi - \alpha\}, \tag{3-5a}$$

$$\alpha_{41}^b = \pi - \alpha_{23}^b = \beta, \quad \alpha_{12}^b = \pi - \alpha_{34}^b = \delta, \quad 0 < \delta \leq \min\{\beta, \pi - \beta\}, \tag{3-5b}$$

$$\alpha_{41}^c = \pi - \alpha_{23}^c = \pi - \alpha - \beta, \quad \alpha_{12}^c = \pi - \alpha_{34}^c = \varepsilon, \quad 0 < \varepsilon \leq \min\{\alpha + \beta, \pi - \alpha - \beta\}, \tag{3-5c}$$

so the simplified representation of the triangle twist is shown in Fig. 3-5(b).

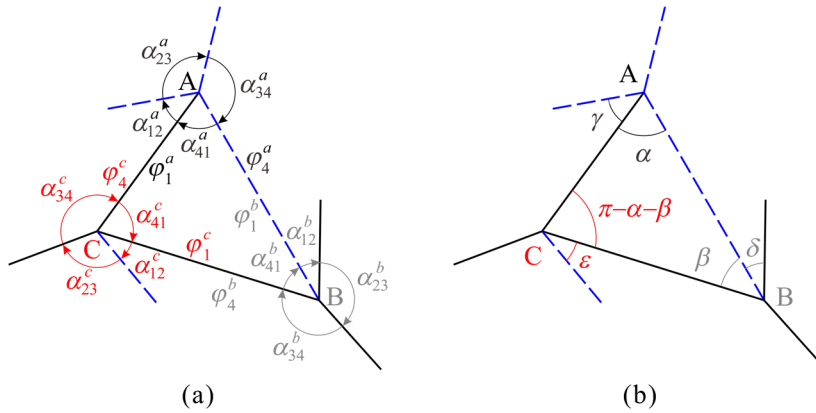


Fig. 3-5 A generalized triangle twist origami pattern with a specific M-V assignment: (a) the general representation, and (b) the simplified one.

In this case, vertices A and B are both Vertex-I in Fig. 3-3(b) and (a), respectively, and vertex C is Vertex-II in Fig. 3-3(c). The relationship of the dihedral angles φ_1^j and φ_4^j can be defined as

$$\mu^j = \frac{\tan \frac{\varphi_4^j}{2}}{\tan \frac{\varphi_1^j}{2}}, \quad j = a, b, c. \quad (3-6)$$

Combining it with Eqs. (3-4) and (3-5), we have

$$\mu^a = \frac{\cos \frac{\alpha + \gamma}{2}}{\cos \frac{\alpha - \gamma}{2}}, \quad \mu^b = \frac{\cos \frac{\beta + \delta}{2}}{\cos \frac{\beta - \delta}{2}}, \quad \mu^c = \frac{\cos \frac{\alpha + \beta - \varepsilon}{2}}{\cos \frac{\alpha + \beta + \varepsilon}{2}}, \quad (3-7)$$

where

$$\cos \alpha \leq \mu^a < 1, \quad \cos \beta \leq \mu^b < 1, \quad 1 < \mu^c \leq 1 / \cos(\alpha + \beta), \quad \text{for } \alpha + \beta < \frac{\pi}{2}, \quad (3-8a)$$

$$\max\{0, \cos \alpha\} \leq \mu^a < 1, \quad \max\{0, \cos \beta\} \leq \mu^b < 1, \quad \mu^c > 1, \quad \text{for } \alpha + \beta \geq \frac{\pi}{2}. \quad (3-8b)$$

Since each crease along the edge of the central triangle is shared by two adjacent vertices as shown in Fig. 3-5, we have

$$\varphi_4^a = \varphi_1^b, \quad \varphi_4^b = \varphi_1^c, \quad \varphi_4^c = \varphi_1^a. \quad (3-9)$$

Further, the following relationship can be established,

$$\frac{\tan \frac{\varphi_4^a}{2}}{\tan \frac{\varphi_1^a}{2}} \cdot \frac{\tan \frac{\varphi_4^b}{2}}{\tan \frac{\varphi_1^b}{2}} \cdot \frac{\tan \frac{\varphi_4^c}{2}}{\tan \frac{\varphi_1^c}{2}} = 1. \quad (3-10)$$

Therefore, the compatible condition of the triangle twist pattern [161] is

$$\mu^a \cdot \mu^b \cdot \mu^c = 1. \quad (3-11)$$

With defined values of α and β , assigning arbitrary values within the domain of definition in Eq. (3-5) to γ and δ , we can always find a ε to satisfy the compatible condition in Eq. (3-11) as

$$\varepsilon = 2 \arctan \frac{\zeta - 1}{(\zeta + 1) \tan \frac{\alpha + \beta}{2}}, \quad \zeta = \frac{1}{\mu^a \cdot \mu^b}. \quad (3-12)$$

Once the value of ε obtained by Eq. (3-12) locates in the domain $(0, \pi)$, the triangle twist pattern is rigidly foldable.

Depending on the position relation of the three crease-pairs z_3^a & z_2^b , z_3^b & z_2^c

and z_3^c & z_2^a , the triangle twist origami pattern can be divided into three types, where each crease-pair is intersected, or only one crease-pair is parallel, or each crease-pair is parallel as shown in Fig. 3-6(a-c) respectively.

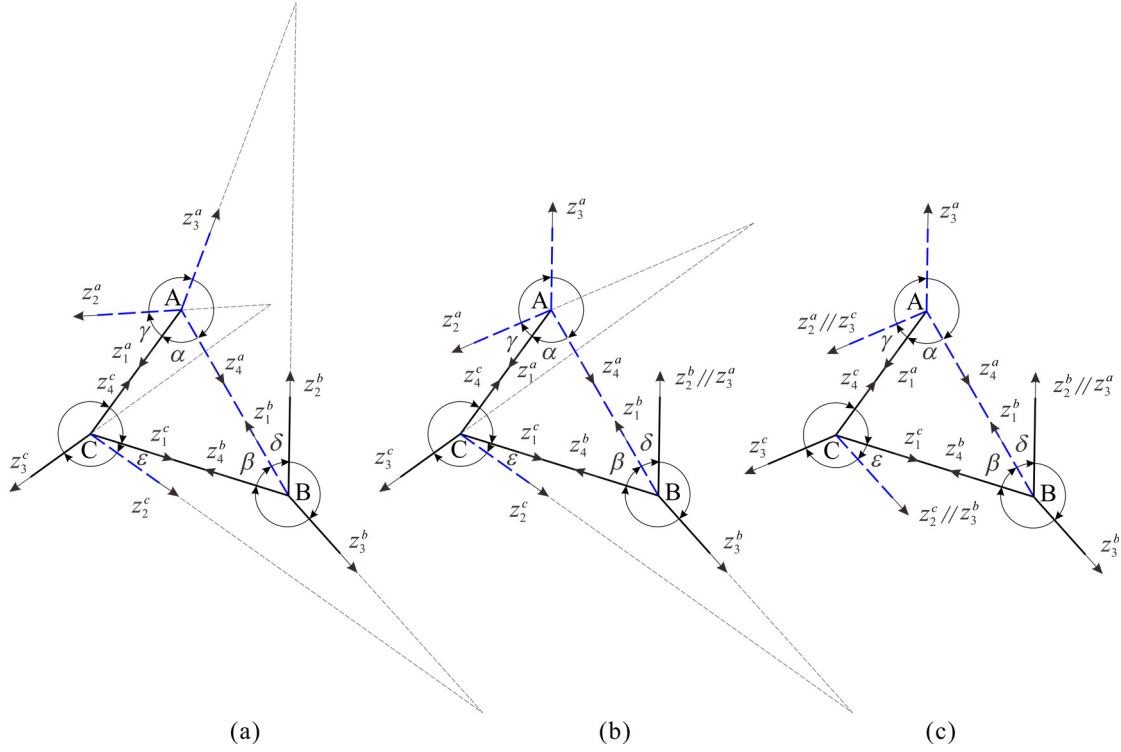


Fig. 3-6 Three types of the triangle twist pattern where (a) each crease-pair is intersected, or (b) only one crease-pair is parallel, or (c) each crease-pair is parallel.

When each crease-pair is intersected, we can always find a ε as Eq. (3-12) for any value of γ and δ in the domain of definition. This type of pattern is rigidly foldable once $\varepsilon \in (0, \pi)$.

When only one crease-pair is parallel, supposing that $z_3^a // z_2^b$, then $\gamma = \delta$, and ε can also be derived from Eq. (3-12). If $z_3^b // z_2^c$, then $\delta = \varepsilon$, and

$$\gamma = 2 \arctan \frac{1 - \zeta}{(\zeta + 1) \tan \frac{\alpha}{2}}, \quad \zeta = \frac{1}{\mu^b \cdot \mu^c}. \quad (3-13)$$

If $z_3^c // z_2^a$, then $\varepsilon = \gamma$, and

$$\delta = 2 \arctan \frac{1 - \zeta}{(\zeta + 1) \tan \frac{\beta}{2}}, \quad \zeta = \frac{1}{\mu^a \cdot \mu^c}. \quad (3-14)$$

Thus the pattern is also rigidly foldable with one parallel crease-pair when the calculated angle locates in the domain $(0, \pi)$.

When each crease-pair is parallel, then $\gamma = \delta = \varepsilon$, Eq. (3-11) can be rewritten as

$$\frac{\cos \frac{\alpha + \gamma}{2}}{\cos \frac{\alpha - \gamma}{2}} \cdot \frac{\cos \frac{\beta + \gamma}{2}}{\cos \frac{\beta - \gamma}{2}} \cdot \frac{\cos \frac{\alpha + \beta - \gamma}{2}}{\cos \frac{\alpha + \beta + \gamma}{2}} = 1, \quad (3-15)$$

which can be further simplified as

$$\sin \frac{\alpha}{2} \cdot \sin \frac{\beta}{2} = 0. \quad (3-16)$$

Since α and β are interior angles of a triangle, no solution of Eq. (3-16) exists. Therefore, the parallel triangle twist is not rigidly foldable.

3.3 M-V Assignment and Its Effect on Rigid Foldability

The rigid foldability and motion of the triangle twist with one specific scheme of M-V assignment have been analyzed as above. Since the rigid foldability of an origami pattern may vary with the change of M-V assignment, here we are going to find out all possible schemes of M-V assignment for the generalized triangle twist origami pattern and discuss their effect on rigid foldability.

According to the flat-foldable conditions of a four-crease vertex, the number difference between mountain creases and valley ones should be equal to two [159]. It forms the criteria for determining schemes of M-V assignment, together with the condition on the opposite M-V assignment of the two creases around the minimum sector angle. Hence, the M-V assignment of the generalized triangle twist is related to the position of the minimum angle in the pattern. Considering the connection between adjacent vertices in a triangle twist, α_{41} is always set as the interior angle in the central triangle. Since α_{12} , α_{23} , α_{34} and α_{41} could be chosen alternatively as the minimum angle, eight cases exist for one vertex in the triangle twist pattern. The kinematic relationship between dihedral angles of the vertices with identical M-V assignments is uniform. Therefore, the M-V assignment for one vertex in the triangle twist can be classified into four types defined as Type P, Type Q, Type R and Type S in Fig. 3-7 by combining repeated cases.

By defining $\mu_k = \tan \frac{\varphi_4}{2} / \tan \frac{\varphi_1}{2}$, where the subscript $k = p, q, r, s$ that represents the type of the vertex, kinematic relationship of the two dihedral angles φ_1 and φ_4 along the creases in the central triangle can be obtained. For Type P with α_{12} as the minimum angle, it is a Vertex-II as shown in Fig. 3-3(c), and for Type P with α_{23} as the minimum angle, it is a rotated Vertex-I as shown Fig. 3-3(a). According to Eqs. (3-4b), (3-4a) and (3-1), we have

$$\mu_p = \frac{\sin \frac{\alpha_{41} + \alpha_{12}}{2}}{\sin \frac{\alpha_{41} - \alpha_{12}}{2}}. \quad (3-17a)$$

For Type Q with α_{23} as the minimum angle, it is a rotated Vertex-II as shown in Fig. 3-3(c), and for Type Q with α_{34} as the minimum angle, it is a rotated Vertex-I as shown Fig. 3-3(a). According to Eqs. (3-4b), (3-4a) and (3-1), we have

$$\mu_q = \frac{-\cos \frac{\alpha_{41} + \alpha_{12}}{2}}{\cos \frac{\alpha_{41} - \alpha_{12}}{2}}. \quad (3-17b)$$

For Type R with α_{34} as the minimum angle, it is a rotated Vertex-II as shown in Fig. 3-3(c), and for Type R with α_{41} as the minimum angle, it is a rotated Vertex-I as shown Fig. 3-3(a). According to Eqs. (3-4b), (3-4a) and (3-1), we have

$$\mu_r = \frac{-\sin \frac{\alpha_{41} + \alpha_{12}}{2}}{\sin \frac{\alpha_{41} - \alpha_{12}}{2}}. \quad (3-17c)$$

For Type S with α_{41} as the minimum angle, it is a rotated Vertex-II as shown in Fig. 3-3(c), and for Type S with α_{12} as the minimum angle, it is a Vertex-I as shown Fig. 3-3(a). According to Eqs. (3-4b), (3-4a) and (3-1), we have

$$\mu_s = \frac{\cos \frac{\alpha_{41} + \alpha_{12}}{2}}{\cos \frac{\alpha_{41} - \alpha_{12}}{2}}. \quad (3-17d)$$

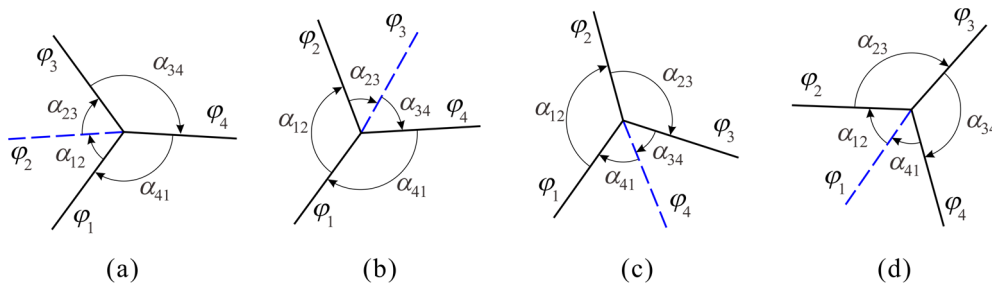


Fig. 3-7 Four types of M-V assignment of one vertex in the generalized triangle twist where the minimum angle is (a) α_{12} or α_{23} for Type P, (b) α_{23} or α_{34} for Type Q, (c) α_{34} or α_{41} for Type R, and (d) α_{41} or α_{12} for Type S.

As there are three vertices for a triangle twist and each vertex has four types of M-V assignment, so there are $64 (=4^3)$ combinations of vertices arrangements for the

triangle twist. Considering the crease common to adjacent vertices has the same assignment, only 32 schemes of M-V assignment are left as presented in Fig. 3-8, where only the minimum angle of each vertex is presented and the character in frame indicates the type of the vertex.

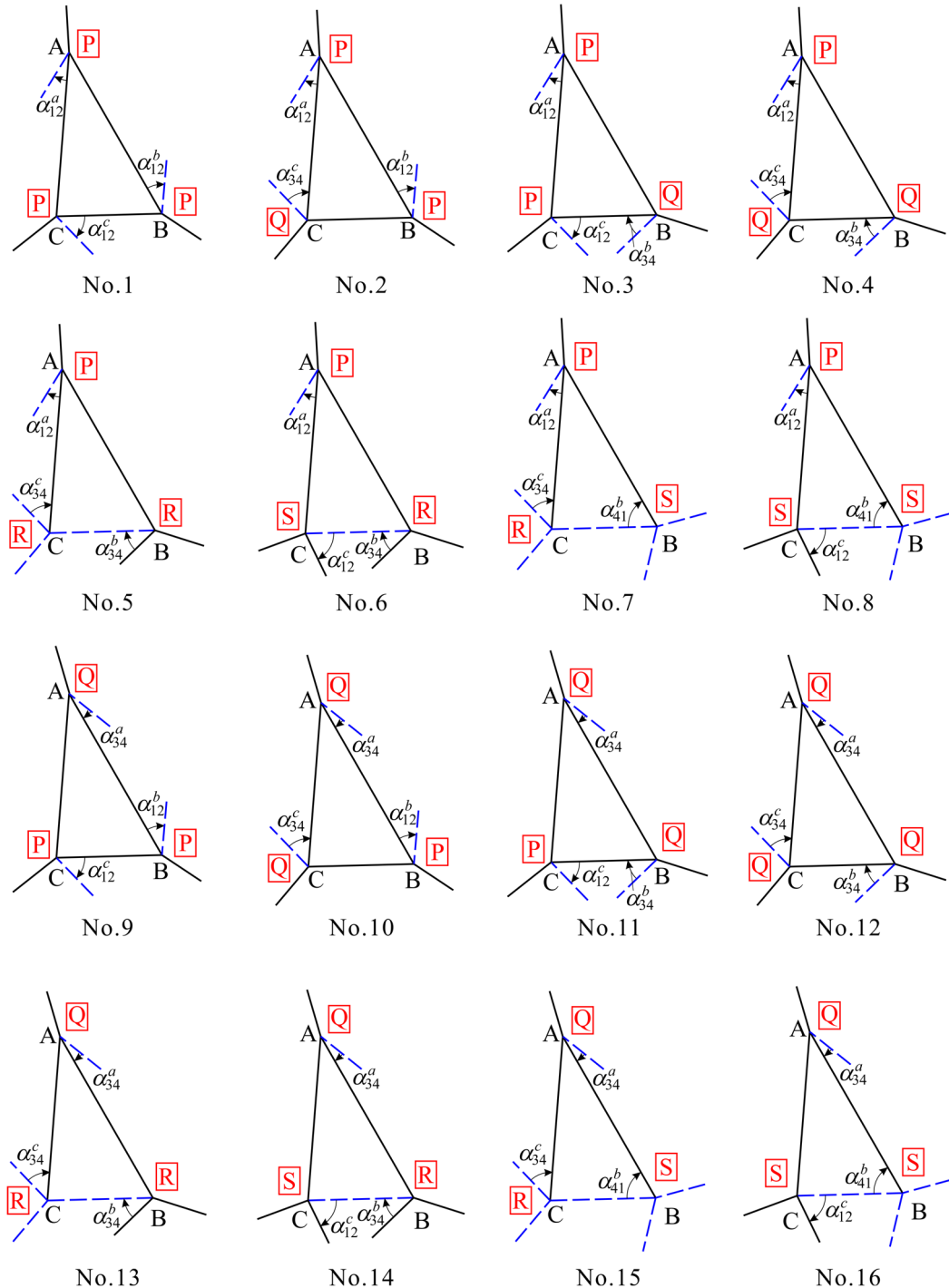


Fig. 3-8 All possible schemes of M-V assignment of a generalized triangle twist: No.1 PPP, No.2 PPQ, No.3 PQQ, No.4 PQQ, No.5 PRR, No.6 PRS, No.7 PSR, No.8 PSS, No.9 QPP, No.10 QPQ, No.11 QQP, No.12 QQQ, No.13 QRR, No.14 QRS, No.15 QSR, No.16 QSS, No.17 RPR, No.18 RPS, No.19 RQR, No.20 RQS, No.21 RRP, No.22 RRQ, No.23 RSP, No.24 RSQ, No.25 SPR, No.26 SPS, No.27 SQR, No.28 SQS, No.29 SRP, No.30 SRQ, No.31 SSP, and No.32 SSQ.

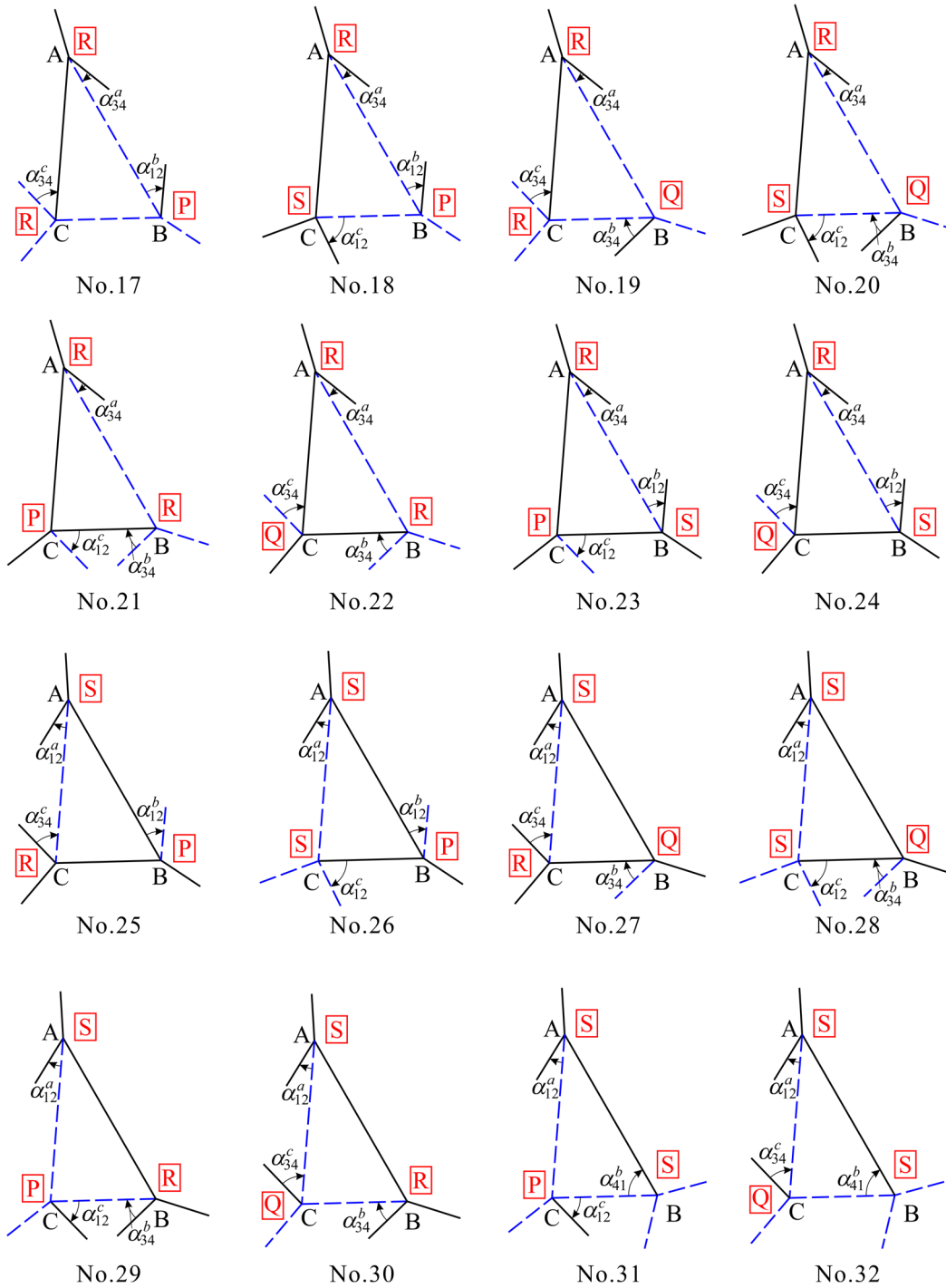


Fig. 3-8 All possible schemes of M-V assignment of a generalized triangle twist: No.1 PPP, No.2 PPQ, No.3 PQP, No.4 PQQ, No.5 PRR, No.6 PRS, No.7 PSR, No.8 PSS, No.9 QPP, No.10 QPQ, No.11 QQP, No.12 QQQ, No.13 QRR, No.14 QRS, No.15 QSR, No.16 QSS, No.17 RPR, No.18 RPS, No.19 RQR, No.20 RQS, No.21 RRP, No.22 RRQ, No.23 RSP, No.24 RSQ, No.25 SPR, No.26 SPS, No.27 SQR, No.28 SQS, No.29 SRP, No.30 SRQ, No.31 SSP, and No.32 SSQ.

(Continued.)

Two special scenarios exist where the M-V assignment would be duplicated. First, if we flip the paper, the mountain creases then become the valley creases. That is to say,

these kinds of M-V assignment would be the inverted configurations. For example, the M-V assignment in Fig. 3-9(a) (PRR) is a duplicate of the one in Fig. 3-8 No.5 with the inverted configuration. Second, the M-V assignment would be duplicated if we change the vertex arrangement by rotating it along the centre of the triangle. For example, the M-V assignment in Fig. 3-9(b) is a duplicate of the one in Fig. 3-9(a) obtained by rotation. Considering the generality of the central triangle, the M-V assignment in Fig. 3-9(b) is equal to the one in Fig. 3-9(c) (RPR) that copied from Fig. 3-8 No.17. That is, the PRR twist in Fig. 3-8 No.5 and the RPR twist in Fig. 3-8 No.17 can be regarded as the same. As a result, twelve unique schemes of M-V assignment are obtained, which are denoted as PPP, PPQ, PQQ, PRR, PRS, PSS, QQQ, QRR, QRS, QSS, PSR and QSR as shown in Fig. 3-10, where the pattern shown in Fig. 3-5 is a duplicate obtained by rotating the type of PSS twist shown in Fig. 3-10(f).

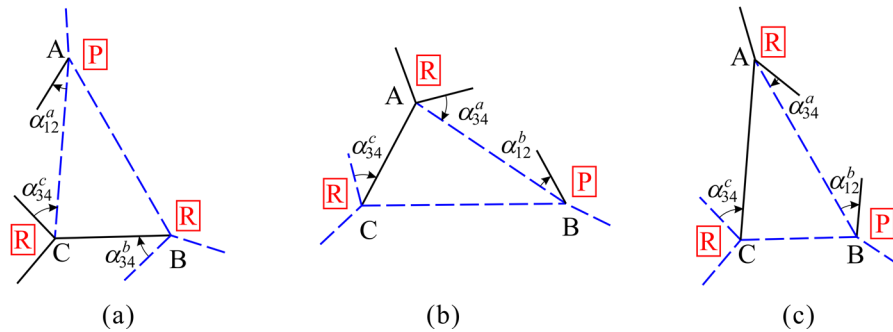


Fig. 3-9 Duplicated M-V assignments: (a) the M-V assignment obtained by flipping the paper in Fig. 3-8 No.5, (b) the one obtained by rotating (a) along the centre of the triangle, and (c) the one copied from Fig. 3-8 No.17.

From Fig. 3-10, we can see that there are two schemes (PRS and QRS) with seven mountain creases and two valley ones (Fig. 3-10 (e) and (i)), four schemes (PPP, PPQ, PQQ and QQQ) with six mountain creases and three valley ones (Fig. 3-10 (a), (b), (c) and (g)), four schemes (PRR, PSS, QRR and QSS) with five mountain creases and four valley ones (Fig. 3-10 (d), (f), (h) and (j)), and two schemes (PSR and QSR) with three mountain creases and six valley ones (Fig. 3-10 (k) and (l)). The difference between those schemes with identical numbers of mountain and valley creases is the position of the minimum angle, which affects the kinematics of each vertex and their compatibility. The detailed classification of these schemes are represented in Table 3-1.

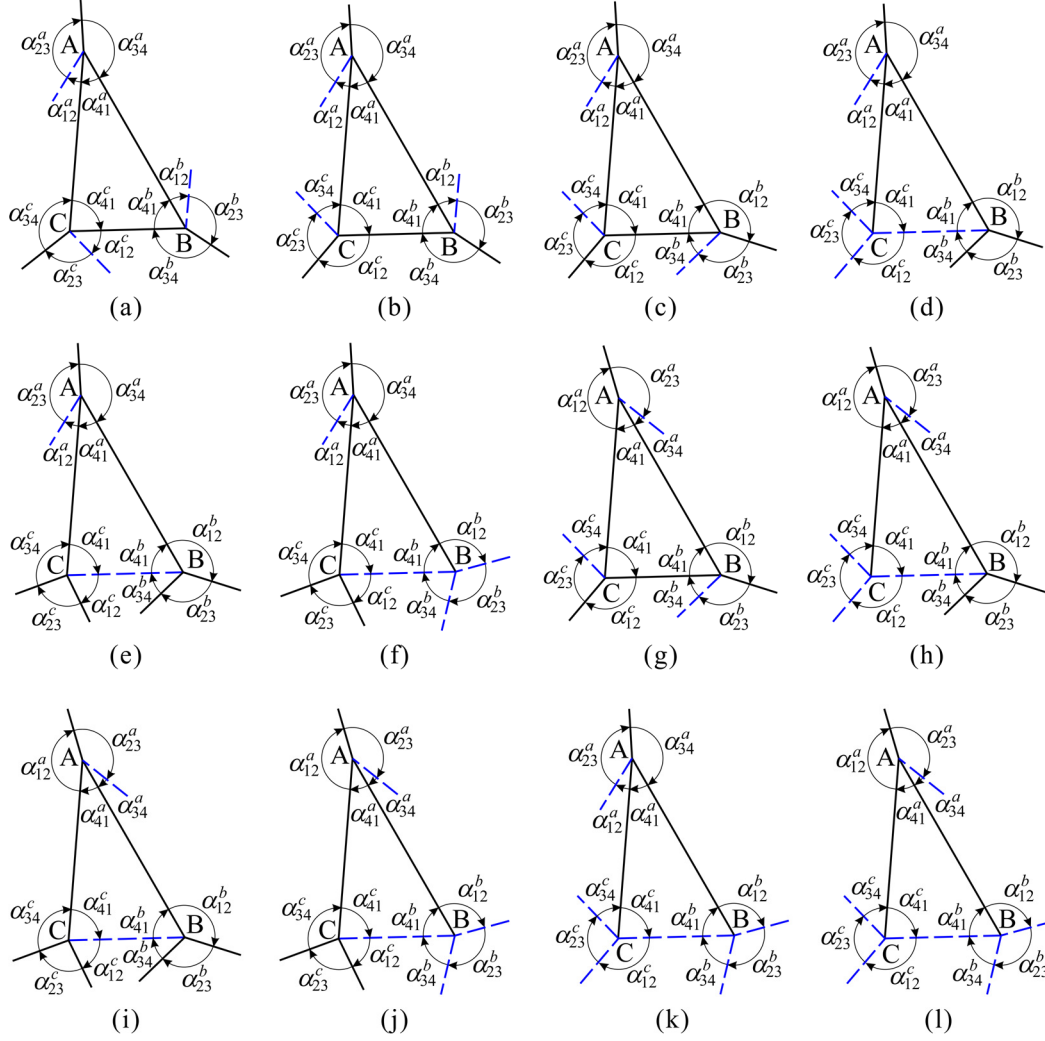


Fig. 3-10 Twelve unique schemes of M-V assignment of the generalized triangle twist pattern with vertex-types being (a) PPP, (b) PPQ, (c) PQQ, (d) PRR, (e) PRS, (f) PSS, (g)QQQ, (h) QRR, (i) QRS, (j) QSS, (k) PSR, and (l) QSR.

Similar to the analysis procedure in section 3.2, the relationships μ_i^j ($i=1, 2, \dots, 12$, $j=a, b, c$) between φ_1^j and φ_4^j are substituted to the compatible condition as Eq. (3-11) in order to find out the rigid foldability of all these types of triangle twist with various M-V assignments. For the PPP twist (Fig. 3-10(a)), the μ_i^j of this type are

$$\mu_1^a = \frac{\sin \frac{\alpha + \gamma}{2}}{\sin \frac{\alpha - \gamma}{2}}, \quad \mu_1^b = \frac{\sin \frac{\beta + \delta}{2}}{\sin \frac{\beta - \delta}{2}}, \quad \mu_1^c = \frac{\cos \frac{\alpha + \beta - \varepsilon}{2}}{\cos \frac{\alpha + \beta + \varepsilon}{2}}, \quad (3-18)$$

with $\mu_1^a > 1$, $\mu_1^b > 1$, $\mu_1^c > 1$, so it is impossible to find solutions for Eq. (3-11). Therefore, the type of PPP twist is not rigidly foldable.

Table 3-1 Classification of M-V assignments for a generalized triangle twist

Number of mountain creases	Number of valley creases	Schemes of M-V assignment (Fig. 3-8)	Duplicated schemes of M-V assignment (Fig. 3-8)	Rigidity
7	2	PRS (No.6)	RSP (No.23), SPR (No.25)	Rigid
		QRS (No.14)	RSQ (No.24), SQR (No.27)	Rigid
6	3	PPP (No.1)	non-existent	Non-rigid
		PPQ (No.2)	PQP (No.3), QPP (No.9)	Rigid
		PQQ (No.4)	QPQ (No.10), QQP (No.11)	Rigid
5	4	QQQ (No.12)	non-existent	Non-rigid
		PRR (No.5)	RPR (No.17), RRP (No.21)	Non-rigid
		PSS (No.8)	SPS (No.26), SSP (No.31)	Rigid
		QRR (No.13)	RQR (No.19), RRQ (No.22)	Rigid
		QSS (No.16)	SQS (No.28), SSQ (No.32)	Non-rigid
3	6	PSR (No.7)	RPS (No.18), SRP (No.29)	Rigid
		QSR (No.15)	RQS (No.20), SRQ (No.30)	Rigid

For the PPQ twist (Fig. 3-10(b)), the μ_i^j of this type are

$$\mu_2^a = \frac{\sin \frac{\alpha + \gamma}{2}}{\sin \frac{\alpha - \gamma}{2}}, \quad \mu_2^b = \frac{\sin \frac{\beta + \delta}{2}}{\sin \frac{\beta - \delta}{2}}, \quad \mu_2^c = \frac{-\sin \frac{\alpha + \beta - \varepsilon}{2}}{\sin \frac{\alpha + \beta + \varepsilon}{2}}, \quad (3-19)$$

with $\mu_2^a > 1$, $\mu_2^b > 1$, $\mu_2^c < 1$. When arbitrary values are assigned to α , β , γ and δ , we can find a ε according to the compatible condition in Eq. (3-11) as

$$\varepsilon = 2 \arctan \frac{(\zeta_2 + 1) \tan \frac{\alpha + \beta}{2}}{1 - \zeta_2}, \quad \zeta_2 = \frac{1}{\mu_2^a \cdot \mu_2^b}. \quad (3-20)$$

Therefore, the type of PPQ twist is rigidly foldable once the obtained ε is within the range $(0, \pi)$.

For the PQQ twist (Fig. 3-10(c)), the μ_i^j of this type are

$$\mu_3^a = \frac{\sin \frac{\alpha + \gamma}{2}}{\sin \frac{\alpha - \gamma}{2}}, \quad \mu_3^b = \frac{-\cos \frac{\beta + \delta}{2}}{\cos \frac{\beta - \delta}{2}}, \quad \mu_3^c = \frac{-\sin \frac{\alpha + \beta - \varepsilon}{2}}{\sin \frac{\alpha + \beta + \varepsilon}{2}}, \quad (3-21)$$

with $\mu_3^a > 1$, $\mu_3^b < 1$, $\mu_3^c < 1$. When arbitrary values are assigned to α , β , γ and δ , we can find a ε according to the compatible condition in Eq. (3-11) as

$$\varepsilon = 2 \arctan \frac{(\zeta_3 + 1) \tan \frac{\alpha + \beta}{2}}{1 - \zeta_3}, \quad \zeta_3 = \frac{1}{\mu_3^a \cdot \mu_3^b}. \quad (3-22)$$

Therefore, the type of PQQ twist is rigidly foldable once the obtained ε is within the range $(0, \pi)$.

For the PRR twist (Fig. 3-10(d)), the μ_i^j of this type are

$$\mu_4^a = \frac{\sin \frac{\alpha + \gamma}{2}}{\sin \frac{\alpha - \gamma}{2}}, \quad \mu_4^b = \frac{\sin \frac{\beta + \delta}{2}}{\sin \frac{\delta - \beta}{2}}, \quad \mu_4^c = \frac{-\cos \frac{\alpha + \beta - \varepsilon}{2}}{\cos \frac{\alpha + \beta + \varepsilon}{2}}, \quad (3-23)$$

with $\mu_4^a > 1$, $\mu_4^b > 1$, $\mu_4^c > 1$, so it is impossible to find solutions for Eq. (3-11). Therefore, the type of PRR twist is not rigidly foldable.

For the PRS twist (Fig. 3-10(e)), the μ_i^j of this type are

$$\mu_5^a = \frac{\sin \frac{\alpha + \gamma}{2}}{\sin \frac{\alpha - \gamma}{2}}, \quad \mu_5^b = \frac{\sin \frac{\beta + \delta}{2}}{\sin \frac{\delta - \beta}{2}}, \quad \mu_5^c = \frac{\sin \frac{\alpha + \beta - \varepsilon}{2}}{\sin \frac{\alpha + \beta + \varepsilon}{2}}, \quad (3-24)$$

with $\mu_5^a > 1$, $\mu_5^b > 1$, $\mu_5^c < 1$. When arbitrary values are assigned to α , β , γ and δ , we can find a ε according to the compatible condition in Eq. (3-11) as

$$\varepsilon = 2 \arctan \frac{(1 - \zeta_5) \tan \frac{\alpha + \beta}{2}}{\zeta_5 + 1}, \quad \zeta_5 = \frac{1}{\mu_5^a \cdot \mu_5^b}. \quad (3-25)$$

Therefore, the type of PRS twist is rigidly foldable once the obtained ε is within the range $(0, \pi)$.

For the PSS twist (Fig. 3-10(f)), the μ_i^j of this type are

$$\mu_6^a = \frac{\sin \frac{\alpha + \gamma}{2}}{\sin \frac{\alpha - \gamma}{2}}, \quad \mu_6^b = \frac{\cos \frac{\beta + \delta}{2}}{\cos \frac{\beta - \delta}{2}}, \quad \mu_6^c = \frac{\sin \frac{\alpha + \beta - \varepsilon}{2}}{\sin \frac{\alpha + \beta + \varepsilon}{2}}, \quad (3-26)$$

with $\mu_6^a > 1$, $\mu_6^b < 1$, $\mu_6^c < 1$. When arbitrary values are assigned to α , β , γ and δ , we can find a ε according to the compatible condition in Eq. (3-11) as

$$\varepsilon = 2 \arctan \frac{(1 - \zeta_6) \tan \frac{\alpha + \beta}{2}}{\zeta_6 + 1}, \quad \zeta_6 = \frac{1}{\mu_6^a \cdot \mu_6^b}. \quad (3-27)$$

Therefore, the type of PSS twist is rigidly foldable once the obtained ε is within the range $(0, \pi)$.

For the QQQ twist (Fig. 3-10(g)), the μ_i^j of this type are

$$\mu_7^a = \frac{-\cos \frac{\alpha + \gamma}{2}}{\cos \frac{\alpha - \gamma}{2}}, \quad \mu_7^b = \frac{-\cos \frac{\beta + \delta}{2}}{\cos \frac{\beta - \delta}{2}}, \quad \mu_7^c = \frac{-\sin \frac{\alpha + \beta - \varepsilon}{2}}{\sin \frac{\alpha + \beta + \varepsilon}{2}}, \quad (3-28)$$

with $\mu_7^a < 1$, $\mu_7^b < 1$, $\mu_7^c < 1$, so it is impossible to find solutions for Eq. (3-11). Therefore, the type of QQQ twist is not rigidly foldable.

For the QRR twist (Fig. 3-10(h)), the μ_i^j of this type are

$$\mu_8^a = \frac{-\cos \frac{\alpha + \gamma}{2}}{\cos \frac{\alpha - \gamma}{2}}, \quad \mu_8^b = \frac{\sin \frac{\beta + \delta}{2}}{\sin \frac{\delta - \beta}{2}}, \quad \mu_8^c = \frac{-\cos \frac{\alpha + \beta - \varepsilon}{2}}{\cos \frac{\alpha + \beta + \varepsilon}{2}}, \quad (3-29)$$

with $\mu_8^a < 1$, $\mu_8^b > 1$, $\mu_8^c > 1$. When arbitrary values are assigned to α , β , γ and δ , we can find a ε according to the compatible condition in Eq. (3-11) as

$$\varepsilon = 2 \arctan \frac{\zeta_8 + 1}{(\zeta_8 - 1) \tan \frac{\alpha + \beta}{2}}, \quad \zeta_8 = \frac{1}{\mu_8^a \cdot \mu_8^b}. \quad (3-30)$$

Therefore, the type of QRR twist is rigidly foldable once the obtained ε is within the range $(0, \pi)$.

For the QRS twist (Fig. 3-10(i)), the μ_i^j of this type are

$$\mu_9^a = \frac{-\cos \frac{\alpha + \gamma}{2}}{\cos \frac{\alpha - \gamma}{2}}, \quad \mu_9^b = \frac{\sin \frac{\beta + \delta}{2}}{\sin \frac{\delta - \beta}{2}}, \quad \mu_9^c = \frac{\sin \frac{\alpha + \beta - \varepsilon}{2}}{\sin \frac{\alpha + \beta + \varepsilon}{2}}, \quad (3-31)$$

with $\mu_9^a < 1$, $\mu_9^b > 1$, $\mu_9^c < 1$. When arbitrary values are assigned to α , β , γ and δ , we can find a ε according to the compatible condition in Eq. (3-11) as

$$\varepsilon = 2 \arctan \frac{(1 - \zeta_9) \tan \frac{\alpha + \beta}{2}}{\zeta_9 + 1}, \quad \zeta_9 = \frac{1}{\mu_9^a \cdot \mu_9^b}. \quad (3-32)$$

Therefore, the type of QRS twist is rigidly foldable once the obtained ε is within the range $(0, \pi)$.

For the QSS twist (Fig. 3-10(j)), the μ_i^j of this type are

$$\mu_{10}^a = \frac{-\cos \frac{\alpha + \gamma}{2}}{\cos \frac{\alpha - \gamma}{2}}, \quad \mu_{10}^b = \frac{\cos \frac{\beta + \delta}{2}}{\cos \frac{\beta - \delta}{2}}, \quad \mu_{10}^c = \frac{\sin \frac{\alpha + \beta - \varepsilon}{2}}{\sin \frac{\alpha + \beta + \varepsilon}{2}}, \quad (3-33)$$

with $\mu_{10}^a < 1$, $\mu_{10}^b < 1$, $\mu_{10}^c < 1$, so it is impossible to find solutions for Eq. (3-11). Therefore, the type of QSS twist is not rigidly foldable.

For the PSR twist (Fig. 3-10(k)), the μ_i^j of this type are

$$\mu_{11}^a = \frac{\sin \frac{\alpha + \gamma}{2}}{\sin \frac{\alpha - \gamma}{2}}, \quad \mu_{11}^b = \frac{\cos \frac{\beta + \delta}{2}}{\cos \frac{\beta - \delta}{2}}, \quad \mu_{11}^c = \frac{-\cos \frac{\alpha + \beta - \varepsilon}{2}}{\cos \frac{\alpha + \beta + \varepsilon}{2}}, \quad (3-34)$$

with $\mu_{11}^a > 1$, $\mu_{11}^b < 1$, $\mu_{11}^c > 1$. When arbitrary values are assigned to α , β , γ and δ , we can find a ε according to the compatible condition in Eq. (3-11) as

$$\varepsilon = 2 \arctan \frac{\zeta_{11} + 1}{(\zeta_{11} - 1) \tan \frac{\alpha + \beta}{2}}, \quad \zeta_{11} = \frac{1}{\mu_{11}^a \cdot \mu_{11}^b}. \quad (3-35)$$

Therefore, the type of PSR twist is rigidly foldable once the obtained ε is within the range $(0, \pi)$.

For the QSR twist (Fig. 3-10(l)), the μ_i^j of this type are

$$\mu_{12}^a = \frac{-\cos \frac{\alpha + \gamma}{2}}{\cos \frac{\alpha - \gamma}{2}}, \quad \mu_{12}^b = \frac{\cos \frac{\beta + \delta}{2}}{\cos \frac{\beta - \delta}{2}}, \quad \mu_{12}^c = \frac{-\cos \frac{\alpha + \beta - \varepsilon}{2}}{\cos \frac{\alpha + \beta + \varepsilon}{2}}, \quad (3-36)$$

with $\mu_{12}^a < 1$, $\mu_{12}^b < 1$, $\mu_{12}^c > 1$. When arbitrary values are assigned to α , β , γ and δ , we can find a ε according to the compatible condition in Eq. (3-11) as

$$\varepsilon = 2 \arctan \frac{\zeta_{12} + 1}{(\zeta_{12} - 1) \tan \frac{\alpha + \beta}{2}}, \quad \zeta_{12} = \frac{1}{\mu_{12}^a \cdot \mu_{12}^b}. \quad (3-37)$$

Therefore, the type of QSR twist is rigidly foldable once the obtained ε is within the range $(0, \pi)$.

In summary, only the PPQ, PQQ, PRS, PSS, QRR, QRS, PSR and QSR twists as shown in Fig. 3-10 (b), (c), (e), (f), (h), (i), (k) and (l) are rigidly foldable, whereas the PPP, PRR, QQQ and QSS twists not. It should be noted that for a given M-V assignment of the triangle twist within these eight types, the rigid foldability depends on the choice of geometrical parameters as well. For example, the triangle twist pattern of type PSR

with $\alpha = 30^\circ$, $\beta = 80^\circ$, $\gamma = 90^\circ$, $\delta = 45^\circ$ and a calculated $\varepsilon = 7.04^\circ$ is rigidly foldable. However, when we change it to $\alpha = \beta = 60^\circ$ while $\gamma = 90^\circ$ and $\delta = 45^\circ$ unchanged, it is impossible to find a compatible ε for the pattern. That is, the triangle twist becomes a non-rigid case. Therefore, we can design a rigid or non-rigid triangle twist by choosing proper M-V assignment and geometrical parameters according to our demands.

3.4 Derived Overconstrained 6R Linkages

Although the M-V assignment has an impact on rigid foldability of the generalized triangle twist origami pattern, it does not affect geometric conditions of its kinematically equivalent spherical linkages. Here the generalized triangle twist presented in section 3.2 is used to demonstrate the derivation of spatial 6R linkage from this pattern. Considering geometric conditions in Eq. (3-5), there are five design parameters α , β , γ , δ and ε for this pattern, whereas only four are independent. A physical origami model of the triangle twist pattern and its corresponding folding process are designed as shown in Fig. 3-11(a). Since the vertices A, B and C always keep in a single plane, the central triangle ABC can be removed without affecting the motion of the pattern. Then a triangle twist kirigami pattern, which has only six creases as shown in Fig. 3-11(b), is obtained.

Recalling the relationship between mechanisms and origami patterns, a network of three spherical 4R linkages that corresponds to the triangle twist origami pattern in Fig. 3-11(a), can be built as shown in Fig. 3-12(a). Creases of vertices A, B and C are equivalent to joints a_i , b_i and c_i respectively, where joints a_4 & b_1 , b_4 & c_1 and c_4 & a_1 are coaxial. The adjacent links a_3a_4 in the spherical 4R linkage **A** and b_1b_2 in the spherical 4R linkage **B** are connected into one rigid body, and the same connection method is applied to other adjacent links in Fig. 3-12(a), such as links a_4a_1 & b_4b_1 , b_3b_4 & c_1c_2 , b_4b_1 & c_4c_1 , c_3c_4 & a_1a_2 and c_4c_1 & a_4a_1 . When the origami pattern is rigid with one DOF, its corresponding linkage network also has one DOF.

Once the central triangle is removed, a mobile linkage from the kirigami pattern in Fig. 3-11(b), can also be built as a 6R linkage, see Fig. 3-12(b), after joints in the central triangle being removed, and joints a_3 & b_2 being connected by one link, so do joints b_3 & c_2 and c_3 & a_2 . So the derived 6R linkage in Fig. 3-12(b) should also have one DOF as the network of spherical 4R linkages in Fig. 3-12(a). The six joints in the new derived 6R linkage have identical motion as joints a_3 , b_2 , b_3 , c_2 , c_3 and a_2

in the network of three spherical $4R$ linkages. Therefore, the kinematic analysis in section 3.2 can be applicable to the new $6R$ linkage as well.

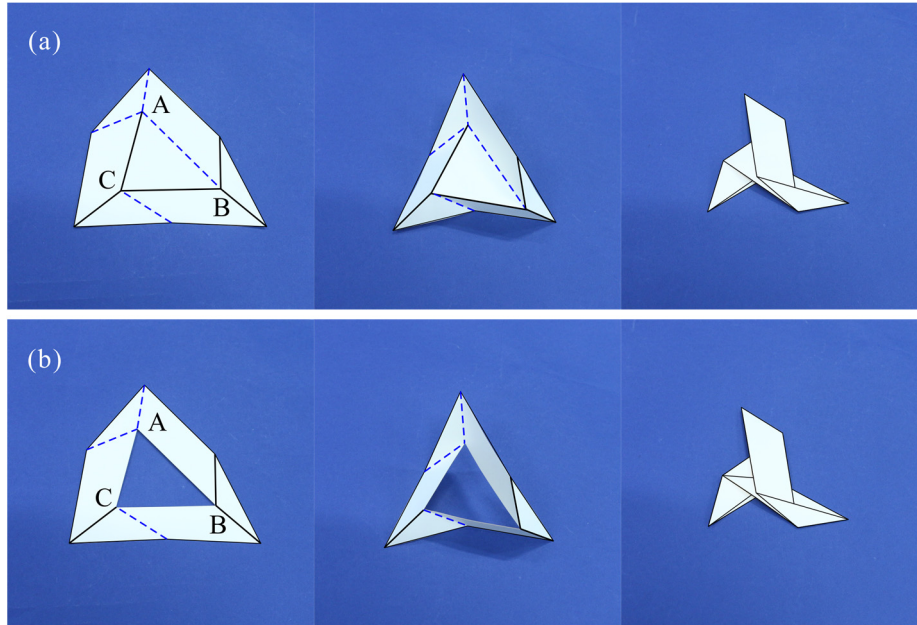


Fig. 3-11 Physical triangle twist models with $\alpha = 55^\circ$, $\beta = 50^\circ$, $\gamma = 50^\circ$, $\delta = 45^\circ$ and $\varepsilon = 35.44^\circ$ for (a) origami pattern, and (b) kirigami pattern.

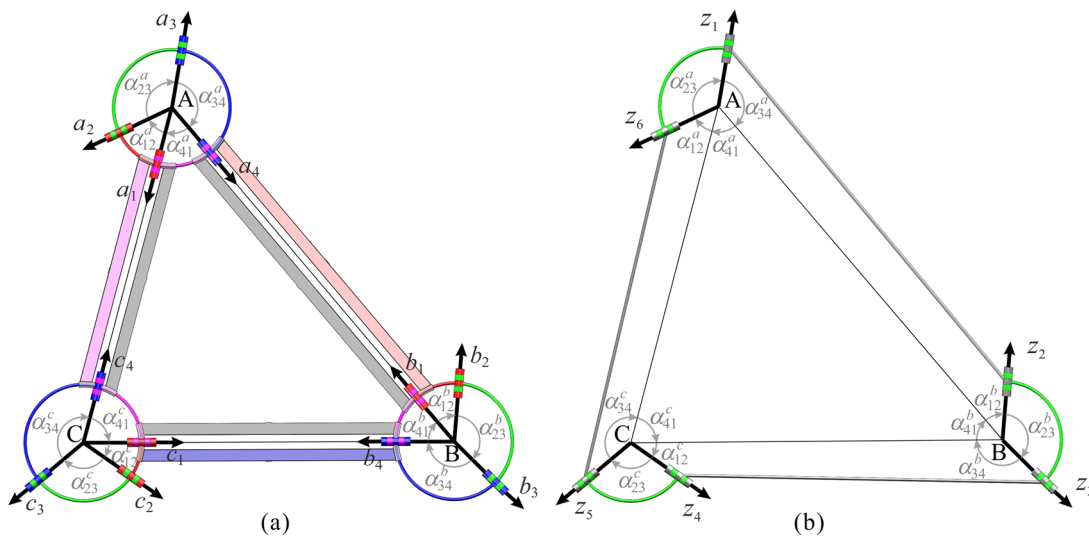


Fig. 3-12 Equivalent mechanisms of the generalized triangle twist: (a) the network of three spherical $4R$ linkages for the origami pattern, and (b) the derived overconstrained $6R$ linkage for the kirigami pattern.

It has been proved that the generalized triangle twist pattern in section 3.2 is rigidly foldable except for the parallel twist. Here the derived $6R$ linkages from kirigami patterns of the two rigidly foldable triangle twists are to be discussed. First considering the case where each crease-pair is intersected, the links have zero length with $\gamma \neq \delta$

correspondingly. The D-H notations of this new 6R linkage is depicted in Fig. 3-13(a). The axes of adjacent rotation joints intersect, and the intersection points of z_6 & z_1 , z_2 & z_3 , z_4 & z_5 , z_1 & z_2 , z_3 & z_4 and z_5 & z_6 are denoted as A, B, C, D, E and F respectively. Suppose the length of edge AB in the central triangle be d . The geometrical parameters of the 6R linkage can be calculated as follows.

$$a_{12} = a_{23} = a_{34} = a_{45} = a_{56} = a_{61} = 0, \quad (3-38a)$$

$$\alpha_{12} = 2\pi - \gamma + \delta, \quad \alpha_{23} = \pi - \beta, \quad \alpha_{34} = 2\pi - \delta + \varepsilon,$$

$$\alpha_{45} = \alpha + \beta, \quad \alpha_{56} = \gamma - \varepsilon, \quad \alpha_{61} = \pi - \alpha, \quad (3-38b)$$

$$\begin{aligned} R_1 = \overline{AD} &= \left| \frac{\sin \delta}{\sin(\gamma - \delta)} \right| \cdot d, \quad R_2 = -\overline{BD} = -\left| \frac{\sin \gamma}{\sin(\gamma - \delta)} \right| \cdot d, \\ R_3 = \overline{BE} &= \left| \frac{\sin \varepsilon}{\sin(\delta - \varepsilon)} \right| \cdot \frac{d \sin \alpha}{\sin(\alpha + \beta)}, \quad R_4 = -\overline{CE} = -\left| \frac{\sin \delta}{\sin(\delta - \varepsilon)} \right| \cdot \frac{d \sin \alpha}{\sin(\alpha + \beta)}, \\ R_5 = -\overline{CF} &= -\left| \frac{\sin \gamma}{\sin(\gamma - \varepsilon)} \right| \cdot \frac{d \sin \beta}{\sin(\alpha + \beta)}, \quad R_6 = \overline{AF} = \left| \frac{\sin \varepsilon}{\sin(\gamma - \varepsilon)} \right| \cdot \frac{d \sin \beta}{\sin(\alpha + \beta)}, \end{aligned} \quad (3-38c)$$

where γ , δ and ε should satisfy Eqs. (3-5) and (3-12). According to Eq. (3-38c), the relationship $R_1 \cdot R_3 \cdot R_5 + R_2 \cdot R_4 \cdot R_6 = 0$ holds and all lengths of the links are zero in Eq. (3-38a), which reveals that the derived 6R linkage is actually a variation of doubly collapsible octahedral Bricard [99]. The kinematic relationship of the derived 6R linkage is

$$\begin{aligned} \tan \frac{\theta_2}{2} &= \frac{\cos \frac{\alpha - \gamma}{2} \cos \frac{\beta - \delta}{2}}{\cos \frac{\alpha + \gamma}{2} \cos \frac{\beta + \delta}{2}} \cdot \tan \frac{\theta_1}{2}, \quad \tan \frac{\theta_3}{2} = \frac{\cos \frac{\alpha - \gamma}{2}}{\cos \frac{\alpha + \gamma}{2}} \cdot \tan \frac{\theta_1}{2}, \\ \theta_4 &= -\theta_1, \quad \theta_5 = \theta_2, \quad \theta_6 = \theta_3. \end{aligned} \quad (3-39)$$

It can be seen that kinematics of the derived doubly collapsible octahedral Bricard is not related to the value of d . It is determined by relative position of their axes. Kinematic paths of an instance with $\alpha = 55^\circ$, $\beta = 50^\circ$, $\gamma = 50^\circ$, $\delta = 45^\circ$ and $\varepsilon = 35.44^\circ$ are plotted as solid lines in Fig. 3-14.

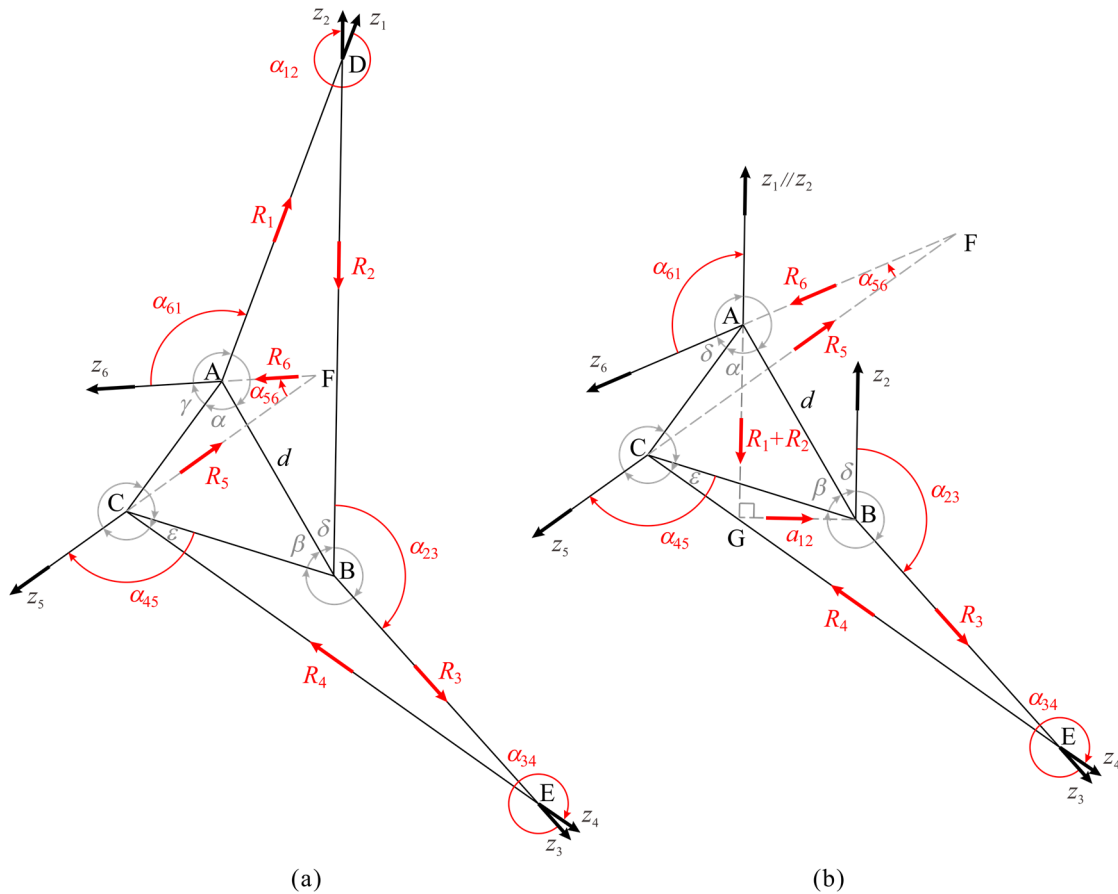


Fig. 3-13 Schematic diagrams of the derived overconstrained 6R linkages when (a) $\gamma \neq \delta$, and (b) $\gamma = \delta$.

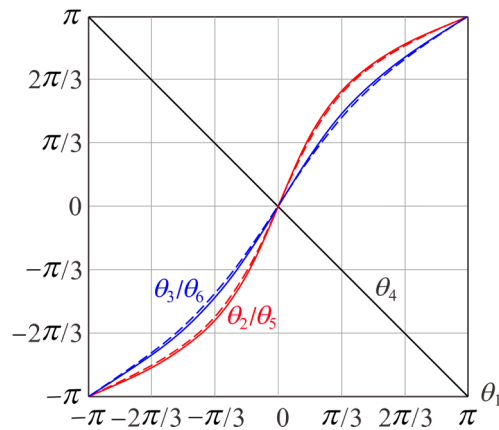


Fig. 3-14 Kinematic paths of the derived overconstrained 6R linkages with $\alpha = 55^\circ$, $\beta = 50^\circ$, $\gamma = 50^\circ$, $\delta = 45^\circ$, $\varepsilon = 35.44^\circ$ as solid lines and $\alpha = 55^\circ$, $\beta = 50^\circ$, $\gamma = \delta = 45^\circ$, $\varepsilon = 33.52^\circ$ as dashed lines.

Then consider the second case in which only one crease-pair is parallel, that is, the length of one link is non-zero by setting $\gamma = \delta$, see Fig. 3-13(b). In this case, axis z_1

is parallel to z_2 , and GB is their common perpendicular. z_6 & z_1 , z_2 & z_3 , z_4 & z_5 , z_3 & z_4 and z_5 & z_6 intersect at the points A, B, C, E and F respectively. The length of link 12 is the distance between the parallel crease-pair, whereas those of all the other links and the twist angle of link 12 are zero. The geometrical parameters of the 6R linkage are

$$a_{12} = \overline{GB} = d \sin \delta, \quad a_{23} = a_{34} = a_{45} = a_{56} = a_{61} = 0, \quad (3-40a)$$

$$\alpha_{12} = 0, \quad \alpha_{23} = \pi - \beta, \quad \alpha_{34} = 2\pi - \delta + \varepsilon,$$

$$\alpha_{45} = \alpha + \beta, \quad \alpha_{56} = \delta - \varepsilon, \quad \alpha_{61} = \pi - \alpha, \quad (3-40b)$$

$$R_1 + R_2 = -d \cos \delta,$$

$$R_3 = \overline{BE} = \left| \frac{\sin \varepsilon}{\sin(\delta - \varepsilon)} \right| \cdot \frac{d \sin \alpha}{\sin(\alpha + \beta)}, \quad R_4 = -\overline{CE} = -\left| \frac{\sin \delta}{\sin(\delta - \varepsilon)} \right| \cdot \frac{d \sin \alpha}{\sin(\alpha + \beta)},$$

$$R_5 = -\overline{CF} = -\left| \frac{\sin \delta}{\sin(\delta - \varepsilon)} \right| \cdot \frac{d \sin \beta}{\sin(\alpha + \beta)}, \quad R_6 = \overline{AF} = \left| \frac{\sin \varepsilon}{\sin(\delta - \varepsilon)} \right| \cdot \frac{d \sin \beta}{\sin(\alpha + \beta)}.$$

(3-40c)

It is found that $R_1 \cdot R_3 \cdot R_5 + R_2 \cdot R_4 \cdot R_6 = \frac{d^3 \sin \alpha \sin \beta \sin \delta \cos \delta \sin \varepsilon}{\sin^2(\alpha + \beta) \sin^2(\delta - \varepsilon)}$ for the 6R

linkage derived from the triangle twist kirigami pattern with only one parallel crease-pair. It neither satisfies the geometric conditions of doubly collapsible octahedral Bricard nor other existing overconstrained 6R linkages reviewed in section 2.1.3, such as Bricard linkages [100] and Bennett-based overconstrained linkages [89] etc., which indicates that a new type of overconstrained 6R linkage is obtained. Similarly, the kinematic relationship of this linkage is obtained by making $\gamma = \delta$ in Eq. (3-39). Changing geometrical parameters of the exemplified derived 6R linkage to $\gamma = 45^\circ$, $\varepsilon = 33.52^\circ$ while keeping other parameters identical with the previous case, the kinematic paths are plotted as dashed lines in Fig. 3-14. It can be found that both the geometrical parameters and kinematic paths differ little, which implies that the new derived overconstrained 6R linkage could be treated as an extension of the doubly collapsible octahedral Bricard.

3.5 Conclusions

This chapter has presented rigid foldability and motion analysis of the generalized triangle twist with varying geometrical parameters and M-V assignments. They have been analyzed based on the kinematic equivalence between rigid origami pattern and the network of spherical linkages. Twelve unique schemes of M-V assignment of the generalized triangle twist have been found. However, only eight types are possible to be rigidly foldable. The compatible conditions have been derived for these types of

triangle twist. Furthermore, the rigid foldability has been discussed according to the position relation of three crease-pairs around edges of the central triangle. It has been found that the triangle twist can be rigidly foldable only when at least one crease-pair is not parallel. In addition, a triangle twist kirigami pattern has been developed by removing the central triangle in the rigid origami pattern. A variation of doubly collapsible octahedral Bricard has been derived from the triangle twist kirigami pattern where each crease-pair is intersected. And a new type of overconstrained $6R$ linkage has been obtained when only one crease-pair is parallel.

Chapter 4 Kinematic Study of Plane-symmetric Bricard Linkage and Its Bifurcation Variations

4.1 Introduction

In Chapter 3, we derived a variation of the doubly collapsible Bricard octahedral case and a new type of overconstrained 6R linkage. Recently, several overconstrained 6R linkages have been applied in the design of deployable structures due to their structural stiffness and performance reliability such as the plane-symmetric Bricard linkage. Because of the symmetry property, the plane-symmetric Bricard 6R linkage tends to have complicated bifurcation behaviours, which should be avoided in the application of deployable structures, but could be made use of in the design of reconfigurable mechanisms. In this chapter, the aim is to setup the general geometric conditions for the bifurcation of plane-symmetric Bricard linkage.

The layout of this chapter is as follows. The explicit solutions to closure equations of the general plane-symmetric Bricard linkage are derived, and the comparison between kinematic properties of different plane-symmetric Bricard linkages based on these solutions are conducted in section 4.2. Section 4.3 introduces the derived 5R/4R linkages from the general case and their corresponding geometric conditions. Section 4.4 addresses the bifurcation between the plane-symmetric Bricard linkage and the Bennett linkage. Section 4.5 discusses other bifurcation cases of the plane-symmetric Bricard linkage under different geometric conditions. Final conclusions are drawn in section 4.6.

4.2 Explicit Closure Equations and Kinematic Properties

The geometrical parameters of the general plane-symmetric Bricard linkage are defined as shown in Fig. 4-1 with the conditions that

$$a_{12} = a_{61} = a, \quad a_{23} = a_{56} = b, \quad a_{34} = a_{45} = c, \quad (4-1a)$$

$$\alpha_{12} = 2\pi - \alpha_{61} = \alpha, \quad \alpha_{23} = 2\pi - \alpha_{56} = \beta, \quad \alpha_{34} = 2\pi - \alpha_{45} = \gamma, \quad (4-1b)$$

$$R_1 = R_4 = 0, \quad R_6 = -R_2, \quad R_5 = -R_3, \quad (4-1c)$$

where the setup of coordinate frames is in accordance with the D-H notation. Here, a , b , c , α , β , γ , R_2 and R_3 are taken as the geometrical parameters of the plane-symmetric Bricard linkage.

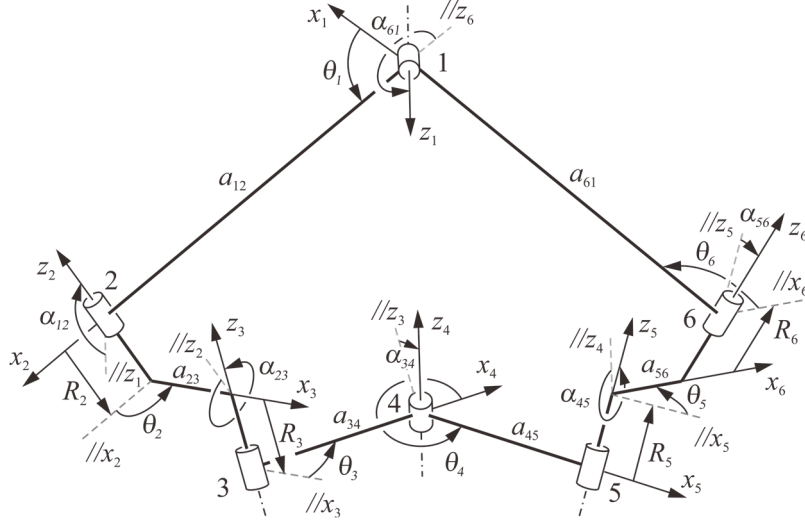


Fig. 4-1 D-H parameters of the plane-symmetric Bricard linkage

As it is a single loop linkage, the closure equation of the general plane-symmetric Bricard linkage can be obtained by rewriting Eq. (2-1) as

$$\mathbf{T}_{21}\mathbf{T}_{32}\mathbf{T}_{43} = \mathbf{T}_{61}\mathbf{T}_{56}\mathbf{T}_{45}. \quad (4-2)$$

Due to the plane symmetry, we have

$$\theta_5 = \theta_3, \quad \theta_6 = \theta_2. \quad (4-3)$$

Substituting Eq. (4-3) to Eq. (4-2) and simplifying entries (1, 3) and (1, 4) (shown in Appendix A) in Eq. (4-2), the following equation is obtained,

$$\frac{\sin \gamma (\cos \theta_2 \sin \theta_3 + \cos \beta \sin \theta_2 \cos \theta_3) + \sin \beta \cos \gamma \sin \theta_2}{\left[\begin{array}{l} \cos \alpha \sin \gamma \sin \theta_2 \sin \theta_3 - \cos \alpha \cos \beta \sin \gamma \cos \theta_2 \cos \theta_3 \\ + \sin \alpha \sin \beta \sin \gamma \cos \theta_3 - \cos \alpha \sin \beta \cos \gamma \cos \theta_2 - \sin \alpha \cos \beta \cos \gamma \end{array} \right]}, \quad (4-4)$$

$$= \frac{c(\cos \theta_2 \cos \theta_3 - \cos \beta \sin \theta_2 \sin \theta_3) + b \cos \theta_2 + a + R_3 \sin \beta \sin \theta_2}{\left[\begin{array}{l} c(\cos \alpha \sin \theta_2 \cos \theta_3 + \cos \alpha \cos \beta \cos \theta_2 \sin \theta_3 - \sin \alpha \sin \beta \sin \theta_3) \\ + b \cos \alpha \sin \theta_2 - R_3 \cos \alpha \sin \beta \cos \theta_2 - R_2 \sin \alpha - R_3 \sin \alpha \cos \beta \end{array} \right]}$$

which can be further simplified as

$$A \tan^2 \frac{\theta_3}{2} + B \tan \frac{\theta_3}{2} + C = 0, \quad (4-5)$$

where

$$A = \left[\begin{array}{l} (a - b + c) \sin(\alpha - \beta + \gamma) \tan^2 \frac{\theta_2}{2} + 2 \sin \alpha (R_3 \sin \gamma) \\ + R_2 \sin(\gamma - \beta) \tan \frac{\theta_2}{2} + (a + b - c) \sin(\alpha + \beta - \gamma) \end{array} \right], \quad (4-6a)$$

$$B = \begin{bmatrix} 2 \sin \gamma (R_2 \sin \alpha + R_3 \sin(\alpha - \beta)) \tan^2 \frac{\theta_2}{2} + 2((a - c) \sin(\alpha - \gamma)) \\ -(a + c) \sin(\alpha + \gamma) \tan \frac{\theta_2}{2} - 2 \sin \gamma (R_2 \sin \alpha + R_3 \sin(\alpha + \beta)) \end{bmatrix}, \quad (4-6b)$$

$$C = \begin{bmatrix} (a - b - c) \sin(\alpha - \beta - \gamma) \tan^2 \frac{\theta_2}{2} + 2 \sin \alpha (R_3 \sin \gamma) \\ + R_2 \sin(\gamma + \beta) \tan \frac{\theta_2}{2} + (a + b + c) \sin(\alpha + \beta + \gamma) \end{bmatrix}, \quad (4-6c)$$

and θ_2 is taken as the input kinematic variable.

Moreover, the other kinematic variables θ_1 and θ_4 could be calculated by simplifying entries (1, 3) and (3, 1) (shown in Appendix A) in Eq. (4-2) as

$$\tan \frac{\theta_1}{2} = \frac{\sin \gamma (\cos \theta_2 \sin \theta_3 + \cos \beta \sin \theta_2 \cos \theta_3) + \sin \beta \cos \gamma \sin \theta_2}{\begin{bmatrix} \sin \alpha \sin \beta \sin \gamma \cos \theta_3 - \cos \alpha \sin \beta \cos \gamma \cos \theta_2 - \sin \alpha \cos \beta \cos \gamma \\ -\cos \alpha \cos \beta \sin \gamma \cos \theta_2 \cos \theta_3 + \cos \alpha \sin \gamma \sin \theta_2 \sin \theta_3 \end{bmatrix}}, \quad (4-7)$$

$$\tan \frac{\theta_4}{2} = \frac{\sin \alpha \sin \theta_2 \cos \theta_3 + \sin \theta_3 (\sin \alpha \cos \beta \cos \theta_2 + \cos \alpha \sin \beta)}{\begin{bmatrix} \cos \gamma (\sin \alpha \sin \theta_2 \sin \theta_3 - \sin \alpha \cos \beta \cos \theta_2 \cos \theta_3) \\ -\cos \alpha \sin \beta \cos \theta_3 + \sin \gamma (\sin \alpha \sin \beta \cos \theta_2 - \cos \alpha \cos \beta) \end{bmatrix}}. \quad (4-8)$$

The solutions to Eq. (4-5) can be divided into following three cases.

1) When $A = 0$,

$$\tan \frac{\theta_3}{2} = \frac{-C}{B}. \quad (4-9)$$

Substituting Eq. (4-9) to Eqs. (4-7) and (4-8), the relationship between θ_1 , θ_4 and θ_2 can be derived as

$$\tan \frac{\theta_1}{2} = \frac{D}{E}, \quad (4-10)$$

$$\tan \frac{\theta_4}{2} = \frac{F}{G}, \quad (4-11)$$

in which

$$D = 2BC \sin \gamma \tan^2 \frac{\theta_2}{2} + 2(B^2 \sin(\beta + \gamma) + C^2 \sin(\beta - \gamma)) \tan \frac{\theta_2}{2} - 2BC \sin \gamma,$$

$$E = \begin{bmatrix} -(B^2 \sin(\alpha - \beta - \gamma) + C^2 \sin(\alpha - \beta + \gamma)) \tan^2 \frac{\theta_2}{2} - 4BC \cos \alpha \sin \gamma \tan \frac{\theta_2}{2} \\ -(B^2 \sin(\alpha + \beta + \gamma) + C^2 \sin(\alpha + \beta - \gamma)) \end{bmatrix},$$

$$F = 2BC \sin(\alpha - \beta) \tan^2 \frac{\theta_2}{2} + 2(B^2 - C^2) \sin \alpha \tan \frac{\theta_2}{2} - 2BC \sin(\alpha + \beta),$$

$$G = \begin{bmatrix} (B^2 \sin(\alpha - \beta - \gamma) - C^2 \sin(\alpha - \beta + \gamma)) \tan^2 \frac{\theta_2}{2} \\ -4BC \sin \alpha \cos \gamma \tan \frac{\theta_2}{2} - B^2 \sin(\alpha + \beta + \gamma) + C^2 \sin(\alpha + \beta - \gamma) \end{bmatrix}.$$

Therefore, Eqs. (4-3), (4-9), (4-10) and (4-11) form the only set of explicit solutions to closure equation of the plane-symmetric Bricard linkage when $A = 0$. According to the definition of term A as Eq. (4-6a), the following equation can be obtained,

$$\begin{bmatrix} (a - b + c) \sin(\alpha - \beta + \gamma) \tan^2 \frac{\theta_2}{2} + 2 \sin \alpha (R_3 \sin \gamma) \\ + R_2 \sin(\gamma - \beta) \tan \frac{\theta_2}{2} + (a + b - c) \sin(\alpha + \beta - \gamma) \end{bmatrix} = 0. \quad (4-12)$$

Equation (4-12) should be always true for all values of θ_2 , so we have

$$\begin{cases} (a - b + c) \sin(\alpha - \beta + \gamma) = 0 \\ 2 \sin \alpha (R_3 \sin \gamma + R_2 \sin(\gamma - \beta)) = 0 \\ (a + b - c) \sin(\alpha + \beta - \gamma) = 0 \end{cases} \quad (4-13)$$

Therefore, the geometric conditions for a plane-symmetric Bricard linkage with only one solution in this case are

$$\begin{cases} a - b + c = 0 \text{ or } \alpha - \beta + \gamma = k_1 \pi \\ \alpha = k_2 \pi \text{ or } R_3 \sin \gamma + R_2 \sin(\gamma - \beta) = 0, \\ a + b - c = 0 \text{ or } \alpha + \beta - \gamma = k_3 \pi \end{cases} \quad (4-14)$$

where $k_1, k_2, k_3 \in R$.

2) When $A \neq 0$ and $\Delta = B^2 - 4AC \geq 0$, the relationship between θ_3 and θ_2 are

$$\tan \frac{\theta_3}{2} = \frac{-B \pm \sqrt{B^2 - 4AC}}{2A}. \quad (4-15)$$

Further, substituting Eq. (4-15) to Eqs. (4-7) and (4-8), we have

$$\tan \frac{\theta_1}{2} = \frac{HI + J}{KI + L}, \quad (4-16)$$

$$\tan \frac{\theta_4}{2} = \frac{MI + N}{OI + P}, \quad (4-17)$$

in which

$$H = -2A \sin \gamma \tan^2 \frac{\theta_2}{2} - 2B \sin(\beta - \gamma) \tan \frac{\theta_2}{2} + 2A \sin \gamma,$$

$$I = -B \pm \sqrt{B^2 - 4AC},$$

$$J = 4A \tan \frac{\theta_2}{2} (A \sin(\beta + \gamma) - C \sin(\beta - \gamma)),$$

$$K = B \sin(\alpha - \beta + \gamma) \tan^2 \frac{\theta_2}{2} + 4A \cos \alpha \sin \gamma \tan \frac{\theta_2}{2} + B \sin(\alpha + \beta - \gamma),$$

$$L = 2A((C \sin(\alpha - \beta + \gamma) - A \sin(\alpha - \beta - \gamma)) \tan^2 \frac{\theta_2}{2} + C \sin(\alpha + \beta - \gamma) - A \sin(\alpha + \beta + \gamma)),$$

$$M = -2A \sin(\alpha - \beta) \tan^2 \frac{\theta_2}{2} + 2B \sin \alpha \tan \frac{\theta_2}{2} + 2A \sin(\alpha + \beta),$$

$$N = 4A(A + C) \sin \alpha \tan \frac{\theta_2}{2},$$

$$O = B \sin(\alpha - \beta + \gamma) \tan^2 \frac{\theta_2}{2} + 4A \sin \alpha \cos \gamma \tan \frac{\theta_2}{2} - B \sin(\alpha + \beta - \gamma),$$

$$P = 2A((C \sin(\alpha - \beta + \gamma) + A \sin(\alpha - \beta - \gamma)) \tan^2 \frac{\theta_2}{2} - C \sin(\alpha + \beta - \gamma) - A \sin(\alpha + \beta + \gamma)).$$

Therefore, when $A \neq 0$ and $\Delta \geq 0$, the solutions to closure equation of the plane-symmetric Bricard linkage are the equation set Eqs. (4-3), (4-15), (4-16) and (4-17). Applying the definition of the terms A , B and C in Eq. (4-6) to the discriminant Δ , a quartic equation with $\tan(\theta_2/2)$ being the independent variable can be obtained. According to the characteristics of the curve of quartic equation, the discriminant is semi-positive only under the conditions that the highest-degree coefficient and the minimum value of the discriminant Δ are non-negative.

3) When $A \neq 0$ and $\Delta < 0$, there is no solution to Eq. (4-5), which means that the linkage is a rigid structure.

Based on explicit solutions, the plane-symmetric Bricard linkage can be classified by the values of A and Δ . The detailed kinematic paths and motion behaviour of the plane-symmetric Bricard linkage with different geometrical parameters are given in Table 4-1. Several typical cases can be seen from Table 4-1 as follows.

- (a) When $A = 0$, six cases (Cases 1 to 6) can be derived from Eq. (4-14) where only one kinematic path exists.
- (b) When $A \neq 0$ and $\Delta < 0$, there is no kinematic path, i.e., the mechanism is rigid structure in Case 7.
- (c) When $A \neq 0$ and $\Delta = 0$, there is one kinematic path, corresponding to Case 8.
- (d) When $A \neq 0$ and $\Delta > 0$, there are two set of solutions with θ_2 as the input variable. A careful check reveals that for Case 10, two sets of different kinematic curves exists corresponding to two different linkage closures, which can switch to each other at the collinear configurations.

Table 4-1 The kinematic properties of the plane-symmetric Bricard linkage


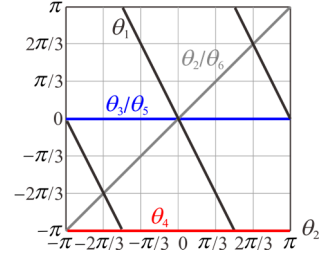
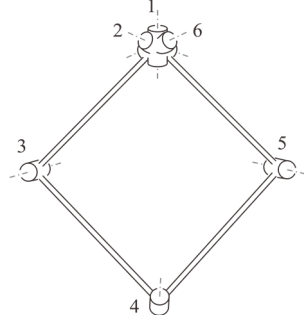
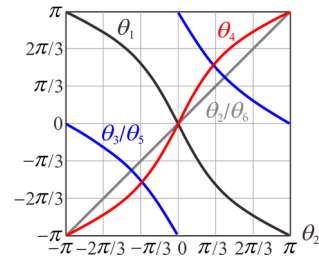
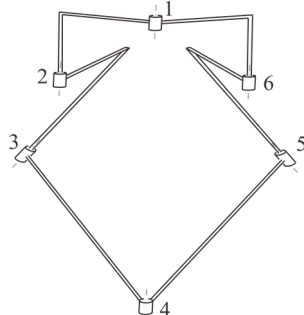
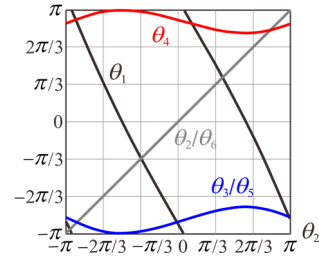
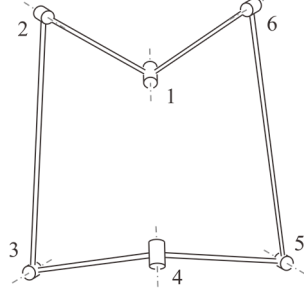
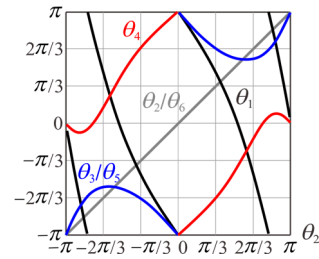
Case	Geometric conditions	Linkage model	Kinematic paths		
			N	curves	Motion behaviour
1	$A=0,$ $a=0,$ $b=c,$ $\alpha=k_2\pi.$	 Geometrical parameters: $a=0, b=c=1,$ $\alpha=0, \beta=\pi/3, \gamma=\pi/6,$ $R_2=R_3=0.$	1		Three joint axes 6, 1 and 2 coincide and the linkage would rotate along this joint as a whole. $\theta_2=\theta_6,$ while $\theta_1=-2\theta_2.$
2	$A=0,$ $a=0,$ $b=c,$ $R_2 \sin(\gamma-\beta)$ $=-R_3 \sin \gamma.$	 Geometrical parameters: $a=0, b=c=1, \alpha=\pi/3,$ $\beta=\gamma=\pi/6, R_2=R_3=0.$	1		The linkage has a 6R motion branch with joint axes 6, 1 and 2 intersect.
3	$A=0,$ $\alpha=k_2\pi,$ $\beta-\gamma$ $=(k_2-k_1)\pi.$	 Geometrical parameters: $a=1, b=2, c=4, \alpha=0,$ $\beta=7\pi/6, \gamma=\pi/6,$ $R_2=-1, R_3=-2.$	1		The linkage has a 6R motion branch with joint axes 6, 1 and 2 parallel.
4	$A=0,$ $b=a+c,$ $\alpha+\beta-\gamma$ $=k_3\pi,$ $R_2 \sin(\gamma-\beta)$ $=-R_3 \sin \gamma.$	 Geometrical parameters: $a=c=1, b=2, R_2=R_3=0,$ $\alpha=\beta=\pi/6, \gamma=\pi/3.$	1		The linkage has a 6R motion branch.

Table 4-1 The kinematic properties of the plane-symmetric Bricard linkage (Continued.)

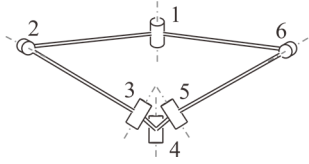
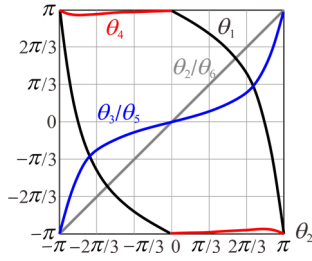
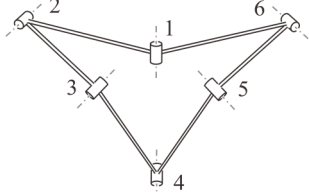
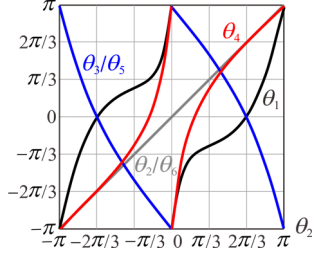
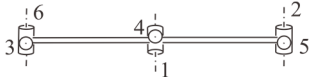
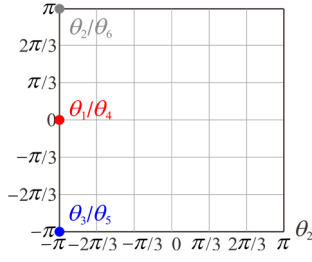
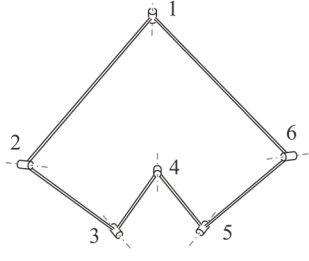
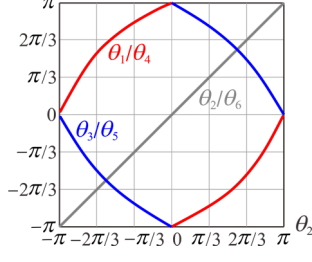
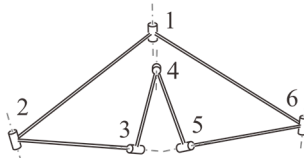
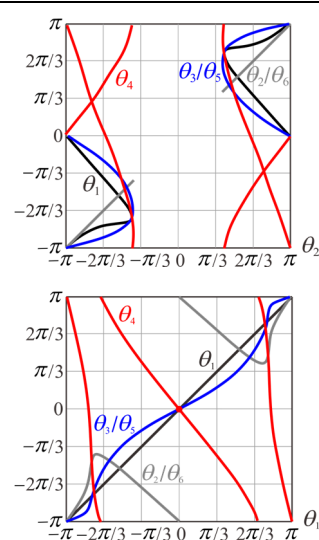
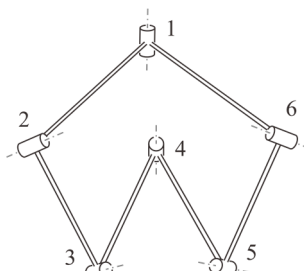
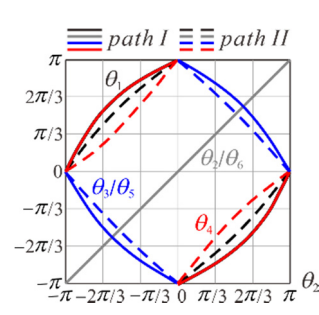
Case	Geometric conditions	Linkage model	Kinematic paths		
			N	curves	Motion behaviour
5	$A = 0,$ $c = a + b,$ $\alpha - \beta + \gamma = k_1\pi,$ $R_2 \sin(\gamma - \beta) = -R_3 \sin \gamma.$	 Geometrical parameters: $a = b = 1, c = 2, \alpha = \pi/3,$ $\beta = \pi/2, \gamma = \pi/6,$ $R_2 = R_3 = 0.$	1		The linkage has a 6R motion branch.
6	$A = 0,$ $\alpha = \frac{(k_1 + k_3)\pi}{2}$ $\beta - \gamma = \frac{(k_3 - k_1)\pi}{2},$ $R_2 \sin(\gamma - \beta) = -R_3 \sin \gamma.$	 Geometrical parameters: $a = 1.5, b = 1, c = 2,$ $\alpha = \frac{\pi}{2}, \beta = \frac{\pi}{4}, \gamma = -\frac{\pi}{4},$ $R_2 = R_3 = 0.$	1		The linkage has a 6R motion branch.
7	$A \neq 0,$ $\Delta < 0.$	 Geometrical parameters: $a = c = 1, b = 2,$ $\alpha = \gamma = \pi/6, \beta = \pi/2,$ $R_2 = R_3 = 0.$	0		The mechanism is a rigid structure and no motion exists.
8	$A \neq 0,$ $\Delta = 0.$	 Geometrical parameters: $a = 3, b = 2, c = 1,$ $\alpha = \frac{2\pi}{3}, \beta = \frac{\pi}{6}, \gamma = -\frac{\pi}{6},$ $R_2 = R_3 = 0.$	1		The linkage has only one 6R motion branch.

Table 4-1 The kinematic properties of the plane-symmetric Bricard linkage (Continued.)

Case	Geometric conditions	Linkage model	Kinematic paths		
			N	curves	Motion behaviour
9	$A \neq 0,$ $\Delta > 0.$	 <p>Geometrical parameters: $a = 3, b = 2, c = 1,$ $\alpha = \frac{\pi}{12}, \beta = \frac{\pi}{3}, \gamma = \frac{\pi}{4},$ $R_2 = R_3 = 0.$</p>	1		<p>Joints 2 and 6 have no complete rotation in the top left figure. (So joint 1 is taken as input in bottom left figure.) Joint 4 rotates three angular strokes while joints 1, 3 and 5 rotate one.</p>
10	$A \neq 0,$ $\Delta > 0.$	 <p>Geometrical parameters: $a = 2, b = c = 1,$ $\alpha = \frac{2\pi}{3}, \beta = \frac{\pi}{6}, \gamma = -\frac{\pi}{6},$ $R_2 = R_3 = 0.$</p>	2		<p>The linkage has two different plane-symmetric 6R motion branches corresponding to two kinematic paths, shown in the kinematic curves as solid and dash lines, respectively.</p>

However, there is an exception as Case 9. When $A \neq 0, \Delta > 0,$ taking θ_2 as the input variable, there are two sets of solutions. Yet, if converting them into the format with θ_1 as the input variable, there is only one set of explicit solutions, i.e., one kinematic path obtained. This is because that the θ_2 has no complete rotation in the whole path.

4.3 Derived 5R/4R Linkages

The above solutions to the closure equations of the general plane-symmetric Bricard linkage are conditional to the constraint that $\theta_i \neq \pi (i = 1, 2, 3, 4, 5, 6).$ When any one of the kinematic variable θ_i is kept to $\pi,$ the linkage may degenerate to 5R/4R linkages.

- 1) When $\theta_1 = \pi$

As shown in Fig. 4-2(a), link 12 coincides with link 61 in this case, making the resultant linkage a 5R linkage. The problem is to find out when the linkage is moveable.

Substituting $\theta_1 = \pi$ to the closure equation as Eq. (4-2), it is found that the linkage is moveable only when entries (2, 3) and (2, 4) (shown in Appendix A) of Eq. (4-2), which contain kinematic variables θ_2 and θ_3 , are linearly dependent. Thus, the geometric condition to make the plane-symmetric Bricard linkage degenerate to a movable 5R linkage can be derived from

$$\begin{aligned}
 & \begin{bmatrix} \sin(\beta - \alpha - \gamma)m^2 + \sin(\gamma - \alpha - \beta) \\ 4 \cos \alpha \sin \gamma m \\ \sin(\alpha - \beta - \gamma)m^2 - \sin(\alpha + \beta + \gamma) \end{bmatrix}^T \begin{bmatrix} n^2 \\ n \\ 1 \end{bmatrix} \\
 &= k \begin{bmatrix} [R_3 \sin(\beta - \alpha) - R_2 \sin \alpha]m^2 + 2(b - c) \cos \alpha m - R_3 \sin(\alpha + \beta) - R_2 \sin \alpha \\ -2c \cos(\alpha - \beta)m^2 + 2c \cos(\alpha + \beta) \\ [R_3 \sin(\beta - \alpha) - R_2 \sin \alpha]m^2 + 2(b + c) \cos \alpha m - R_3 \sin(\alpha + \beta) - R_2 \sin \alpha \end{bmatrix}^T \begin{bmatrix} n^2 \\ n \\ 1 \end{bmatrix}, \quad (4-18)
 \end{aligned}$$

where $m = \tan(\theta_2 / 2)$, $n = \tan(\theta_3 / 2)$ and $k \in R$.

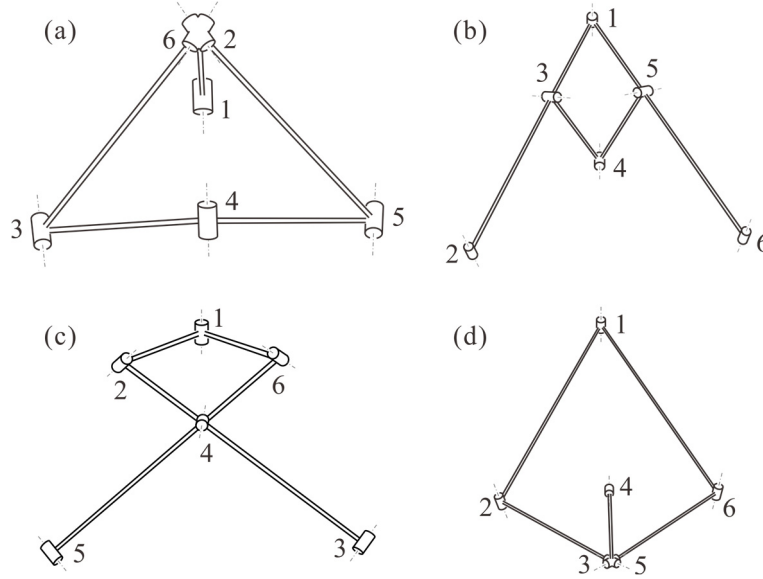


Fig. 4-2 The degenerated plane-symmetric Bricard linkage: (a) when $\theta_1 = \pi$, (b) when $\theta_2 = \theta_6 = \pi$, (c) when $\theta_3 = \theta_5 = \pi$, and (d) when $\theta_4 = \pi$.

The type of the degenerated linkage is depending on the choice of geometrical parameters that meet Eq. (4-18). The plane-symmetric Bricard linkage could degenerate to a planar 5R linkage as shown in Fig. 4-3(a) when all twist is zero whatever the values of link lengths and offsets are. In this case, the joint 1 is disabled since θ_1 is kept to π . The resultant planar 5R linkage has two joints 2 and 6 coincide, which works as two

separated parts including a rotation motion about joint 2/6 and a planar 4R motion formed by joints 3, 4, 5 and 2/6.

As shown in Fig. 4-3(b), the plane-symmetric Bricard linkage could also degenerate to a spherical 5R linkage if we set all link lengths and offsets zero. Take $a = b = c = 0$, $\alpha = \pi/4$, $\beta = \pi/3$, $\gamma = \pi/5$, $R_2 = R_3 = 0$ as an example. The resultant spherical 5R linkage also has two joints 2 and 6 coincide, so the resultant linkage works as a spherical 4R linkage formed by joints 3, 4, 5 and 2/6 with an additional rotation about joint 2/6.

Besides, the plane-symmetric Bricard linkage would degenerate to an equivalent serial kinematic chain with revolute joints when the parameters are set $a = b = 1$, $c = 1$, $\alpha = \pi/2$, $\beta = 0$, $\gamma = \pi/2$, $R_2 = R_3 = 0$ as shown in Fig. 4-3(c). In this case, joints 2, 6 and 3, 5 coincide. The resultant linkage works as a serial kinematic chain with two effective revolute joints 2/6 and 3/5.

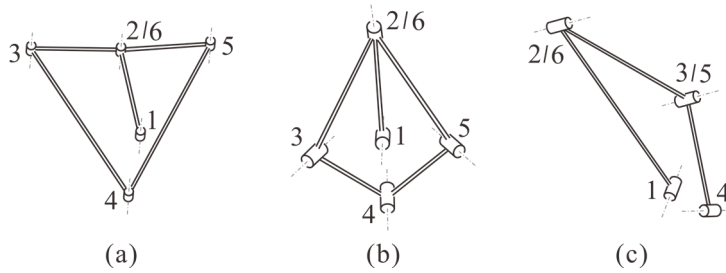


Fig. 4-3 The plane-symmetric Bricard when $\theta_1 = \pi$: (a) the degenerated planar 5R linkage with two joints 2 and 6 coincide, (b) the degenerated spherical 5R linkage with two joints 2 and 6 coincide, and (c) the degenerated serial kinematic chain with joints 2, 6 and 3, 5 both coincide.

2) When $\theta_2 = \theta_6 = \pi$

As shown in Fig. 4-2(b), links 12 and 23 are coincident as well as links 56 and 61, which generates a 4R linkage. In order to make the linkage moveable, we need to substitute $\theta_2 = \theta_6 = \pi$ to the closure equation as Eq. (4-2). Taking entries (1, 3) and (1, 4) (shown in Appendix A) of Eq. (4-2), which contain kinematic variables θ_1 and θ_3 , the linkage is moveable only when the following equation is satisfied.

$$\frac{-\sin \gamma \sin \theta_3}{\sin \gamma \cos(\alpha - \beta) \cos \theta_3 + \cos \gamma \sin(\beta - \alpha)} = \frac{-c \cos \theta_3 - b + a}{-c \cos(\alpha - \beta) \sin \theta_3 + R_3 \sin(\beta - \alpha) - R_2 \sin \alpha} \quad (4-19)$$

Further simplifying Eq. (4-19), we have

$$c \sin \gamma \cos(\alpha - \beta) + (b - a) \cos \gamma \sin(\beta - \alpha) + \sin \gamma [R_2 \sin \alpha - R_3 \sin(\beta - \alpha)] \sin \theta_3 + [c \cos \gamma \sin(\beta - \alpha) + (b - a) \sin \gamma \cos(\alpha - \beta)] \cos \theta_3 = 0. \quad (4-20)$$

To make Eq. (4-20) always true for all values of θ_3 , all coefficients should equal to zero, that is,

$$\begin{cases} c \sin \gamma \cos(\alpha - \beta) + (b - a) \cos \gamma \sin(\beta - \alpha) = 0, \\ \sin \gamma [R_2 \sin \alpha - R_3 \sin(\beta - \alpha)] = 0, \\ c \cos \gamma \sin(\beta - \alpha) + (b - a) \sin \gamma \cos(\alpha - \beta) = 0. \end{cases} \quad (4-21)$$

By solving Eq. (4-21), the geometric condition to make the plane-symmetric Bricard linkage degenerate to a movable 4R linkage is obtained

$$b - a + c = 0, \quad c \sin(\gamma + \alpha - \beta) = 0, \quad \sin \gamma [R_2 \sin \alpha - R_3 \sin(\beta - \alpha)] = 0, \quad (4-22)$$

or

$$\sin(\beta - \alpha + \gamma) = 0, \quad (a - b + c) \sin 2\gamma = 0, \quad \sin \gamma [R_2 \sin \alpha - R_3 \sin(\beta - \alpha)] = 0. \quad (4-23)$$

The type of the resultant 4R linkage depends on the choice of geometrical parameters that meet Eq. (4-22) or (4-23). For example, if we set the geometric condition as $a = b = c = 0$, $R_2 = R_3 = 0$, the movable linkage is a spherical 4R linkage. If the condition is $\alpha = \beta = \gamma = 0$, $R_2 = R_3 = 0$, the linkage degenerates to a planar 4R linkage. Moreover, a Bennett linkage is obtained when the condition is set as $a = b + c$, $\beta = \alpha + \gamma$, $R_2 = R_3 = 0$ or $b = a + c$, $\alpha = \beta + \gamma$, $R_2 = R_3 = 0$.

3) When $\theta_3 = \theta_5 = \pi$

Similarly, in Fig. 4-2(c) links 23 and 34 are coincident as well as links 45 and 56, which makes the linkage generate a 4R linkage. The condition of a moveable 4R linkage is obtained by substituting $\theta_3 = \theta_5 = \pi$ to the closure equation as Eq. (4-2). Considering entries (1, 3) and (1, 4) (shown in Appendix A) of Eq. (4-2), which contain kinematic variables θ_1 and θ_2 , the linkage is moveable only when

$$\begin{aligned} & \frac{\sin(\beta - \gamma) \sin \theta_2}{\cos \alpha \sin(\gamma - \beta) \cos \theta_2 - \sin \alpha \cos(\beta - \gamma)} \\ &= \frac{(b - c) \cos \theta_2 + R_3 \sin \beta \sin \theta_2 + a}{(b - c) \cos \alpha \sin \theta_2 - R_3 \cos \alpha \sin \beta \cos \theta_2 - R_3 \sin \alpha \cos \beta - R_2 \sin \alpha}, \end{aligned} \quad (4-24)$$

which can be simplified as

$$\begin{aligned} & (b - c) \cos \alpha \sin(\gamma - \beta) - a \sin \alpha \cos(\beta - \gamma) + \sin \alpha [R_2 \sin(\beta - \gamma) - R_3 \sin \gamma] \sin \theta_2 \\ & + [a \cos \alpha \sin(\gamma - \beta) + (c - b) \sin \alpha \cos(\beta - \gamma)] \cos \theta_2 = 0. \end{aligned} \quad (4-25)$$

Since Eq. (4-25) is always true for all values of θ_2 , all coefficients should equal to zero,

$$\begin{cases} (b-c)\cos\alpha\sin(\gamma-\beta)-a\sin\alpha\cos(\beta-\gamma)=0, \\ \sin\alpha[R_2\sin(\beta-\gamma)-R_3\sin\gamma]=0, \\ a\cos\alpha\sin(\gamma-\beta)+(c-b)\sin\alpha\cos(\beta-\gamma)=0, \end{cases} \quad (4-26)$$

i.e.,

$$a-b+c=0, \quad a\sin(\gamma-\alpha-\beta)=0, \quad \sin\alpha[R_2\sin(\beta-\gamma)-R_3\sin\gamma]=0, \quad (4-27)$$

or

$$\sin(\alpha-\beta+\gamma)=0, \quad (a+b-c)\sin 2\alpha=0, \quad \sin\alpha[R_2\sin(\beta-\gamma)-R_3\sin\gamma]=0. \quad (4-28)$$

The type of the resultant movable 4R linkage varies with the choice of geometrical parameters according to Eq. (4-27) or (4-28). When all link lengths and offsets are set zero, the resultant 4R linkage could be a spherical 4R linkage. When all twists and offsets are zero, a planar 4R linkage is obtained. The condition to obtain a Bennett linkage is $b=a+c$, $\gamma=\alpha+\beta$, $R_2=R_3=0$ or $c=a+b$, $\beta=\alpha+\gamma$, $R_2=R_3=0$.

4) When $\theta_4=\pi$

As shown in Fig. 4-2(d), link 34 coincides with link 45 in this case, making the resultant linkage a 5R linkage. Substituting $\theta_4=\pi$ to the closure equation as Eq. (4-2), it is found that the linkage is moveable only when entries (1, 3), (1, 4) and (3, 2) (shown in Appendix A) of Eq. (4-2), which contain kinematic variables θ_1 , θ_2 and θ_3 , are linearly dependent. Thus, the geometric condition to make the plane-symmetric Bricard linkage degenerate to a movable 5R linkage can be derived as

$$\begin{aligned} & \begin{bmatrix} \left((a-b+c)\sin(\alpha-\beta+\gamma)m^2+2\sin\alpha(R_3\sin\gamma+R_2\sin(\gamma-\beta))m \right) \\ \left((a+b-c)\sin(\alpha+\beta-\gamma) \right) \\ \left(2\sin\gamma(R_2\sin\alpha+R_3\sin(\alpha-\beta))m^2+2((a-c)\sin(\alpha-\gamma)) \right) \\ \left(-(a+c)\sin(\alpha+\gamma)m-2\sin\gamma(R_2\sin\alpha+R_3\sin(\alpha+\beta)) \right) \\ \left((a-b-c)\sin(\alpha-\beta-\gamma)m^2+2\sin\alpha(R_3\sin\gamma+R_2\sin(\gamma+\beta))m \right) \\ \left((a+b+c)\sin(\alpha+\beta+\gamma) \right) \end{bmatrix}^T \begin{bmatrix} n^2 \\ n \\ 1 \end{bmatrix} \\ & = k \begin{bmatrix} \sin(\beta-\alpha-\gamma)m^2+\sin(\alpha+\beta-\gamma) \\ 4\sin\alpha\sin\gamma m \\ \sin(\alpha-\beta-\gamma)m^2-\sin(\alpha+\beta+\gamma) \end{bmatrix}^T \begin{bmatrix} n^2 \\ n \\ 1 \end{bmatrix}, \end{aligned} \quad (4-29)$$

where $m=\tan(\theta_2/2)$, $n=\tan(\theta_3/2)$ and $k \in R$. Considering the plane symmetry of the Bricard linkage, the degenerated linkage is similar as the case when $\theta_1=\pi$.

Moreover, when θ_i is kept constant but not equal to π , the linkage will also degenerate to 5R/4R linkages.

4.4 Bifurcation between Plane-symmetric Bricard Linkage and Bennett Linkage

Based on the analysis in section 4.3, the linkage could bifurcate from the plane-symmetric Bricard linkage to the Bennett linkage. When the geometric condition is

$$a = b + c, \beta = \alpha + \gamma, R_2 = R_3 = 0 \text{ or } b = a + c, \alpha = \beta + \gamma, R_2 = R_3 = 0, \quad (4-30)$$

$A \neq 0$ and $\Delta > 0$. The linkage would have two solutions given as the equation set (4-3), (4-15), (4-16) and (4-17). However, there is only one plane-symmetric 6R motion branch represented by the solid line as shown in Fig. 4-4 and denoted as *path I*, which corresponds to Case 9 in Table 4-1. The revolute joints θ_2 and θ_6 have no complete rotation.

Moreover, there is another motion branch when $\theta_2 = \theta_6 = \pi$, shown as the dashed line in Fig. 4-4 and denoted as *path II*, where the linkage works as a Bennett linkage actually. The whole bifurcation process is presented in Fig. 4-4, where the actuated joint 1 is highlighted with a rotation in red.

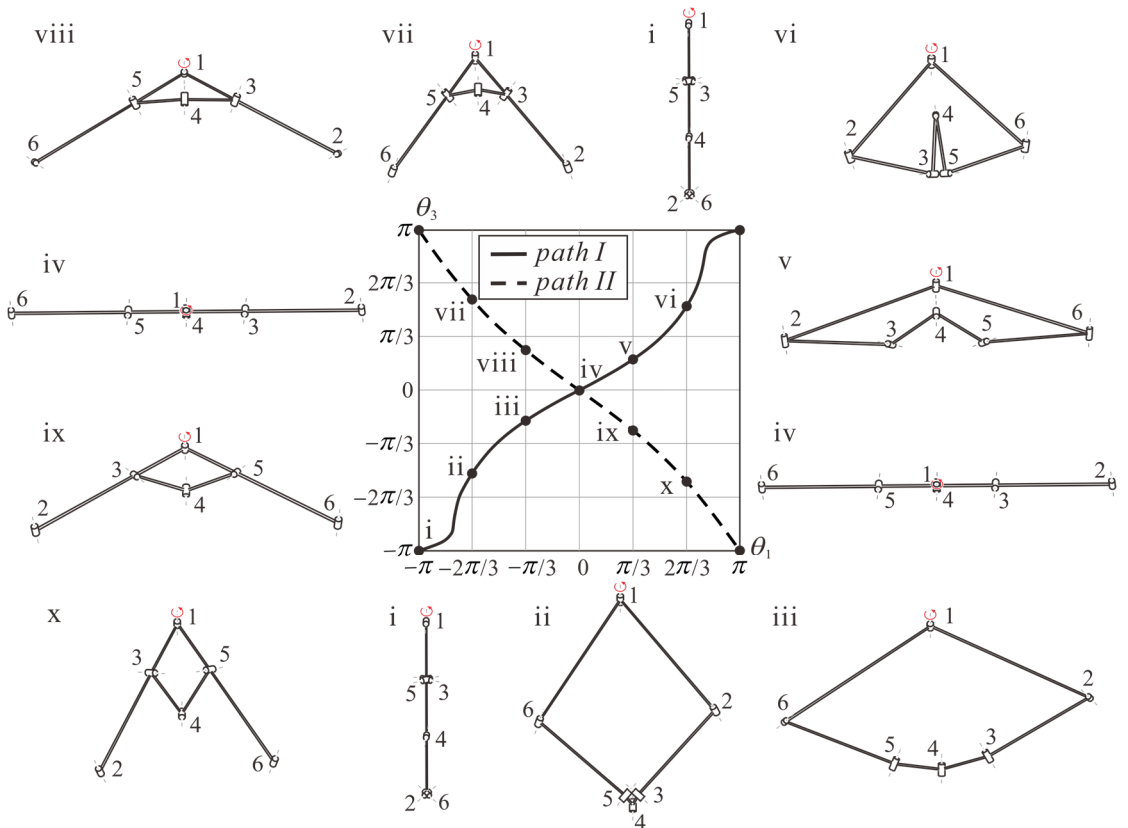


Fig. 4-4 Bifurcation between the plane-symmetric Bricard linkage and the Bennett linkage when $\theta_2 = \theta_6 = \pi$, where i-ii-iii-iv-v-vi-i correspond to configurations of the linkage along the plane-symmetric Bricard motion branch and i-vii-viii-iv-ix-x-i correspond to configurations of the linkage along the Bennett motion branch. Here the geometrical parameters of this linkage are

$$a = 3, b = 2, c = 1, \alpha = \pi/12, \beta = \pi/3, \gamma = \pi/4 \text{ and } R_2 = R_3 = 0.$$

Similarly, once the geometric conditions are

$$b = a + c, \quad \gamma = \alpha + \beta, \quad R_2 = R_3 = 0 \quad \text{or} \quad c = a + b, \quad \beta = \alpha + \gamma, \quad R_2 = R_3 = 0, \quad (4-31)$$

$A = 0$. The linkage would have only one $6R$ motion branch given as the equation set (4-3), (4-9), (4-10) and (4-11), which is represented by the solid line shown in Fig. 4-5 where the actuated joint 2 is highlighted with a rotation in red.

All the revolute joints have complete rotation, and some revolute joints have strokes more than 2π such as the stroke of θ_1 is 6π . And there is one more motion branch when $\theta_3 = \theta_5 = \pi$, as the dashed line in Fig. 4-5, in which the linkage also works as a Bennett linkage.

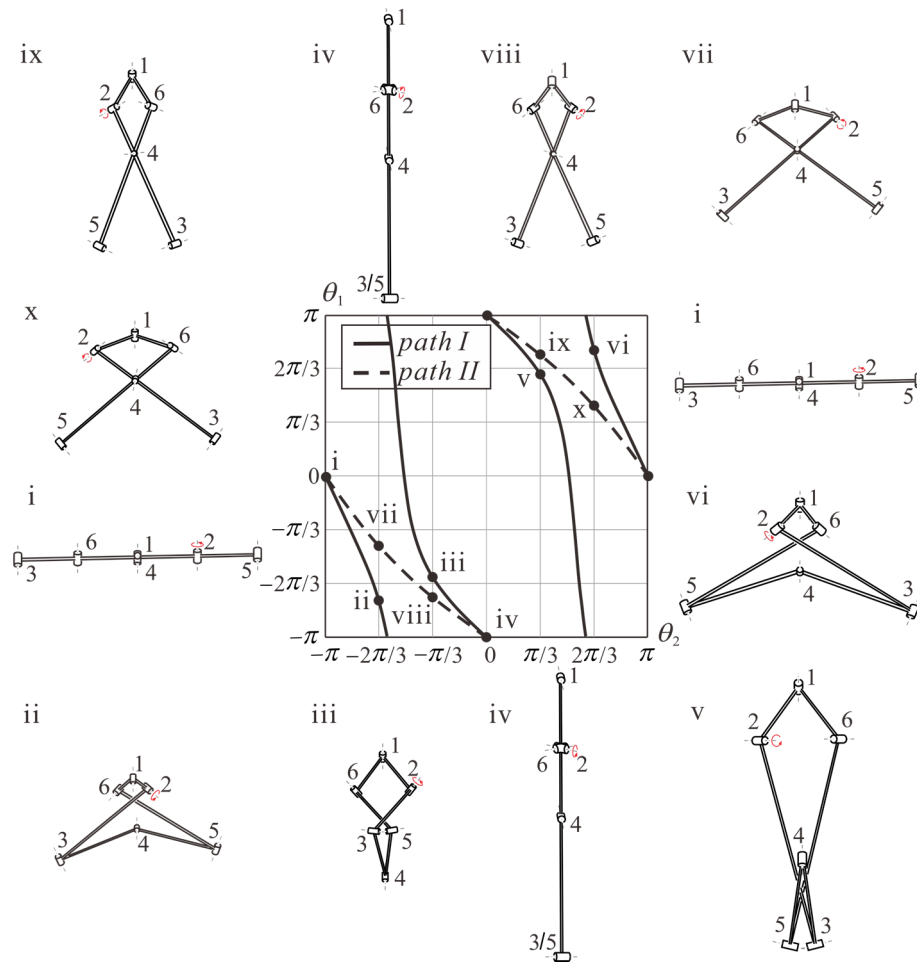


Fig. 4-5 Bifurcation between the plane-symmetric Bricard linkage and the Bennett linkage when $\theta_3 = \theta_5 = \pi$, where i-ii-iii-iv-v-vi-i correspond to configurations of the linkage along the plane-symmetric Bricard motion branch and i-vii-viii-iv-ix-x-i correspond to configurations of the linkage along the Bennett motion branch. Here the geometrical parameters of this linkage are

$$a = 1, \quad b = 3, \quad c = 2, \quad \alpha = \pi/4, \quad \beta = \pi/3, \quad \gamma = 7\pi/12 \quad \text{and} \quad R_2 = R_3 = 0.$$

4.5 Other Bifurcation Behaviours

The last section deals with a special case of the bifurcation between the plane-symmetric Bricard linkage and the Bennett linkage. Additional various bifurcation cases depending on the different choice of geometrical parameters are revealed in this section.

4.5.1 Bifurcation between Two 6R Motion Branches

In order to make the plane-symmetric Bricard linkage have two 6R motion branches, $A \neq 0$ and $\Delta > 0$ must be satisfied according to the analysis in section 4.2.

If we set the geometric condition as

$$a = 2b, \quad c = b, \quad \alpha = \pi - 2\beta, \quad \gamma = -\beta, \quad R_2 = R_3 = 0, \quad (4-32)$$

the linkage would have two solutions as

$$\tan \frac{\theta_2}{2} = -\frac{1}{\cos 2\beta} / \tan \frac{\theta_1}{2}, \quad \tan \frac{\theta_3}{2} = -\cos \beta \tan \frac{\theta_1}{2}, \quad \theta_4 = \theta_1, \quad \theta_5 = \theta_3, \quad \theta_6 = \theta_2, \quad (4-33)$$

and

$$\tan \frac{\theta_1}{2} = -\frac{1}{\cos^2 \beta} / \tan \frac{\theta_6}{2}, \quad \tan \frac{\theta_3}{2} = \frac{1}{\cos \beta} / \tan \frac{\theta_6}{2},$$

$$\tan \frac{\theta_4}{2} = -\frac{\cos 2\beta \tan^2 \frac{\theta_6}{2} + 1}{\tan \frac{\theta_6}{2} (\cos^2 \beta \tan^2 \frac{\theta_2}{2} + 2 - \cos^2 \beta)}, \quad \theta_5 = \theta_3, \quad \theta_6 = \theta_2. \quad (4-34)$$

As shown in Fig. 4-6, the two kinematic paths intersect at points $(\pi, 0)$ and $(0, \pi)$, indicating these two points are the bifurcation points. The actuated joint is highlighted with a rotation in red. The linkage would work along *path I* if we choose joint 1 as the actuated joint, and it would change to *path II* when the actuated joint is joint 2.

Physically, the link cannot penetrate the other as shown in Fig. 4-6. Therefore, the physical links are designed with curve profiles to avoid the collisions. A design of such a plane-symmetric Bricard linkage with two motion branches where there is no collision between physical links has been proposed as shown in Fig. 4-7, where the actuators are simplified as two red blocks. It can be seen that the links defined by the D-H notation in the blue dashed lines differ greatly from the physical links. The geometrical parameters of this linkage are

$$a_{12} = a_{61} = 160\text{mm}, \quad a_{23} = a_{56} = 80\text{mm}, \quad a_{34} = a_{45} = 80\text{mm}, \quad (4-35a)$$

$$\alpha_{12} = 2\pi - \alpha_{61} = 100^\circ, \quad \alpha_{23} = 2\pi - \alpha_{56} = 40^\circ, \quad \alpha_{45} = 2\pi - \alpha_{34} = 40^\circ, \quad (4-35b)$$

$$R_1 = R_2 = R_3 = R_4 = R_5 = R_6 = 0. \quad (4-35c)$$

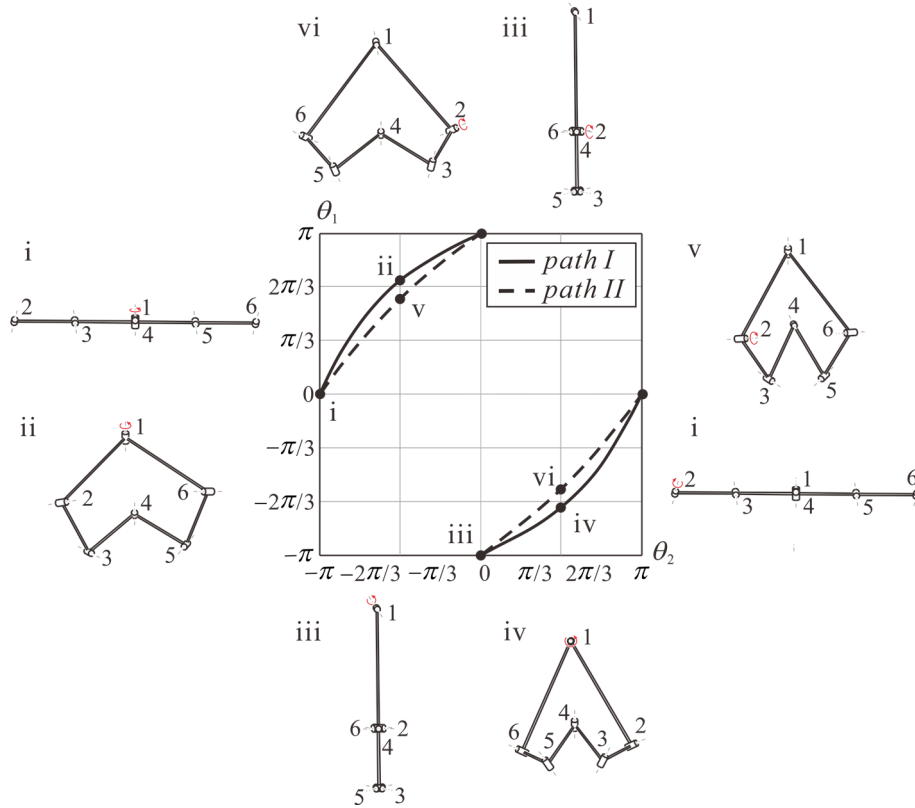


Fig. 4-6 Bifurcation between two 6R motion branches, where i-ii-iii-iv-i correspond to configurations of the linkage along *path I* and i-vi-iii-v-i correspond to configurations of the linkage along *path II*. Here the geometrical parameters of this linkage are $a = 2$, $b = 1$, $c = 1$, $\alpha = 2\pi/3$, $\beta = \pi/6$, $\gamma = -\pi/6$ and $R_2 = R_3 = 0$, which corresponds to Case 10 in Table 4-1.

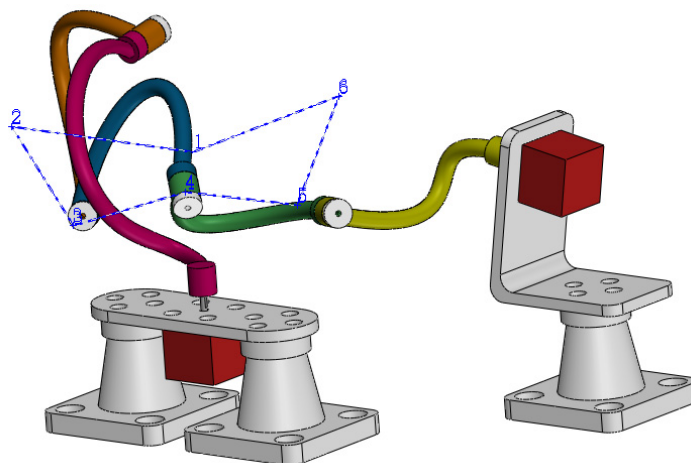


Fig. 4-7 A plane-symmetric Bricard linkage with two 6R motion branches where no collision happens

4.5.2 Bifurcation between Kinematic Chains and a 4R Linkage

There is a special case where A , B and C all equal to zero, where the solution set in section 4.2 is no longer true. For example, if we set the geometrical parameters as

$$a = 3, \quad b = 2, \quad c = 4, \quad \alpha = \frac{\pi}{2}, \quad \beta = 0, \quad \gamma = \frac{\pi}{2}, \quad R_2 = R_3 = 0, \quad (4-36)$$

by solving Eq. (4-2), the solutions can be obtained as

$$\theta_1 = -\theta_4, \quad \theta_2 = \theta_6 = \frac{\pi}{3}, \quad \theta_3 = \theta_5 = \frac{2\pi}{3}, \quad (4-37a)$$

$$\theta_1 = -\theta_4, \quad \theta_2 = \theta_6 = -\frac{\pi}{3}, \quad \theta_3 = \theta_5 = -\frac{2\pi}{3}, \quad (4-37b)$$

$$\theta_1 = \theta_4 = \pi, \quad \theta_2 = \theta_6 \in (-\pi, \pi), \quad \theta_3 = \theta_5 \in (-\pi, \pi), \quad (4-37c)$$

and

$$\theta_1 = \theta_4 = 0, \quad \tan \frac{\theta_6}{2} = \frac{-4 \tan \frac{\theta_2}{2} \pm \sqrt{3(7 \tan^2 \frac{\theta_2}{2} + 3)(7 - 5 \tan^2 \frac{\theta_2}{2})}}{15 \tan^2 \frac{\theta_2}{2} + 7},$$

$$\sin(\theta_2 + \theta_3) = \frac{\sin \theta_6 - \sin \theta_2}{4}, \quad \theta_5 = -(\theta_2 + \theta_3 + \theta_6). \quad (4-37d)$$

It is found that Eq. (4-37a) and Eq. (4-37b) correspond to the cases that the linkage degenerates to a revolute joint, where links 12, 23 and 34 work as a whole part that rotates about joint 1, relative to the part consisting of links 45, 56 and 61. It is represented in Fig. 4-8(a) as *path I* and *path III* respectively where the joint 1 is chosen as the actuated joint highlighted with a rotation in red. Eq. (4-37c) corresponds to the case that the linkage degenerates to a serial kinematic chain with two revolute joints as shown in Fig. 4-8(a) as *path II* where there are two actuated joints 2 and 3. It should be noticed that there exists a case represented by Eq. (4-37d) that violates the plane-symmetric motion shown as *path IV* along which configurations of the linkage are shown in Fig. 4-8(b). The linkage is actually a four-bar double-rocker linkage.

The plotted paths define the values of two chosen kinematic variables at those selected points where corresponding configurations are presented, and other kinematic variables can be determined similarly. Once all kinematic variables are given, configurations of the linkage at these points are definitely determined. The whole bifurcation behaviour is presented in Fig. 4-8, where Fig. 4-8(a) shows the bifurcation between two equivalent single-revolute-joint motion branches and a serial kinematic chain with two revolute joints, and Fig. 4-8(b) shows the bifurcation between two equivalent single-revolute-joint motion branches and a four-bar double-rocker linkage motion branch.

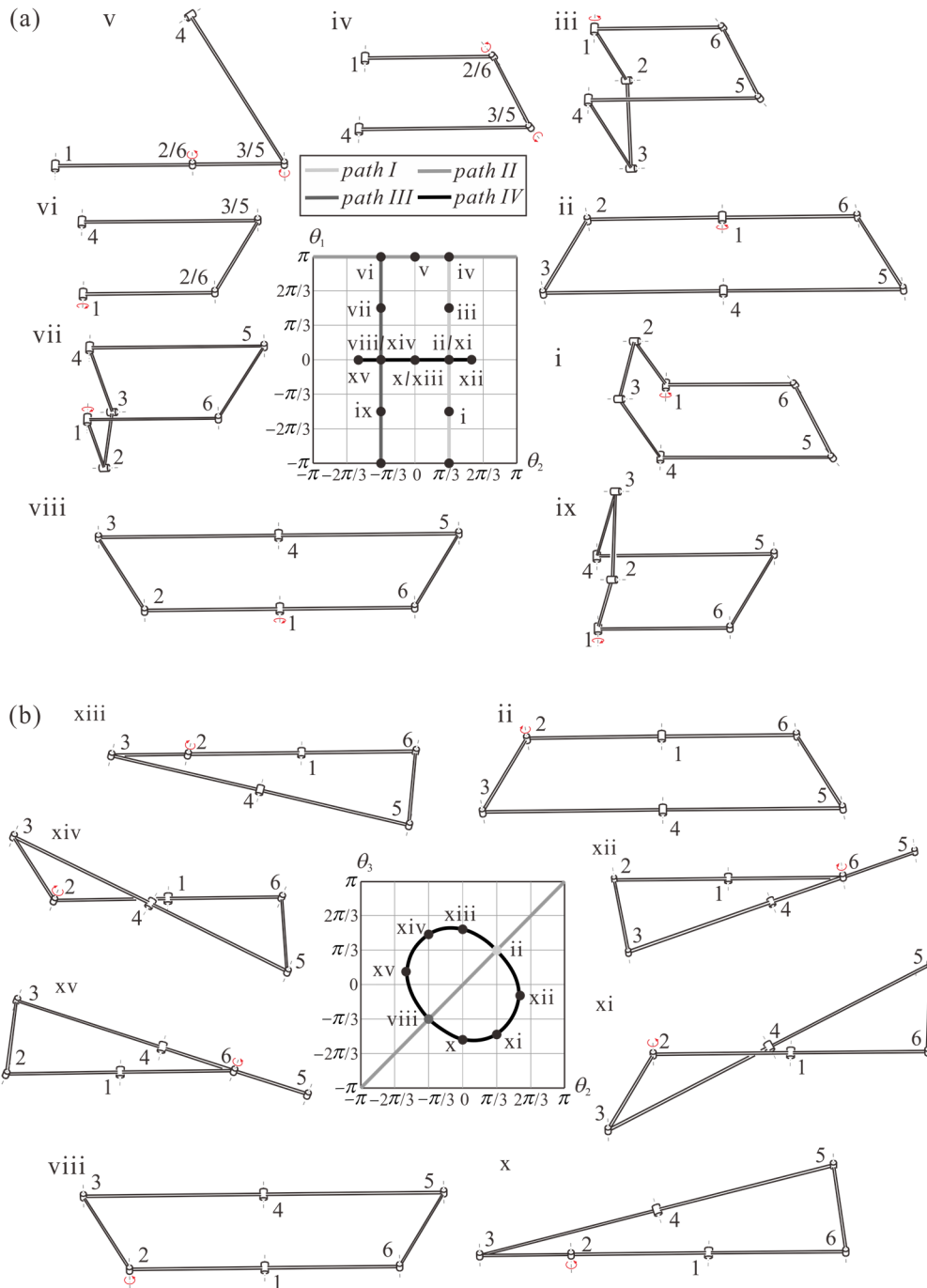


Fig. 4-8 Bifurcation of the plane-symmetric Bricard linkage: (a) between two equivalent single-revolute-joint branches and a serial kinematic chain with two revolute joints branch; (b) between two equivalent single-revolute-joint branches and a four-bar double-rocker linkage branch, where i-ii-iii-iv correspond to configurations of the linkage along *path I*, iv-v-vi correspond to configurations of the linkage along *path II*, vi-vii-viii-ix correspond to configurations of the linkage along *path III*, and viii-x-xi-xii-ii-xiii-xiv-xv correspond to configurations of the linkage along *path IV*.

4.6 Conclusions

In this chapter, a thorough kinematic study of the general plane-symmetric Bricard

linkage has been conducted. Based on the D-H matrix method, the explicit solutions to closure equations of the plane-symmetric Bricard linkage have been derived first. Once the geometric condition is given, the relationship between different kinematic variables can be easily obtained. Even though Baker gave the implicit closure equations of a general plane-symmetric Bricard linkage [116], the explicit solutions provide a more effective way on kinematic and bifurcation analysis. Various cases of the plane-symmetric Bricard linkage with none, one or two $6R$ motion paths have been compared. Moreover, the conditions to obtain degenerated $5R/4R$ linkages from this kind of linkage have been elaborated.

Furthermore, various bifurcation cases of the plane-symmetric Bricard linkage with different geometric conditions, including the bifurcation between overconstrained $6R$ and $4R$ linkages, two overconstrained $6R$ linkages and among equivalent kinematic chains with single or double revolute joints and a four-bar double-rocker linkage, have been revealed. Especially, the bifurcation from the plane-symmetric Bricard linkage to the Bennett linkage has been proposed. Normally, Bricard-related linkages and Bennett-based linkages [89] compose two major separated groups of single-loop spatial overconstrained linkages. This work further reveals the intrinsic relationship between these two groups after the proposal of the linkage that can reconfigure between Bennett linkage and general line-symmetric Bricard linkage [71].

Chapter 5 Symmetric Flat-foldable Waterbomb Origami

5.1 Introduction

The traditional waterbomb origami, produced from a pattern consisting of a series of vertices where six creases meet, is one of the most widely utilized origami patterns. Although the waterbomb pattern is of multiple degrees of freedom, the symmetric folding is often preferred in most of research or art work, which is done by constraining it with symmetric conditions and then controlling the motion to reach an ideal flat-foldable state. However, the symmetric folding is hard to realize and the thickness of the material cannot simply be ignored in most of the practical engineering applications. Therefore, the thick-panel origami approach [29] is adopted. This chapter provides a comprehensive kinematic analysis on foldability of the waterbomb tessellation that made from the six-crease waterbomb bases of both a zero-thickness sheet and panels of finite thickness. Kinematically the folding of zero-thickness sheet is modelled as spherical $6R$ linkages whereas that of thick panels is treated as an assembly of the Bricard linkages. The motion behaviour of the thick-panel waterbomb origami will be analyzed based on the kinematics and bifurcation analysis of the plane-symmetric Bricard linkage in Chapter 4.

The layout of this chapter is as follows. Section 5.2 setups the geometry and kinematics of the waterbomb origami pattern. Section 5.3 presents a detailed analysis on rigid foldability of the waterbomb tessellation for zero-thickness sheet. This is followed by the design and kinematic behaviour of its corresponding thick-panel origami in section 5.4. Comparisons and further discussion are made in section 5.5.

5.2 Geometry and Kinematic Setup

The six-crease waterbomb base comprises four diagonal valley creases (dashed lines) and two co-linear mountain creases (solid lines), all of which meet at a single vertex as shown in Fig. 5-1(a), where t is the half-width of the base, α and β are the design angles of the base. Placing the base shown in blue side-by-side to form a row and shifting the bases by half a base (red) on the adjacent rows, a generalized waterbomb origami pattern is formed as shown in Fig. 5-1(b), where m and n are the number of bases in the vertical and horizontal direction, respectively. There are three representative vertices marked by circles, A_i , B_i and C_i , where i is the row number that the waterbomb base locates.

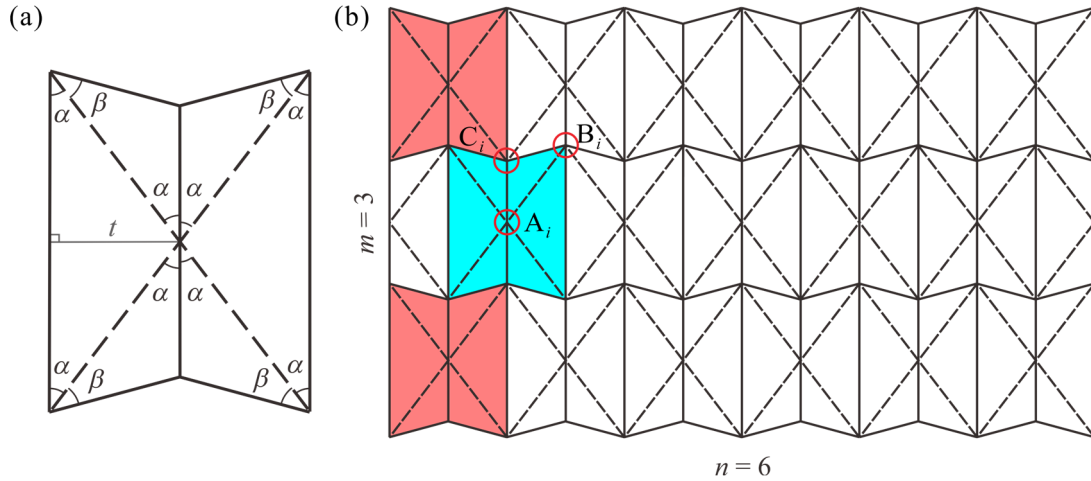


Fig. 5-1 (a) The six-crease waterbomb base, and (b) the waterbomb origami pattern formed by tessellating the waterbomb bases

According to the kinematic equivalence between rigid origami and spherical linkages, the motion around each vertex of the waterbomb origami pattern can be modelled as a spherical $6R$ linkage where adjacent rigid links (sheets) are connected by only revolute joints (creases) that meet at the vertex, then the pattern becomes a network of such linkages, which can be analyzed with the matrix method in kinematics with the D-H notation as shown in Fig. 2-. Therefore, the three vertices A_i , B_i and C_i in the generalized waterbomb tube can be considered as three spherical $6R$ linkages, A_i , B_i and C_i as shown in Fig. 5-2, where the dihedral angles between adjacent sheets connected by the crease are defined as $\varphi_{i,j}$, $\phi_{B_i,j}$ and $\phi_{C_i,j}$ ($j=1, 2, \dots, 6$), respectively.

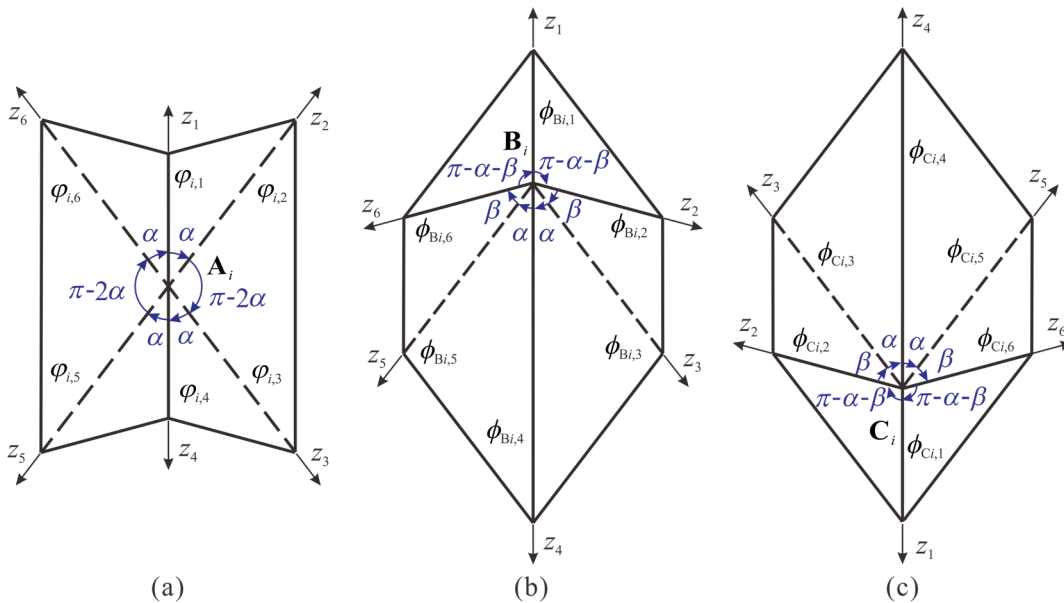


Fig. 5-2 Kinematic modelling of the generalized waterbomb tube: (a), (b) and (c), spherical linkage A_i , B_i and C_i , respectively.

Substituting the geometrical parameters of each vertex into the closure equation

$$\mathbf{Q}_{21}\mathbf{Q}_{32}\mathbf{Q}_{43}\mathbf{Q}_{54}\mathbf{Q}_{65}\mathbf{Q}_{16} = \mathbf{I}_3, \quad (5-1)$$

their kinematic relationships are obtained. Since each crease links two vertices, the dihedral angle on that crease is related to the motion of spherical linkages on both vertices, and the compatibility between neighbouring linkages \mathbf{A}_i , \mathbf{B}_i and \mathbf{C}_i yields

$$\phi_{\mathbf{B}_i,3} = \varphi_{i,6}, \quad \phi_{\mathbf{C}_i,1} = \varphi_{i,1}, \quad \phi_{\mathbf{C}_i,2} = \phi_{\mathbf{B}_i,2}, \quad \varphi_{i+1,4} = \phi_{\mathbf{B}_i,1}, \quad \varphi_{i+1,3} = \phi_{\mathbf{C}_i,3}. \quad (5-2)$$

These relationships hold for the entire waterbomb pattern. Once these compatibility conditions are satisfied, the motion of the entire pattern would be rigid.

5.3 Symmetric Rigid Folding of Zero-thickness Waterbomb

In general, a spherical $6R$ linkage is of three DOFs, the whole waterbomb pattern is therefore of multiple DOFs, but this number is reduced if only the symmetric folding is allowed. That is, each six-crease waterbomb base has identical motion behaviour. Therefore, linkage \mathbf{C}_i in Fig. 5-2 is an inverted configuration of linkage \mathbf{B}_i . In such a way, only two types of vertices, A and B, exist. Denote

$$\varphi_{i,j} = \varphi_j, \quad \phi_{\mathbf{B}_i,j} = \phi_{\mathbf{C}_i,j} = \phi_j, \quad j = 1, 2, \dots, 6. \quad (5-3)$$

Vertex A can be regarded as a spherical $6R$ linkage with the geometric parameters $\alpha_{12} = \alpha_{34} = \alpha_{45} = \alpha_{61} = \alpha$, $\alpha_{23} = \alpha_{56} = \pi - 2\alpha$, where $0 < \alpha \leq \pi/2$. Imposing the line and plane symmetry conditions, i.e., $\delta_1 = \delta_4$ and $\delta_2 = \delta_3 = \delta_5 = \delta_6$, to the closure condition of the linkage, Eq. (5-1), we can then write the closure equations as

$$\tan \frac{\delta_1}{2} = -\cos \alpha \tan \frac{\delta_2}{2}, \quad \delta_1 = \delta_4, \quad \delta_2 = \delta_3 = \delta_5 = \delta_6, \quad (5-4)$$

where δ_i is the kinematic variable of crease i in the vertex A according to the D-H notation as shown in Fig. 5-3(a).

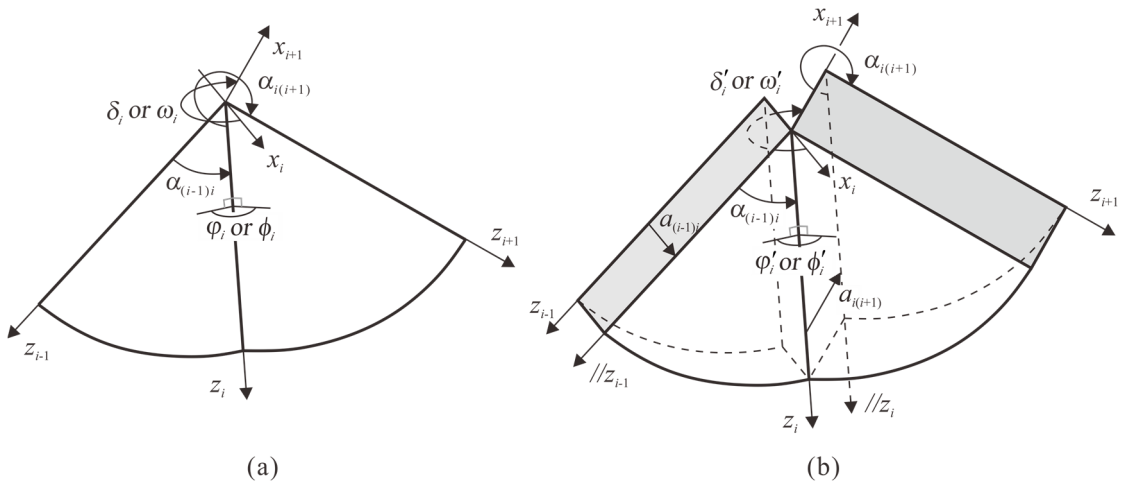


Fig. 5-3 Set-up of coordinates and kinematic parameters for (a) zero-thickness, and (b) thick-panel origami according to the D-H notation

Similarly applying the symmetry condition to vertex B, it becomes a plane-symmetric spherical $6R$ linkage with the geometric parameters $\alpha_{12} = \alpha_{61} = \pi - \alpha - \beta$, $\alpha_{23} = \alpha_{56} = \beta$, $\alpha_{34} = \alpha_{45} = \alpha$, where $0 < \beta \leq \pi/2$, and

$$\omega_5 = \omega_3, \quad \omega_6 = \omega_2, \quad (5-5a)$$

where ω_i is the kinematic variable of crease i in the vertex B according to the D-H notation as shown in Fig. 5-3(a). To ensure the compatibility of the entire pattern, the kinematic relationship between ω_1 and ω_3 of vertex B must be identical to that between δ_1 and δ_2 of vertex A. Replacing δ_1 and δ_2 in Eq. (5-4) with ω_1 and ω_3 , respectively, yields

$$\tan \frac{\omega_1}{2} = -\cos \alpha \tan \frac{\omega_3}{2}. \quad (5-5b)$$

Now considering the closure condition of the linkage at vertex B, we obtain two sets of equations. The first set is

$$\tan \frac{\omega_2}{2} = -\frac{\cos \alpha}{\cos(\alpha + \beta)} \tan \frac{\omega_3}{2}, \quad (5-6a)$$

$$\omega_4 = \omega_1, \quad (5-6b)$$

while the second one is

$$\tan \frac{\omega_2}{2} = -\frac{2 \sin \alpha \tan \frac{\omega_3}{2}}{\sin(\beta - \alpha) \tan^2 \frac{\omega_3}{2} + \sin(\alpha + \beta)}, \quad (5-7a)$$

and

$$\tan \frac{\omega_4}{2} = \frac{\left[\tan \frac{\omega_3}{2} (-2 \cos \alpha \sin^2(\beta - \alpha) \tan^4 \frac{\omega_3}{2} + 4(\sin \alpha \sin 2\beta + \cos \alpha \sin(\alpha + \beta) \sin(\beta - \alpha)) \tan^2 \frac{\omega_3}{2} + \sin(\alpha + \beta)(7 \sin \beta - \sin(2\alpha + \beta))) \right]}{\left[2 \sin(\beta - \alpha)(2 \sin(\alpha + \beta) + \sin(\beta - \alpha)) \tan^4 \frac{\omega_3}{2} + 4(\cos^2(\alpha + \beta) - \cos 2\beta) \tan^2 \frac{\omega_3}{2} - 2 \sin^2(\alpha + \beta) \right]}. \quad (5-7b)$$

Together with Eqs. (5-4) and (5-5), the entire sets of closure equations of waterbomb pattern have been obtained.

The kinematic variables, or rotations about each crease, can be replaced by the dihedral angles φ_i and ϕ_i between adjacent panels connected by the crease as shown in Fig. 5-3(a). The relationship between the kinematic variables and dihedral angles are $\delta_1 = \pi - \varphi_1$, $\delta_2 = \pi + \varphi_2$, $\delta_3 = \pi + \varphi_3$, $\delta_4 = \pi - \varphi_4$, $\delta_5 = \pi + \varphi_5$, $\delta_6 = \pi + \varphi_6$ for

vertex A and $\omega_1 = \pi - \phi_1$, $\omega_2 = \pi - \phi_2$, $\omega_3 = \pi + \phi_3$, $\omega_4 = \pi - \phi_4$, $\omega_5 = \pi + \phi_5$, $\omega_6 = \pi - \phi_6$ for vertex B. Thus the two sets of kinematic relationships of the waterbomb pattern presented by the dihedral angels become

$$\tan \frac{\phi_1}{2} = \frac{1}{\cos \alpha} \tan \frac{\phi_3}{2}, \quad (5-8a)$$

$$\tan \frac{\phi_2}{2} = \frac{\cos(\alpha + \beta)}{\cos \alpha} \tan \frac{\phi_3}{2}, \quad (5-8b)$$

$$\phi_4 = \phi_1, \quad \phi_5 = \phi_3, \quad \phi_6 = \phi_2, \quad (5-8c)$$

$$\phi_2 = \phi_3, \quad (5-8d)$$

$$\tan \frac{\phi_1}{2} = \frac{1}{\cos \alpha} \tan \frac{\phi_2}{2}, \quad \phi_1 = \phi_4, \quad \phi_2 = \phi_3 = \phi_5 = \phi_6; \quad (5-8e)$$

and

$$\tan \frac{\phi_1}{2} = \frac{1}{\cos \alpha} \tan \frac{\phi_3}{2}, \quad (5-9a)$$

$$\tan \frac{\phi_2}{2} = \frac{\sin(\alpha + \beta) \tan^2 \frac{\phi_3}{2} + \sin(\beta - \alpha)}{2 \sin \alpha \tan \frac{\phi_3}{2}}, \quad (5-9b)$$

$$\tan \frac{\phi_4}{2} = \frac{\left[\begin{array}{l} \tan \frac{\phi_3}{2} (2 \sin^2(\alpha + \beta) \tan^4 \frac{\phi_3}{2} - 4(\cos^2(\alpha + \beta) - \cos 2\beta) \tan^2 \frac{\phi_3}{2}) \\ - 2 \sin(\beta - \alpha) (2 \sin(\alpha + \beta) + \sin(\beta - \alpha)) \end{array} \right]}{\left[\begin{array}{l} \sin(\alpha + \beta) (7 \sin \beta - \sin(2\alpha + \beta)) \tan^4 \frac{\phi_3}{2} + 4(\sin \alpha \sin 2\beta \\ + \cos \alpha \sin(\alpha + \beta) \sin(\beta - \alpha)) \tan^2 \frac{\phi_3}{2} - 2 \cos \alpha \sin^2(\beta - \alpha) \end{array} \right]}, \quad (5-9c)$$

$$\phi_5 = \phi_3, \quad \phi_6 = \phi_2, \quad (5-9d)$$

$$\phi_2 = \phi_3, \quad (5-9e)$$

$$\tan \frac{\phi_1}{2} = \frac{1}{\cos \alpha} \tan \frac{\phi_2}{2}, \quad \phi_1 = \phi_4, \quad \phi_2 = \phi_3 = \phi_5 = \phi_6. \quad (5-9f)$$

Considering a pattern with $\alpha = 2\pi/9$, $\beta = 2\pi/9$, and taking ϕ_1 as an input, the variations of other dihedral angles at vertex B with respect to ϕ_1 are plotted in Fig. 5-4(a). There are two paths with the same starting point (π, π) and ending point $(0, 0)$: *path I* based on Eqs. (5-8a) – (5-8e) and *path II* on Eqs. (5-9a) – (5-9f). It indicates that vertex B can be folded compactly along two different paths. Since Eq. (5-8a) and Eq. (5-9a) are identical, the two paths coincide in the ϕ_3 or ϕ_5 vs. ϕ_1 curve in Fig. 5-4(a). Yet for vertex A, with $\phi_1 = \phi_4 = \phi_1$, there is only one path, see Fig. 5-

4(b). Therefore, in general the patterns with a large number of vertices A and B will fold in two different manners, from i, ii, iii, iv to v, or from i, viii, vii, vi to v, as demonstrated in Fig. 5-4(c).

There are a few special cases of the waterbomb pattern which are mostly interesting. First, when $\alpha + \beta = \pi/2$, creases along z_2 and z_6 at vertex B shown in Fig. 5-2(b) become collinear. As a result, they fold together like a single crease with $\phi_1 = \pi$. When $\phi_1 \neq \pi$, Eq. (5-8) becomes a straight line with $\phi_2 = 0$. Therefore, *Path I* breaks down into two straight lines. A particular case with $\alpha = \beta = \pi/4$ is shown in Fig. 5-5. At the first folding stage, ϕ_2 (and ϕ_6) starts from π and finishes at 0 from i, xi, x and ix, while ϕ_1, ϕ_3, ϕ_4 , and ϕ_5 remain to be π , then ϕ_2 (and ϕ_6) is kept at constant 0 and ϕ_1, ϕ_3, ϕ_4 , and ϕ_5 changes from π to 0 along ix, viii, vii, vi and v. Both reach the compactly folded configuration. At the latter stage, vertex B behaves like a spherical 4R linkage because ϕ_2 and ϕ_6 are frozen. The movement around vertex B will drive vertex A to move accordingly.

Second, Eqs. (5-8) or (5-9) could give negative dihedral angles, which indicates blockage occurring during folding, because physically the dihedral angles cannot be less than zero. By analysing Eq. (5-8b), it can be found that for *path I* when $\alpha + \beta > \pi/2$, ϕ_2 is always negative except at points (0, 0) and (π, π) . So a blockage is always there. And from Eq. (5-9c), it can be found that on *path II* when $\alpha \neq \beta$, a blockage will occur when

$$\frac{1}{\cos \alpha} \sqrt{\frac{-2 \left(\begin{matrix} \cos \alpha \sin(\alpha + \beta) \sin(\beta) \\ -\alpha + \sin \alpha \sin 2\beta \end{matrix} \right) + \sqrt{4(\sin \alpha \sin 2\beta + \cos \alpha \sin(\alpha + \beta) \sin(\beta - \alpha))^2 + 2 \cos \alpha \sin^2(\beta - \alpha) \sin(\alpha + \beta)(7 \sin \beta - \sin(2\alpha + \beta))}}{\sin(\alpha + \beta)(7 \sin \beta - \sin(2\alpha + \beta))}} < \tan \frac{\phi_1}{2} < \frac{\sqrt{\cos^2(\alpha + \beta) - \cos 2\beta} + \sqrt{(\cos^2(\alpha + \beta) - \cos 2\beta)^2 + (2 \sin(\alpha + \beta) \sin(\beta - \alpha) \sin(\beta - \alpha) \sin^2(\alpha + \beta))}}{\cos \alpha \sin(\alpha + \beta)} \quad (5-10)$$

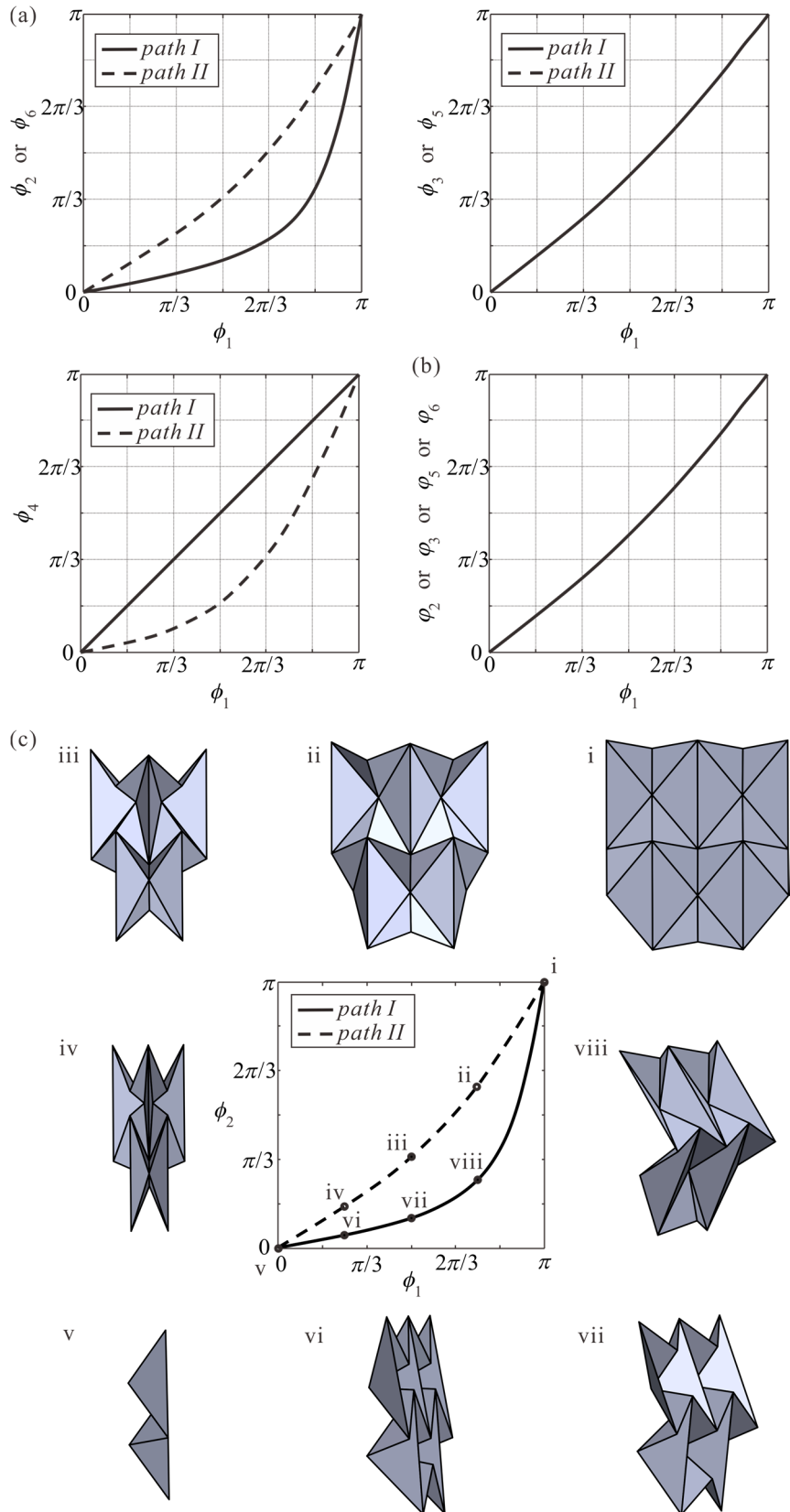


Fig. 5-4 Kinematic behaviour of the waterbomb origami pattern with $\alpha = 2\pi/9$, $\beta = 2\pi/9$. Kinematic relationships of vertices (a) B, and (b) A; and (c) two folding paths with configurations i-viii.

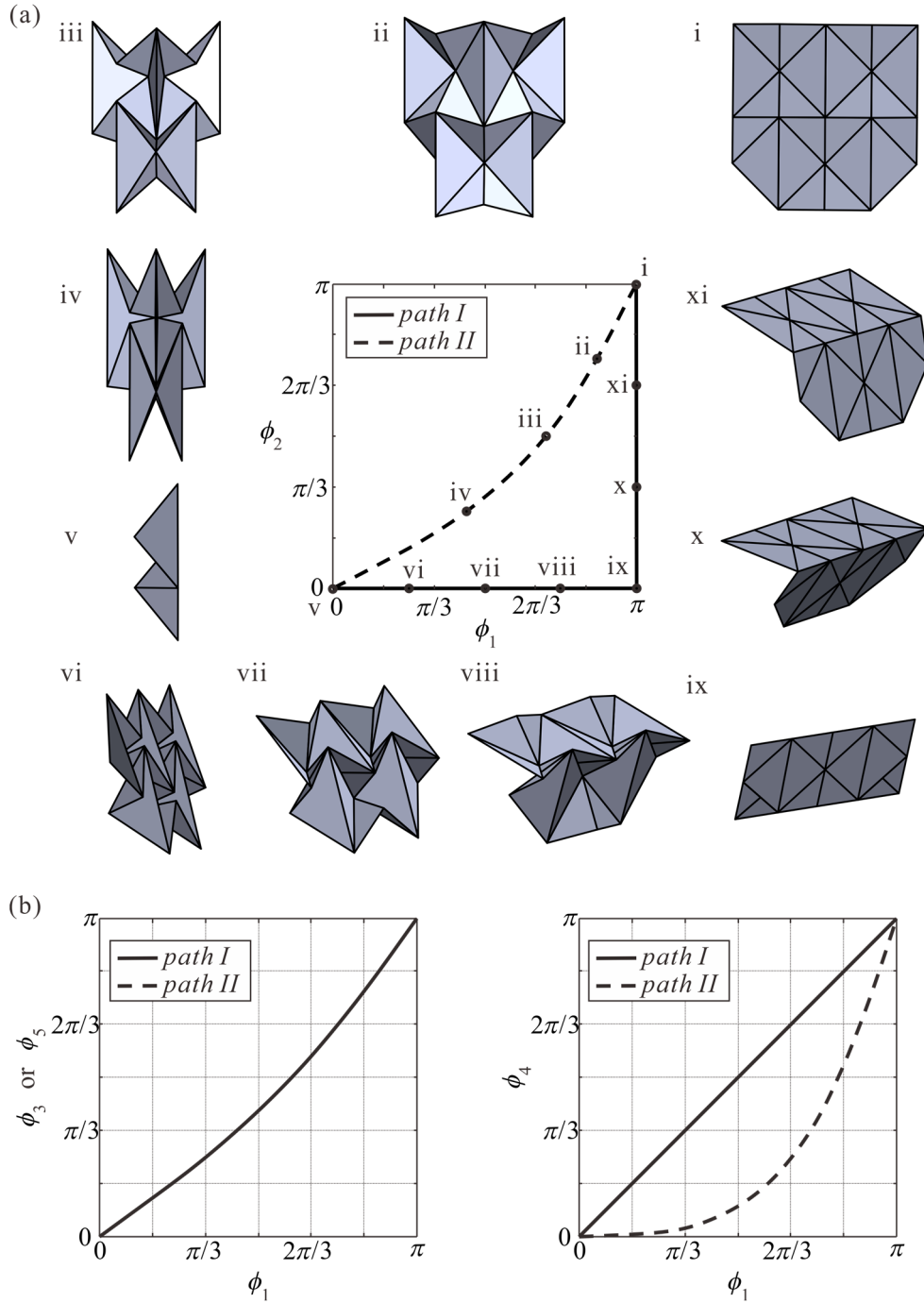


Fig. 5-5 Two-stage motion of *path I* with $\alpha = \pi/4$, $\beta = \pi/4$. (a) Folding paths with configurations i-xi, and (b) kinematic relationships of vertex B.

For example, when $\alpha = 7\pi/36$, $\beta = \pi/4$, the kinematic curve between ϕ_4 and ϕ_1 is shown in Fig. 5-6(a) and the folding sequences are demonstrated in Fig. 5-6(b). Along *path I*, the pattern can be folded from a sheet at i to fully folded configuration at vii, whereas along *path II*, the folding process terminates at iii. The framed configurations are physically impossible due to blockage because these

configurations correspond to cases where ϕ_4 becomes negative. Even if the penetrations were allowed, the folding along *path II* would end up in a fully folded configuration at vi that differs from that at vii along *path I*.

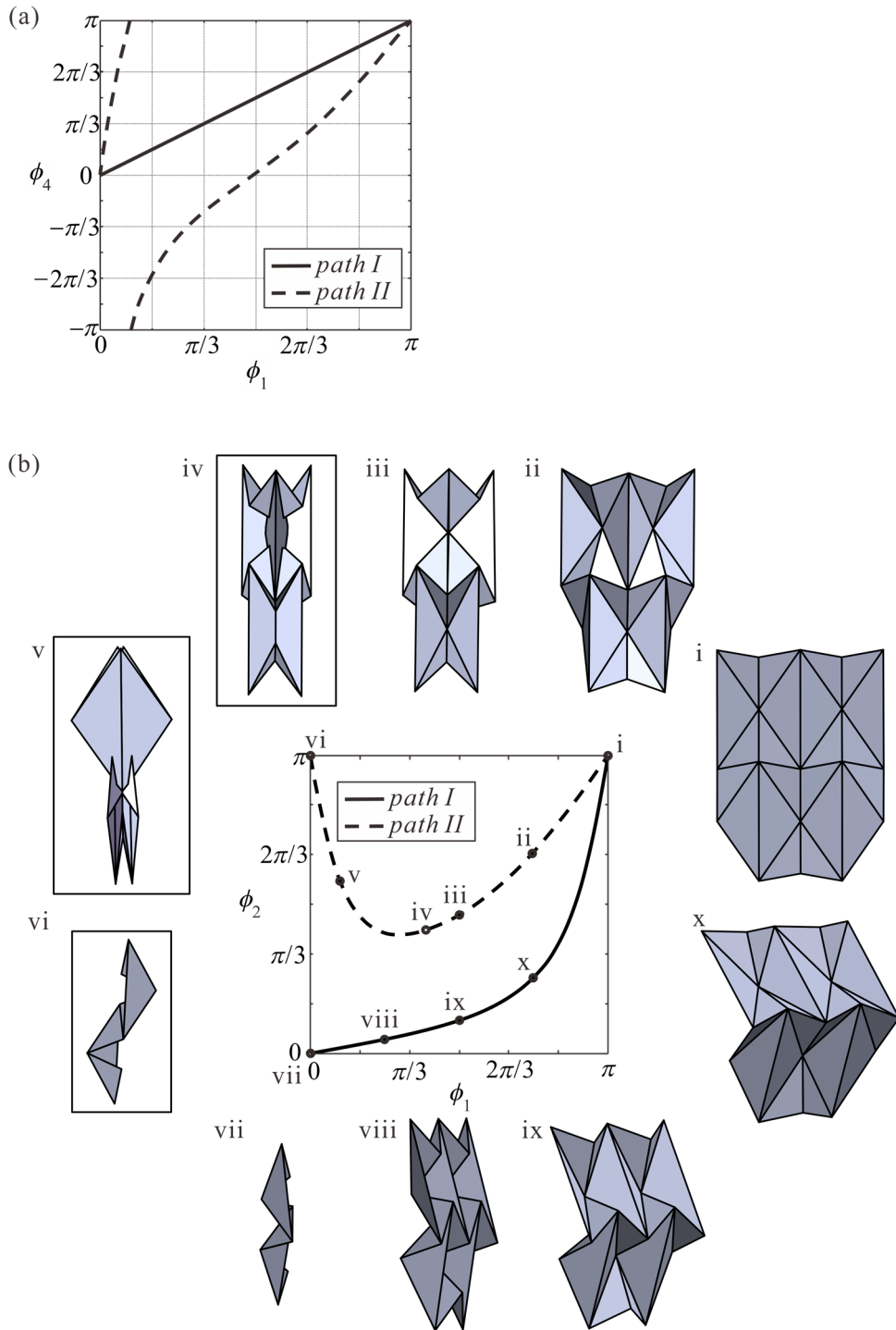


Fig. 5-6 Blockage of waterbomb origami pattern with $\alpha = 7\pi/36$, $\beta = \pi/4$. (a) Kinematic curve between ϕ_4 and ϕ_1 of vertex B, and (b) folding manners in which the framed configurations are with physical blockage.

The physical blockage can also occur when $\alpha + \beta = \pi/2$ but $\alpha \neq \beta$. Figure 5-7 shows a two-stage motion on *path I* and blockage on *path II* for a pattern with $\alpha = \pi/6$ and $\beta = \pi/3$.

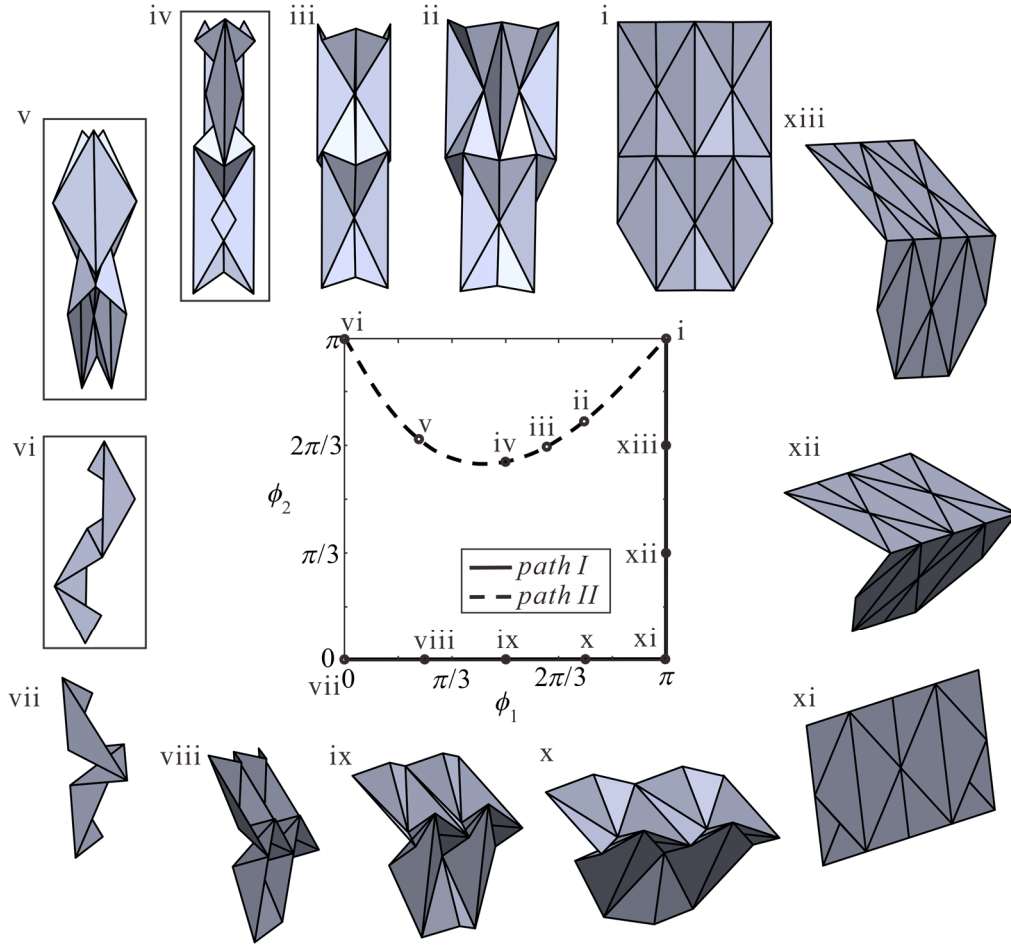


Fig. 5-7 Two-stage motion and blockage during the folding manners of waterbomb origami pattern with $\alpha = \pi/6$, $\beta = \pi/3$ in which the framed configurations are with physical blockage.

Based on the above analysis, the behaviour of the waterbomb tessellation can be summarized as follows.

- When $\alpha + \beta < \pi/2$ and $\alpha = \beta$, there are two smooth folding paths with neither two-stage motion nor blockage.
- When $\alpha + \beta < \pi/2$ and $\alpha \neq \beta$, *path II* is blocked and *path I* is smooth.
- When $\alpha + \beta = \pi/2$ and $\alpha = \beta$, *path I* is in two-stage motion while *path II* is smooth;
- When $\alpha + \beta = \pi/2$ and $\alpha \neq \beta$, both two-stage motion on *path I* and blockage on *path II* happen.
- When $\alpha + \beta > \pi/2$ and $\alpha = \beta$, only *path II* for vertex B is smooth, but

vertex A is blocked. Thus the whole pattern is blocked from compact folding.

(f) When $\alpha + \beta > \pi/2$ but $\alpha \neq \beta$, both paths are blocked.

Among them, only cases (a) – (c) can have one or two smooth folding paths.

5.4 Folding Thick Panels with the Waterbomb Pattern

The waterbomb tessellation can also be used to fold panels with non-zero thickness. This is done by mapping the same pattern in Fig. 5- onto a thick panel while placing the fold lines either on top or bottom surfaces of the panel. Now at vertices A and B, there will still be six fold lines in places of creases, but these fold lines no longer converge to a vertex. In other words, dissimilar to zero-thickness sheet, the distances between the adjacent fold lines are no longer zero. The set-up of coordinates and kinematic parameters for thick-panel origami according to the D-H notation is presented in Fig. 5-3(b). In terms of kinematic model, the spherical $6R$ linkage in section 5.3 is now replaced by spatial $6R$ linkages. Among all possible spatial $6R$ linkages, the plane-symmetric Bricard linkage, is the most suitable one [29]. Let us select two Bricard linkages for A and B, respectively, Fig. 5-8(a) and Fig. 5-8(b), with their link lengths being the panel thicknesses. As the linkages are overconstrained, the geometric conditions of the linkage at vertex A are

$$a_{12}^A = a_{61}^A = a_{34}^A = a_{45}^A = (2 + \mu)a', \quad a_{23}^A = a_{56}^A = 0, \quad (5-11a)$$

$$\alpha_{12}^A = 2\pi - \alpha, \quad \alpha_{61}^A = \alpha, \quad \alpha_{23}^A = \pi - 2\alpha, \quad \alpha_{56}^A = \pi + 2\alpha, \quad \alpha_{34}^A = \alpha, \quad \alpha_{45}^A = 2\pi - \alpha, \quad (5-11b)$$

$$R_i^A = 0 \quad (i = 1, 2, 3, 4, 5, 6), \quad (5-11c)$$

and those at vertex B are

$$a_{12}^B = a_{61}^B = (1 + \mu)a', \quad a_{23}^B = a_{56}^B = a', \quad a_{34}^B = a_{45}^B = \mu a', \quad (5-12a)$$

$$\alpha_{12}^B = \pi - \alpha - \beta, \quad \alpha_{61}^B = \pi + \alpha + \beta, \quad \alpha_{23}^B = \beta, \quad \alpha_{56}^B = 2\pi - \beta, \quad \alpha_{34}^B = 2\pi - \alpha, \quad \alpha_{45}^B = \alpha, \quad (5-12b)$$

$$R_i^B = 0 \quad (i = 1, 2, 3, 4, 5, 6). \quad (5-12c)$$

α and β are the same as the sector angles of the origami pattern in Fig. 5-2(a) and Fig. 5-2(b), α_{ij}^A and α_{ij}^B are expressed using the D-H notation, while a' is the thickness of link 23 and μ is the proportion between the thickness of link 34 and link 23 in the vertex B of the thick-panel waterbomb pattern where $a' \neq 0$ and $\mu \neq 0$.

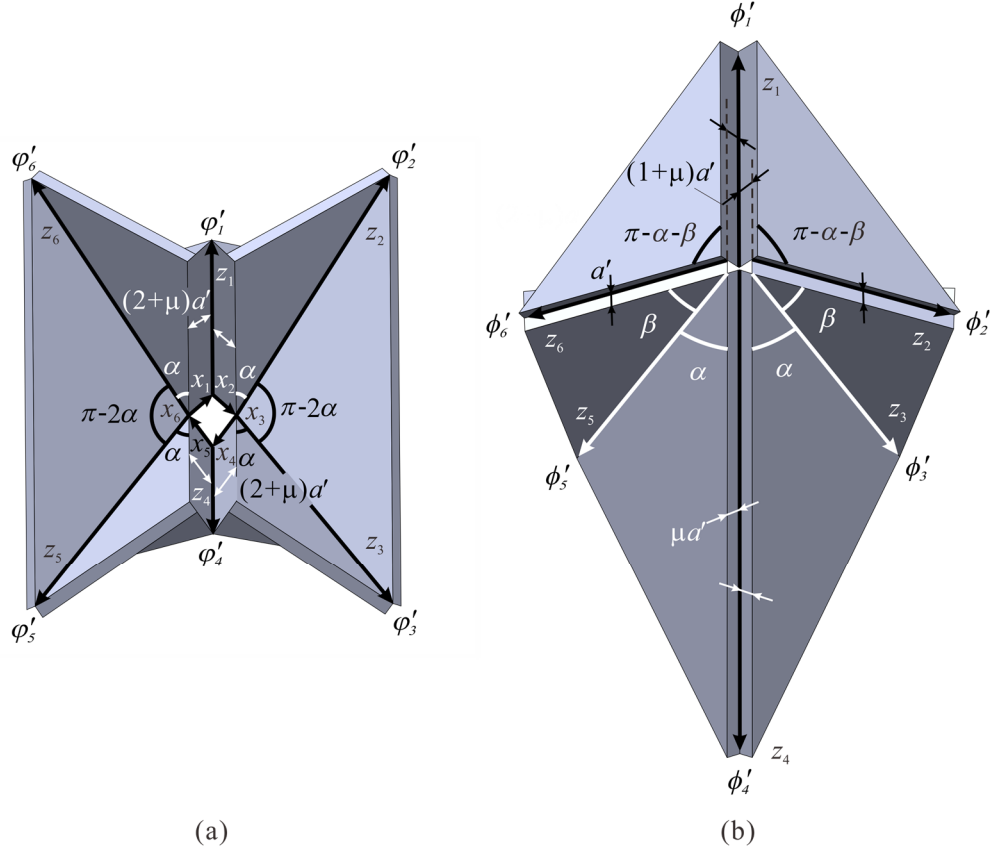


Fig. 5-8 Fold lines around the vertices (a) A, and (b) B in thick panels

Applying the geometric conditions of these linkages to Eq. (4-6a) in last section, $A \neq 0$, subsequently closure equations of the plane-symmetric Bricard linkage are Eq. (4-3), (4-15), (4-16) and (4-17). For vertex A, two set of closure equations can be obtained, which are

$$\tan \frac{\delta'_1}{2} = -\frac{1}{\cos \alpha} \tan \frac{\delta'_2}{2}, \quad \delta'_3 = \delta'_2 + \pi, \quad \delta'_4 = \delta'_1, \quad \delta'_5 = \delta'_3, \quad \delta'_6 = \delta'_2, \quad (5-13)$$

and

$$\tan \frac{\delta'_1}{2} = \frac{2 \cos \alpha \tan \frac{\delta'_2}{2}}{\tan^2 \frac{\delta'_2}{2} - \cos 2\alpha}, \quad \delta'_3 = \pi - \delta'_2, \quad \delta'_4 = -\delta'_1, \quad \delta'_5 = \delta'_3, \quad \delta'_6 = \delta'_2, \quad (5-14)$$

respectively, where δ'_i is the kinematic variable of crease i in the vertex A of the thick-panel origami according to the D-H notation as shown in Fig. 5-3(b). The relationship between the kinematic variables δ'_i and dihedral angles ϕ'_i at vertex A are $\delta'_1 = 2\pi - \phi'_1$, $\delta'_2 = \phi'_2$, $\delta'_3 = \pi + \phi'_3$, $\delta'_4 = 2\pi - \phi'_4$, $\delta'_5 = \pi + \phi'_5$ and $\delta'_6 = \phi'_6$. By conversion of the kinematic variables to the dihedral angles, the two sets of closure equations can be respectively rewritten as

$$\tan \frac{\phi'_1}{2} = \frac{1}{\cos \alpha} \tan \frac{\phi'_2}{2}, \quad (5-15a)$$

$$\phi'_4 = \phi'_1, \quad \phi'_2 = \phi'_3 = \phi'_5 = \phi'_6, \quad (5-15b)$$

and

$$\tan \frac{\phi'_1}{2} = \frac{2 \cos \alpha \tan \frac{\phi'_2}{2}}{-\tan^2 \frac{\phi'_2}{2} + \cos 2\alpha}, \quad (5-16a)$$

$$\phi'_3 = -\phi'_2, \quad \phi'_4 = -\phi'_1, \quad \phi'_5 = \phi'_3, \quad \phi'_6 = \phi'_2 \quad (5-16b)$$

Similarly, we also have two sets of closure equations at vertex B, which are

$$\tan \frac{\omega'_1}{2} = -\frac{1}{\cos \alpha} \tan \frac{\omega'_3}{2}, \quad (5-17a)$$

$$\tan \frac{\omega'_2}{2} = \frac{\cos \alpha}{\cos(\alpha + \beta)} / \tan \frac{\omega'_3}{2}, \quad (5-17b)$$

$$\omega'_4 = \omega'_1, \quad \omega'_5 = \omega'_3, \quad \omega'_6 = \omega'_2, \quad (5-17c)$$

and

$$\tan \frac{\omega'_1}{2} = \frac{-\tan \frac{\omega'_3}{2} (\mu \sin^2(\alpha + \beta) \tan^2 \frac{\omega'_3}{2} + (\mu + 1)(\mu \sin^2 \beta + \sin^2 \alpha))}{\sin(\alpha + \beta)(\mu^2 \sin \beta + \cos(\alpha + \beta) \sin \alpha) \tan^2 \frac{\omega'_3}{2} + (\mu + 1)^2 \sin \alpha \sin \beta \cos \beta}, \quad (5-18a)$$

$$\tan \frac{\omega'_2}{2} = \frac{(\mu + 1) \sin \alpha}{\mu \sin(\alpha + \beta)} / \tan \frac{\omega'_3}{2}, \quad (5-18b)$$

$$\tan \frac{\omega'_4}{2} = \frac{\tan \frac{\omega'_3}{2} (4(\mu + 1) \sin \alpha ((\mu + 1) \sin^2 \beta + \sin^2(\alpha + \beta)) - 4\mu \sin \alpha \sin^2(\alpha + \beta) \tan^2 \frac{\omega'_3}{2})}{\left[2(\mu + 1)^2 \sin^2 \alpha \sin 2\beta + (\cos(3\alpha + \beta) - 2(1 + \mu)^2 \cos(\alpha + \beta)) \right] + (1 + 4\mu + 2\mu^2) \cos(\alpha - \beta) \sin(\alpha + \beta) \tan^2 \frac{\omega'_3}{2}} \quad (5-18c)$$

$$\omega'_5 = \omega'_3, \quad \omega'_6 = \omega'_2, \quad (5-18d)$$

where ω'_i is the kinematic variable of crease i in the vertex B of the thick-panel origami according to the D-H notation as shown in Fig. 5-3(b). The above two sets of closure equations can be written in terms of dihedral angles. Noting that the relationship between the kinematic variables ω'_i and dihedral angles ϕ'_i at vertex B are $\omega'_1 = 2\pi - \phi'_1$, $\omega'_2 = \pi - \phi'_2$, $\omega'_3 = \phi'_3$, $\omega'_4 = 2\pi - \phi'_4$, $\omega'_5 = \phi'_5$ and $\omega'_6 = \pi - \phi'_6$, the two sets of closure equations now become

$$\tan \frac{\phi'_1}{2} = \frac{1}{\cos \alpha} \tan \frac{\phi'_3}{2}, \quad (5-19a)$$

$$\tan \frac{\phi'_2}{2} = \frac{\cos(\alpha + \beta)}{\cos \alpha} \tan \frac{\phi'_3}{2}, \quad (5-19b)$$

$$\phi'_4 = \phi'_1, \quad \phi'_5 = \phi'_3, \quad \phi'_6 = \phi'_2, \quad (5-19c)$$

and

$$\tan \frac{\phi'_1}{2} = \frac{\tan \frac{\phi'_3}{2} (\mu \sin^2(\alpha + \beta) \tan^2 \frac{\phi'_3}{2} + (\mu + 1)(\mu \sin^2 \beta + \sin^2 \alpha))}{\sin(\alpha + \beta)(\mu^2 \sin \beta + \cos(\alpha + \beta) \sin \alpha) \tan^2 \frac{\phi'_3}{2} + (\mu + 1)^2 \sin \alpha \sin \beta \cos \beta}, \quad (5-20a)$$

$$\tan \frac{\phi'_2}{2} = \frac{\mu \sin(\alpha + \beta)}{(\mu + 1) \sin \alpha} \tan \frac{\phi'_3}{2}, \quad (5-20b)$$

$$\tan \frac{\phi'_4}{2} = \frac{\tan \frac{\phi'_3}{2} \left(4\mu \sin \alpha \sin^2(\alpha + \beta) \tan^2 \frac{\phi'_3}{2} - 4(\mu + 1) \sin \alpha ((\mu + 1) \sin^2 \beta - \sin^2(\alpha + \beta)) \right)}{2(\mu + 1)^2 \sin^2 \alpha \sin 2\beta + \left(\cos(3\alpha + \beta) - 2(1 + \mu)^2 \cos(\alpha + \beta) \right) \sin(\alpha + \beta) \tan^2 \frac{\phi'_3}{2} + (1 + 4\mu + 2\mu^2) \cos(\alpha - \beta)} \quad (5-20c)$$

$$\phi'_5 = \phi'_3, \quad \phi'_6 = \phi'_2. \quad (5-20d)$$

So far, two complete sets of closure equations have been obtained. It can be noted from all closure equations that the motions of the linkages retain the plane symmetry. Additional compatibility conditions between the vertices A and B need to be added, which are

$$\phi'_1 = \phi'_1, \quad \phi'_3 = \phi'_2. \quad (5-21)$$

We shall now discuss the respective motion paths provided by two sets of closure equations.

- The first set of closure equations, Eq. (5-15), at vertex A and the first set of closure equations, Eq. (5-19) at vertex B

Because Eqs. (5-15a) and (5-19a) are identical, the compatibility between vertex A and B, Eq. (5-21), is satisfied automatically. Therefore, there is always a smooth folding path for the thick-panel origami for any $\mu \neq 0$, see Fig. 5-9(a-c), in which μ is randomly selected as 0.5. By comparing Eqs. (5-15) and (5-19) for the thick panel with Eq. (5-8) for the zero-thickness sheet, we can conclude that the thick-panel origami and the *path I* of the original waterbomb origami pattern are kinematically identical, as demonstrated by the folding sequence of the physical models in Fig. 5-10. The motions of both structures are line- and plane-symmetric.

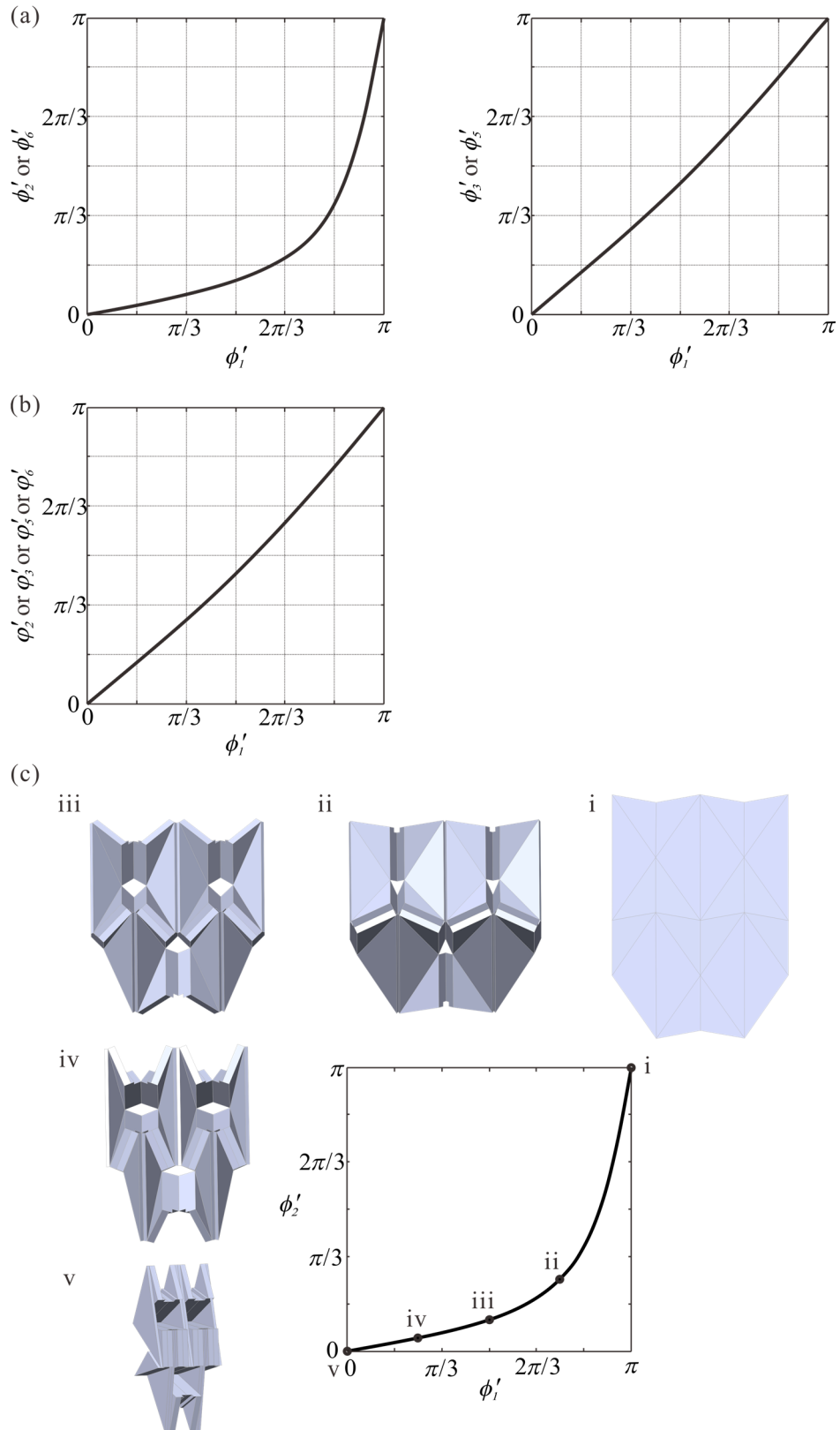


Fig. 5-9 The kinematic paths of thick-panel waterbomb when $\alpha = 7\pi/36$, $\beta = \pi/4$, $\mu = 0.5$. Kinematic relationships at vertices (a) A, and (b) B with ϕ'_1 taken as input, where vertex B works as a plane-symmetric Bricard linkage while vertex A works as a line- and plane-symmetric Bricard linkage; (c) folding path of the Solidworks model of thick-panel waterbomb.

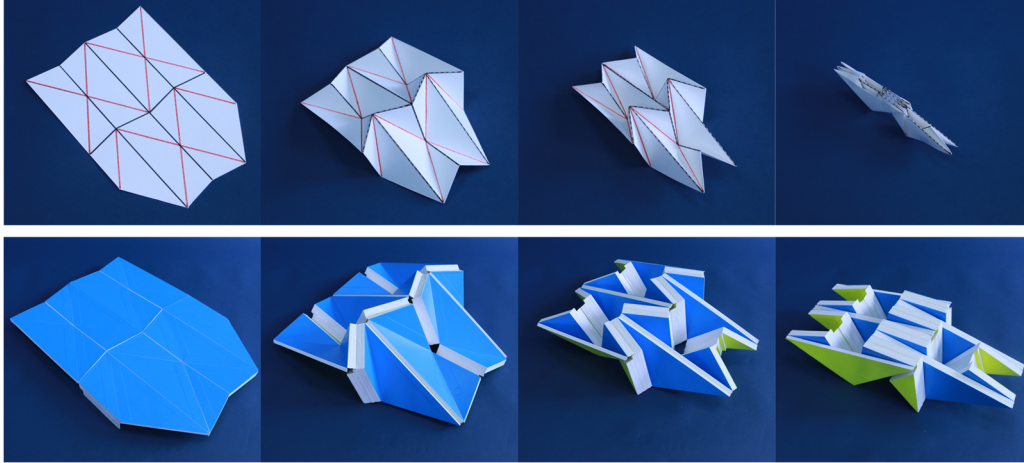


Fig. 5-10 Deployable sequences of physical models of the waterbomb pattern with zero-thickness sheets and thick panels when $\alpha = 7\pi/36$, $\beta = \pi/4$, $\mu = 0.5$.

Moreover, when $\alpha + \beta = \pi/2$, *path I* becomes a two-stage motion, where ϕ'_2 and ϕ'_6 changing from π to 0 while ϕ'_1 , ϕ'_3 , ϕ'_4 , and ϕ'_5 kept to π , followed by the process that ϕ'_1 , ϕ'_3 , ϕ'_4 , and ϕ'_5 move as a spatial 4R linkage. This linkage is actually a Bennett linkage. And it eventually reaches the compact folding position. However, blockage could be occurred during the motion due to the panel thickness, which makes the structure cannot be fully folded, see Fig. 5-11, in which μ is randomly selected as 0.7.

- The first set of closure equations, Eq. (5-15), at vertex A and the second set of closure equations, Eq. (5-20) at vertex B

Consider Eqs. (5-15a) and (5-20a). Under the compatibility condition given by Eq. (5-21), there must be

$$\mu = \frac{\cos(\alpha + \beta) \sin \alpha}{\sin \beta}. \quad (5-22a)$$

Additionally when $\alpha = \beta$, another solution exists, which is

$$\mu = 1. \quad (5-22b)$$

Under the first solution given in Eq. (5-22a), Eq. (5-20) effectively coincides with Eq. (5-19), and thus there is only one set of closure equations for vertex B. Only one folding path exists as shown in Fig. 5-12 for the case where $\alpha = 7\pi/36$, $\beta = \pi/4$ and $\mu = 0.14$. Note that this path matches that shown in Fig. 5-9(c) despite that in the latter, μ is randomly selected as 0.5. The motion behaviour of the thick-panel waterbomb remains the same as the zero-thickness origami in *path I*, and thus it is named as *path I* for thick panel origami. Moreover, when $\alpha + \beta = \pi/2$, $\mu = 0$ from

Eq. (5-22a). So it will not be considered.

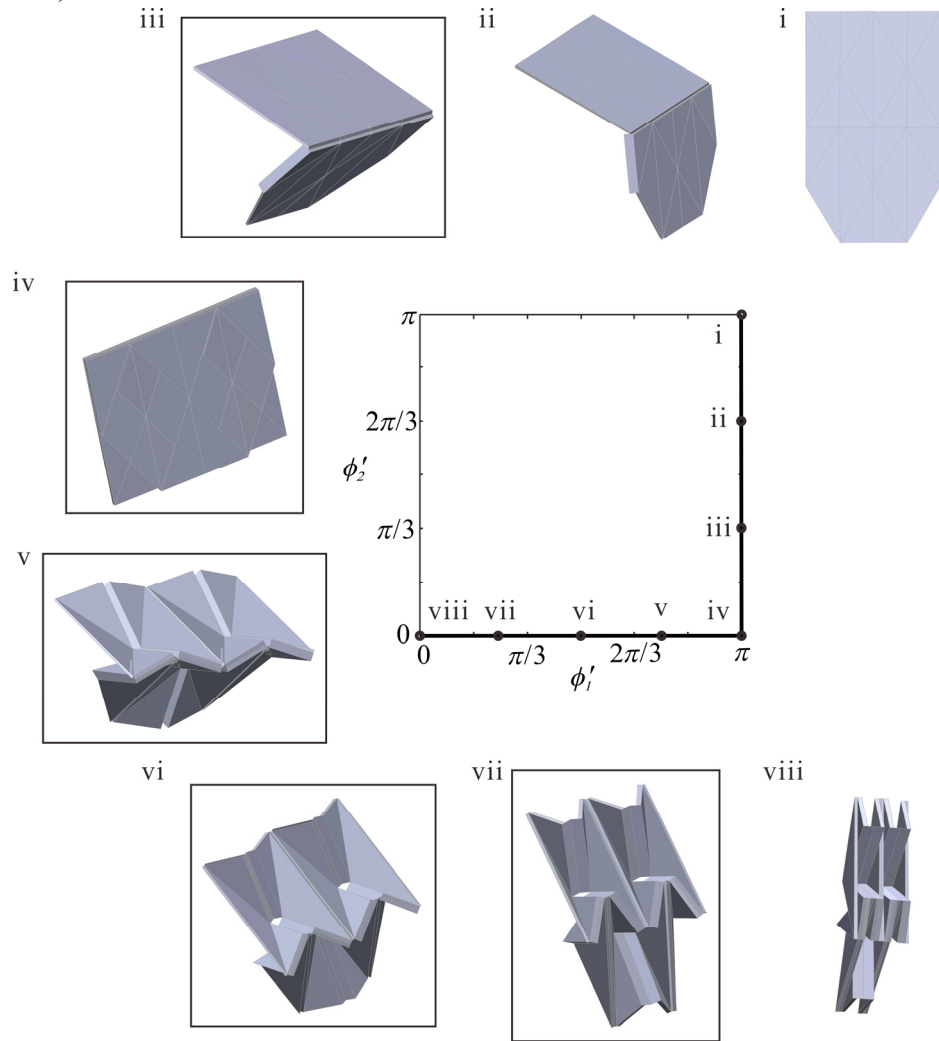


Fig. 5-11 Folding path of thick-panel waterbomb pattern with $\alpha = \pi/6$, $\beta = \pi/3$, $\mu = 0.7$, in which the framed configurations are with physical blockage.

Under the second solution given by Eq. (5-22b), $\mu = 1$, Eq. (5-19) and Eq. (5-20) are different. In other words, together with Eq. (5-15), there are two sets of closure equations for the thick-panel origami with $\mu = 1$ that result in two folding paths. The first, based on Eqs. (5-15) and (5-19), has been discussed earlier. The second, based on Eqs. (5-15) and (5-20), are actually identical to Eq. (5-9) of the zero-thickness sheet. This shows that the corresponding folding path is kinematically identical to the *path II* of the waterbomb origami pattern of the zero-thickness sheet, and thus it is named as *path II* of the thick panel origami. One of such example is shown in Fig. 5-13.

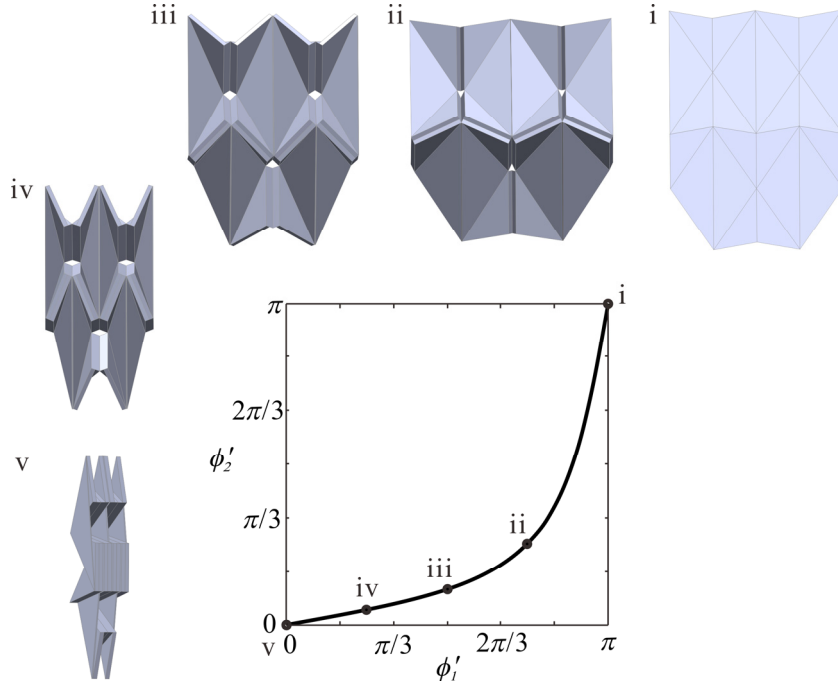


Fig. 5-12 Folding path of thick-panel waterbomb pattern with $\alpha = 7\pi/36$, $\beta = \pi/4$ and $\mu = \cos(\alpha + \beta) \cdot \sin \alpha / \sin \beta = 0.14$.

In thick-panel origami, there is also blockage because of collision of panels during the folding process. Generally along *path I* of vertex B, the blockage would appear when one of the dihedral angles becomes negative. The condition without blockage is $\phi_2' > 0$. Considering Eq. (5-19b) leads to $\alpha + \beta < \pi/2$, which is the same conclusion as zero-thickness origami pattern summarized in section 5.3. And to avoid the interference at vertex A during the folding, $0 < \alpha \leq \pi/4$ must be satisfied.

- The second set of closure equations, Eq. (5-16), at vertex A

The other set of closure equations given by Eq. (5-16) at vertex A signify that in the thick-panel case, there exists a folding path that violates the line symmetry. However, this path is practically always blocked since ϕ_3' and ϕ_2' , ϕ_4' and ϕ_1' always have opposite signs as indicated by Eq. (5-16b).

Therefore, the behaviour of the general thick-panel waterbomb can be summarized as follows.

- For any $\mu \neq 0$, when $\alpha + \beta < \pi/2$, there is only one smooth folding path: *path I*.
- For any $\mu \neq 0$, when $\alpha + \beta = \pi/2$, there is one two-stage folding path, *path I*, with blockage.
- For any $\mu \neq 0$, when $\alpha + \beta > \pi/2$, there is one blocked folding path.

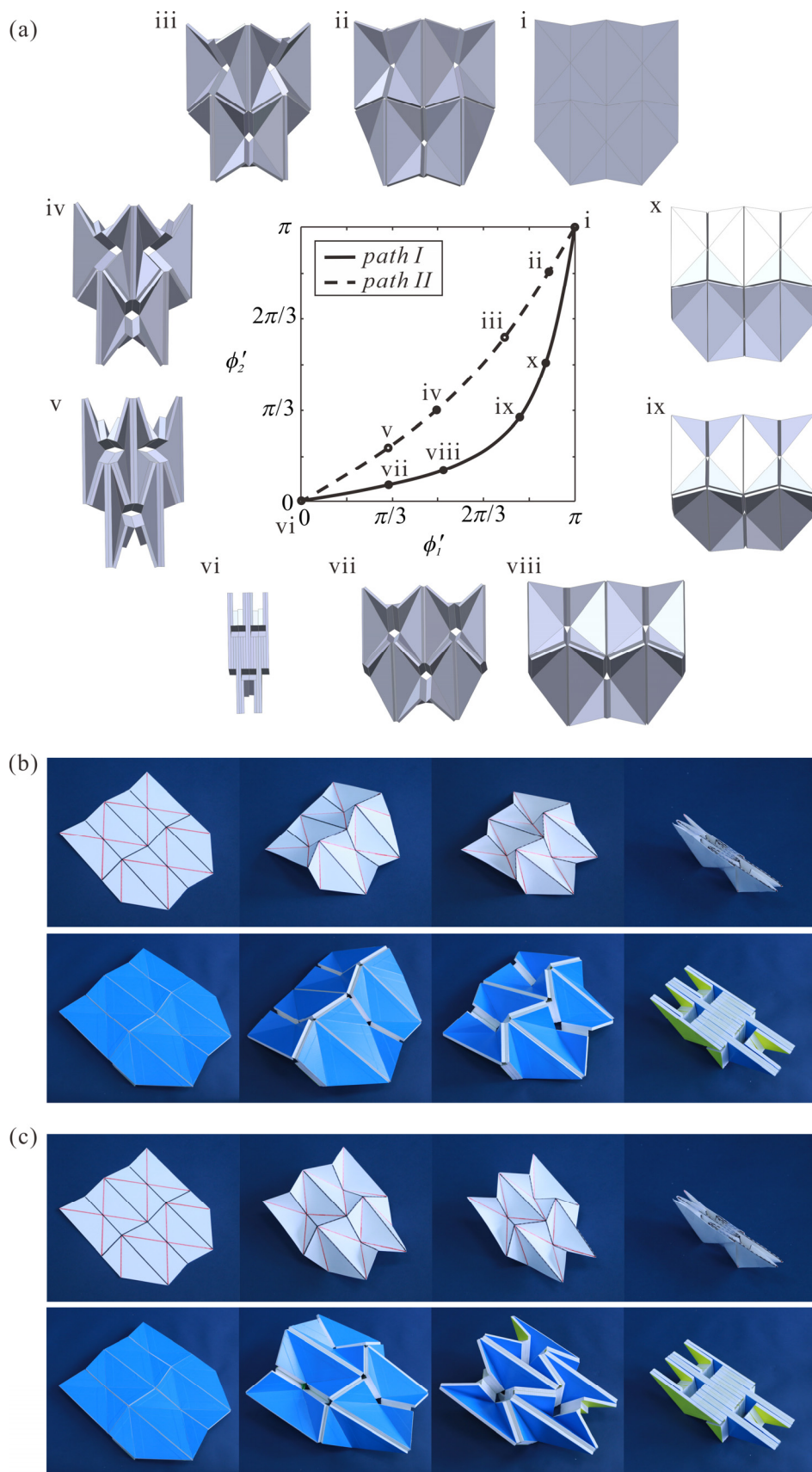


Fig. 5-13 Folding sequence for patterns with $\alpha = \beta = 2\pi/9$ and $\mu = 1$. (a) Two folding paths exist; physical models of zero-thickness sheet (top) and thick panels that fold along (b) *path I*, and (c) *path II*.

- (d) For $\mu = 1$, when $\alpha + \beta < \pi / 2$, $\alpha = \beta$, there are two smooth folding paths, kinematically equivalent to *paths I* and *II* in the zero-thickness origami.
- (e) For $\mu = 1$, when $\alpha = \beta = \pi / 4$, *path I* is in two-stage motion and blocked, but *path II* can achieve smooth folding.

Here, *paths I* and *II* cannot be switch from one to another once the motions are underway. The choice of folding paths has to be made at the start and end configurations. The detailed comparison on the kinematic behaviour of the general waterbomb tessellation of zero-thickness sheets and thick panels for different design parameters is given in Table 5-1.

Table 5-1 Kinematic behaviour of the general waterbomb tessellation of zero-thickness sheets and thick panels

geometric conditions	folding paths	the waterbomb tessellation of zero-thickness sheets	the waterbomb tessellation of thick panels
$\alpha + \beta < \frac{\pi}{2}$	$\alpha = \beta$ <i>path I</i>	smooth	smooth
	<i>path II</i>	smooth	exists only when $\mu = 1$ and the path is smooth
	$\alpha \neq \beta$ <i>path I</i>	smooth	smooth
	<i>path II</i>	blocked	non-existent
$\alpha + \beta = \frac{\pi}{2}$	$\alpha = \beta$ <i>path I</i>	two-stage motion	two-stage motion and blocked
	<i>path II</i>	smooth	exists only when $\mu = 1$ and the path is smooth
	$\alpha \neq \beta$ <i>path I</i>	two-stage motion	two-stage motion and blocked
	<i>path II</i>	blocked	non-existent
$\alpha + \beta > \frac{\pi}{2}$	$\alpha = \beta$ <i>path I</i>	blocked	blocked
	<i>path II</i>	blocked while the path for vertex B is smooth	exists only when $\mu = 1$ but the path is blocked
	$\alpha \neq \beta$ <i>path I</i>	blocked	blocked
	<i>path II</i>	blocked	non-existent

It can be seen from Table 5-1 that there is always a bifurcation behaviour with two different folding paths for zero-thickness waterbomb origami. However, the bifurcation can be eliminated in the thick-panel form by properly choosing thickness, as the thickness provides additional geometric constraints.

5.5 Conclusions and Discussion

In this chapter, the rigid origami of the waterbomb tessellation of both zero-thickness sheet and thick panels have been analyzed under the symmetric motion condition. By introducing the plane-symmetric Bricard linkages to replace the spherical $6R$ linkages in the origami pattern, the thick-panel waterbomb structure has been

successfully formed. The rigorous enforcement of compatibility conditions ensures the mobility and flat foldability of the thick panel. It has been proved that the thick-panel origami and that of the zero-thickness sheet are kinematically equivalent.

Despite the fact that the thick-panel origami is born from an existing origami of zero-thickness sheet, it has a number of advantages over its parent. First, kinematically the thick-panel origami structure is a mobile assembly of overconstrained Bricard linkages with only one DOF, and thus no additional constraints are required to keep its motion symmetrical. This could be a great benefit for real engineering applications as its control system could become much more simple and reliable. Second, in general, the origami of waterbomb tessellation for zero-thickness sheet has kinematic singularity when it is flat and fully compact. However, for thick-panel origami, the singularity only appears when a very specific thickness is chosen. A suitable selection of the thickness of the panels make the latter possible to achieve compact folding without bifurcations. The unique motion path is certainly much desirable for most practical applications.

The waterbomb tessellation for the thick panels enables the structure to be folded compactly. The compactness of the package depends on the thickness coefficient and the number of vertices within the pattern. The pattern can be divided into strips formed by vertices A in the horizontal direction. Consider a pattern consisting of m strips, each with n vertices A as shown in Fig. 5-1. In the completely packaged configuration, the dimension in the vertical direction will be $(m+1)/2$ of the height of the larger triangles in the vertex A and the cross-section dimensions are the width of the larger triangles in the vertex A and the overall thickness as $2n(2+2\mu)a'$, where n is the number of vertices A in the strip and $\mu \leq 1$. $\mu > 1$ is not recommended because it results in panels with considerable thickness and in turn, the overall thickness of the package when the panels are packaged. So the ratio between the area of a fully expanded shape and that of completely folded is about $4n$. This indicates that the concept is very suitable to fold a structure in a long rectangular shape. On the other hand, to meet the geometric conditions of the spatial linkages, each panel within the pattern could not be of the same thickness. As a result, the overall structure in the fully deployed configuration is flat but not absolutely even. However, for this waterbomb pattern, we have manage to make sure that one side of the expanded surface is completely flat, which enables the waterbomb origami pattern to be directly applicable to fold thick-panel structures such as solar panels and space mirrors.

Chapter 6 Rigid Foldability of the Waterbomb Tube

6.1 Introduction

The flat-foldable waterbomb tessellation of zero-thickness sheet is modeled as a network of interconnected spherical $6R$ linkages in Chapter 5. To be further, the tubular tessellation is discussed here. When the two vertical sides of the pattern in Fig. 5-(b) are joined together, a waterbomb tube is formed as shown in Fig. 6-1. Since the DOF of a spherical $6R$ linkage is three, the waterbomb tube is of multiple DOFs. It can also be simplified by constraining it with symmetric conditions. In this chapter, the rigid foldability of generalized waterbomb tube is analyzed and the dependency between its motion behaviour and geometrical parameters is revealed.

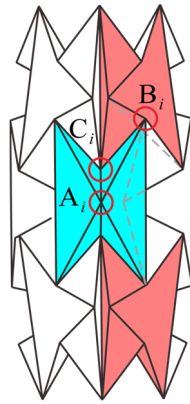


Fig. 6-1 The generalized waterbomb tube with $m = 3$ and $n = 6$ formed by joining together two vertical sides of the waterbomb origami pattern in Fig. 5-1(b).

The layout of this chapter is as follows. Section 6.2 presents a detailed kinematic derivation of the generalized waterbomb tube under contraction motion, including the interference and the uniform radius configuration of the tube. Section 6.3 discusses long and truncated tubes, which indicates the effect of the number of rows on the motion behaviour of the waterbomb tube. Section 6.4 analyzes several features in the twist motion of the waterbomb tube, including the rigidity, trigger condition, existence, range of the input kinematic variable and the transition of twist motion between different rows. Final conclusions are drawn in Section 6.5.

6.2 Contraction Motion

The behaviour of the waterbomb tube is best explained by a representative model with $n = 6$, $m = 7$, $\alpha = \beta = 45^\circ$ and $a = 23\text{mm}$ as shown in Fig. 6-2. First, a waterbomb tube is created of uniform radius, Fig. 6-2(i) (It will be demonstrated later that such a configuration exists in this case). When the tube contracts slightly along its longitudinal axis, both its radius and length reduce, Fig. 6-2(ii). With further contraction,

the tube develops a pineapple shape, Fig. 6-2 (iii) and (iv), and subsequently the tube regains uniform radius, Fig. 6-2(v). This is followed by a shrinkage in radius at the equatorial row of the tube. It then reaches a stage where longitudinal contraction is no longer possible following the same kind of movement, Fig. 6-2(vi), as some facets have collided with their neighbouring ones. This signals the end of a motion sequence referred to as *the contraction phase*. However, the tube's motion does not stop there. At the end of *the contraction phase*, a twist motion, starting at the equatorial row of the tube, can be activated with a small perturbation, Fig. 6-2(vii). The twist motion successively spreads to the neighbouring rows of the tube, and the bases on these rows turn either clockwise or counter-clockwise about the longitudinal axis. This motion, referred to as *the twist phase*, further reduces the length of the tube, but its diameter slightly increases, Fig. 6-2(viii). In both phases of motion, the tube generally maintains its symmetry.

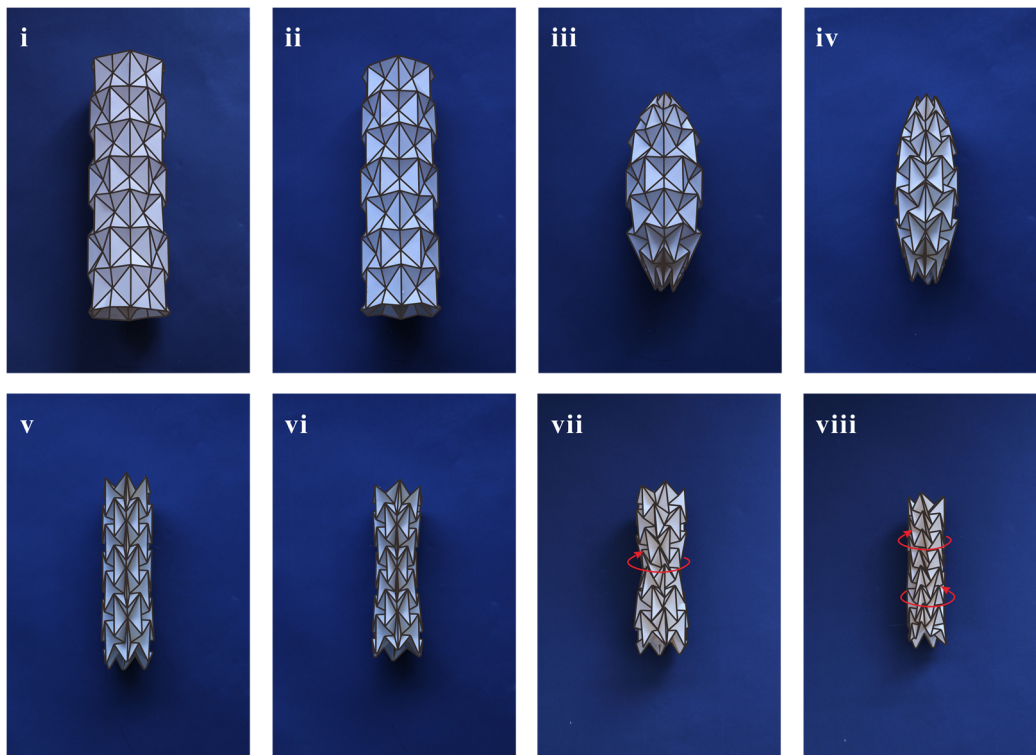


Fig. 6-2 Card model of a waterbomb tube from the expanded configuration (i) to the fully contracted configuration (vi). Additional twist is possible (vii and viii) that further shortens the model.

Based on our observation, the following assumptions of symmetry are made in the subsequent analysis. First, all of the bases on the same row behave in an identical manner, and they are placed side-by-side circumferentially. This is different from the case in Chapter 5 where all waterbomb bases have identical motion behaviour. Second,

during *the contraction phase*, each individual base is plane-symmetric, i.e., it is symmetric about a plane formed by two mid mountain creases. This plane also passes through the longitudinal axis of the tube. When the twist of a base occurs during *the twist phase*, the base is line-symmetric, i.e., the upper half of the base is in rotational symmetry to the lower half about a line that passes through the central vertex of the base and is perpendicular to the axis of the tube. Finally the top and bottom halves of the tube have the same motion behaviour, and the plane that divides the tube into two equal halves is termed the equatorial plane (EP).

6.2.1 Kinematics of Linkages A, B, C

Based on the assumptions, all linkages \mathbf{A}_i , \mathbf{B}_i and \mathbf{C}_i (Fig. 5-2) work in a plane-symmetric way during *the contraction phase*. Different from the flat-foldable case, the linkage \mathbf{A}_i is regarded as a spherical 6R linkage with only plane symmetry here. Its geometrical parameters are $\alpha_{23}^\Lambda = \alpha_{56}^\Lambda = \pi - 2\alpha$ and $\alpha_{12}^\Lambda = \alpha_{34}^\Lambda = \alpha_{45}^\Lambda = \alpha_{61}^\Lambda = \alpha$, see Fig. 5-2(a). Because of plane symmetry, there are

$$\delta_{i,5} = \delta_{i,3}, \quad \delta_{i,6} = \delta_{i,2}, \quad (6-1)$$

where $\delta_{i,j}$ (i indicates the row number where the base locates, and $j = 1, 2, \dots, 6$) are the kinematic variables of the linkage \mathbf{A}_i defined according to the D-H notation. Applying the closure equation as Eq. (5-1) to this linkage and considering Eq. (6-1), the following equations are obtained,

$$\tan \frac{\delta_{i,1}}{2} = \frac{\left[\cos \alpha (\cos \alpha \sin 2\alpha \cos \delta_{i,2} - \sin \alpha \cos 2\alpha) - \sin \alpha (\cos \alpha \sin \delta_{i,2} \sin \delta_{i,3}) \right.}{\left. + \cos \alpha \cos 2\alpha \cos \delta_{i,2} \cos \delta_{i,3} + \sin \alpha \sin 2\alpha \cos \delta_{i,3} \right)}{\sin \alpha (\sin \delta_{i,3} \cos \delta_{i,2} - \cos 2\alpha \sin \delta_{i,2} \cos \delta_{i,3}) + \cos \alpha \sin 2\alpha \sin \delta_{i,2}}, \quad (6-2a)$$

$$\tan \frac{\delta_{i,4}}{2} = \frac{\left[\cos \alpha (\cos \alpha \sin 2\alpha \cos \delta_{i,3} - \sin \alpha \cos 2\alpha \cos \delta_{i,2} \cos \delta_{i,3}) \right.}{\left. - \sin \alpha \sin \delta_{i,2} \sin \delta_{i,3} - \sin \alpha (\sin \alpha \sin 2\alpha \cos \delta_{i,2} + \cos \alpha \cos 2\alpha) \right]}{\sin \alpha (\sin \delta_{i,2} \cos \delta_{i,3} - \cos 2\alpha \sin \delta_{i,3} \cos \delta_{i,2}) + \cos \alpha \sin 2\alpha \sin \delta_{i,3}}. \quad (6-2b)$$

The kinematic variables can be replaced by the dihedral angles $\varphi_{i,j}$ ($j = 1, 2, \dots, 6$) as shown in Fig. 5-2(a). Noting that $\delta_{i,1} = \pi - \varphi_{i,1}$, $\delta_{i,2} = \pi + \varphi_{i,2}$, $\delta_{i,3} = \pi + \varphi_{i,3}$, $\delta_{i,4} = \pi - \varphi_{i,4}$, $\delta_{i,5} = \pi + \varphi_{i,5}$ and $\delta_{i,6} = \pi + \varphi_{i,6}$, Eqs. (6-1), (6-2a) and (6-2b) become

$$\varphi_{i,5} = \varphi_{i,3}, \quad \varphi_{i,6} = \varphi_{i,2}, \quad (6-3a)$$

$$\tan \frac{\varphi_{i,1}}{2} = \frac{\sin \alpha (\sin \varphi_{i,3} \cos \varphi_{i,2} - \cos 2\alpha \sin \varphi_{i,2} \cos \varphi_{i,3}) - \cos \alpha \sin 2\alpha \sin \varphi_{i,2}}{\left[\sin \alpha (\sin \alpha \sin 2\alpha \cos \varphi_{i,3} - \cos \alpha \sin \varphi_{i,2} \sin \varphi_{i,3} - \cos \alpha \cos 2\alpha \cos \varphi_{i,2} \cos \varphi_{i,3}) \right.}{\left. - \cos \alpha (\cos \alpha \sin 2\alpha \cos \varphi_{i,2} + \sin \alpha \cos 2\alpha) \right]},$$

(6-3b)

$$\tan \frac{\varphi_{i,4}}{2} = \frac{\sin \alpha (\sin \varphi_{i,2} \cos \varphi_{i,3} - \cos 2\alpha \sin \varphi_{i,3} \cos \varphi_{i,2}) - \cos \alpha \sin 2\alpha \sin \varphi_{i,3}}{\left[\begin{array}{l} \sin \alpha (\sin \alpha \sin 2\alpha \cos \varphi_{i,2} - \cos \alpha \cos 2\alpha) - \cos \alpha (\cos \alpha \sin 2\alpha \cos \varphi_{i,3}) \\ + \sin \alpha \sin \varphi_{i,2} \sin \varphi_{i,3} + \sin \alpha \cos 2\alpha \cos \varphi_{i,2} \cos \varphi_{i,3} \end{array} \right]}.$$

(6-3c)

For the linkage \mathbf{B}_i (Fig. 5-2(b)), its kinematic twists are $\alpha_{12}^{\mathbf{B}} = \alpha_{61}^{\mathbf{B}} = \pi - \alpha - \beta$, $\alpha_{23}^{\mathbf{B}} = \alpha_{56}^{\mathbf{B}} = \beta$ and $\alpha_{34}^{\mathbf{B}} = \alpha_{45}^{\mathbf{B}} = \alpha$. We have

$$\omega_{\mathbf{B}_i,5} = \omega_{\mathbf{B}_i,3}, \quad \omega_{\mathbf{B}_i,6} = \omega_{\mathbf{B}_i,2}, \quad (6-4a)$$

$$\tan \frac{\omega_{\mathbf{B}_i,1}}{2} = \frac{\left[\begin{array}{l} \cos \alpha (\sin(\alpha + \beta) \cos \beta - \cos(\alpha + \beta) \sin \beta \cos \omega_{\mathbf{B}_i,2}) - \sin \alpha (\sin \beta \sin(\alpha \\ + \beta) \cos \omega_{\mathbf{B}_i,3} - \cos(\alpha + \beta) \sin \omega_{\mathbf{B}_i,2} \sin \omega_{\mathbf{B}_i,3} + \cos(\alpha + \beta) \cos \beta \cos \omega_{\mathbf{B}_i,2} \cos \omega_{\mathbf{B}_i,3}) \end{array} \right]}{\sin \alpha (\sin \omega_{\mathbf{B}_i,3} \cos \omega_{\mathbf{B}_i,2} + \cos \beta \sin \omega_{\mathbf{B}_i,2} \cos \omega_{\mathbf{B}_i,3}) + \cos \alpha \sin \beta \sin \omega_{\mathbf{B}_i,2}},$$

(6-4b)

$$\tan \frac{\omega_{\mathbf{B}_i,4}}{2} = \frac{\left[\begin{array}{l} \cos \alpha (\sin(\alpha + \beta) (\cos \beta \cos \omega_{\mathbf{B}_i,2} \cos \omega_{\mathbf{B}_i,3} - \sin \omega_{\mathbf{B}_i,2} \sin \omega_{\mathbf{B}_i,3}) - \cos(\alpha \\ + \beta) \sin \beta \cos \omega_{\mathbf{B}_i,3}) - \sin \alpha (\sin(\alpha + \beta) \sin \beta \cos \omega_{\mathbf{B}_i,2} + \cos(\alpha + \beta) \cos \beta) \end{array} \right]}{\sin(\alpha + \beta) (\sin \omega_{\mathbf{B}_i,2} \cos \omega_{\mathbf{B}_i,3} + \cos \beta \sin \omega_{\mathbf{B}_i,3} \cos \omega_{\mathbf{B}_i,2}) - \cos(\alpha + \beta) \sin \beta \sin \omega_{\mathbf{B}_i,3}},$$

(6-4c)

where $\omega_{\mathbf{B}_i,j}$ (i indicates the row number where the base locates, and $j = 1, 2, \dots, 6$) are the kinematic variables of the linkage \mathbf{B}_i defined according to the D-H notation. Again replace the kinematic variables with dihedral angels using $\omega_{\mathbf{B}_i,1} = \pi - \phi_{\mathbf{B}_i,1}$, $\omega_{\mathbf{B}_i,2} = \pi - \phi_{\mathbf{B}_i,2}$, $\omega_{\mathbf{B}_i,3} = \pi + \phi_{\mathbf{B}_i,3}$, $\omega_{\mathbf{B}_i,4} = \pi - \phi_{\mathbf{B}_i,4}$, $\omega_{\mathbf{B}_i,5} = \pi + \phi_{\mathbf{B}_i,5}$, $\omega_{\mathbf{B}_i,6} = \pi - \phi_{\mathbf{B}_i,6}$. Equations (6-4a), (6-4b) and (6-4c) become

$$\phi_{\mathbf{B}_i,5} = \phi_{\mathbf{B}_i,3}, \quad \phi_{\mathbf{B}_i,6} = \phi_{\mathbf{B}_i,2}, \quad (6-5a)$$

$$\tan \frac{\phi_{\mathbf{B}_i,1}}{2} = \frac{\sin \alpha (\sin \phi_{\mathbf{B}_i,3} \cos \phi_{\mathbf{B}_i,2} - \cos \beta \sin \phi_{\mathbf{B}_i,2} \cos \phi_{\mathbf{B}_i,3}) + \cos \alpha \sin \beta \sin \phi_{\mathbf{B}_i,2}}{\left[\begin{array}{l} \cos \alpha (\sin(\alpha + \beta) \cos \beta + \cos(\alpha + \beta) \sin \beta \cos \phi_{\mathbf{B}_i,2}) + \sin \alpha (\sin \beta \sin(\alpha \\ + \beta) \cos \phi_{\mathbf{B}_i,3} - \cos(\alpha + \beta) \sin \phi_{\mathbf{B}_i,2} \sin \phi_{\mathbf{B}_i,3} - \cos(\alpha + \beta) \cos \beta \cos \phi_{\mathbf{B}_i,2} \cos \phi_{\mathbf{B}_i,3}) \end{array} \right]},$$

(6-5b)

$$\tan \frac{\phi_{\mathbf{B}_i,4}}{2} = \frac{\sin(\alpha + \beta) (\cos \beta \sin \phi_{\mathbf{B}_i,3} \cos \phi_{\mathbf{B}_i,2} - \sin \phi_{\mathbf{B}_i,2} \cos \phi_{\mathbf{B}_i,3}) + \cos(\alpha + \beta) \sin \beta \sin \phi_{\mathbf{B}_i,3}}{\left[\begin{array}{l} \cos \alpha (\sin(\alpha + \beta) (\cos \beta \cos \phi_{\mathbf{B}_i,2} \cos \phi_{\mathbf{B}_i,3} + \sin \phi_{\mathbf{B}_i,2} \sin \phi_{\mathbf{B}_i,3}) + \cos(\alpha \\ + \beta) \sin \beta \cos \phi_{\mathbf{B}_i,3}) + \sin \alpha (\sin(\alpha + \beta) \sin \beta \cos \phi_{\mathbf{B}_i,2} - \cos(\alpha + \beta) \cos \beta) \end{array} \right]}.$$

(6-5c)

Similarly for the linkage \mathbf{C}_i (Fig. 5-2(c)), we have

$$\phi_{\mathbf{C}_i,5} = \phi_{\mathbf{C}_i,3}, \quad \phi_{\mathbf{C}_i,6} = \phi_{\mathbf{C}_i,2}, \quad (6-6a)$$

$$\tan \frac{\phi_{Ci,1}}{2} = \frac{\sin \alpha (\sin \phi_{Ci,3} \cos \phi_{Ci,2} - \cos \beta \sin \phi_{Ci,2} \cos \phi_{Ci,3}) + \cos \alpha \sin \beta \sin \phi_{Ci,2}}{\left[\cos \alpha (\sin(\alpha + \beta) \cos \beta + \cos(\alpha + \beta) \sin \beta \cos \phi_{Ci,2}) + \sin \alpha (\sin \beta \sin(\alpha + \beta) \cos \phi_{Ci,3} - \cos(\alpha + \beta) \sin \phi_{Ci,2} \sin \phi_{Ci,3} - \cos(\alpha + \beta) \cos \beta \cos \phi_{Ci,2} \cos \phi_{Ci,3}) \right]}, \quad (6-6b)$$

$$\tan \frac{\phi_{Ci,4}}{2} = \frac{\sin(\alpha + \beta) (\cos \beta \sin \phi_{Ci,3} \cos \phi_{Ci,2} - \sin \phi_{Ci,2} \cos \phi_{Ci,3}) + \cos(\alpha + \beta) \sin \beta \sin \phi_{Ci,3}}{\left[\cos \alpha (\sin(\alpha + \beta) (\cos \beta \cos \phi_{Ci,2} \cos \phi_{Ci,3} + \sin \phi_{Ci,2} \sin \phi_{Ci,3}) + \cos(\alpha + \beta) \sin \beta \cos \phi_{Ci,3}) + \sin \alpha (\sin(\alpha + \beta) \sin \beta \cos \phi_{Ci,2} - \cos(\alpha + \beta) \cos \beta) \right]}. \quad (6-6c)$$

The compatibility between neighbouring linkages \mathbf{A}_i , \mathbf{B}_i and \mathbf{C}_i is given in Eq. (5-2), which holds for the entire tube. In order to further solve the kinematics of the pattern, two cases, where the number of rows for the generalized waterbomb tube, m , is odd or even, are discussed separately as follows.

6.2.2 Contraction of a Tube with an Odd Number of Rows

We start by the tube consisting of an odd number of rows (m is odd), where the EP slices through the centre of the equatorial row (known as *Row 0*). In general, each spherical $6R$ linkage would have three DOFs. However, since linkage \mathbf{A}_i , the linkage at the central vertex A_i of each base, preserves plane symmetry in *the contraction phase*, its DOF is reduced to two. Moreover, linkages \mathbf{A}_0 , the linkage on the *Row 0*, is symmetric about the EP, which further cuts the DOF of linkage \mathbf{A}_0 to one as it is both plane- and line-symmetric.

A strip out of the origami pattern with an odd m is shown in Fig. 6-3(a). If we take the dihedral angle of the top mountain crease $\phi_{0,1}$ as the input (Fig. 6-3(b)), the other five dihedral angles of the linkage \mathbf{A}_0 can be obtained,

$$\tan \frac{\phi_{0,2}}{2} = \cos \alpha \tan \frac{\phi_{0,1}}{2}, \quad \phi_{0,4} = \phi_{0,1}, \quad \phi_{0,2} = \phi_{0,3} = \phi_{0,5} = \phi_{0,6}. \quad (6-7)$$

The projection of *Row 0* onto the EP is presented in Fig. 6-3(c), where $B_0F_0 \perp A_0F_0$ and $B'_0F_0 \perp A_0F_0$ with F_0 as the feet of the perpendiculars. Since

$$\overline{EE'} = \overline{B_0B'_0}, \quad \overline{EE'} = 2t \sin \frac{\theta}{2}, \quad \overline{B_0B'_0} = 2t \sin \frac{\phi_{0,1}}{2}, \quad (6-8)$$

$$\theta = \phi_{0,1}, \quad (6-9)$$

where θ is the dihedral angle between two largest triangular facets of the base with A_0 as its central vertex. Moreover, as the inter-connected bases on *Row 0* complete a circle (Fig. 6-3(c)), the dihedral angle about crease $B'_0C'_{-1}$ that is shared by

neighbouring two bases on *Row 0*, $\phi_{B_0,4}$, is

$$\phi_{B_0,4} = 2 \left(\frac{\varphi_{0,1}}{2} - \frac{\pi}{n} \right). \quad (6-10)$$

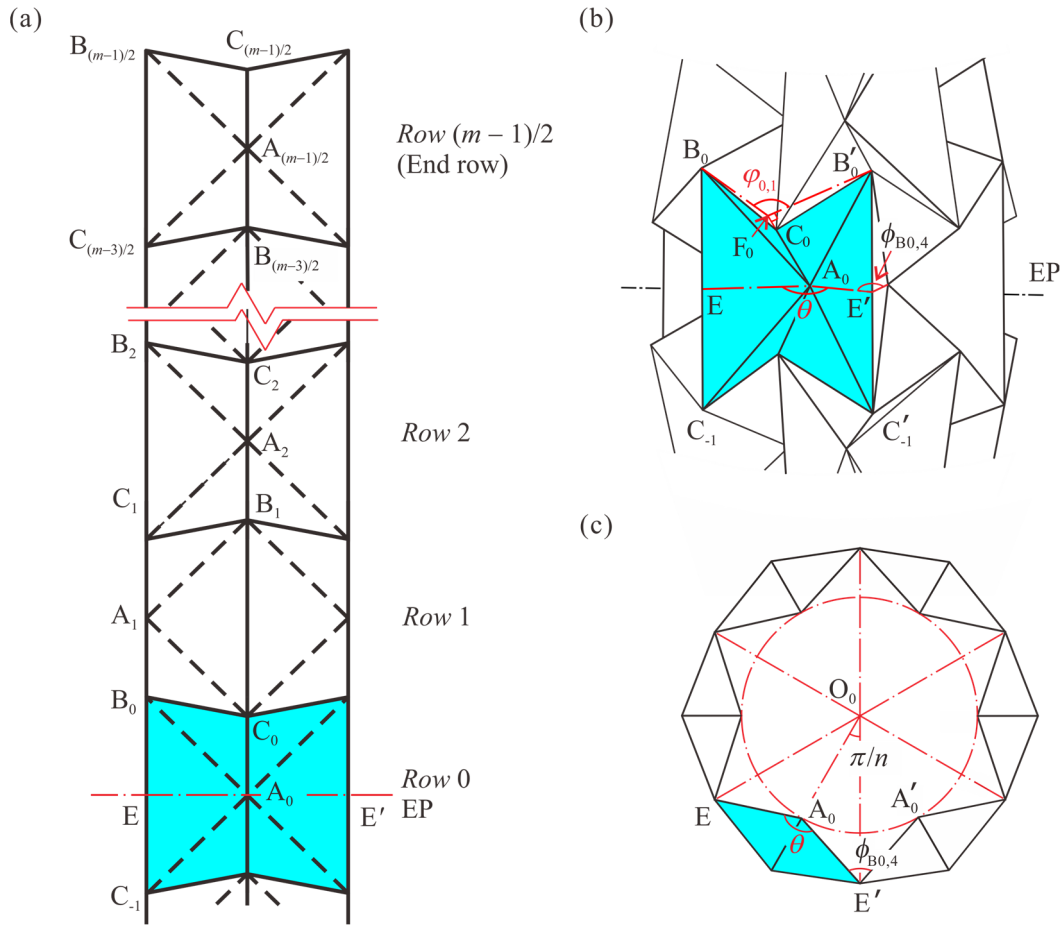


Fig. 6-3 (a) Top half of a longitudinal strip in a waterbomb tube. Vertices are marked as A, B and C. E – E' is the equator of the tube. (b) A 3D view of a waterbomb tube with equatorial row (*Row 0*) and rows immediately adjacent to it. One of the base on *Row 0* is shown in blue. (c) The projection view of the waterbomb tube with only *Row 0* shown. O_0 is the centre of the tube. EP is short for equatorial plane.

All angles obtained are subsequently used as input angles for adjacent linkages such as \mathbf{B}_0 and \mathbf{C}_0 . Using the closure equations of these linkages, their motions, described by their respective dihedral angles, can be found. The process is repeated until all of the dihedral angles are determined. In short, the motion of the entire tube is driven by the motion of *Row 0* spreading simultaneously through the neighbouring rows until the ends of the tube. The kinematic relationships presented by the dihedral angle are as follows.

For linkage \mathbf{B}_i ,

$$\phi_{B_i,3} = \phi_{B_i,5} = \varphi_{i,6}, \quad \phi_{B_i,4} = \phi_{C_{(i-1),4}}, \quad \phi_{B_i,6} = \phi_{B_i,2}, \quad (6-11a)$$

$$\tan \frac{\phi_{Bi,2}}{2} = \frac{\left[\sin(\alpha+\beta) \left(\cos \alpha \tan \frac{\phi_{Bi,4}}{2} \sin \phi_{Bi,3} + \cos \phi_{Bi,3} \right) - \left\{ \sin \alpha \left[\cos \alpha \tan \frac{\phi_{Bi,4}}{2} (\cos \phi_{Bi,3} + 1) - \sin \phi_{Bi,3} \right] \left[\cos \alpha \sin(\alpha+2\beta) \tan \frac{\phi_{Bi,4}}{2} \cos \phi_{Bi,3} - \sin(\alpha+2\beta) \sin \phi_{Bi,3} - \sin \alpha \cos(\alpha+2\beta) \tan \frac{\phi_{Bi,4}}{2} \right] + \sin^2(\alpha+\beta) \left(\cos \alpha \tan \frac{\phi_{Bi,4}}{2} \sin \phi_{Bi,3} + \cos \phi_{Bi,3} \right)^2 \right\}^{1/2}}{\sin \alpha \left[\cos \alpha \tan \frac{\phi_{Bi,4}}{2} (\cos \phi_{Bi,3} + 1) - \sin \phi_{Bi,3} \right]} \right], \quad (6-11b)$$

$$\tan \frac{\phi_{Bi,1}}{2} = \frac{\sin \alpha (\sin \phi_{Bi,3} \cos \phi_{Bi,2} - \cos \beta \sin \phi_{Bi,2} \cos \phi_{Bi,3}) + \cos \alpha \sin \beta \sin \phi_{Bi,2}}{\left[\cos \alpha (\sin(\alpha+\beta) \cos \beta + \cos(\alpha+\beta) \sin \beta \cos \phi_{Bi,2}) + \sin \alpha (\sin \beta \sin(\alpha+\beta) \cos \phi_{Bi,3} - \cos(\alpha+\beta) \sin \phi_{Bi,2} \sin \phi_{Bi,3} - \cos(\alpha+\beta) \cos \beta \cos \phi_{Bi,2} \cos \phi_{Bi,3}) \right]}; \quad (6-11c)$$

for linkage C_i ,

$$\phi_{Ci,1} = \varphi_{i,1}, \quad \phi_{Ci,2} = \phi_{Ci,6} = \phi_{Bi,2}, \quad \phi_{Ci,5} = \phi_{Ci,3}, \quad (6-12a)$$

$$\tan \frac{\phi_{Ci,3}}{2} = \frac{\left[\sin \alpha \cos(\alpha+\beta) \tan \frac{\phi_{Ci,1}}{2} \sin \phi_{Ci,2} + \sin \alpha \cos \phi_{Ci,2} - \left\{ \left[\sin \alpha \cos \phi_{Ci,2} + \sin \alpha \cos(\alpha+\beta) \sin \phi_{Ci,2} \tan \frac{\phi_{Ci,1}}{2} \right]^2 - \sin(\alpha+\beta) \left[\sin(\alpha+\beta) \cos(\beta - \alpha) \tan \frac{\phi_{Ci,1}}{2} + \cos(\alpha+\beta) \sin(\beta - \alpha) \tan \frac{\phi_{Ci,1}}{2} \cos \phi_{Ci,2} - \sin(\beta - \alpha) \sin \phi_{Ci,2} \right] \left[\cos(\alpha+\beta) \tan \frac{\phi_{Ci,1}}{2} (\cos \phi_{Ci,2} + 1) - \sin \phi_{Ci,2} \right] \right\}^{1/2}}{\sin(\alpha+\beta) \left[\cos(\alpha+\beta) \tan \frac{\phi_{Ci,1}}{2} (\cos \phi_{Ci,2} + 1) - \sin \phi_{Ci,2} \right]} \right], \quad (6-12b)$$

$$\tan \frac{\phi_{Ci,4}}{2} = \frac{\sin(\alpha+\beta) (\cos \beta \sin \phi_{Ci,3} \cos \phi_{Ci,2} - \sin \phi_{Ci,2} \cos \phi_{Ci,3}) + \cos(\alpha+\beta) \sin \beta \sin \phi_{Ci,3}}{\left[\cos \alpha (\sin(\alpha+\beta) (\cos \beta \cos \phi_{Ci,2} \cos \phi_{Ci,3} + \sin \phi_{Ci,2} \sin \phi_{Ci,3}) + \cos(\alpha+\beta) \sin \beta \cos \phi_{Ci,3}) + \sin \alpha (\sin(\alpha+\beta) \sin \beta \cos \phi_{Ci,2} - \cos(\alpha+\beta) \cos \beta) \right]}; \quad (6-12c)$$

and for linkage A_{i+1} ,

$$\varphi_{i+1,4} = \phi_{Bi,1}, \quad \varphi_{i+1,3} = \varphi_{i+1,5} = \phi_{Ci,3}, \quad \varphi_{i+1,2} = \varphi_{i+1,6}, \quad (6-13a)$$

$$\tan \frac{\varphi_{i+1,6}}{2} = \frac{\left[\begin{aligned} &\cos \varphi_{i+1,5} + \tan \frac{\varphi_{i+1,4}}{2} \cos \alpha \sin \varphi_{i+1,5} - \left\{ (\cos \varphi_{i+1,5} + \tan \frac{\varphi_{i+1,4}}{2} \cos \alpha \sin \varphi_{i+1,5})^2 \right. \\ &- (2 \cos^2 \alpha + \cos 2\alpha) \left[\sin \varphi_{i+1,5} - \tan \frac{\varphi_{i+1,4}}{2} \cos \alpha (\cos \varphi_{i+1,5} + 1) \right]^2 \\ &\left. - 2 \cos \alpha \tan \frac{\varphi_{i+1,4}}{2} \left[\sin \varphi_{i+1,5} - \tan \frac{\varphi_{i+1,4}}{2} \cos \alpha (\cos \varphi_{i+1,5} + 1) \right] \right\}^{1/2}}{\sin \varphi_{i+1,5} - \tan \frac{\varphi_{i+1,4}}{2} \cos \alpha (\cos \varphi_{i+1,5} + 1)} \right]}{\sin \varphi_{i+1,5} - \tan \frac{\varphi_{i+1,4}}{2} \cos \alpha (\cos \varphi_{i+1,5} + 1)}, \end{aligned} \right. \quad (6-13b)$$

$$\tan \frac{\varphi_{i+1,1}}{2} = \frac{\sin \alpha (\sin \varphi_{i+1,5} \cos \varphi_{i+1,6} - \cos 2\alpha \sin \varphi_{i+1,6} \cos \varphi_{i+1,5}) - \cos \alpha \sin 2\alpha \sin \varphi_{i+1,6}}{\left[\begin{aligned} &\sin \alpha (\sin \alpha \sin 2\alpha \cos \varphi_{i+1,5} - \cos \alpha \cos 2\alpha) - \cos \alpha (\cos \alpha \sin 2\alpha \cos \varphi_{i+1,6}) \\ &+ \sin \alpha \sin \varphi_{i+1,5} \sin \varphi_{i+1,6} + \sin \alpha \cos 2\alpha \cos \varphi_{i+1,5} \cos \varphi_{i+1,6} \end{aligned} \right]}. \quad (6-13c)$$

Eqs. (6-11), (6-12) and (6-13) hold for $i=1, 2, \dots, (m-3)/2$, except that $\phi_{B_0,4}$ is obtained by Eq. (6-10). Because the top and bottom halves of the tube have the same motion, hereafter only the equations for top half are given. Therefore, the whole kinematic set of the waterbomb tube is formed by Eqs. (6-7) and (6-10) to (6-13). Only $\varphi_{0,1}$ is needed to determine the motion of the entire waterbomb tube, which demonstrates that the DOF of the tube under circumferential and longitudinal symmetry is one.

- Rigid motion range and interferences at both ends of a tube

Two limiting values of θ , θ_{\min} and θ_{\max} , exist. They are determined by three constraints. First, the tube will not be further contracted when it arrives at the most compact-folding cylindrical configuration where linkage \mathbf{B}_0 is fully folded with $\phi_{B_0,4} = 0$, i.e., two triangular facets on either side of the shared crease B_0C_{-1} connecting two adjacent bases of Row 0 completely overlap. By using Eq. (6-10), we have

$$\varphi_{0,1\min} = \frac{2\pi}{n}. \quad (6-14)$$

Second, the tube will not be further expanded when it arrives at the most deployed configuration in which top sides of the bases on Row $(m-1)/2$ form an n -sided regular polygon with a side length of $2t$. That is, the linkage $\mathbf{A}_{(m-1)/2}$ on Row $(m-1)/2$ is fully deployed with $\varphi_{(m-1)/2,1} = \pi$. In this case, by making the square root in the expression of $\tan(\varphi_{(m-1)/2,6}/2)$ in Eq. (6-13b) zero, i.e.,

$$\left[\begin{array}{l} (\cos \varphi_{(m-1)/2,5} + \tan \frac{\varphi_{(m-1)/2,4}}{2} \cos \alpha \sin \varphi_{(m-1)/2,5})^2 - (2\cos^2 \alpha + \cos 2\alpha)[\sin \varphi_{(m-1)/2,5}] \\ -\tan \frac{\varphi_{(m-1)/2,4}}{2} \cos \alpha (\cos \varphi_{(m-1)/2,5} + 1)^2 - 2 \cos \alpha \tan \frac{\varphi_{(m-1)/2,4}}{2} [\sin \varphi_{(m-1)/2,5}] \\ -\tan \frac{\varphi_{(m-1)/2,4}}{2} \cos \alpha (1 + \cos \varphi_{(m-1)/2,5}) \end{array} \right] = 0, \quad (6-15)$$

$\varphi_{0,1\max}$ is obtained. However, due to the highly nonlinear property of Eq. (6-15), there are up to three solutions for $\varphi_{0,1}$. $\varphi_{0,1\min}$ is the smallest of the solutions that are larger than $2\pi/n$ whereas $\varphi_{0,1\max}$ is the largest.

Moreover, in order to avoid the interference of facets during the contraction folding of the generalized waterbomb tube, the equation below holds

$$\phi_{Bi,4} \geq 0, \quad i = 0, 1, \dots, \frac{m-1}{2}. \quad (6-16)$$

Substituting Eqs. (6-7) and (6-10) to (6-13) into Eq. (6-16), the solutions of Eq. (6-16) can be obtained. Therefore, the range of the input kinematic variable $\varphi_{0,1}$ under the rigid contraction folding is the intersection of those solutions of Eqs. (6-14), (6-15) and (6-16).

Because of Eq. (6-9), the limits for $\varphi_{0,1}$ are also limits for θ . Hence, within the range from θ_{\min} to θ_{\max} , the folding of the waterbomb tube is rigid motion without kinematic interference, and its kinematic relationship is given by Eqs. (6-7) and (6-10) to (6-13). Take a tube with $n=6$, $m=3$ and $\alpha=\beta=45^\circ$ as an example. The motion of the tube is given in Fig. 6-4. $\theta_{\min}=60^\circ$ and $\theta_{\max}=147.96^\circ$. Its kinematic paths are plotted as Fig. 6-5.

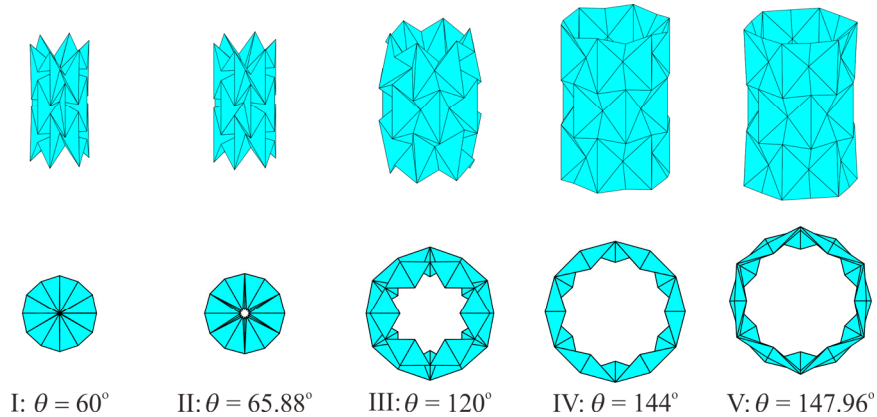


Fig. 6-4 3D and projected views of a tube with $m=3$, $n=6$ and $\alpha=\beta=45^\circ$ deploying from configurations I to V. The corresponding folding angles θ are listed below the motion sequence.

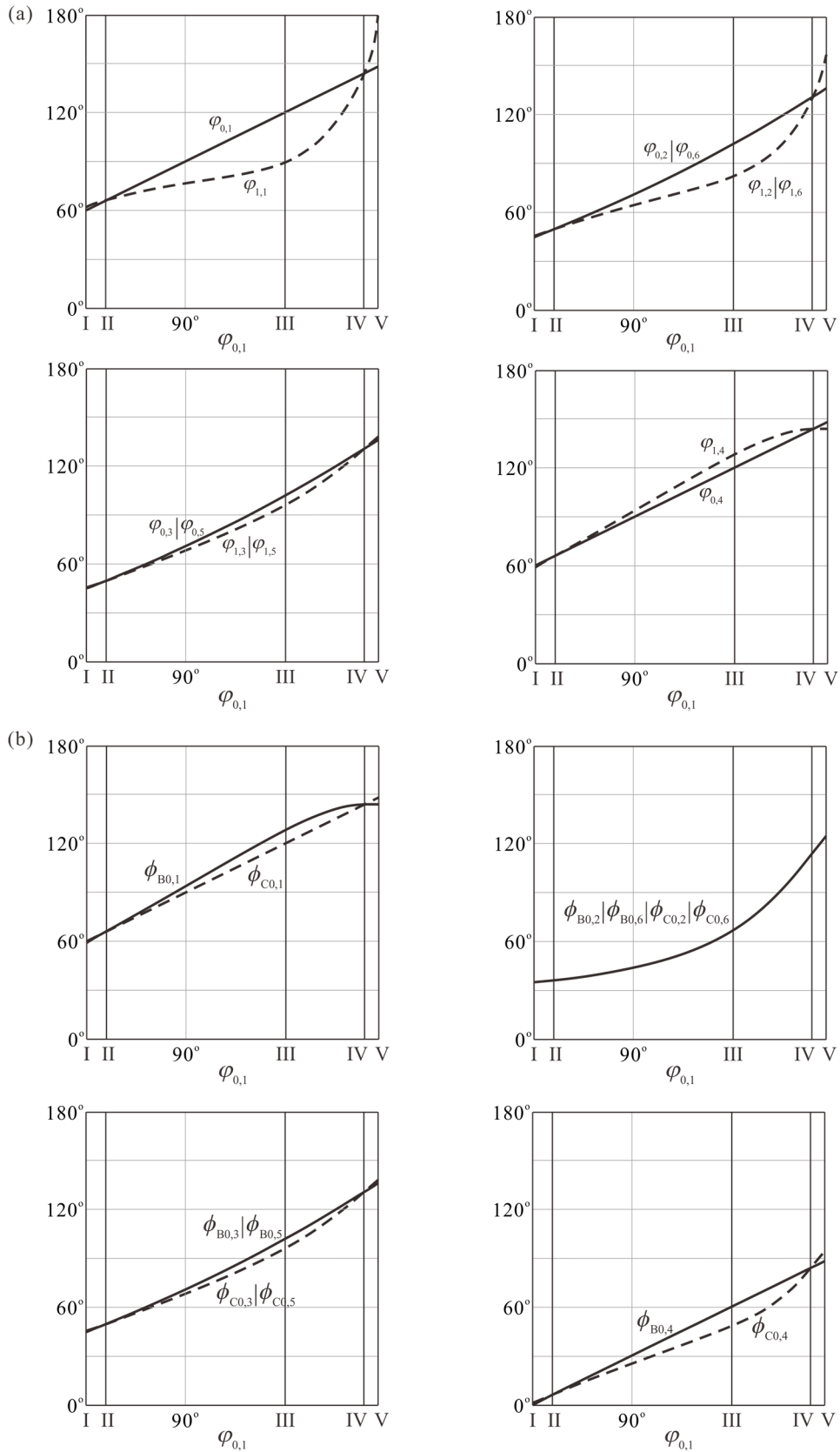


Fig. 6-5 Kinematic paths of a waterbomb tube when $n = 6$, $m = 3$ and $\alpha = \beta = 45^\circ$ for (a) linkages \mathbf{A}_0 and \mathbf{A}_1 , and (b) linkages \mathbf{B}_0 and \mathbf{C}_0 . At configurations I: $\varphi_{0,1} = 60^\circ$, II: $\varphi_{0,1} = 65.88^\circ$, III: $\varphi_{0,1} = 120^\circ$, IV: $\varphi_{0,1} = 144^\circ$, V: $\varphi_{0,1} = 147.96^\circ$.

When $\alpha + \beta = \pi/2$, the cylindrical coordinates of each vertex in the longitudinal strip as shown in Fig. 6-3(a) can be calculated as

$$r_{Bi} = \frac{t \sin \frac{\varphi_{i,1}}{2}}{\sin \frac{\pi}{n}}, \quad z_{Bi} = z_{Ai} + \sqrt{(1 + \cot^2 \alpha)t^2 - r_{Bi}^2 - r_{Ai}^2 + 2r_{Ai}r_{Bi} \cos \frac{\pi}{n}}, \quad (6-17a)$$

$$r_{Ci} = \frac{t \sin \frac{\varphi_{i+1,4}}{2}}{\sin \frac{\pi}{n}}, \quad z_{Ci} = z_{Ai} + \sqrt{t^2 \cot^2 \alpha - (r_{Ci} - r_{Ai})^2}, \quad (6-17b)$$

$$r_{Ai} = r_{Ci} - \frac{\sqrt{t^2 \cos^2 \frac{\varphi_{i,1}}{2} - (r_{Ci} - r_{Bi} \cos \frac{\pi}{n})^2}}{\cos \frac{\varphi_{i,1}}{2} \tan \alpha}, \quad z_{A0} = 0,$$

$$z_{A(i+1)} = z_{Ci} + \sqrt{(1 + \cot^2 \alpha)t^2 - r_{Ci}^2 - r_{A(i+1)}^2 + 2r_{Ci}r_{A(i+1)} \cos \frac{\pi}{n}}, \quad (6-17c)$$

where $i = 0, 1, \dots, (m-1)/2$. And the overall length of the tube is

$$L = 2z_{B((m-1)/2)}. \quad (6-18)$$

According to Eqs. (6-17) and (6-18), r/t and L/t are plotted against θ in Fig. 6-6(a) and Fig. 6-6(b), respectively.

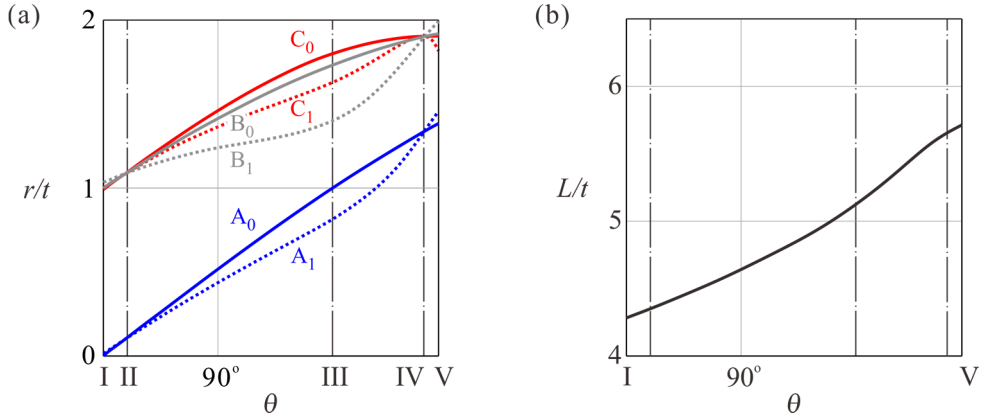
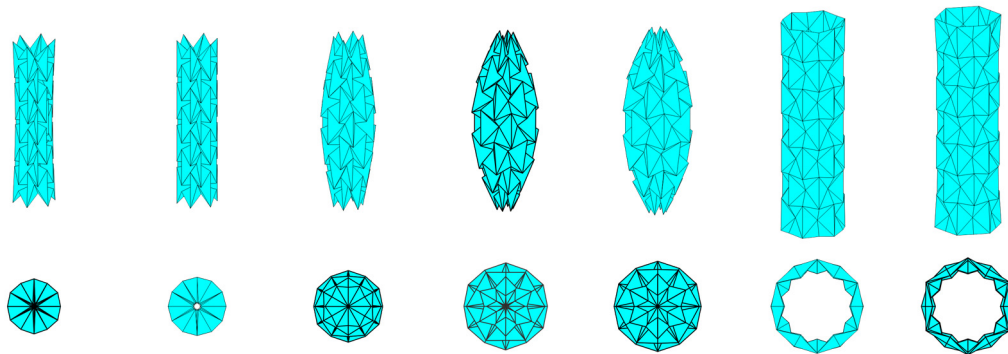


Fig. 6-6 Variation of (a) radii of vertices A, B and C, and (b) the length of the tube with respect to θ when $n = 6$, $m = 3$ and $\alpha = \beta = 45^\circ$.

The motion goes through a number of stages. It can be seen from Fig. 6-6 that at configurations II and IV, all radii of vertices B and C reach the same value, so do those of vertices A. In fact, at both configurations, each row of the tube has an identical shape and all of the bases take the same configuration, resulting in a tube of uniform radius.

If this waterbomb tube is constructed from a flat but rigid sheet, the pattern has to be partially folded in order for its left and right edges to be joined together. It is most likely to reach configuration IV, as it has a larger overall radius. Between these two configurations, the radii of vertices are no longer the same, resulting in a pineapple shape (Fig. 6-3 III) with the largest radius attained at B_0 (and C_{-1}). Likewise, transforming outside of these two configurations, the tube assumes a dog-bone shape (Fig. 6-3 I) with a smallest radius reached at B_0 (and C_{-1}). Throughout the deployment, the radius of A_0 never reaches zero except when θ is at its lower bound θ_{\min} , indicating that there is no collision of the vertices or facets during the motion. At θ_{\min} , the folding of the tube in *the contraction phase* ceases, as vertices A_0 have reached the centre of the tube. Any further contraction becomes impossible for it would lead to collision of these vertices.

When the number of rows increases, *Row 0*, and the rows just above and below it, will exhibit the same motion as that of the tube with $m = 3$, whereas the newly added rows will be concurrently driven by them. However, the motion terminates earlier as the upper sides of the bases on the top row become an n -sided regular polygon. For instance, if m is increased to 7, it can be determined that θ_{\min} remains to be 60° but θ_{\max} is now reduced to 144.24° . The motion sequence of such a tube is shown in Fig. 6-7, where configurations I and V correspond to cases where θ is at its lower and upper bounds, respectively.



I: $\theta = 60^\circ$ II: $\theta = 65.88^\circ$ III_L: $\theta = 90.72^\circ$ III: $\theta = 120^\circ$ III_R: $\theta = 128.52^\circ$ IV: $\theta = 144^\circ$ V: $\theta = 144.24^\circ$

Fig. 6-7 3D and projected views of the tube with $n = 6$, $m = 7$ and $\alpha = \beta = 45^\circ$ deploying from configurations I to V. The corresponding folding angles θ are listed below the motion sequence. The tube is completely concealed at configurations III_L and III_R at which the radii of vertices A on top and bottom rows reach 0.

Figures 6-8 and 6-9 plot the dihedral angles of linkage A_i between adjacent bases

of Row i ($i = 0, 1, 2, 3$), \mathbf{B}_i and \mathbf{C}_i ($i = 0, 1, 2$), against $\varphi_{0,1}$, respectively. r_{A_i} , r_{B_i} and r_{C_i} , the radii of the vertices A_i , B_i , and C_i , vs. θ is given in Fig. 6-10. Similar to the case of $m = 3$, all curves intersect at two points, which are referred to as configurations II and IV, indicating that the tube again has uniform radii. A careful comparison reveals that these two configurations appear at exactly the same θ as those of tubes with $m = 3$. This is intuitively correct as more rows can always be added in configurations II and IV when all of the bases on those rows are in the identical configuration. They can be connected in a geometrically compatible manner without altering the overall configuration.

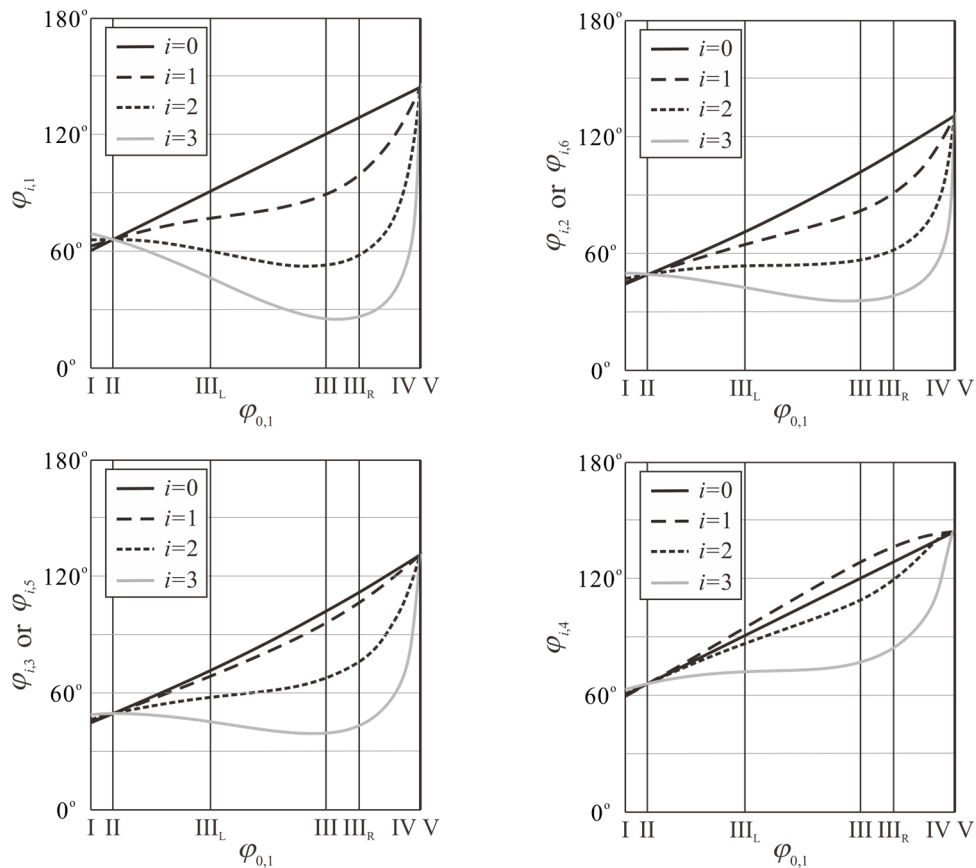


Fig. 6-8 Kinematic paths of a waterbomb tube with $n = 6$, $m = 7$ and $\alpha = \beta = 45^\circ$ for linkages \mathbf{A}_i . At configurations I: $\varphi_{0,1} = 60^\circ$, II: $\varphi_{0,1} = 65.88^\circ$, III_L: $\varphi_{0,1} = 90.72^\circ$, III: $\varphi_{0,1} = 120^\circ$, III_R: $\varphi_{0,1} = 128.52^\circ$, IV: $\varphi_{0,1} = 144^\circ$, V: $\varphi_{0,1} = 144.24^\circ$.

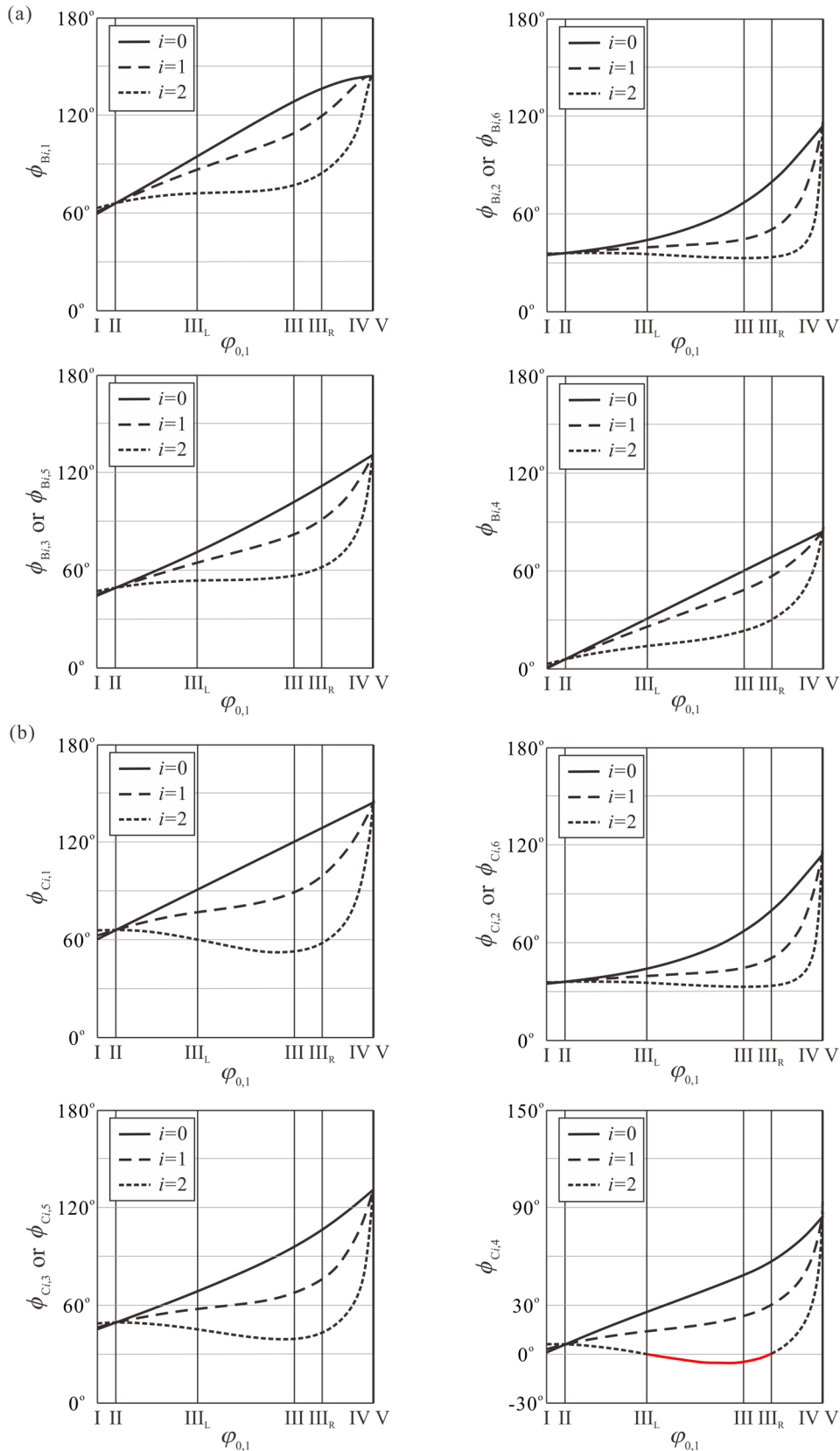


Fig. 6-9 Kinematic paths of a waterbomb tube with $n = 6$, $m = 7$ and $\alpha = \beta = 45^\circ$ for linkages

(a) B_i , and (b) C_i . At configurations I: $\varphi_{0,1} = 60^\circ$, II: $\varphi_{0,1} = 65.88^\circ$, III_L: $\varphi_{0,1} = 90.72^\circ$, III:

$\varphi_{0,1} = 120^\circ$, III_R: $\varphi_{0,1} = 128.52^\circ$, IV: $\varphi_{0,1} = 144^\circ$, V: $\varphi_{0,1} = 144.24^\circ$.

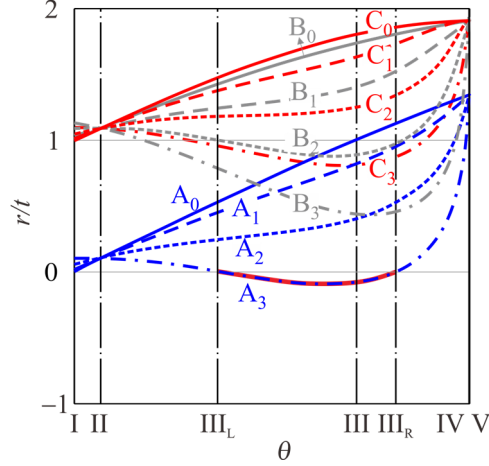


Fig. 6-10 The radii of vertices A, B and C vs. θ of a waterbomb tube with $n = 6$, $m = 7$ and $\alpha = \beta = 45^\circ$. The red curve shows $r_{A_3} < 0$ between configurations III_L and III_R.

Close inspection of Fig. 6-9(b), reveals that there is a region of θ bounded by configurations III_L and III_R where one of the dihedral angles, $\phi_{C_{2,4}} < 0$. A similar occurrence for $r_{A_3} < 0$ is seen in Fig. 6-10 for the same region. This indicates that interference among the facets on Row 3 occurs in this region, and thus the rigid motion becomes physically impossible, i.e., facets would need to penetrate each other. Meanwhile, the central vertices of the bases on Row 3 also collide with each other. To find out the precise boundary angles, a detailed derivation is as follows. On the verge of interference, $r_{A_3} = 0$. Figure 6-3 shows that when $r_{A_0} = 0$, $\phi_{B_{0,4}} = 0$. This can be generalized to other vertices A_i . Hence, if $r_{A_3} = 0$, the corresponding

$$\phi_{B_{3,4}} = 0. \quad (6-19)$$

Using Eq. (6-11a), we have $\phi_{C_{2,4}} = \phi_{B_{3,4}} = 0$, and thus, $\tan(\phi_{C_{2,4}}/2) = 0$. Substituting it into Eq. (6-12c) yields

$$\tan \phi_{C_{2,3}} = \frac{\tan \phi_{C_{2,2}}}{\sin \alpha}. \quad (6-20a)$$

Replacing i with 2 in Eq. (6-12b) gives

$$\tan \frac{\phi_{C_{2,3}}}{2} = \frac{-\sin \alpha \cos \phi_{C_{2,2}} + \sqrt{\sin 2\alpha \sin \phi_{C_{2,2}} \tan \frac{\phi_{C_{2,1}}}{2} + \sin^2 \alpha \cos^2 \phi_{C_{2,2}} - \cos 2\alpha \sin^2 \phi_{C_{2,2}}}}{\sin \phi_{C_{2,2}}}. \quad (6-20b)$$

In these equations, $\phi_{C_{2,2}}$ and $\phi_{C_{2,1}}$ are functions of $\phi_{0,1}$ because of Eqs. (6-11) to (6-13). So two unknowns, $\phi_{C_{2,3}}$ and $\phi_{0,1}$ at the verge of interference, can be obtained by solving simultaneously Eqs. (6-20a) and (6-20b). Three solutions for $\phi_{0,1}$ are obtained:

41.20°, 90.72° and 128.52°. Among them, two are located in the range between $\varphi_{0,1\min} = 60^\circ$ and $\varphi_{0,1\max} = 144.24^\circ$, so interference exists at $90.72^\circ \leq \varphi_{0,1} \leq 128.52^\circ$, i.e., $90.72^\circ \leq \theta \leq 128.52^\circ$. The boundaries of this region are named as configurations III_L and III_R, with $\theta_{III_L} = 90.72^\circ$ and $\theta_{III_R} = 128.52^\circ$.

- Mechanism-structure-mechanism transition

Based on the above analysis, this tube can only have rigid origami motion within two distinct regions in terms of θ : $60^\circ \leq \theta \leq 90.72^\circ$ and $128.52^\circ \leq \theta \leq 144.24^\circ$. At configurations III_L and III_R, the ends of the cylinder close, forming a concealed polyhedron. Between configurations III_L and III_R, panel intersection occurs at the two end rows, which is clearly shown in configuration III in Fig. 6-7. Thus, a real tube made from a non-rigid sheet has to deform as a structure, instead of a mechanism, in order to move from one rigidly foldable region to the other. The tube must therefore undergo a *mechanism-structure-mechanism transition*.

When a tube undergoes a *mechanism-structure-mechanism transition*, rigid origami no longer applies in the structural range. Instead, material deformation in the facets and along the creases has to take place for the tube to change its shape. In fact, when the vertices A_3 meet, the tube is concealed. Any change in a concealed volume requires structural deformation. The existence of such a transition enables the tube be designed to achieve a programmable stiffness. If appropriate materials are used to create very flexible creases and rigid facets, the tube could have reduced stiffness under compression in the rigid origami range, but significantly increased stiffness when its motion enters the so-called structural range. The precise variation of the stiffness depends on the materials used to construct the tube.

The existence of the *mechanism-structure-mechanism transition* depends on the geometrical parameters α , β , m and n of the waterbomb tube. Take $m = 7$, $n = 6$, $\alpha + \beta = \pi/2$ as an example. Figure 6-11 presents r_{A_3}/t vs. θ for various α . It can be seen that the transition occurs only when $44.63^\circ < \alpha < 45.46^\circ$. When $\alpha \geq 45.46^\circ$, the entire motion of the tube from θ_{\min} to θ_{\max} is rigid origami. The motion range is restricted because θ_{\min} and θ_{\max} are also related to α . If $\alpha \leq 44.63^\circ$, the tube only experiences a mechanism-structure transition. That is, it can shrink from configuration V, but the motion range is curtailed due to physical interference and the fact that there is no second rigid origami region. For instance, when $\alpha = 40^\circ$, the motion region is limited to $142.97^\circ \leq \theta \leq 146.54^\circ$.

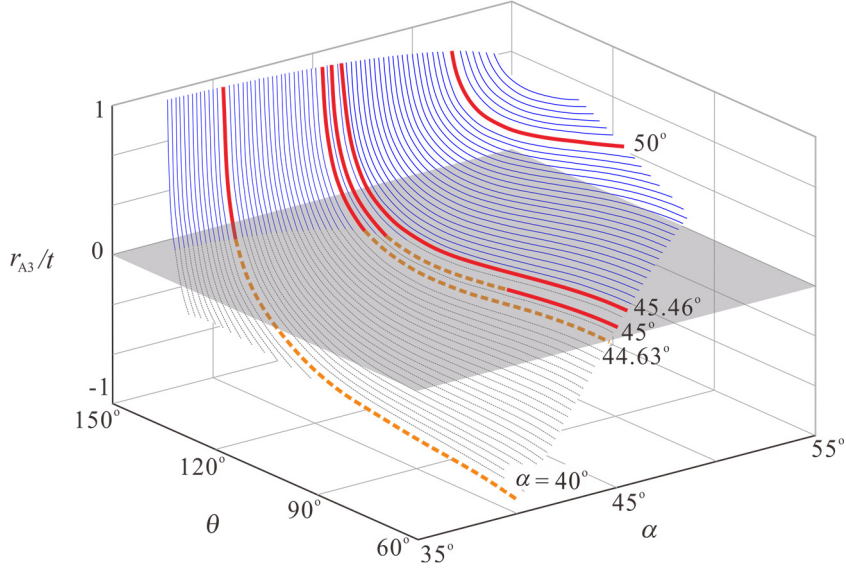


Fig. 6-11 Relationship among r_{A_3}/t , radius of vertices A_3 , θ and α . Some values of α are listed alongside their corresponding curves. The shaded plane is where $r_{A_3} = 0$. Blue solid lines are for $r_{A_3} > 0$ and the grey dashed line for $r_{A_3} < 0$. Physical interference happens when $r_{A_3} < 0$.

- Uniform radius configuration of a tube

Now we are going to check the existence and number of uniform radius configurations for the waterbomb tube. It can be calculated by the kinematics of flat-foldable waterbomb pattern as in Eq. (5-9). When we fold the flat paper into the waterbomb tube, all the waterbomb bases are folded in the identical manner, i.e., all linkages A_i are in the same motion, so do linkages B_i and C_i . The relationship between the dihedral angles $\phi_{B_{0,4}}$ and $\phi_{0,1}$ can be calculated as

$$\tan \frac{\phi_{B_{0,4}}}{2} = \frac{\left[\begin{array}{l} 2 \tan \frac{\phi_{0,1}}{2} (\cos^4 \alpha \sin^2 (\alpha + \beta) \tan^4 \frac{\phi_{0,1}}{2} - 2 \cos^2 \alpha (\cos^2 (\alpha + \beta))) \\ - \cos 2\beta \tan^2 \frac{\phi_{0,1}}{2} - \sin(\beta - \alpha) (2 \sin(\alpha + \beta) + \sin(\beta - \alpha)) \end{array} \right]}{\left[\begin{array}{l} \cos^3 \alpha \sin(\alpha + \beta) (7 \sin \beta - \sin(2\alpha + \beta)) \tan^4 \frac{\phi_{0,1}}{2} + 4(\sin \alpha \sin 2\beta) \\ + \cos \alpha \sin(\alpha + \beta) \sin(\beta - \alpha) \cos \alpha \tan^2 \frac{\phi_{0,1}}{2} - 2 \sin^2(\beta - \alpha) \end{array} \right]}. \quad (6-21)$$

Once both Eqs. (6-10) and (6-21) are satisfied, the flat paper would fold to a waterbomb tube with a uniform radius. Take $n = 6$ and $\alpha = \beta = 45^\circ$ as an example. Substituting Eq. (6-21) into Eq. (6-10) gives

$$\frac{\tan^3 \frac{\varphi_{0,1}}{2}}{3 \tan^2 \frac{\varphi_{0,1}}{2} + 4} = \frac{\sqrt{3} \tan \frac{\varphi_{0,1}}{2} - 1}{\sqrt{3} + \tan \frac{\varphi_{0,1}}{2}}, \quad (6-22)$$

which yields two solutions for $\varphi_{0,1}$ (or θ , due to Eq. (6-9)): 65.88° and 144° . These solutions correspond to configurations II and IV, respectively, given in Fig. 6-4 to Fig. 6-10. When a flat sheet of paper is folded according to the waterbomb pattern, the dihedral angle $\varphi_{0,1}$ will be reduced from 180° . The first reached cylindrical shape will be the configuration IV as it has a larger radius than that of configuration II.

It should be pointed out that the existence of tube configurations with uniform radius is solely decided by parameters α , β and n . It is not related to m . Moreover, the tube with a uniform radius can be obtained only when $n \geq 5$ for $\alpha = \beta = 45^\circ$. Figure 6-12 shows $\varphi_{0,1}/2 - \phi_{B0,4}/2$ vs. $\varphi_{0,1}$ based on Eq. (6-21). It can be seen that there is no intersection between line $180^\circ/n$ and curve $\varphi_{0,1}/2 - \phi_{B0,4}/2$ vs. $\varphi_{0,1}$ when $n < 5$.

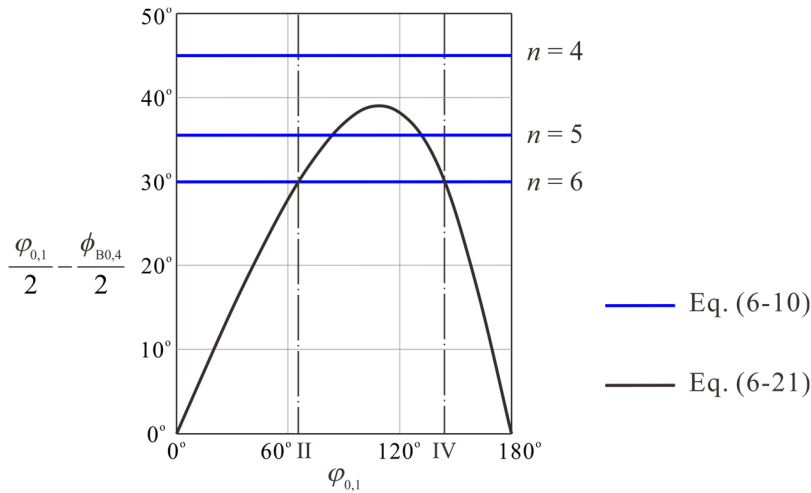


Fig. 6-12 The configuration of tube with a uniform radius to be obtained by folding the flat origami pattern into the tube presenting with curve of $\varphi_{0,1}/2 - \phi_{B0,4}/2$ against $\varphi_{0,1}$ when $\alpha = \beta = 45^\circ$.

The intersection of Eqs. (6-10) and (6-21) varies with the tube geometries. Take the case of $n = 6$, $m = 7$ and $\alpha + \beta = \pi/2$ as an instance. Figure 6-13 presents $\varphi_{0,1}/2 - \phi_{B0,4}/2$ against $\varphi_{0,1}$ for various α . To find out the number of uniform radius configurations, the intersection point should be within the rigid motion range of tube.

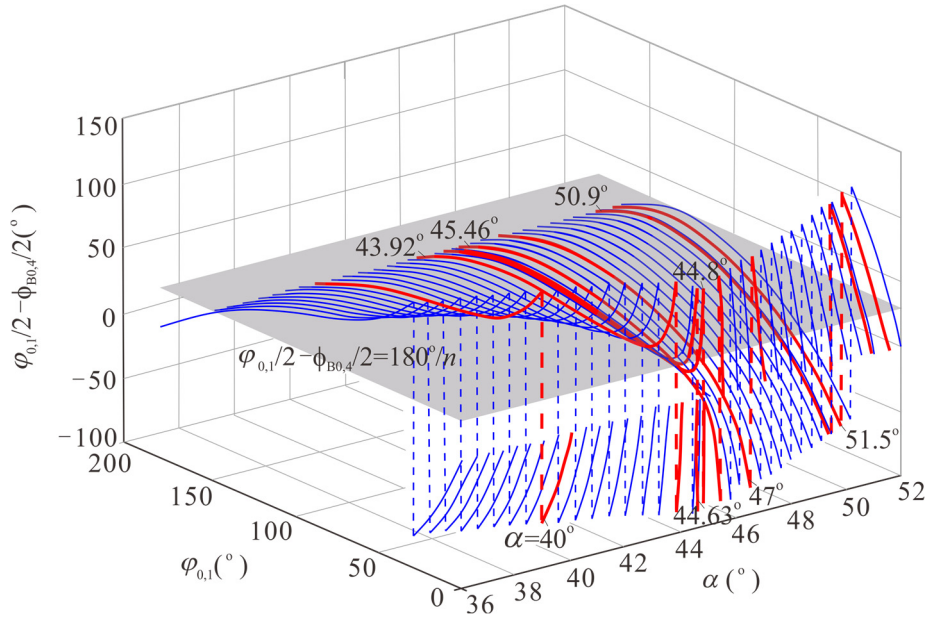


Fig. 6-13 Relationship among $\varphi_{0,1}/2 - \phi_{B0,4}/2$, $\varphi_{0,1}$ and α when $n=6$, $m=7$ and $\alpha + \beta = 90^\circ$.

When $\alpha = 50.9^\circ$, there are two intersection points between $\varphi_{0,1}/2 - \phi_{B0,4}/2$ and $180^\circ/n$ as presented in Fig. 6-14(a) by the blue line and the black line respectively, meaning that the tube has uniform radius configuration at these two points. However, only the larger point is within the rigid motion range of the tube which is represented by the positive part of curve r_{A3}/t as drawn by the red line in Fig. 6-14(a), and therefore only one uniform radius configuration exists.

When $\alpha > 50.9^\circ$, only one solution of $\varphi_{0,1}/2 - \phi_{B0,4}/2 = 180^\circ/n$ exists, which is beyond the rigid motion range of the tube. Therefore, when $\alpha > 50.9^\circ$, no uniform radius configuration can be obtained. An instance of $\alpha = 51.5^\circ$ is presented in Fig. 6-14(b). Notice that when $\alpha > 51.5^\circ$, no rigid motion of the tube exists, which automatically results in the non-existence of the uniform radius configuration.

When $45.46^\circ \leq \alpha < 50.9^\circ$, there are three solutions of $\varphi_{0,1}/2 - \phi_{B0,4}/2 = 180^\circ/n$, two of which are within the rigid motion range, so two uniform radius configurations can be obtained. An instance of this case with $\alpha = 47^\circ$ is presented in Fig. 6-14(c).

When $44.63^\circ < \alpha < 45.46^\circ$, three solutions of $\varphi_{0,1}/2 - \phi_{B0,4}/2 = 180^\circ/n$ exist as well, among which the smallest one is beyond the range of rigid motion. As a result, two uniform radius configuration can be achieved with the *mechanism-structure-mechanism transition*. Figure 6-14(d) presents the case when $\alpha = 44.8^\circ$.

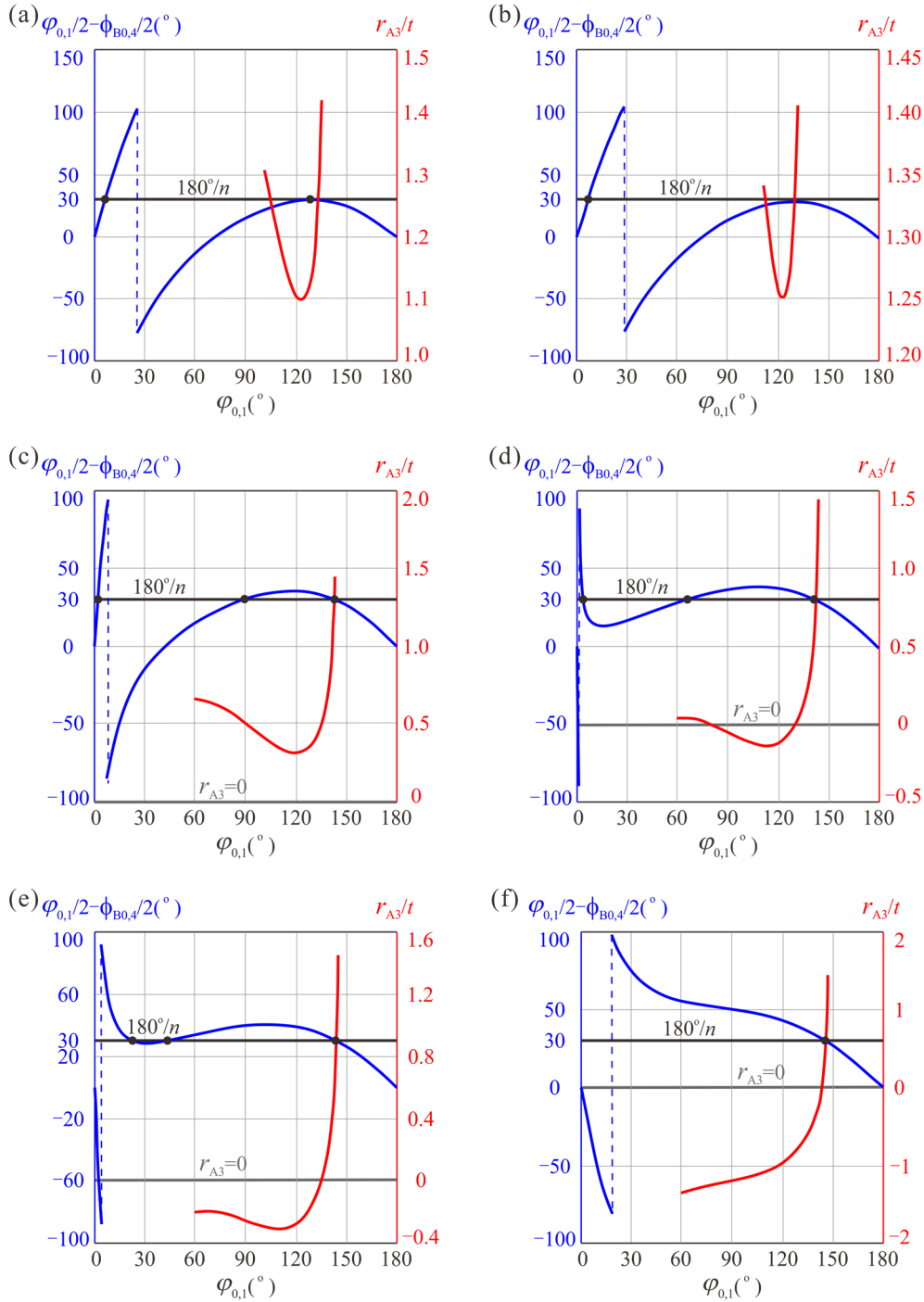


Fig. 6-14 The curves of $\varphi_{0,1}/2 - \phi_{B0,4}/2$ (blue lines), $180^\circ/n$ (black lines) and r_{A3}/t (red lines) against $\varphi_{0,1}$ when $n=6$, $m=7$, $\alpha + \beta = 90^\circ$ and (a) $\alpha = 50.9^\circ$, (b) $\alpha = 51.5^\circ$, (c) $\alpha = 47^\circ$, (d) $\alpha = 44.8^\circ$, (e) $\alpha = 44^\circ$, and (f) $\alpha = 40^\circ$.

When $43.92^\circ \leq \alpha \leq 44.63^\circ$, three solutions of $\varphi_{0,1}/2 - \phi_{B0,4}/2 = 180^\circ/n$ exist. However, two of them are beyond the range of rigid motion. Therefore, only one uniform radius configuration exists. The case when $\alpha = 44^\circ$ is presented in Fig. 6-14(e).

When $\alpha < 43.92^\circ$, there is only one solution of $\phi_{0,1}/2 - \phi_{B_0,4}/2 = 180^\circ/n$ which is within the rigid folding motion range, indicating that there is also one uniform radius configuration. Figure 6-14(f) shows an instance in this case with $\alpha = 40^\circ$.

6.2.3 Contraction of a Tube with an Even Number of Rows

For a waterbomb tube made of an even number of rows (i.e., m is even), there is no equatorial row that is both line- and plane-symmetric. As a result, the EP slices through the middle points of the respective top and bottom edges of the bases on two rows immediately above and below the plane. To facilitate the derivation, the row below is named as *Row 0*, and the row above as *Row 1*, see Fig. 6-15(a). The plane symmetry remains for all the bases. Equations (6-11), (6-12) and (6-13) still hold where $i = 1, 2, \dots, m/2 - 1$. Once the motion of *Row 0* and *Row 1* is determined, the motion of all the other rows can be obtained accordingly.

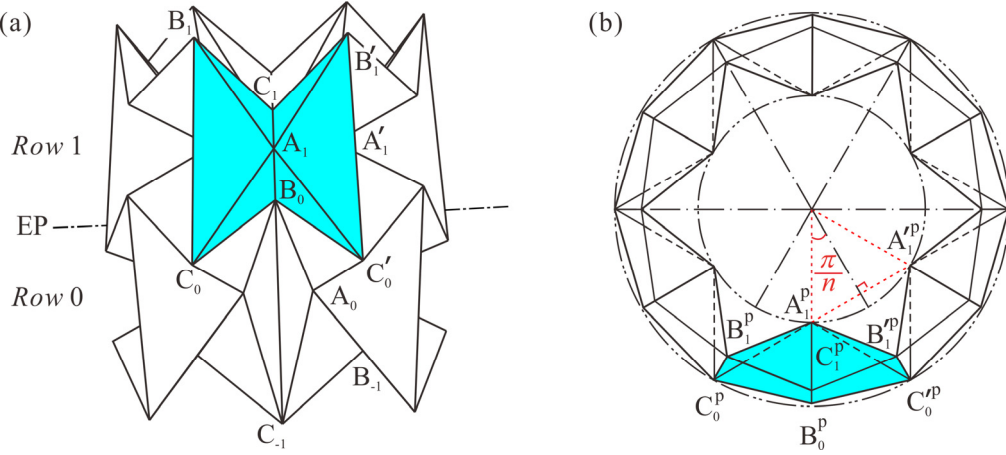


Fig. 6-15 Projection of *Row 1* of the waterbomb tube onto the EP when m is even: (a) 3D view, and (b) top view.

Different from the odd-row case, the linkage \mathbf{A}_0 is no longer line- and plane-symmetric. As the top and bottom halves of the tube moves in the same manner, linkages \mathbf{B}_0 and \mathbf{C}_0 are identical considering the half-a-base shift between adjacent rows, leading to

$$\phi_{0,1} = \phi_{1,4}. \quad (6-23)$$

The projection of *Row 1* onto the EP is presented in Fig. 6-15(b). In order to complete a cylindrical tessellation, the following equation should be satisfied,

$$\cos \phi_{B_0,4} = \cos \phi_{C_0,4} = \frac{t^2 + t^2 - \overline{A_1 A_1'}^2}{2t^2} = 1 - \frac{\overline{A_1^p A_1'^p}^2}{2t^2} = 1 - 2\left(\frac{r_{A1}}{t}\right)^2 \sin^2 \frac{\pi}{n}, \quad (6-24)$$

where

$$r_{A1}=r_{A0}=r_{B0} = \frac{[\cot \alpha - \cot(\alpha + \beta)] \cos \frac{\varphi_{0,1}}{2} \sqrt{t^2 [\cot^2(\alpha + \beta) + \cos^2 \frac{\varphi_{0,1}}{2}] - r_{B0}^2 (1 - \cos \frac{\pi}{n})^2}}{\cot^2(\alpha + \beta) + \cos^2 \frac{\varphi_{0,1}}{2}}, \quad (6-25a)$$

$$r_{B0} = t \sin \frac{\varphi_{0,1}}{2} / \sin \frac{\pi}{n}. \quad (6-25b)$$

Substituting Eq. (6-25) into Eq. (6-24) yields

$$\cos \phi_{B0,4} = \cos \varphi_{0,1} - \frac{\left[2 \sin^2 \frac{\pi}{n} (\cot(\alpha + \beta) - \cot \alpha)^2 \cos^2 \frac{\varphi_{0,1}}{2} (\cot^2(\alpha + \beta) + \cos^2 \frac{\varphi_{0,1}}{2}) - \sin^2 \frac{\varphi_{0,1}}{2} \tan \frac{2\pi}{n} \right]}{[\cot^2(\alpha + \beta) + \cos^2 \frac{\varphi_{0,1}}{2}]^2} + \frac{2 \sin \frac{\pi}{n} [\cot \alpha - \cot(\alpha + \beta)] \sin \varphi_{0,1} \sqrt{\cot^2(\alpha + \beta) + \cos^2 \frac{\varphi_{0,1}}{2} - \sin^2 \frac{\varphi_{0,1}}{2} \tan \frac{2\pi}{n}}}{\cot^2(\alpha + \beta) + \cos^2 \frac{\varphi_{0,1}}{2}}, \quad (6-26)$$

which gives $\phi_{B0,4}$ in terms of $\varphi_{0,1}$.

Due to the identity of linkages \mathbf{B}_0 and \mathbf{C}_0 , we have

$$\phi_{B0,1} = \phi_{C0,1} = \varphi_{0,1}. \quad (6-27)$$

Substituting Eq. (6-27) into Eq. (6-5), the following equations can be obtained,

$$\tan \frac{\varphi_{0,1}}{2} = \frac{\sin \alpha (\sin \phi_{B0,3} \cos \phi_{B0,2} - \cos \beta \sin \phi_{B0,2} \cos \phi_{B0,3}) + \cos \alpha \sin \beta \sin \phi_{B0,2}}{\left[\cos \alpha (\sin(\alpha + \beta) \cos \beta + \cos(\alpha + \beta) \sin \beta \cos \phi_{B0,2}) + \sin \alpha (\sin \beta \cos \phi_{B0,3} \sin(\alpha + \beta) - \cos(\alpha + \beta) \sin \phi_{B0,2} \sin \phi_{B0,3} - \cos(\alpha + \beta) \cos \beta \cos \phi_{B0,2} \cos \phi_{B0,3}) \right]}, \quad (6-28a)$$

$$\tan \frac{\phi_{B0,4}}{2} = \frac{\sin(\alpha + \beta) (\cos \beta \sin \phi_{B0,3} \cos \phi_{B0,2} - \sin \phi_{B0,2} \cos \phi_{B0,3}) + \cos(\alpha + \beta) \sin \beta \sin \phi_{B0,3}}{\left[\cos \alpha (\sin(\alpha + \beta) (\cos \beta \cos \phi_{B0,2} \cos \phi_{B0,3} + \sin \phi_{B0,2} \sin \phi_{B0,3}) + \cos(\alpha + \beta) \sin \beta \cos \phi_{B0,3}) + \sin \alpha (\sin(\alpha + \beta) \sin \beta \cos \phi_{B0,2} - \cos(\alpha + \beta) \cos \beta) \right]}, \quad (6-28b)$$

from which we can obtain $\phi_{B0,2}$ and $\phi_{B0,3}$ in terms of $\varphi_{0,1}$ and $\phi_{B0,4}$.

Eliminating $\phi_{B0,3}$ in Eqs. (6-28a) and (6-28b) give the following equation,

$$\left[\begin{aligned} &U_1 \tan^6 \frac{\phi_{B0,2}}{2} + U_2 \tan^5 \frac{\phi_{B0,2}}{2} + U_3 \tan^4 \frac{\phi_{B0,2}}{2} + U_4 \tan^3 \frac{\phi_{B0,2}}{2} \\ &+ U_5 \tan^2 \frac{\phi_{B0,2}}{2} + U_6 \tan \frac{\phi_{B0,2}}{2} + U_7 \end{aligned} \right] = 0, \quad (6-29)$$

where

$$U_1 = 4 \sin \alpha \sin 2\alpha \left(\tan^2 \frac{\phi_{B0,4}}{2} - \tan^2 \frac{\varphi_{0,1}}{2} \right),$$

$$U_2 = 16 \sin 2\alpha \sin \beta \tan \frac{\varphi_{0,1}}{2} \left(\tan^2 \frac{\phi_{B0,4}}{2} + 1 \right),$$

$$U_3 = \begin{bmatrix} -[16 \sin 2\alpha \sin \beta \cos(\alpha + \beta) \tan^2 \frac{\varphi_{0,1}}{2} + 11 \cos \alpha + 5 \cos 3\alpha \\ + \cos(3\alpha + 2\beta) - 7 \cos(\alpha - 2\beta) - 10 \cos(\alpha + 2\beta)] \tan^2 \frac{\phi_{B0,4}}{2} \\ -2 \sin \alpha [5 \sin 2(\alpha + \beta) + \sin 2\alpha + 3 \sin 2\beta] \tan^2 \frac{\varphi_{0,1}}{2} - 32 \cos \alpha \sin^2 \beta \end{bmatrix},$$

$$U_4 = 16 \sin \beta \sin(\alpha + \beta) [3 \cos(\alpha + \beta) + \cos(\alpha - \beta)] \tan \frac{\varphi_{0,1}}{2} \left(\tan^2 \frac{\phi_{B0,4}}{2} + 1 \right),$$

$$U_5 = \begin{bmatrix} -4 \{ [4 \sin 2\beta \cos(\alpha + \beta) \sin(2\alpha + \beta) \tan^2 \frac{\varphi_{0,1}}{2} - \sin 2\alpha \sin(\alpha + 2\beta) \\ -2 \sin 2(\alpha + \beta) \sin(\alpha - 2\beta)] \tan^2 \frac{\phi_{B0,4}}{2} + 2 \sin(\alpha + 2\beta) [\sin 2(\alpha + \beta) \\ + \sin \alpha \cos \alpha] \tan^2 \frac{\varphi_{0,1}}{2} + 4 \sin \beta \sin 2\beta \cos(\alpha + \beta) \} \end{bmatrix},$$

$$U_6 = 16 \sin 2\beta \sin(\alpha + 2\beta) \cos(\alpha + \beta) \tan \frac{\varphi_{0,1}}{2} \left(\tan^2 \frac{\phi_{B0,4}}{2} + 1 \right), \text{ and}$$

$$U_7 = \begin{bmatrix} -8 \cos \beta \cos(\alpha + \beta) \{ [\sin 2(\alpha + \beta) \sin \beta \tan^2 \frac{\varphi_{0,1}}{2} - \sin^2 \alpha] \tan^2 \frac{\phi_{B0,4}}{2} \\ + \sin^2(\alpha + 2\beta) \tan^2 \frac{\varphi_{0,1}}{2} \} \end{bmatrix},$$

which are all functions of $\varphi_{0,1}$ and $\phi_{B0,4}$.

Thus $\phi_{B0,2}$ can be obtained by solving Eq. (6-29). Using Eqs. (6-28a) and (6-28b) again, we find

$$\tan \frac{\phi_{B0,3}}{2} = \frac{\sin \alpha \left(\tan \frac{\phi_{B0,1}}{2} - \cos \phi_{B0,2} \tan \frac{\phi_{B0,4}}{2} \right) - \cos \alpha \sin \phi_{B0,2}}{\sin \phi_{B0,2} \tan \frac{\phi_{B0,4}}{2}}, \quad \phi_{B0,5} = \phi_{B0,3}, \quad \phi_{B0,6} = \phi_{B0,2}; \quad (6-30a)$$

$$\varphi_{0,2} = \varphi_{0,6} = \phi_{B0,3}, \quad \varphi_{0,3} = \varphi_{0,5},$$

$$\tan \frac{\varphi_{0,5}}{2} = \frac{\left[\begin{aligned} & \cos \varphi_{0,6} + \tan \frac{\varphi_{0,1}}{2} \cos \alpha \sin \varphi_{0,6} - \left\{ (\cos \varphi_{0,6} + \tan \frac{\varphi_{0,1}}{2} \cos \alpha \sin \varphi_{0,6})^2 \right. \\ & \left. - (2 \cos^2 \alpha + \cos 2\alpha) \left[\sin \varphi_{0,6} - \tan \frac{\varphi_{0,1}}{2} \cos \alpha (\cos \varphi_{0,6} + 1) \right]^2 \right. \\ & \left. - 2 \cos \alpha \tan \frac{\varphi_{0,1}}{2} \left[\sin \varphi_{0,6} - \tan \frac{\varphi_{0,1}}{2} \cos \alpha (\cos \varphi_{0,6} + 1) \right] \right\}^{1/2}}{\sin \varphi_{0,6} - \tan \frac{\varphi_{0,1}}{2} \cos \alpha (\cos \varphi_{0,6} + 1)} \right], \\ \tan \frac{\varphi_{0,4}}{2} &= \frac{\sin \alpha (\sin \varphi_{0,6} \cos \varphi_{0,5} - \cos 2\alpha \sin \varphi_{0,5} \cos \varphi_{0,6}) - \cos \alpha \sin 2\alpha \sin \varphi_{0,5}}{\left[\begin{aligned} & -\cos \alpha (\sin \alpha \cos 2\alpha \cos \varphi_{0,6} \cos \varphi_{0,5} + \sin \alpha \sin \varphi_{0,6} \sin \varphi_{0,5} \\ & + \cos \alpha \sin 2\alpha \cos \varphi_{0,5}) + \sin \alpha (\sin \alpha \sin 2\alpha \cos \varphi_{0,6} - \cos \alpha \cos 2\alpha) \end{aligned} \right]}; \quad (6-30b)$$

$$\varphi_{C0,1} = \varphi_{B0,1}, \quad \varphi_{C0,2} = \varphi_{C0,6} = \varphi_{B0,2}, \quad \varphi_{C0,3} = \varphi_{C0,5} = \varphi_{B0,3}, \quad \varphi_{C0,4} = \varphi_{B0,4}; \quad (6-30c)$$

$$\varphi_{1,1} = \varphi_{0,4}, \quad \varphi_{1,2} = \varphi_{1,6} = \varphi_{0,5}, \quad \varphi_{1,3} = \varphi_{1,5} = \varphi_{0,6}, \quad \varphi_{1,4} = \varphi_{0,1}. \quad (6-30d)$$

Therefore, Eqs. (6-11) to (6-13), (6-26), (6-27), (6-29) and (6-30) form the kinematic set of the generalized waterbomb tube with even-number row. It can be seen that only one free variable $\varphi_{0,1}$ is needed to determine the motion of the waterbomb tube, meaning the DOF of the tube in this case is again one. The general behaviour of these tubes turned out to be similar to those when m is odd.

Different from the odd-row case, only two constraints hold for the rigid motion of the waterbomb tube without interference: $\varphi_{m/2,1} = \pi$ and $\phi_{Bi,4} \geq 0$ ($i = 0, 1, \dots, m/2$). This is due to that Row 0 and Row 1 are in general impossible to be fully squeezed simultaneously. One exception is all rows being fully squeezed with some specific geometrical parameters. This is not taken into consideration since the number of rows makes no sense in this case. $\varphi_{0,1\min}$ can be found from Eq. (6-26) for $\phi_{B0,4} > 0$. On the other hand, when $\varphi_{m/2,1} = \pi$, letting the square root of $\tan(\varphi_{m/2,6}/2)$ in Eq. (6-13b) be zero leads to

$$\left[\begin{aligned} & \left(\cos \varphi_{m/2,5} + \tan \frac{\varphi_{m/2,4}}{2} \cos \alpha \sin \varphi_{m/2,5} \right)^2 - (2 \cos^2 \alpha + \cos 2\alpha) \left[\sin \varphi_{m/2,5} - (\cos \varphi_{m/2,5} \right. \\ & \left. + 1) \cos \alpha \tan \frac{\varphi_{m/2,4}}{2} \right]^2 - 2 \cos \alpha \tan \frac{\varphi_{m/2,4}}{2} \left[\sin \varphi_{m/2,5} - \tan \frac{\varphi_{m/2,4}}{2} \cos \alpha (1 + \cos \varphi_{m/2,5}) \right] \end{aligned} \right] = 0. \quad (6-31)$$

Since $\varphi_{m/2,5}$ and $\varphi_{m/2,4}$ are functions of $\varphi_{0,1}$ because of Eqs. (6-11) to (6-13), $\varphi_{0,1\max}$ can now be obtained. Intersecting with the solutions of $\phi_{Bi,4} \geq 0$ ($i = 0, 1, \dots, m/2$), the range of rigid motion without interference can be obtained. To acquire the corresponding $\varphi_{0,1}$ when physical interference occurs, let

$\phi_{B(m/2),4} = 0$, which is equivalent to $\phi_{C(m/2-1),4} = 0$ from Eq. (6-11a). We can recycle simultaneous equations in Eqs. (6-11) to (6-13) to obtain $\varphi_{0,1}$, where the row number i in those equation is replaced by $m/2-1$. Now there are

$$\left[\begin{array}{l} \sin(\alpha + \beta)(\cos \beta \sin \phi_{C(m/2-1),3} \cos \phi_{C(m/2-1),2} \\ -\sin \phi_{C(m/2-1),2} \cos \phi_{C(m/2-1),3}) + \cos(\alpha + \beta) \sin \beta \sin \phi_{C(m/2-1),3} \end{array} \right] = 0, \quad (6-32a)$$

$$\tan \frac{\phi_{C(m/2-1),3}}{2} = \frac{\left[\begin{array}{l} \sin \alpha \cos(\alpha + \beta) \tan \frac{\phi_{C(m/2-1),1}}{2} \sin \phi_{C(m/2-1),2} + \sin \alpha \cos \phi_{C(m/2-1),2} \\ -\{[\sin \alpha \cos \phi_{C(m/2-1),2} + \sin \alpha \cos(\alpha + \beta) \tan \frac{\phi_{C(m/2-1),1}}{2} \sin \phi_{C(m/2-1),2}]^2 \\ -\sin(\alpha + \beta)[\sin(\alpha + \beta) \cos(\beta - \alpha) \tan \frac{\phi_{C(m/2-1),1}}{2} + \cos(\alpha + \beta) \sin(\beta \\ -\alpha) \tan \frac{\phi_{C(m/2-1),1}}{2} \cos \phi_{C(m/2-1),2} - \sin(\beta - \alpha) \sin \phi_{C(m/2-1),2}] [\cos(\alpha \\ + \beta) \tan \frac{\phi_{C(m/2-1),1}}{2} (\cos \phi_{C(m/2-1),2} + 1) - \sin \phi_{C(m/2-1),2}] \}^{1/2} \end{array} \right]}{\sin(\alpha + \beta) [\cos(\alpha + \beta) \tan \frac{\phi_{C(m/2-1),1}}{2} (\cos \phi_{C(m/2-1),2} + 1) - \sin \phi_{C(m/2-1),2}]}, \quad (6-32b)$$

from which we obtain $\varphi_{0,1}$ on the verge of interference.

Taking $n = 6$, $m = 8$ and $\alpha = \beta = 45^\circ$ as an example, $\varphi_{0,1\min} = 59.22^\circ$ and $\varphi_{0,1\max} = 144.09^\circ$ from Eqs. (6-26) and (6-31), and the corresponding configurations of the tube are named as configurations I and V, respectively. By solving simultaneous equations as Eqs. (6-32a) and (6-32b) with $\phi_{C3,4} = \phi_{B4,4} = 0$, two solutions of $\varphi_{0,1}$ can be obtained: 81° and 140.94° , indicating that interferences exist when $81^\circ \leq \varphi_{0,1} \leq 140.94^\circ$. The boundaries are referred to as configurations III_L and III_R.

Figure 6-16(a-b) shows the kinematic relationships of the dihedral angles $\phi_{Bi,4}$ and radii of vertices with respect to $\varphi_{0,1}$, respectively. At configurations II and IV, corresponding to $\varphi_{0,1} = 65.88^\circ$ and 144° , respectively, linkages A_i , B_i or C_i are all in the identical configurations, which are configurations corresponding to the tube with a uniform radius. These configurations are the same as those of a tube with odd rows. Between configurations III_L and III_R, it is clear that both $\phi_{B4,4}$ and r_{A4} are negative. Hence, the *mechanism-structure-mechanism transition* also exists for tubes made from an even number of rows.

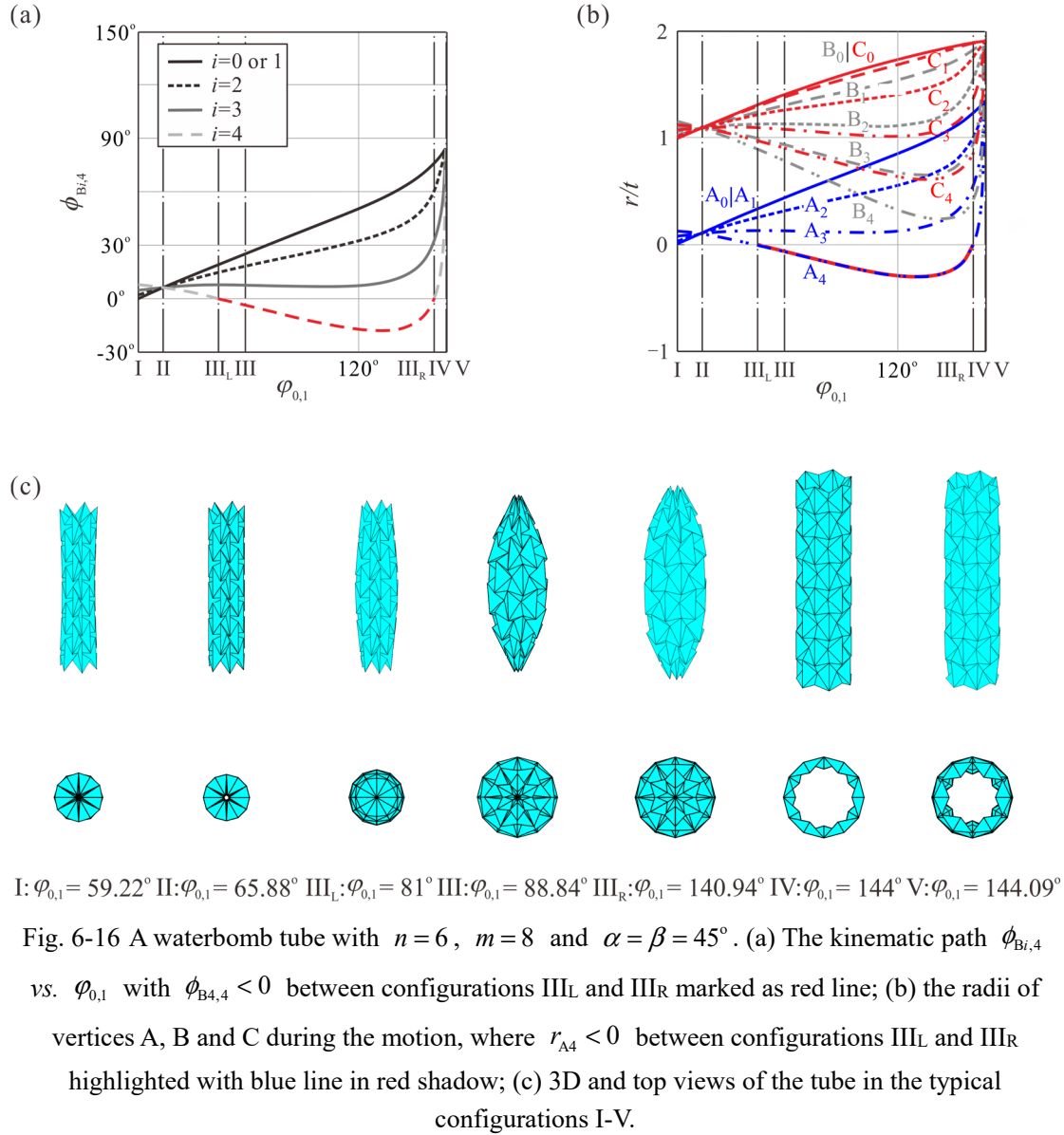


Fig. 6-16 A waterbomb tube with $n = 6$, $m = 8$ and $\alpha = \beta = 45^\circ$. (a) The kinematic path $\phi_{B_i,4}$ vs. $\phi_{0,1}$ with $\phi_{B_{4,4}} < 0$ between configurations III_L and III_R marked as red line; (b) the radii of vertices A, B and C during the motion, where $r_{A_4} < 0$ between configurations III_L and III_R highlighted with blue line in red shadow; (c) 3D and top views of the tube in the typical configurations I-V.

Similar to the case of an odd m , the radii of vertex A_i rise with the increase of α . For instance, by preserving $m = 8$, the *mechanism-structure-mechanism transition* occurs only when $44.66^\circ < \alpha < 46.26^\circ$. If $\alpha \geq 46.26^\circ$, r_{A_4} are positive and the rigid origami range of the tube decreases when α gets larger. When $\alpha \leq 44.66^\circ$, the range of rigid origami range shrinks when α decreases.

Therefore, once the geometrical parameters are given, the range of the input kinematic variable $\phi_{0,1}$ under rigid contraction folding can be figured out definitely, which is not only related to the design angles α and β , but also to m and n . On the other hand, the geometric conditions of α and β for the generalized waterbomb tube with rigid foldability can be obtained by making the solutions of the kinematic equation set be a non-void set.

6.3 Long and Truncated Tubes

6.3.1 Long Tubes

For longer tubes with additional rows, a number of conclusions can be drawn based on the previous analysis. First, for the same pattern with larger m , θ_{\max} will be further reduced when more rows are added. Second, some tubes will exhibit a *mechanism-structure-mechanism transition* depending on pattern parameters α and β . It is particularly interesting to consider a tube with $n=6$ and $\alpha=\beta=45^\circ$. The interference at the two ends of the tube occurs sooner with an increase in the row number m . For instance, when $m=13$, there are two rigid origami regions around the two uniform radius configurations: $60^\circ \leq \theta \leq 71.64^\circ$ and $143.94^\circ \leq \theta \leq 144.06^\circ$. In the subsequent discussions, the focus is only put on the first range as the second range is rather narrow.

For the first range, the radius of each vertex on the equatorial row (r_{A_0} , r_{B_0} , r_{C_0} , $r_{B_{-1}}$, $r_{C_{-1}}$) and the end row (r_{A_6} , r_{B_6} , r_{C_6} , r_{B_5} , r_{C_5}) where interference may occur vs. θ are plotted as in Fig. 6-17(a), where the blue, black and red lines represent the radii of vertices A, B and C, respectively. It can be seen from Fig. 6-17(a) that $r_{A_0} = 0$ at configuration I and $r_{A_6} = 0$ at configuration III_L. The curves of $r_{B_{-1}}$ and r_{C_0} coincide, so do the curves of $r_{C_{-1}}$ and r_{B_0} , which means the equatorial row is in both line and plane symmetry and creases $B_{-1}C_0$ and B_0C_{-1} are parallel to the axis of the tube. However, the curves of r_{B_5} and r_{C_5} approximate to the curves of r_{C_6} and r_{B_6} respectively, meaning that the creases B_5C_6 and B_6C_5 on two sides of bases on Row 6 (Fig. 6-18) become almost parallel to the axis of the tube. This particular configuration indicates that more rows can be added to the tube, but the fundamental behaviour of the tube is governed by a tube with 13 consecutive rows. Any additional rows simply repeat the motion of all or part of 13 rows. As a result, a tube with $m > 13$ will assume a periodic wave shape and its motion range is identical to that of a tube with 13 rows. This is verified by a tube with 25 rows. The radius of vertex A_i (plotted in Fig. 6-17(b)) shows that at the configuration I, it increases from $i=0$ to $i=6$ and subsequently decreases from $i=7$ to $i=12$, which reveals the wave-like shape of the tube. So do other configurations for $60^\circ < \theta < 71.64^\circ$. The tube with two completed waves is presented in Fig. 6-18.

The waterbomb tubes with wave-like shape exist for various n and α . θ_{III_L} , angle θ at configuration III_L can be obtained where $r_{A_i} = 0$. When $\alpha = \beta = 45^\circ$, the

wave-shaped tube with rigid foldability exists only when $n \geq 5$, as there is no uniform radius configuration for the tube when $n < 5$. The changes of θ_I , θ_{II} (angles θ corresponding to configurations I, II, respectively) and θ_{III_L} are plotted in Fig. 6-19(a) with n taken from 5 to 20. On the other hand, θ_I , θ_{II} and θ_{III_L} vs. α when $\alpha + \beta = \pi/2$ are plotted in Fig. 6-19(b) where n is chosen to be 6.

Meanwhile, when n varies, α_{\min} , the minimum value of α is obtained by letting $\theta_I = \theta_{II}$, which gives

$$\left(-\tan^4 \frac{\pi}{n} + 4 \tan^2 \frac{\pi}{n} + 4\right) \cos^4 \alpha_{\min} - 2 \tan^2 \frac{\pi}{n} \cos^2 \alpha_{\min} - 1 = 0, \quad (6-33)$$

If $\alpha < \alpha_{\min}$, the wave-shaped tube without interference does not exist. Similarly, α_{\max} , the maximum value of α , can be obtained by letting $\theta_{II} = \theta_{III_L}$.

For the tubes with even number of rows, the middle two rows are in plane symmetry, and the top and bottom halves of the tube, partitioned by the EP, have the same motion. When $n = 6$, $\alpha = \beta = 45^\circ$, and $m = 12$, the creases connecting the adjacent two bases on Rows $-5, 0, 1$ and 6 are all nearly parallel to the axis of the tube. As a result, more rows can be added to the tube, and the fundamental behaviour of the tube is governed by a tube with 12 consecutive rows.

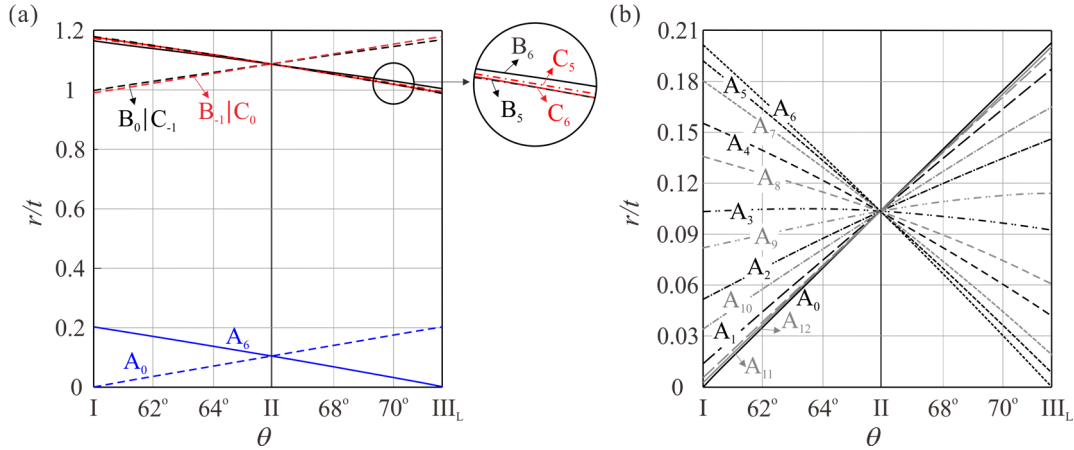


Fig. 6-17 Radii of some vertices of the tube vs. θ when $n = 6$ and $\alpha = \beta = 45^\circ$. At I: $\theta = 60^\circ$; II: $\theta = 65.88^\circ$; III_L: $\theta = 71.64^\circ$. (a) Radius of vertex on the equatorial row (r_{A_0} , r_{B_0} , r_{C_0} , $r_{B_{-1}}$, $r_{C_{-1}}$) and the end row (r_{A_6} , r_{B_6} , r_{C_6} , r_{B_5} , r_{C_5}) when $m = 13$. (b) The radius of vertex A_i for a longer tube when $m = 25$.

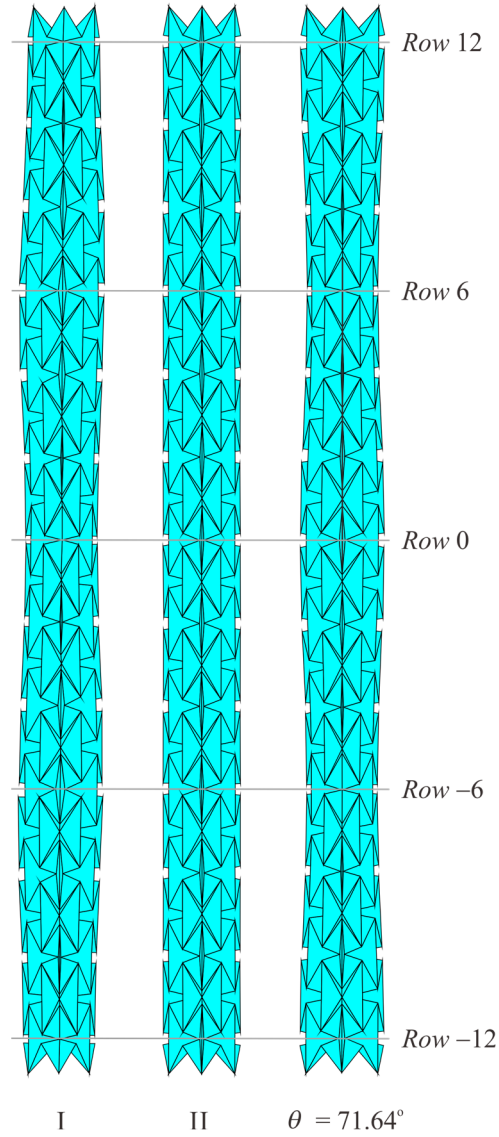


Fig. 6-18 Three configurations of a long tube with $n = 6$, $m = 25$ and $\alpha = \beta = 45^\circ$ when it undergoes rigid motion.

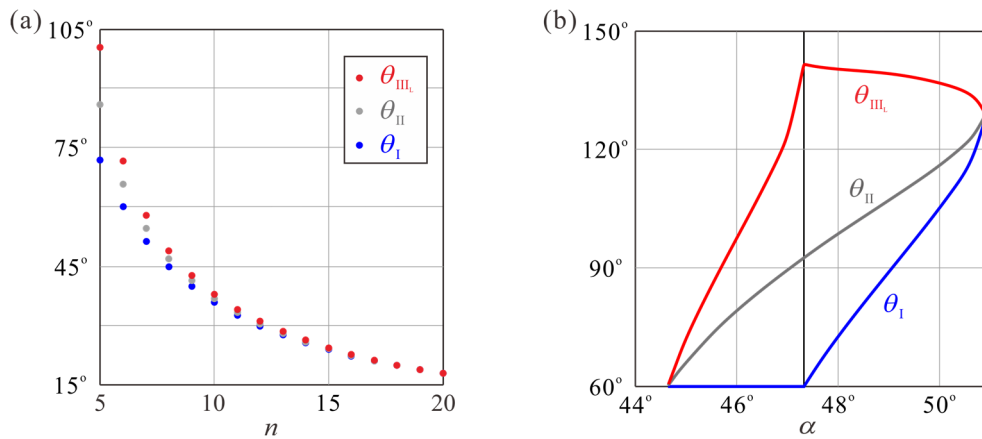


Fig. 6-19 The changes of θ_I , θ_{II} and θ_{III} vs. (a) various n when $\alpha = \beta = 45^\circ$, and (b) various α when $n = 6$ and $\alpha + \beta = 90^\circ$.

6.3.2 Truncated Tubes

It is particularly interesting to note that a shorter tube can also be obtained by truncating a number of rows off a long tube shown in Fig. 6-18. Not only can we obtain a tube whose top and bottom halves mirror each other, but it is also possible to have one with more rows above the EP than below it, or vice versa. Figure 6-20(a) shows such a truncated tube of 8 rows, 5 above and 2 below *Row 0*. This 8-row tube is actually able to follow the motion of an odd row tube ($m = 11$) during *the contraction phase*, with bases on *Row 0* being kept in both plane and line symmetry. Moreover, the same 8-row tube may also track the motion of an even row tube as shown in Fig. 6-20(b), this particular tube can in fact switch from an odd row tube motion to an even row tube motion at the configurations where it has the uniform radius. For instance, the tube can also expand from configuration I', to II (the middle configurations in Figs. 6-20(a-b)), and then further to III_L (Fig. 6-20(b)). In the language of kinematics, a bifurcation of motion exists, and the uniform radius configuration is the bifurcation configuration.

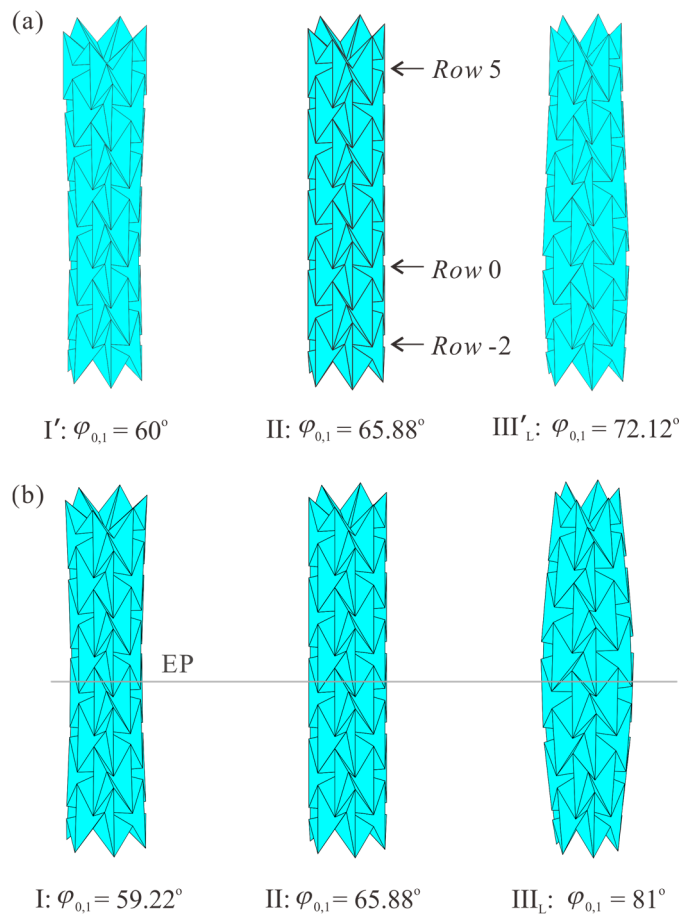


Fig. 6-20 (a) Three configurations of an 8-row tube obtained by truncating a long tube. It keeps on the motion path of an odd row tube. (b) Three configurations of the same tube if it tracks the motion of an even-row tube (This is in fact a reproduction of first three configurations of Fig. 6-16(c)).

6.4 Twist Motion

6.4.1 Rigid Twist Motion

Now we examine the motion of the tube during *the twist phase*. For tubes made of an odd number of rows, it is found that *the contraction phase* of the tube motion terminates at the fully squeezed configuration where all vertices A_0 coincide, see Fig. 6-21(a), that is, r_{A_0} , the radius of the circle formed by all vertices A_0 about the axis of waterbomb tube, becomes 0. Consequently, the dihedral angle $\phi_{B_0,4}$ reaches zero. Every crease B_0C_{-1} is parallel to the axis of the tube. For this instance, the spherical $6R$ linkage at the central vertex A_0 of a base on Row 0 has just completed its motion with both plane and line symmetry, whereas the spherical $6R$ linkage at the central vertex of bases on other rows has only plane symmetry. To facilitate the twist motion, the plane- and line-symmetric spherical $6R$ linkage at vertex A_0 needs to activate its tilting motion with only line symmetry (i.e., a rotational symmetry where bottom half of the linkage reproduces the motion of the top half about an axis passing through A_0 and perpendicular to the axis of the tube), see Fig. 6-21(b), where the tube is partially twisted. Due to the line symmetry, we have

$$\delta_{0,1} = \delta_{0,4}, \quad \delta_{0,2} = \delta_{0,5}, \quad \delta_{0,3} = \delta_{0,6}. \quad (6-34)$$

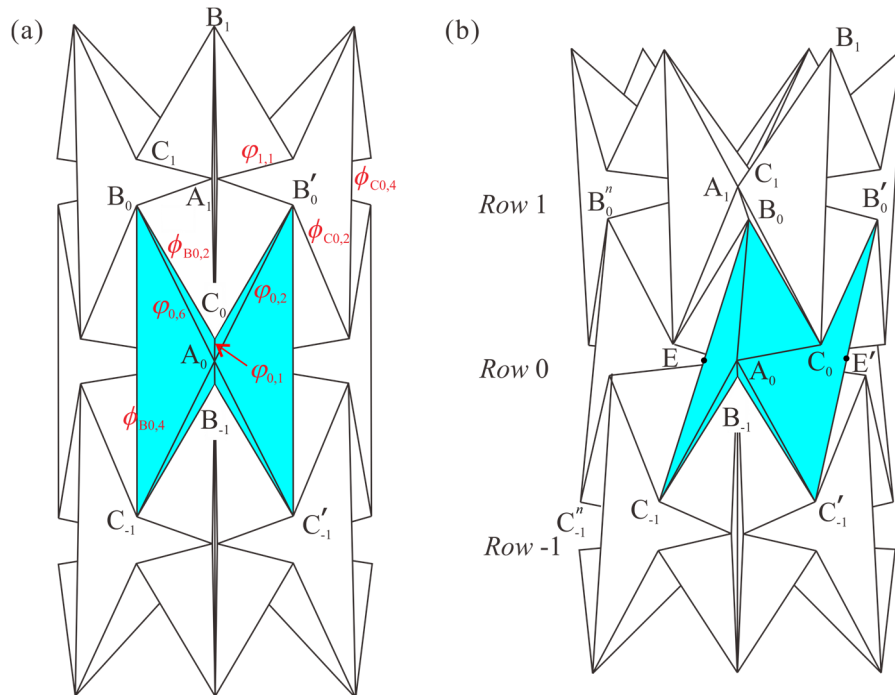


Fig. 6-21 *The twist phase* of the waterbomb tube. (a) 3D view of a portion of tube when it completes the *the contraction phase*. Some of the representative vertices and dihedral angles are marked. Only three rows of the tube are shown: the equatorial row and two rows immediately adjacent to it. (b) Partially twist configuration of the tube.

By applying Eq. (6-34) to the closure equation (Eq. (5-1)), the following equation can be obtained

$$\tan \delta_{0,1} = \frac{2\cos\alpha[\sin \delta_{0,2} + \sin \delta_{0,3} - \sin(\delta_{0,2} + \delta_{0,3})]}{(1 + 2\cos^2\alpha)\cos\delta_{0,2}\cos\delta_{0,3} - \sin\delta_{0,2}\sin\delta_{0,3} - 2\cos^2\alpha(\cos\delta_{0,2} + \cos\delta_{0,3}) + \cos 2\alpha}. \quad (6-35)$$

Applying the relationship between the kinematic variables and dihedral angles to Eqs. (6-34) and (6-35), the kinematic relationship of the generalized waterbomb base presented by the dihedral angles is

$$\tan \varphi_{0,1} = \frac{2\cos\alpha[\sin \varphi_{0,2} + \sin \varphi_{0,3} + \sin(\varphi_{0,2} + \varphi_{0,3})]}{(1 + 2\cos^2\alpha)\cos\varphi_{0,2}\cos\varphi_{0,3} - \sin\varphi_{0,2}\sin\varphi_{0,3} + 2\cos^2\alpha(\cos\varphi_{0,2} + \cos\varphi_{0,3}) + \cos 2\alpha}, \quad (6-36a)$$

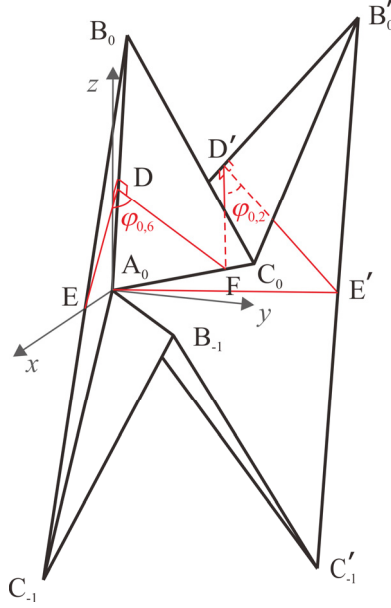
$$\varphi_{0,1} = \varphi_{0,4}, \quad \varphi_{0,2} = \varphi_{0,5}, \quad \varphi_{0,3} = \varphi_{0,6}. \quad (6-36b)$$

At the fully squeezed configuration as shown in Fig. 6-21(b), all the vertices A_0 at the middle row meet at a single point on the axis of the waterbomb tube, and all points E and E' in the same row form a circle with point A_0 as the centre and angle $\angle EA_0E'$ as one of the sector angles, where E and E' are the midpoints of edges B_0C_{-1} and $B'_0C'_{-1}$ respectively. Since each waterbomb base in the same row has identical motion, angle $\angle EA_0E'$ should be equal to $2\pi/n$. Now let us set up a coordinate system as shown in Fig. 6-22 with its origin at A_0 , x along the direction of $\overline{A_0E}$, and z perpendicular to the plane EA_0E' . Take points D and D' as the feet of the perpendiculars of creases A_0B_0 and $A_0B'_0$ passing through points E and E' , respectively. Making $DF \perp A_0B_0$ and $D'F \perp A_0B'_0$ with F as the point on crease A_0C_0 , the following relationship can be obtained

$$\varphi_{0,2} = \angle FD'E' \quad \text{and} \quad \varphi_{0,6} = \angle FDE. \quad (6-37)$$

Since $\angle EA_0E' = 2\pi/n$, the coordinates of E and E' are $(t, 0, 0)$ and $(t \cos(2\pi/n), t \sin(2\pi/n), 0)$, respectively. Should the coordinates of B_0 , D , F , B'_0 and D' are denoted by $(x_{B_0}, y_{B_0}, z_{B_0})$, (x_D, y_D, z_D) , (x_F, y_F, z_F) , $(x_{B'_0}, y_{B'_0}, z_{B'_0})$ and $(x_{D'}, y_{D'}, z_{D'})$, the following vectors can be obtained

$$\begin{aligned} \overline{ED} &= (x_D - t, y_D, z_D), \quad \overline{FD} = (x_D - x_F, y_D - y_F, z_D - z_F), \\ \overline{E'D'} &= (x_{D'} - t \cos \frac{2\pi}{n}, y_{D'} - t \sin \frac{2\pi}{n}, z_{D'}), \quad \overline{FD'} = (x_{D'} - x_F, y_{D'} - y_F, z_{D'} - z_F). \end{aligned} \quad (6-38)$$


 Fig. 6-22 The geometry of the line-symmetric linkage A_0 on the equatorial row

According to the space geometry, the length of each segment can be calculated as

$$\begin{aligned} \overline{A_0D} &= \overline{A_0D'} = t \sin \alpha, \quad \overline{DE} = \overline{D'E'} = t \cos \alpha, \\ \overline{B_0F} &= \overline{B'_0F} = t\sqrt{1-3\sin^2\alpha+3\sin^4\alpha}/\sin\alpha\cos\alpha, \quad \overline{DF} = \overline{D'F} = t \sin^2\alpha / \cos\alpha, \\ \overline{A_0B_0} &= \overline{A_0B'_0} = t / \sin\alpha, \quad \overline{A_0F} = t \tan\alpha. \end{aligned} \quad (6-39)$$

So we have

$$\begin{aligned} x_D^2 + y_D^2 + z_D^2 &= t^2 \sin^2 \alpha, \quad x_{D'}^2 + y_{D'}^2 + z_{D'}^2 = t^2 \sin^2 \alpha, \\ (x_D - a)^2 + y_D^2 + z_D^2 &= t^2 \cos^2 \alpha, \quad (x_{D'} - t \cos \frac{2\pi}{n})^2 + (y_{D'} - t \sin \frac{2\pi}{n})^2 + z_{D'}^2 = t^2 \cos^2 \alpha, \\ x_{B_0}^2 + y_{B_0}^2 + z_{B_0}^2 &= \frac{t^2}{\sin^2 \alpha}, \quad x_{B'_0}^2 + y_{B'_0}^2 + z_{B'_0}^2 = \frac{t^2}{\sin^2 \alpha}, \end{aligned} \quad (6-40a)$$

$$\begin{aligned} x_D x_F + y_D y_F + z_D z_F &= t^2 \sin^2 \alpha, \quad x_{D'} x_F + y_{D'} y_F + z_{D'} z_F = t^2 \sin^2 \alpha, \\ x_{B_0} x_F + y_{B_0} y_F + z_{B_0} z_F &= t^2, \quad x_{B'_0} x_F + y_{B'_0} y_F + z_{B'_0} z_F = t^2. \end{aligned} \quad (6-40b)$$

Additionally, since $A_0E \perp B_0E$ and $\overline{B_0E} = \overline{B'_0E'} = t \cos \alpha / \sin \alpha$, there are

$$x_{B_0} = t \quad \text{and} \quad \cos \frac{2\pi}{n} x_{B'_0} + \sin \frac{2\pi}{n} y_{B'_0} = t. \quad (6-41)$$

According to the line symmetry of the waterbomb base, the relationship between y coordinates of B_0 and B'_0 is

$$y_{B_0} = (y_{B'_0} - t \sin \frac{2\pi}{n}) / \cos \frac{2\pi}{n}. \quad (6-42)$$

Substituting Eqs. (6-41) and (6-42) to Eq. (6-40) yields

$$z_{B_0} = z_{B'_0} = \frac{\sqrt{-y_{B'_0}^2 + 2t \sin \frac{2\pi}{n} y_{B'_0} + t^2 (\cos^2 \frac{2\pi}{n} / \sin^2 \alpha - 1)}}{\cos \frac{2\pi}{n}},$$

$$[(1 - \cos \frac{2\pi}{n}) y_{B'_0} - t \sin \frac{2\pi}{n}] y_F = [(1 - \cos \frac{2\pi}{n}) t - \sin \frac{2\pi}{n} y_{B'_0}] x_F. \quad (6-43)$$

Combining Eqs. (6-40) to (6-43) and applying the law of cosines give

$$x_F = t \sin^2 \alpha (\cos \varphi_{0,6} + 1), \quad (6-44a)$$

$$y_F = t \sin^2 \alpha (\cos \varphi_{0,2} - \cos \frac{2\pi}{n} \cos \varphi_{0,6} + 1 - \cos \frac{2\pi}{n}) / \sin \frac{2\pi}{n}, \quad (6-44b)$$

$$z_F = \frac{\left[t \sin \alpha \left[-\sin^2 \alpha (\cos^2 \varphi_{0,2} + \cos^2 \varphi_{0,6} - 2 \cos \frac{2\pi}{n} \cos \varphi_{0,2} \cos \varphi_{0,6}) \right] + (1 - \cos \frac{2\pi}{n}) (\cos 2\alpha \cos \varphi_{0,2} + \cos 2\alpha \cos \varphi_{0,6} + 2 \cos^2 \alpha) \right]}{\left[(1 - \cos \frac{2\pi}{n}) (\cos 2\alpha - \cos \frac{2\pi}{n}) (\cos^2 \varphi_{0,2} + \cos^2 \varphi_{0,6}) + 4 \cos^2 \alpha (\cos \varphi_{0,2} + \cos \varphi_{0,6} + 1) (1 - \cos \frac{2\pi}{n}) + 2 (1 - \cos 2\alpha \cos \frac{2\pi}{n}) \cos \varphi_{0,2} \cos \varphi_{0,6} \right]^{1/2}}. \quad (6-44c)$$

Noting $\overline{A_0 F} = t \tan \alpha$, we can now establish the relationship between $\varphi_{0,2}$ and $\varphi_{0,6}$ as

$$V_1 \cos^4 \varphi_{0,6} + V_2 \cos^3 \varphi_{0,6} + V_3 \cos^2 \varphi_{0,6} + V_4 \cos \varphi_{0,6} + V_5 = 0, \quad (6-45)$$

where

$$V_1 = \sin^2 \alpha \cos^4 \alpha,$$

$$V_2 = 2 \sin^2 \alpha \cos^2 \alpha \left[(1 - \cos 2\alpha \cos \frac{2\pi}{n}) \cos \varphi_{0,2} + 2 \cos^2 \alpha (1 - \cos \frac{2\pi}{n}) \right],$$

$$V_3 = \left[\begin{array}{l} 2 \sin^2 \alpha \cos^2 \alpha (\cos^2 \alpha - 2 \sin^2 \alpha \cos^2 \frac{2\pi}{n} - 2 \cos \frac{2\pi}{n}) \cos^2 \varphi_{0,2} + 4 \sin^2 \alpha \cos^2 \alpha (1 \\ - \cos \frac{2\pi}{n}) (1 + \cos^2 \alpha - \cos 2\alpha \cos \frac{2\pi}{n}) \cos \varphi_{0,2} + \sin^2 \alpha (4 \cos^4 \alpha + 1) \cos^2 \frac{2\pi}{n} \\ + 2 (6 \cos^6 \alpha - 5 \cos^4 \alpha - \cos 2\alpha) \cos \frac{2\pi}{n} - 8 \cos^6 \alpha + 10 \cos^4 \alpha - 3 \cos^2 \alpha + 1 \end{array} \right],$$

$$V_4 = \left[\begin{array}{l} 2 \sin^2 \alpha \cos^2 \alpha (1 - \cos 2\alpha \cos \frac{2\pi}{n}) \cos^3 \varphi_{0,2} + 4 \sin^2 \alpha \cos^2 \alpha (\cos^2 \alpha \\ + 1 - \cos 2\alpha \cos \frac{2\pi}{n}) (1 - \cos \frac{2\pi}{n}) \cos^2 \varphi_{0,2} + 2 [\sin^2 \alpha (8 \cos^4 \alpha - 1) \cos^2 \frac{2\pi}{n} \\ + 2(6 \cos^6 \alpha - 7 \cos^4 \alpha + 2 \cos^2 \alpha - 1) \cos \frac{2\pi}{n} - 4 \cos^6 \alpha + 2 \cos^4 \alpha + 3 \cos^2 \alpha \\ - 1] \cos \varphi_{0,2} + 4 \sin^2 \alpha \cos^2 \alpha (1 - \cos \frac{2\pi}{n}) [\cos 2\alpha - (1 + 2 \cos^2 \alpha) \cos \frac{2\pi}{n}] \end{array} \right],$$

$$V_5 = \left[\begin{array}{l} \sin^2 \alpha \cos^4 \alpha \cos^4 \varphi_{0,2} + 4 \sin^2 \alpha \cos^4 \alpha (1 - \cos \frac{2\pi}{n}) \cos^3 \varphi_{0,2} + [\sin^2 \alpha (4 \cos^4 \alpha \\ + 1) \cos^2 \frac{2\pi}{n} + 2(6 \cos^6 \alpha - \cos 2\alpha - 5 \cos^4 \alpha) \cos \frac{2\pi}{n} - 8 \cos^6 \alpha + 10 \cos^4 \alpha - 3 \cos^2 \alpha \\ + 1] \cos^2 \varphi_{0,2} + 4 \sin^2 \alpha \cos^2 \alpha (1 - \cos \frac{2\pi}{n}) [\cos 2\alpha - (1 + 2 \cos^2 \alpha) \cos \frac{2\pi}{n}] \cos \varphi_{0,2} \\ - 4 \sin^2 \alpha \cos^2 \alpha (1 - \cos \frac{2\pi}{n}) [(\cos^2 \alpha + 1) \cos \frac{2\pi}{n} + \sin^2 \alpha] \end{array} \right],$$

which are all functions of $\varphi_{0,2}$. Therefore, only one kinematic variable $\varphi_{0,2}$ is needed to determine the motion of the equatorial row (*Row 0*) under line symmetry.

Since $\phi_{B_{0,4}} = 0$, linkage \mathbf{B}_0 degenerates to a spherical 4R linkage with joint 4 frozen and joints 3 and 5 combining into one joint. The geometrical parameters of this linkage are $\alpha_{12}^{B_0} = \alpha_{41}^{B_0} = \pi - \alpha - \beta$, $\alpha_{23}^{B_0} = \alpha_{34}^{B_0} = \beta$. So its closure equations are

$$\tan \frac{\phi_{B_{0,2}}}{2} = \frac{-\sin(\alpha + \beta) + \sqrt{\sin^2(\alpha + \beta) + \sin \alpha \sin(\alpha + 2\beta) \tan^2 \frac{\phi_{B_{0,3}} + \phi_{B_{0,5}}}{2}}}{\sin \alpha \tan \frac{\phi_{B_{0,3}} + \phi_{B_{0,5}}}{2}},$$

$$\tan \frac{\phi_{B_{0,1}}}{2} = \frac{\sin \beta \sin \phi_{B_{0,2}}}{\sin(\alpha + \beta) \cos \beta + \sin \beta \cos(\alpha + \beta) \cos \phi_{B_{0,2}}},$$

$$\phi_{B_{0,6}} = \phi_{B_{0,2}}, \quad \phi_{B_{0,3}} = \phi_{0,6}, \quad \phi_{B_{0,5}} = \phi_{0,2}. \quad (6-46)$$

Linkage \mathbf{C}_0 remains to be a spherical 6R linkage and the closure equation is the same as Eq. (6-12), which reveals that it is plane-symmetric. Closure equations of other vertices can also be set up. Motions of those linkages on rest of the rows are plane-symmetric and their kinematic relationships are given in Eqs. (6-11), (6-12) and (6-13).

Hence, Eqs. (6-36), (6-45), (6-46) and (6-11) to (6-13) complete the set of kinematic relationships of the entire tube. Only one variable, $\varphi_{0,2}$, is needed to determine the motion of the tube, i.e., the tube is rigidly foldable with one DOF. The kinematic paths of the tube with $n = 6$ and $\alpha = \beta = 45^\circ$ are plotted as shown in Fig. 6-23, where the range of $\varphi_{0,2}$ is determined by the two limiting positions: $\varphi_{0,2} = 0^\circ$

and $\varphi_{0,2} = 90^\circ$, which correspond to counter-clockwise and clockwise twist, respectively.

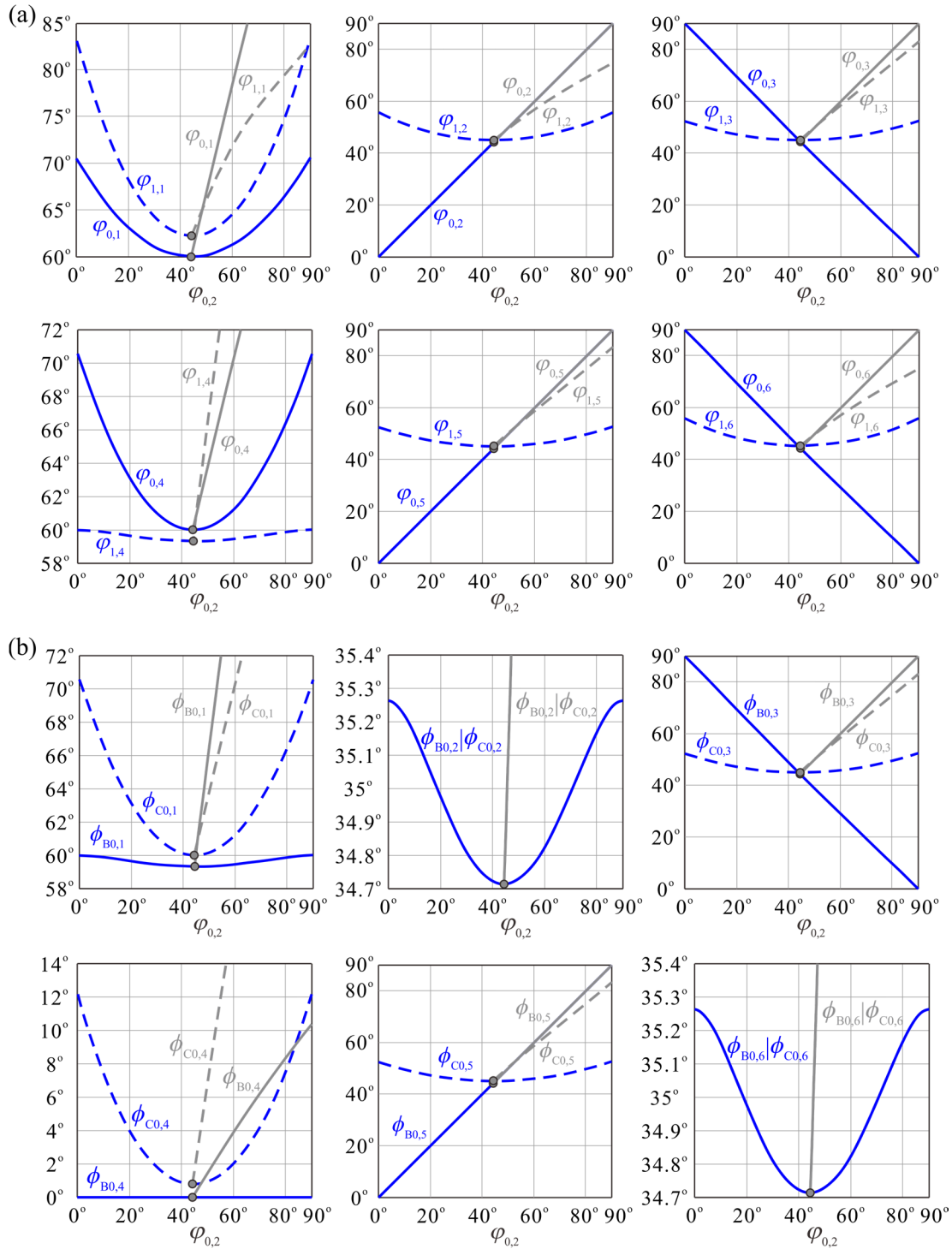


Fig. 6-23 Twist motion on the equatorial row of a waterbomb tube with $n = 6$ and $\alpha = \beta = 45^\circ$.

Kinematic paths of (a) linkages \mathbf{A}_0 and \mathbf{A}_1 , and (b) linkages \mathbf{B}_0 and \mathbf{C}_0 in the twist phase (blue) and in the contraction phase (grey). $\varphi_{0,2}$ is taken as input. The bifurcation points are marked by small grey circles.

In Fig. 6-23(a), the blue lines show the kinematic paths of linkage \mathbf{A}_0 (in blue solid lines) and \mathbf{A}_1 (in blue dash lines) in the twist motion, which presents that linkage \mathbf{A}_0 is in the line-symmetric motion, yet linkage \mathbf{A}_1 is still in the plane-symmetric motion similar to the tube contraction motion. In Fig. 6-23(b), blue lines show the kinematic paths of linkages \mathbf{B}_0 (in blue solid lines) and \mathbf{C}_0 (in blue dash lines) in the twist motion, which presents $\phi_{\mathbf{B}_0,4} = 0$ for the whole twist motion. It can be seen that $\phi_{\mathbf{C}_0,4}$ is always positive during *the twist phase*.

Furthermore, the switch from the contraction to the twist motion is, in fact, a motion bifurcation of linkage \mathbf{A}_0 from a line- and plane-symmetric motion to a line-symmetric motion. This can be clearly demonstrated by plotting the kinematic paths of the contraction motion in the same diagrams given in Figs. 6-23(a-b) (grey and grey dash lines), in which those bifurcation points are marked by shaded circles. The twist motion further shortens the overall length of the tube (Fig. 6-24(a)), but the radii of the vertices become slightly larger (Fig. 6-24(b)). It enables all the bases on *Row 0* to reach its most compact folding configuration at either $\varphi_{0,2} = 0^\circ$ or $\varphi_{0,2} = 90^\circ$.

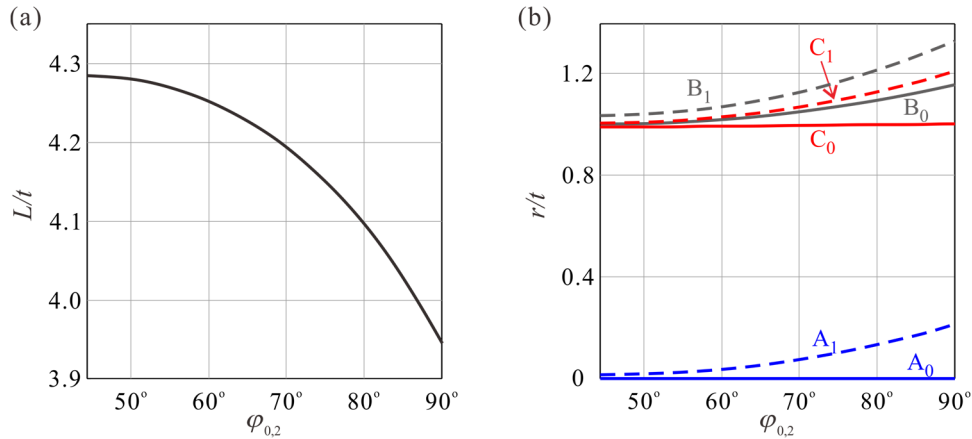


Fig. 6-24 Twist motion on the equatorial row of a waterbomb tube with $n = 6$, $m = 3$ and $\alpha = \beta = 45^\circ$. (a) Length of the tube vs. $\varphi_{0,2}$. (b) Radii of vertices A, B, and C vs. $\varphi_{0,2}$.

Having demonstrated from the kinematic analysis that the twist of *Row 0* is a rigid motion, next we investigate the existence of rigid twist motion and the range of the input kinematic variable $\varphi_{0,2}$ under rigid twist folding of waterbomb tubes with different geometrical parameters.

- Existence of rigid twist motion

The existence condition of the rigid twist folding is that there exists a fully squeezed row with both line and plane symmetry. It is related to the geometrical parameters α , β , n and m . When m is odd, there is an equatorial row with both

line and plane symmetry, so we need to check the existence of fully squeezed configuration. Thus $r_{A_0} = 0$ and $r_{A_i} \geq 0$ should be satisfied. With a given value of n , two conditions limit the range of α . The two points C_0 and B_{-1} (Fig. 6-25) get closer when α increases. Considering the interference between the two halves of the waterbomb base cut by the EP, α achieves the limitation when the crease A_0C_0 coincides with A_0B_{-1} as shown in Fig. 6-25, so the angle $\angle EA_0C_0$ should equal to π/n .

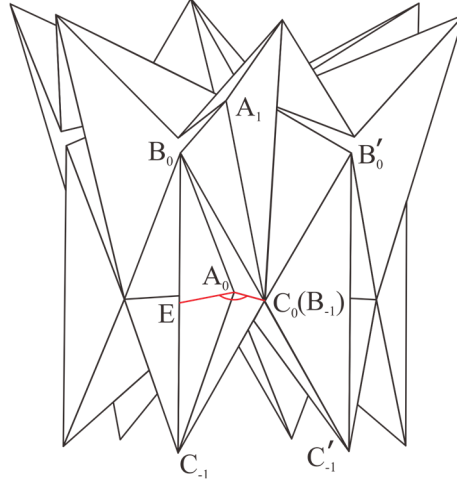


Fig. 6-25 The limitation of α obtained when the creases A_0C_0 and A_0B_{-1} coincide, where β is randomly chosen as 40° .

Since $\overline{A_0E} = t$, $\overline{C_0E} = t\sqrt{\sin^2 \alpha - \cos^2 \alpha \sin^2(\alpha + \beta)} / [\sin \alpha \sin(\alpha + \beta)]$, and $\overline{A_0C_0} = t \sin \beta / [\sin \alpha \sin(\alpha + \beta)]$, the following equation can be obtained according to the law of cosines

$$\tan \alpha = 1 / \cos \frac{\pi}{n}, \quad (6-47)$$

where the value of α is only related to n .

The other condition is obtained when linkage $\mathbf{A}_{(m-1)/2}$ on $Row (m-1)/2$ is fully deployed with $\varphi_{(m-1)/2,1} = \pi$ while the equatorial row is fully squeezed with $\phi_{B_{0,4}} = 0$. Substituting Eqs. (6-11) - (6-13) into Eq. (6-15), another α is obtained, which is not only related to n but also to β and m . The maximum of α , α_{\max} , is the smaller one obtained by Eqs. (6-15) and (6-47). Therefore, the range of α for the generalized waterbomb tube with rigid twist folding is $0 < \alpha \leq \alpha_{\max}$.

Once α is determined, the radius of the adjacent rows to the equatorial row decreases with the increase of β . When all radius of point A_i are set zero, i.e., $r_{A_i} = 0$,

β reaches the maximum. In this instant, we have for linkage \mathbf{A}_0 ,

$$\tan \frac{\varphi_{0,2}}{2} = \cos \alpha \tan \frac{\varphi_{0,1}}{2}, \quad \phi_{B_{0,4}} = \varphi_{0,1} - \frac{2\pi}{n} = 0, \quad (6-48a)$$

for linkage \mathbf{B}_0 ,

$$\tan \frac{\phi_{B_{0,2}}}{2} = \frac{-\sin(\alpha + \beta) + \sqrt{\sin^2(\alpha + \beta) + \sin \alpha \sin(\alpha + 2\beta) \tan^2 \varphi_{0,2}}}{\sin \alpha \tan \varphi_{0,2}}, \quad (6-48b)$$

for linkage \mathbf{C}_0 ,

$$\tan \frac{\varphi_{0,1}}{2} = \frac{2 \sin \beta \tan \frac{\phi_{B_{0,2}}}{2}}{\sin(\alpha + 2\beta) + \sin \alpha \tan^2 \frac{\phi_{B_{0,2}}}{2}}. \quad (6-48c)$$

Therefore, β_{\max} is obtained by

$$\left[\begin{array}{l} \cos^4 \alpha \sin^2(\alpha + \beta) \tan^4 \frac{\pi}{n} + 2 \cos^2 \alpha [\cos 2\beta - \cos^2(\alpha + \beta)] \tan^2 \frac{\pi}{n} \\ + \sin^2(\alpha + \beta) - 4 \cos^2 \alpha \sin^2 \beta \end{array} \right] = 0. \quad (6-49)$$

It should be noticed that all rows are in the fully squeezed configuration with both line and plane symmetry, indicating that the rigid twist folding can begin from any row in this case. When $\beta > \beta_{\max}$, $r_{A1} < 0$, there is interference in Row 1 and no rigid twist folding exists. When $\beta < \beta_{\max}$, $r_{A1} > 0$, the existence of rigid twist folding is determined by the most deployed configuration when linkage $\mathbf{A}_{(m-1)/2}$ on Row $(m-1)/2$ is fully deployed with $\varphi_{(m-1)/2,1} = \pi$. The minimum of β , β_{\min} , is obtained by Eq. (6-15), which is related to α , m and n . Therefore, the range of β for the generalized waterbomb tube with rigid twist folding is $\beta_{\min} \leq \beta \leq \beta_{\max}$.

When m is even, except the case where all $r_{A_i} = 0$, there exists no row with line and plane symmetry and therefore no rigid twist folding occurs. Once the geometrical parameters α , β , n and m are given, the existence of rigid twist motion is determined.

- Range of rigid twist motion

Now we are going to find out the range of folding angle $\varphi_{0,2}$ if the existence of rigid twist folding is certain. Firstly, the range of $\varphi_{0,2}$ is determined by the two limiting positions where $\varphi_{0,2} = 0^\circ$ and $\varphi_{0,3} = 0^\circ$ which correspond to counter-clockwise and clockwise twist respectively as shown in Fig. 6-26.

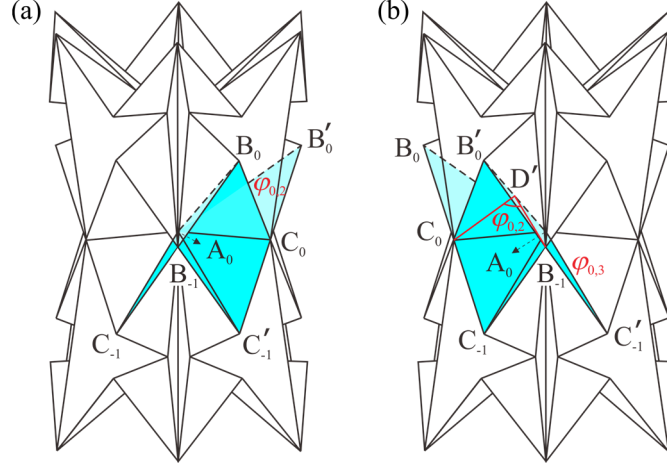


Fig. 6-26 Limiting positions of the twisted case: (a) $\varphi_{0,2} = 0^\circ$, and (b) $\varphi_{0,3} = 0^\circ$.

Substituting $\varphi_{0,3} = 0^\circ$ into Eq. (6-45), the limit for $\varphi_{0,2}$ in Fig. 6-26(b) can be obtained by

$$W_1 \cos^4 \varphi_{0,2} + W_2 \cos^3 \varphi_{0,2} + W_3 \cos^2 \varphi_{0,2} + W_4 \cos \varphi_{0,2} + W_5 = 0, \quad (6-50)$$

where

$$W_1 = \sin^2 \alpha \cos^4 \alpha,$$

$$W_2 = 2 \sin^2 \alpha \cos^2 \alpha \left[(1 - 4 \cos^2 \alpha) \cos \frac{2\pi}{n} + 1 + 2 \cos^2 \alpha \right],$$

$$W_3 = \begin{bmatrix} (-16 \cos^6 \alpha + 24 \cos^4 \alpha - 9 \cos^2 \alpha + 1) \cos^2 \frac{2\pi}{n} + 2(12 \cos^6 \alpha - 9 \cos^4 \alpha) \\ -4 \cos^2 \alpha + 1 \cos \frac{2\pi}{n} - 14 \cos^6 \alpha + 12 \cos^4 \alpha + \cos^2 \alpha + 1 \end{bmatrix},$$

$$W_4 = \begin{bmatrix} 2[\sin^2 \alpha (16 \cos^4 \alpha - 1) \cos^2 \frac{2\pi}{n} + (28 \cos^6 \alpha - 31 \cos^4 \alpha + 5 \cos^2 \alpha - 2) \cos \frac{2\pi}{n}] \\ -10 \cos^6 \alpha + 7 \cos^4 \alpha + 4 \cos^2 \alpha - 1 \end{bmatrix},$$

$$W_5 = \begin{bmatrix} (-16 \cos^6 \alpha + 8 \cos^4 \alpha + 7 \cos^2 \alpha + 1) \cos^2 \frac{2\pi}{n} + 2(20 \cos^6 \alpha - 19 \cos^4 \alpha) \\ -\cos 2\alpha \cos \frac{2\pi}{n} - 25 \cos^6 \alpha + 35 \cos^4 \alpha - 11 \cos^2 \alpha + 1 \end{bmatrix},$$

which are all functions of α and n .

On the other hand, by analyzing the set of kinematic relationships of the entire tube as Eqs. (6-37), (6-45), (6-46) and (6-11) to (6-13), the tube become expanded when it twists. So the other limitation to $\varphi_{0,2}$ is the linkage $\mathbf{A}_{(m-1)/2}$ on Row $(m-1)/2$ being fully deployed with $\varphi_{(m-1)/2,1} = \pi$. With Eq. (6-15), the solutions for $\varphi_{0,2}$ in this case can be obtained. Comparing these solutions with the two limits in Fig. 6-26, the range

of folding angle $\varphi_{0,2}$ under rigid twist folding is determined.

To be noticed, other rows except the twisted one move with plane symmetry similar as the contraction folding of the tube, and therefore interferences of facets should be taken into account when determining the range of folding angle under rigid twist motion. $r_{Ai} \geq 0$ and $\phi_{Bi,4} \geq 0$ should always be satisfied during the motion. By solving the equation set (Eqs. (6-37), (6-45), (6-46) and (6-11) to (6-13)), the value range of $\varphi_{0,2}$ is further restricted.

- Twist angle per axial strain

With the range of the input kinematic variable $\varphi_{0,2}$, the maximum twist angle between two ends, $B_0^n B_0 B_0'$ and $C_{-1}^n C_{-1} C_{-1}'$, of Row 0 along tube axis in Fig. 6-21(b), θ_t , can be calculated

$$\tan \frac{\theta_t}{2} = \frac{\cos \varphi_{0,2 \min} - \cos \varphi_{0,6 \max}}{\tan \frac{\pi}{n} (\cos \varphi_{0,2 \min} + \cos \varphi_{0,6 \max} + 2)}, \quad (6-51)$$

where $\varphi_{0,2 \min}$ is the minimum value of $\varphi_{0,2}$, and $\varphi_{0,6 \max}$ is calculated by Eq. (6-45) when $\varphi_{0,2}$ is taken as $\varphi_{0,2 \min}$.

Since only Row 0 of a tube generates rigid twist motion while all the other rows keep plane symmetry, the twist angle θ_t between two ends of the tube is independent of the number of rows m , while affected only by the number of bases in a row n . We take $\alpha = \beta = 45^\circ$ and $m = 3$ to demonstrate the relationship between θ_t and n , see Fig. 6-27(a). Here n is taken from 4 to 40 since no rigid twist motion exists when $n < 4$. It can be seen that θ_t increases when n increases from 4 to 5. This is due to the fact that when $n = 4$, the twist angle θ_t is obtained where Row 1 is fully expanded with $\varphi_{1,1} = 180^\circ$. The tube cannot reach the most compact folding configuration with $\varphi_{0,2} = 0^\circ$ (Fig. 6-26(a)) as the case of $n = 5$, leading to a smaller twist angle. When n surpasses 4, θ_t monotonically reduces with n for the reason that Eq. (6-51) degenerates to $\theta_t = 360^\circ / n$ in this case. The maximum value of θ_t is reached when $n = 5$, where $\theta_t = 72^\circ$.

The rigid twist degree of freedom of the waterbomb tube makes it a suitable candidate for the design of chiral mechanical metamaterials which twist when axially deformed. This property can be characterized by the twist angle per axial strain, θ_t / ε_t [216]. The axial strain, ε_t , considering compression strain as positive, can be calculated as

$$\varepsilon_t = \frac{L_0 - L_t}{L_0}, \quad (6-52)$$

where L_0 and L_t are the overall length of the tube at the fully squeezed configuration with $\phi_{B0,4} = 0$ and at the fully twisted configuration with $\phi_{0,2} = \phi_{0,2 \min}$, respectively. They can be calculated by Eqs. (6-17) and (6-18).

It is obvious from Eqs. (6-52), (6-17) and (6-18) that ε_t is dependent on m , and therefore θ_t / ε_t is tunable by both m and n . First consider the effects of n by taking $m = 3$ and n from 4 to 40. The relationship between ε_t and n is presented in Fig. 6-27(b). The change tendency of ε_t is similar as θ_t vs. n , but it varies more rapidly. As a result, except for the special case $n = 4$, θ_t / ε_t is in general increased with the increase in n as shown in Fig. 6-27(c), which shows a completely different trend from θ_t . A minimum of $\theta_t / \varepsilon_t = 5.8^\circ / \%$ is obtained when $n = 5$, which is almost triple of the maximum one in reference [216].

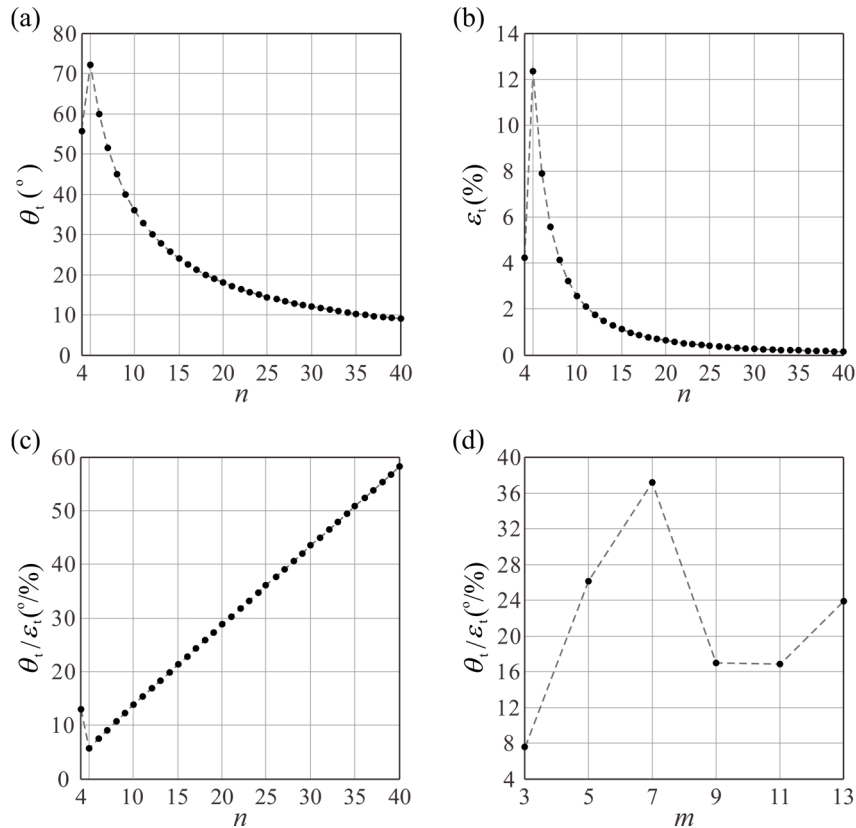


Fig. 6-27 Rigid twist of the waterbomb tube with $\alpha = \beta = 45^\circ$. (a) The twist angle between two ends of a tube, θ_t , vs. the number of bases in a row, n , when the number of rows $m = 3$. (b) The axial strain of the tube ε_t vs. n when $m = 3$. (c) The twist angle per axial strain θ_t / ε_t vs. n when $m = 3$. (d) θ_t / ε_t vs. m when $n = 6$. The twist angle here is calculated as the maximum rigid twist between two ends of a tube, and the axial strain is calculated as the strain when the maximum rigid twist is reached.

The correlation between θ_i / ε_i and m , is less clear, as can be seen in Fig. 6-27(d) in which n is fixed to 6. In this case the twist angle remains constant as 60° whereas the axial strain is changed with m , leading to the variation of θ_i / ε_i . A maximum of $\theta_i / \varepsilon_i = 37.2^\circ / \%$ is obtained when $m = 7$. Therefore, we can design mechanical metamaterials with a wide range of twist angle per axial strain by fine-tuning the geometrical parameters m and n . And such twist can be materialized with minimum efforts as it is a purely rigid motion.

- Bifurcation of rigid twist motion in different rows

The rigid twist motion occurs in the fully squeezed row with both line and plane symmetry. Once the tube begins to twist, the adjacent rows to the fully squeezed one expands and therefore no other rows satisfy the twist trigger condition. The rigid twist motion will not transfer to the other rows without deformation. Kinematically, $\phi_{B0,4} = 0$ holds for the whole twist folding, while $\phi_{C0,4}$ is always positive during the motion. Taking $m = 5$ and $n = 6$ as an instance, three cases with $\alpha_1 = 40^\circ$, $\alpha_2 = 45^\circ$ and $\alpha_3 = 50^\circ$ are discussed. By solving Eq. (6-49), the critical conditions are obtained as $\beta_{1\max} = 42.01^\circ$, $\beta_{2\max} = 45.59^\circ$ and $\beta_{3\max} = 49.17^\circ$, which corresponds to the tube with uniform radius where all rows are fully squeezed.

Figure 6-28(a) shows kinematic paths of the dihedral angles $\phi_{Bi,4}$ and $\phi_{Ci,4}$ against $\varphi_{0,2}$ when $\beta = 40^\circ$, where the blue lines represent the case with $\alpha_1 = 40^\circ$, the red lines with $\alpha_2 = 45^\circ$ while the grey lines with $\alpha_3 = 50^\circ$. It can be found that $\phi_{Ci,4} > 0$, so there is no rigid twist motion in other rows. There exists another phenomenon that the range of folding angle $\varphi_{0,2}$ under twist folding decreases with α increasing when β is set identical.

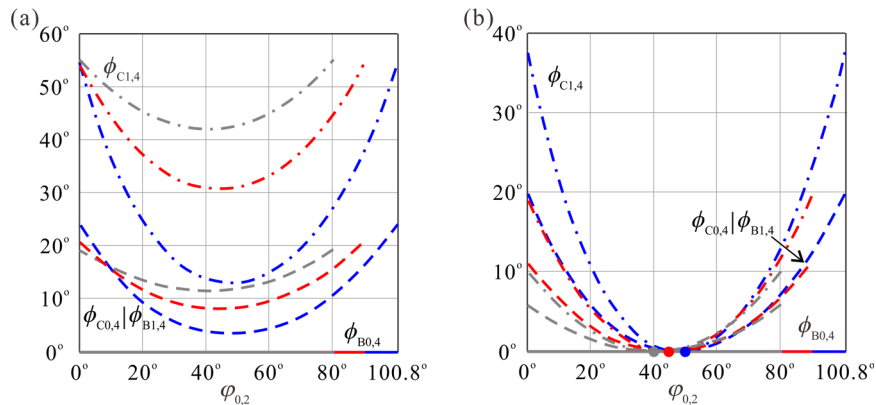


Fig. 6-28 Kinematic paths of the dihedral angles $\phi_{Bi,4}$ and $\phi_{Ci,4}$ against $\varphi_{0,2}$ during the twist motion on the equatorial row of a waterbomb tube in three cases with $m = 5$, $n = 6$, $\alpha_1 = 40^\circ$ (blue), $\alpha_2 = 45^\circ$ (red), $\alpha_3 = 50^\circ$ (grey) when (a) all $\beta = 40^\circ$, and (b) $\beta_1 = 42.01^\circ$, $\beta_2 = 45.59^\circ$, $\beta_3 = 49.17^\circ$.

Maintaining the values of α , m and n identical, the minimum of $\phi_{C_{0,4}}$ decreases with the increase of β . When β reaches the maximum, all $\phi_{C_{i,4}} = 0$ holds in the configuration with uniform radius as presented by the dot in Fig. 6-28(b). It indicates that the rigid twist folding can occur in any row at this configuration, i.e., it is a bifurcation point.

Therefore, with defined values of α and n , the condition of β to obtain fully squeezed waterbomb tube with identical radius is given by Eq. (6-49). In this case, the twist folding can transfer from the equatorial row to other rows through the bifurcation point. For example, when $m = 3$, $n = 6$ and $\alpha = 40^\circ$, this kind of bifurcation occurs with β being 42.01° . The bifurcation behaviour of the waterbomb tube is presented in Fig. 6-29, where kinematic paths of the dihedral angle $\phi_{B_{2,4}}$ against $\phi_{0,2}$ are plotted by *paths I, II and III* when the rigid twist folding occurs in the top, middle and below rows respectively.

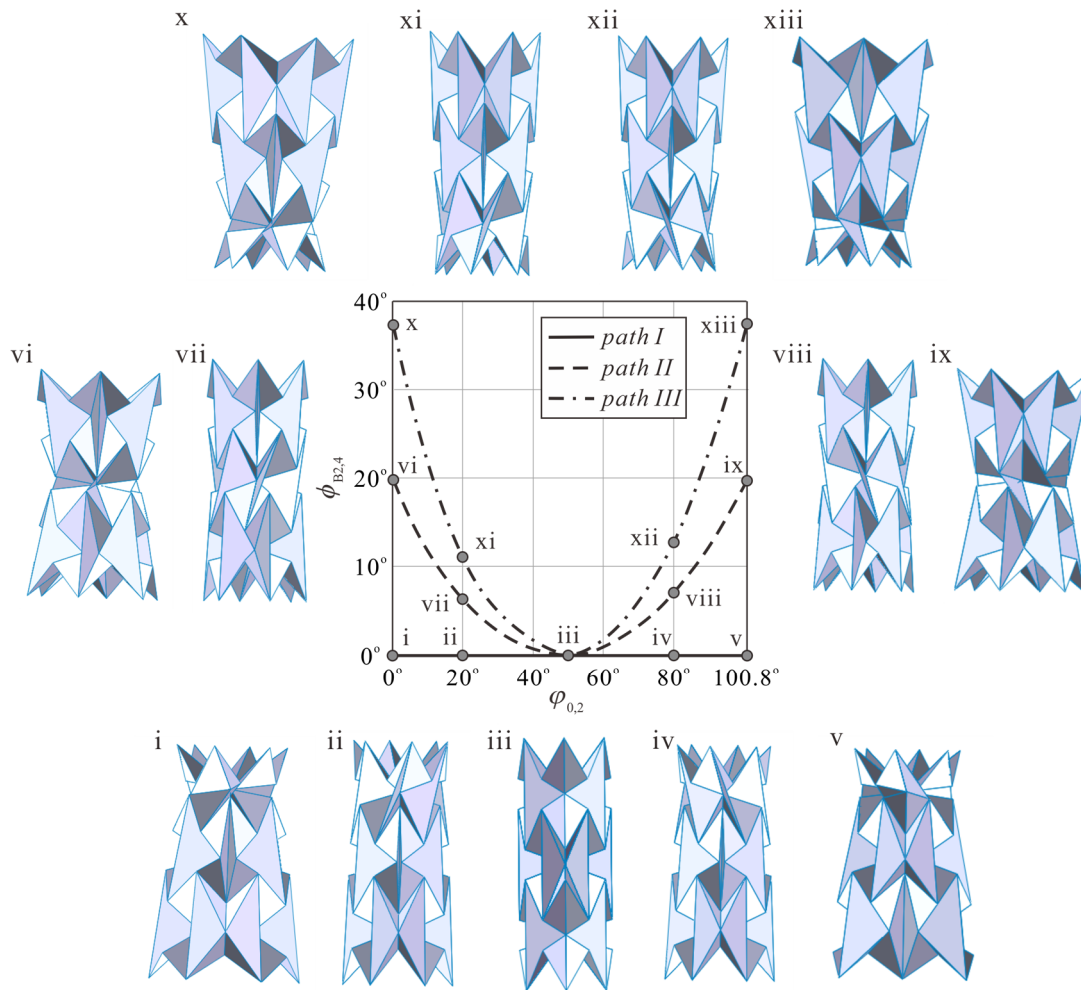


Fig. 6-29 Bifurcation behaviour during the twist motion of the fully squeezed waterbomb tube with uniform radius satisfying Eq. (6-49) where twist motion can occur from any row. Here the geometrical parameters are $m = 3$, $n = 6$, $\alpha = 40^\circ$ and $\beta = 42.01^\circ$.

As shown in Fig. 6-29, configurations i, ii, iii, iv and v represent the motion process of the waterbomb tube when the rigid twist folding occurs in the top row, and it can bifurcate either to *path II* (the rigid twist folding occurs in the middle row with configurations vi, vii, iii, viii, ix) or to *path III* (the rigid twist folding occurs in the below row with configurations x, xi, iii, xii, xiii) at the configuration iii, a configuration with uniform radius where all rows are fully squeezed.

6.4.2 Non-rigid Twist Motion

The sufficient condition of the rigid twist motion has been proved to be that the twisted row is fully squeezed with both line and plane symmetry. Now we are going to check its necessity. Firstly, we need to figure out whether the rigid twist motion will start if the line- and plane- symmetric spherical $6R$ linkage \mathbf{A}_0 is not fully squeezed, that is, $\phi_{B_0,4} \neq 0$, see Fig. 6-30(a). Two adjacent bases on Row 0 of such a waterbomb tube is presented in Fig. 6-30(b), where the coordinate system is the same as that in Fig. 6-22. According to the spatial analytical geometry, the angle between the crease $B'_0C'_{-1}$ and the coordinate axis z , η , can be calculated

$$\cos \eta = \frac{\tan \alpha}{t} \sqrt{\frac{-y_{B'_0}^2 + 2ty_{B'_0} \sin \angle EA_0E' - t^2}{\cos^2 \angle EA_0E'} + \frac{t^2}{\sin^2 \alpha}}. \quad (6-53)$$

As both planes $A_0E'A'_0$ and EA_0E' are perpendicular to the crease $B'_0C'_{-1}$ and the axis z , respectively, the angle between the two planes EA_0E' and $A_0E'A'_0$ is also η . So the vertical distance between the vertices A'_0 and A_0 is

$$z_{A'_0} - z_{A_0} = -\overline{A_0A'_0} \sin \eta = -2t \sin \frac{\phi_{B_0,4}}{2} \sin \eta. \quad (6-54)$$

If $\phi_{B_0,4} \neq 0$, $z_{A'_0} - z_{A_0} \neq 0$. According to the recursion formula in Eq. (6-54), the vertical distance between the vertex A'_0 and the plane xA_0y becomes larger and larger with the increase of the number of the bases on Row 0, which makes the vertex C'_{-1} of the n th base that obtained after twist cannot match the vertex C_{-1} of the first base, so that the bases on Row 0 cannot complete a cylindrical tessellation. Therefore, no rigid twist motion occurs when the line- and plane- symmetric row of the tube is not fully squeezed. To this point, we can conclude that only the twist of the fully squeezed row in the middle of the tube in Figure 1b is a rigid motion.

Secondly, the necessity of line and plane symmetry is studied, that is, whether the twist motion is rigid if the twisted row is fully squeezed without line and plane symmetry. Figure 6-30(c) shows such a case that the Row 3 is fully squeezed with only plane symmetry. Due to the lack of two-fold symmetry necessary to reach the

bifurcation configuration, the plane-symmetric linkage A_3 cannot bifurcate to a tilting motion. That is, the twist motion on the fully squeezed row without both line and plane symmetry is not rigid.

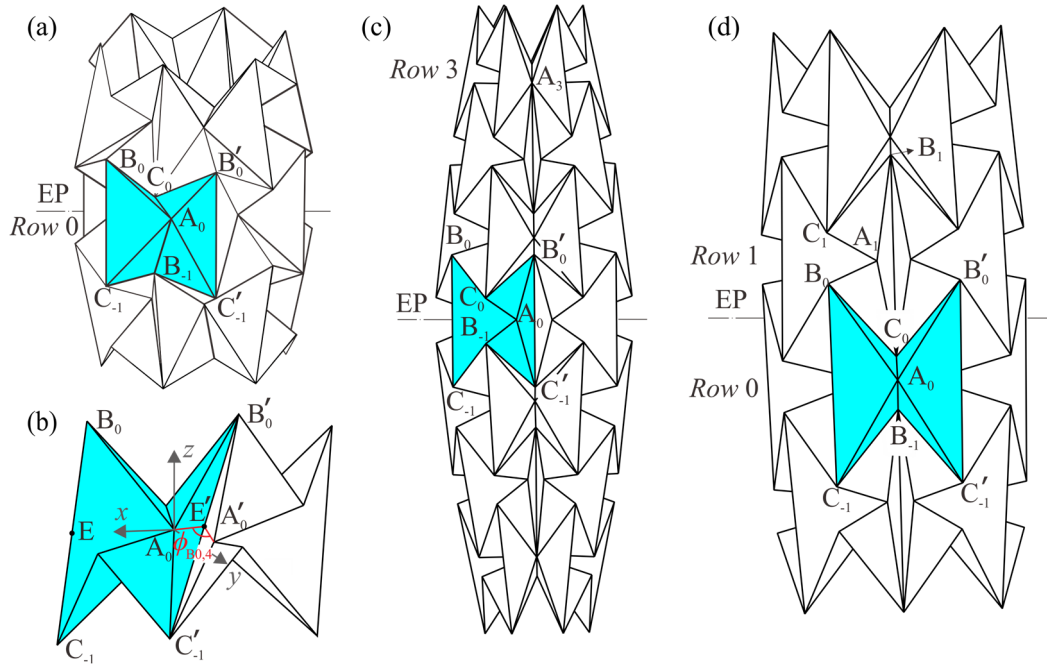


Fig. 6-30 Non-rigid twist of the waterbomb tube when $n = 6$. (a) 3D view of a waterbomb tube with $m = 3$ when twist starts from the not-fully-squeezed line- and plane-symmetric row (*Row 0*) with $\phi_{B_0,4} \neq 0$. (b) Geometry of two adjacent bases on such not-fully-squeezed *Row 0*. (c) 3D view of a waterbomb tube with $m = 7$ where the *Row 3* is fully squeezed with only plane symmetry. (d) 3D view of a waterbomb tube when twist starts from a pair of rows, set as *Row 0* and *Row 1*. Only the twisted rows and those immediately adjacent to them are presented. EP is short for equatorial plane.

Therefore, both the fully squeezed configuration and the line and plane symmetry are necessary for a rigid twist motion. Should either one be violated, the twist motion requires material deformation. Obviously, the twist motion with neither fully squeezed configuration nor line and plane symmetry is not rigid. There are two cases of such non-rigid twist motion. First, when the twist occurs on the fully squeezed row, the bases on the other rows is only plane-symmetric and not fully squeezed, so the successive twist of other rows after *Row 0* reaches its limit positions (Fig. 6-26) is non-rigid and it cannot occur without material deformation. Second, when the twist motion occurs from a pair of rows near the equatorial plane, which are set as *Rows 0* and *1* as shown in Fig. 6-30(d), the bases on all rows are not fully squeezed and have only plane symmetry. As a result, there is no rigid twist motion. However, playing with the physical model shows that twist exists in this case as well, and such a process is transmitted from row to row towards the ends of the tube. So we can safely conclude that, the entire twist motion is

due to material deformation. Notice that some rows twist clockwise while the others twist counter-clockwise. The reason is that in such a way, the relative rotation of the two ends of the tube can be cancelled out.

The discovery of the twist motion enables design of origami structures and mechanical metamaterials with graded stiffness through a combination of contraction and twist. To demonstrate the graded stiffness of the waterbomb tube, a tube made from ENDURO Ice material with 0.29mm in thickness and $m = 8$, was compressed in the longitudinal direction from the larger uniform radius configuration with an initial dihedral angle $\theta = 144^\circ$. It has the following geometrical parameters: $\alpha = \beta = 45^\circ$, $n = 6$ and $a = 22.5\text{mm}$. The experiment was conducted on an Instron 5982 testing machine with a load cell of 100 N. The loading speed was chosen as 5 mm/min so that material strain rate effects could be safely neglected. Regarding boundary conditions, it was determined after several rounds of trial-and-errors that placing foams of 15mm in thickness at each end of the tube, as shown in Fig. 6-31(a), was able to generate a roughly symmetric and stable deformation.

As can be seen in Fig. 6-31(a), a radial contraction occurs at the beginning of the compression, with a larger shrinkage in the middle than both ends due to boundary constraints, see configuration B. The contraction phase ceases when *Row 0* and *Row 1* are fully contracted in configuration C, followed by a simultaneous twist of both rows in opposite directions as seen in configuration D. It is known from the analysis above that the twist is structural deformation instead rigid motion. The twist phase proceeds as *Row 2* and *Row -1* twist successively (configurations E and F), after which local material damages appear and the experiment is terminated (configuration G). Regarding stiffness, the force vs. displacement curve in Fig. 6-31(b) indicates that the force is low during the contraction phase before configuration C. With the occurrence of twist, the force level is raised significantly as shown in the shaded region of Fig. 6-31(b), which demonstrates a periodic manner corresponding to the successive twist motion. The local peaks in the twist stage are approximately doubled in comparison with that in the contraction stage. Such graded stiffness would enable the structure/metamaterial to autonomously adapt to non-uniform loading environment. And this adaption is achieved purely through a structural transition of deformation phase, without requirement of gradation in the geometric or material dimensions.

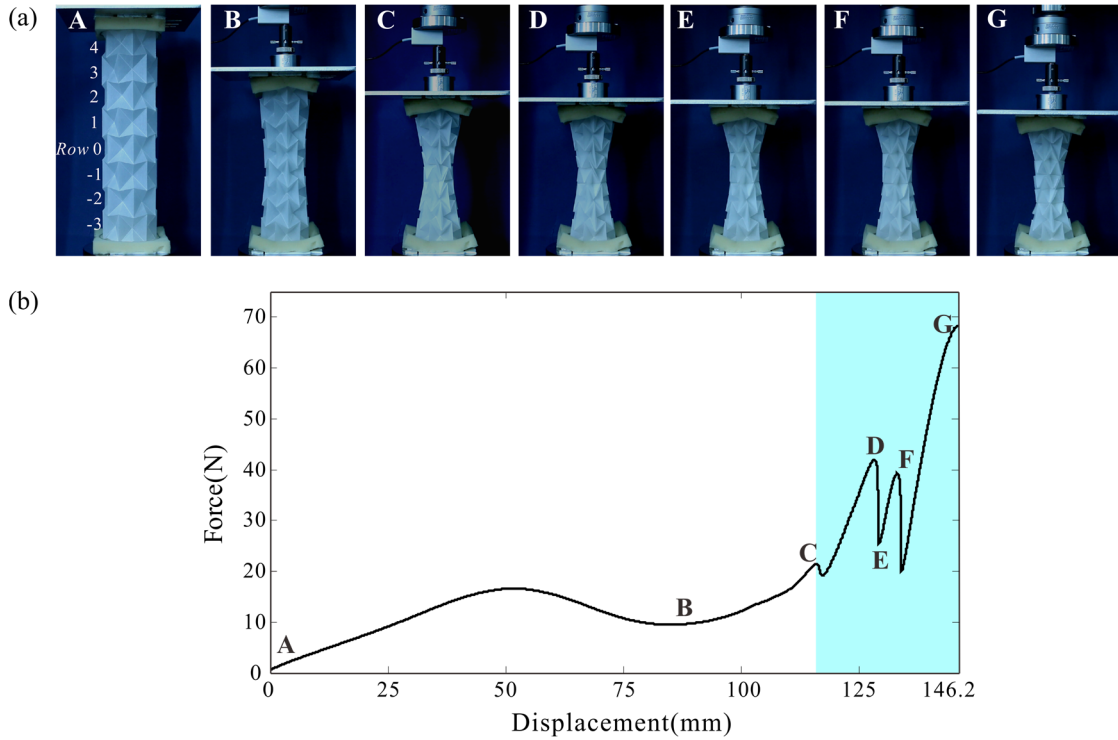


Fig. 6-31 Axial compression experiment of the waterbomb tube. (a) Compression process of the tube. (b) Reaction force of the tube vs. axial displacement curve. The tube in the experiment took a uniform radius with the following geometrical parameters: $\alpha = \beta = 45^\circ$, $n = 6$, $m = 8$, $a = 22.5\text{mm}$, and initial dihedral angle $\theta = 144^\circ$. ENDURO Ice material with 0.29mm in thickness was used to construct the tube. The compression test was conducted on an Instron machine at the loading rate of 5 mm/min.

6.5 Conclusions

In this chapter, a thorough kinematic study of the generalized waterbomb tube has been conducted. By using the D-H matrix method and considering the equivalence of spherical linkages and vertices in rigid origami, the kinematic relationship between different dihedral angles at the creases has been figured out for the waterbomb tubes with both odd and even rows. The contraction folding of the generalized waterbomb tube under both circumferential and longitudinal symmetry has been proved to be rigid with one DOF. Moreover, the relationship between those geometrical parameters and the range of folding angle under rigid contraction folding has been analyzed. The existence of uniform radius configuration has been discussed based on the flat-foldable case. A wave-like profile of the long tube has been revealed, and the corresponding rigid origami region has been given. A bifurcation at the uniform radius configuration of the truncated tube has been discovered.

Furthermore, a twist motion has been found in some specific waterbomb tubes. The rigidity of the twist folding has been explored. Through a detailed kinematic

analysis, the sufficient and necessary condition of a rigid twist motion has been revealed at the fully squeezed line- and plane- symmetric row in the end of contraction. The geometric conditions concerning α and β to make the waterbomb tube with rigid twist folding have been derived. In addition, the rigid twist motion range with given geometrical parameters has also been determined, which is related to both the left/right handed twist and the most expanded configuration at the end rows. The twist angle per axial strain of the waterbomb tube with rigid twist motion has been analyzed, which generally increases with the number of bases in a row. In addition, the behaviours of non-rigid twist motions have been studied. The significant difference in stiffness of the waterbomb tube with and without twist has also been verified by experiments. Except for the bifurcation between *the contraction phase* and *the twist phase*, another bifurcation among rigid twist motion in different rows has been revealed.

Chapter 7 Final Remarks

The aim of this dissertation was to explore the kinematics of spatial linkages ranging from spherical linkages to overconstrained linkages, and apply it to the analysis of rigid origami. The main achievements are summarized and the future works are highlighted in this chapter.

7.1 Main Achievements

- **Generalized triangle twist and its derived overconstrained 6R linkages**

First, a systematic method to analyze the rigid foldability and motion behaviour of the generalized triangle twist pattern has been presented using the kinematic equivalence between rigid origami and spherical linkages. All schemes of M-V assignment have been derived based on the flat-foldable conditions of four-crease vertex, among which rigidly foldable ones have been identified. The compatible conditions have also been derived for these types of triangle twist. It has been found that the triangle twist is rigidly foldable only when at least one crease-pair is not parallel. Moreover, a new type of overconstrained 6R linkage and a variation of doubly collapsible octahedral Bricard have been developed by applying kirigami technique to the rigidly foldable pattern without changing its DOF.

The kinematics of a modular origami unit with four-crease vertices and its corresponding network of spherical 4R linkages has been presented in Chapter 3. The proposed method opens up a new way to generate spatial overconstrained linkage from the network of spherical linkages. It can be readily extended to other types of origami patterns. A journal paper concerning on this work titled “Rigid foldability of generalized triangle twist origami pattern and its derived 6R linkages” has been published on Journal of Mechanisms and Robotics.

- **General plane-symmetric Bricard linkage**

Second, the explicit solutions to closure equations of the plane-symmetric Bricard linkage have been derived and a thorough kinematic study of the general plane-symmetric Bricard linkage has been conducted with D-H matrix method. The derived 5R/4R linkages from this Bricard linkage and their corresponding geometric conditions have been introduced. Various bifurcation cases of the plane-symmetric Bricard linkage with different geometric conditions have been discussed, such as the bifurcation between the plane-symmetric Bricard linkage and the Bennett linkage, the bifurcation between two plane-symmetric Bricard linkage motion branches, and the bifurcation between equivalent serial kinematic chains with revolute joints and a four-bar double-rocker linkage.

The kinematics of an existing spatial overconstrained linkage has been presented

in Chapter 4. The findings not only offer an in-depth understanding about the kinematics of the general plane-symmetric Bricard linkage, but also bridge two overconstrained linkage groups, i.e., the Bennett-based linkages and Bricard-related ones, to reveal their intrinsic relationship. A journal paper concerning on this work titled “Kinematic study of the general plane-symmetric Bricard linkage and its bifurcation variations” has been published on Mechanism and Machine Theory.

- **Symmetric flat-foldable waterbomb origami**

Third, a thorough kinematic investigation on symmetric folding of the flat-foldable waterbomb pattern has been presented. It has been found that the pattern can have two folding paths for the zero-thickness case with singularity at the fully expanded or compact configuration. Moreover, the pattern has been used to fold thick panels, where the vertices are modelled as plane-symmetric Bricard linkages instead of spherical $6R$ linkages. Not only do the additional constraints imposed to fold the thick panels lead to one-DOF folding, but the folding process is kinematically equivalent to the origami of zero-thickness sheet.

The kinematics of a planar origami tessellation with six-crease vertices and its corresponding mobile assemblies of spherical $6R$ linkages and spatial overconstrained $6R$ linkages, have been presented in Chapter 5. The findings pave the way for the waterbomb pattern being readily used to fold deployable structures ranging from flat roofs to large solar panels. A journal paper concerning on this work titled “Symmetric waterbomb origami” has been published on Proceedings of the Royal Society A: Mathematical, Physical and Engineering Science.

- **The waterbomb tube**

Finally, the folding behaviour of the waterbomb tube under certain symmetry has been analyzed. Through a detailed kinematic analysis, the dependency between its motion and geometrical parameters of the origami pattern has been uncovered. It has been demonstrated that the contraction folding of the generalized waterbomb tube under both circumferential and longitudinal symmetry is rigid with one DOF. Some tubes have been found to be capable of pure rigid origami, whilst others will experience structural deformation in-between rigid origami motions. With parametric study, the waterbomb with wave-like profile has been discovered.

Moreover, a twist motion of the waterbomb tube has been reported for the first time. It has been proved that the trigger condition of the rigid twist motion is the corresponding row of the tube under twist being fully squeezed with both line and plane symmetry, whereas all the subsequent twist motion requires material deformation. The existence of rigid twist motion for waterbomb tubes with various geometric conditions has been discussed. The rigid twist motion range has also been determined, which is related to both the left/right handed twist and the most expanded configuration at the

end rows. The twist angle per axial strain of the waterbomb tube with rigid twist motion has been analyzed, which generally increases with the number of bases in a row. In addition, the behaviours of non-rigid twist motions have been studied. The significant difference in stiffness of the waterbomb tube with and without twist has also been verified by experiments.

Three bifurcations have been found during the motion of the waterbomb tube. The first one is the switch of the waterbomb tube from *the contraction phase* to *the twist phase*. The second one is the bifurcation of a waterbomb tube during *the contraction phase* at the uniform radius configuration between the motion of a truncated tube and that of an even-row tube. The last one is the bifurcation during *the twist phase* of a fully-squeezed waterbomb tube with uniform radius configuration, which have bifurcated twist motion in different rows.

The kinematics of a closed cylindrical origami tessellation with six-crease vertices and its corresponding tubular network of spherical $6R$ linkages have been presented in Chapter 6. Our results reveal the kinematic properties of the waterbomb tube, and how certain behaviour can be achieved by fine-tuning the pattern parameters. The results will provide a solid foundation for full exploitation of this ancient but fascinating origami object to create novel shape changing structures and metamaterials. A journal paper concerning on this work titled “Twist of tubular mechanical metamaterials based on waterbomb origami” has been published on Scientific Reports. Two other journal papers titled “A unified kinematic framework for rigid-foldable waterbomb origami” and “Rigid-foldability of the generalized waterbomb tube” have been ready to submit.

7.2 Future Works

The research reported in this dissertation provides us with several topics to be further explored.

First, the potential applications and adaptations of the foldable triangle twist origami pattern in the tessellation as a modular unit, or in the design of bionic deployable structures and origami robots are to be explored. The kinematics of spherical $4R$ linkage network can be further used to analyze the rigid foldability of other existing origami patterns such as hexagon twists, or to generate new origami patterns. The proposed method to generate spatial overconstrained linkage from the network of spherical linkages by the kirigami technique is capable to be extended to other types of origami patterns for the discovery of novel mechanisms.

Second, the bifurcation behaviour of the plane-symmetric Bricard linkage can be utilized in the design of reconfigurable mechanisms. And the kinematics of the plane-symmetric Bricard linkage can be applied to other types of thick-panel origami patterns composed of six-crease vertices, such as the diamond pattern and the Resch pattern, etc. More work of the waterbomb pattern can also be done on its engineering applications

such as solar panels.

Third, tubular waterbomb-based engineering devices and metamaterials with programmable stiffness and shape control are to be designed based on the rigid or non-rigid case of the tube. Taking advantage of the wave-like profile, a worm robot can be designed. The control strategy to maintain symmetry or accomplish transition between the waterbomb's multitude behaviours is to be sought for facilitating its applications. The analysis on the thick-panel origami tube may also be conducted together with the tubular network of spatial overconstrained linkages.

In total, the work in this dissertation focuses on the theoretical study on the spatial linkage kinematics and its applications to rigid origami, ranging from the mobile assembly of spherical $4R$ linkages to the spatial overconstrained $6R$ linkage, then to the mobile assembly of spherical $6R$ linkages and that of spatial overconstrained $6R$ linkages, and finally to the closed-loop network of spherical $6R$ linkages. The future work can be concentrated on the engineering applications of these spatial linkages as well as rigid origami patterns.

References

- [1] Wilson C E, Sadler J P. Kinematics and dynamics of machinery: pearson new international edition [M]. Pearson Higher Ed, 2013.
- [2] Tsai L W. Robot analysis: the mechanics of serial and parallel manipulators [M]. John Wiley & Sons, 1999.
- [3] Hunt K H. Kinematic geometry of mechanisms [M]. London: Oxford University Press, 1978.
- [4] Beggs J S. Advanced mechanism [M]. Macmillan, 1966.
- [5] Silverberg J L, Evans A A, McLeod L, Hayward R C, Hull T, Santangelo C D, Cohen I. Using origami design principles to fold reprogrammable mechanical metamaterials [J]. *Science*, 2014, 345(6197): 647-650.
- [6] Wang F, Gong H, Chen X, Chen C Q. Folding to curved surfaces: a generalized design method and mechanics of origami-based cylindrical structures [J]. *Scientific Reports*, 2016, 6: 33312.
- [7] Lv C, Krishnaraju D, Konjevod G, Yu H, Jiang H. Origami based mechanical metamaterials [J]. *Scientific Reports*, 2014, 4: 5979.
- [8] Schenk M, Guest S D. Geometry of Miura-folded metamaterials [J]. *Proceedings of the National Academy of Sciences*, 2013, 110(9): 3276-3281.
- [9] Silverberg J L, Na J H, Evans A A, Liu B, Hull T C, Santangelo C D, Lang R J, Hayward R C, Cohen I. Origami structures with a critical transition to bistability arising from hidden degrees of freedom [J]. *Nature Materials*, 2015, 14(4): 389.
- [10] Wei Z Y, Guo Z V, Dudte L, Liang H, Mahadevan L. Geometric mechanics of periodic pleated origami [J]. *Physical Review Letters*, 2013, 110(21): 215501.
- [11] Filipov E T, Tachi T, Paulino G H. Origami tubes assembled into stiff, yet reconfigurable structures and metamaterials [J]. *Proceedings of the National Academy of Sciences*, 2015, 112(40): 12321-12326.
- [12] Zhou X, Zang S, You Z. Origami mechanical metamaterials based on the Miura-derivative fold patterns [J]. *Proceedings of the Royal Society A: Mathematical, Physical and Engineering Science*, 2016, 472(2191): 20160361.
- [13] Fang H, Chu S C A, Xia Y, Wang K W. Programmable self-locking origami mechanical metamaterials [J]. *Advanced Materials*, 2018, 30(15): 1706311.
- [14] Felton S, Tolley M, Demaine E, Rus D, Wood R. A method for building self-folding machines [J]. *Science*, 2014, 345(6197): 644-646.
- [15] Zhang K, Qiu C, Dai J S. An extensible continuum robot with integrated origami parallel modules [J]. *Journal of Mechanisms and Robotics*, 2016, 8(3): 031010.

- [16] Zhang K, Qiu C, Dai J S. Helical kirigami-enabled centimeter-scale worm robot with shape-memory-alloy linear actuators [J]. *Journal of Mechanisms and Robotics*, 2015, 7(2): 021014.
- [17] Filipov E T, Paulino G H, Tachi T. Origami tubes with reconfigurable polygonal cross-sections [J]. *Proceedings of the Royal Society A: Mathematical, Physical and Engineering Science*, 2016, 472(2185): 20150607.
- [18] Ma J, You Z. Energy absorption of thin-walled square tubes with a prefolded origami pattern-part I: geometry and numerical simulation [J]. *Journal of Applied Mechanics*, 2014, 81(1): 011003.
- [19] Dai J S, Caldwell D G. Origami-based robotic paper-and-board packaging for food industry [J]. *Trends in Food Science & Technology*, 2010, 21(3): 153-157.
- [20] Yao W, Dai J S. Dexterous manipulation of origami cartons with robotic fingers based on the interactive configuration space [J]. *Journal of Mechanical Design*, 2008, 130(2): 022303.
- [21] Ma J, Song J, Chen Y. An origami-inspired structure with graded stiffness [J]. *International Journal of Mechanical Sciences*, 2018, 136: 134-142.
- [22] Dai J S, Jones J R. Mobility in metamorphic mechanisms of foldable/erectable kinds [J]. *Journal of Mechanical Design*, 1999, 121(3): 375-382.
- [23] Dai J S, Jones J R. Configuration transformations in metamorphic mechanisms of foldable/erectable kinds [C]. *Proceedings of the 10th World Congress on the Theory of Machines and Mechanisms*, Oulu, Finland, June. 1999: 20-24.
- [24] Demaine E D, O'Rourke J. *Geometric folding algorithms* [M]. Cambridge: Cambridge University Press, 2007.
- [25] Stachel H. A kinematic approach to Kokotsakis meshes [J]. *Computer Aided Geometric Design*, 2010, 27(6): 428-437.
- [26] Liu S, Lv W, Chen Y, Lu G. Deployable prismatic structures with rigid origami patterns [J]. *Journal of Mechanisms and Robotics*, 2016, 8(3): 031002.
- [27] Chen Y, Lv W, Li J, You Z. An extended family of rigidly foldable origami tubes [J]. *Journal of Mechanisms and Robotics*, 2017, 9(2): 021002.
- [28] Dai J S, Jones J R. Kinematics and mobility analysis of carton folds in packing manipulation based on the mechanism equivalent [J]. *Proceedings of the Institution of Mechanical Engineers, Part C: Journal of Mechanical Engineering Science*, 2002, 216(10): 959-970.
- [29] Chen Y, Peng R, You Z. Origami of thick panels [J]. *Science*, 2015, 349(6246): 396-400.
- [30] Chiang C H. *Kinematics of spherical mechanisms* [M]. Cambridge: Cambridge University Press, 1988.
- [31] Hartenberg R S, Denavit J. *Kinematic synthesis of linkages* [M]. McGraw-Hill,

- 1964.
- [32] Gogu G. Structural synthesis of parallel robots [M]. Dordrecht: Springer, 2008.
- [33] Dai J S. Geometrical foundations and screw algebra for mechanisms and robotics [M]. Beijing: Higher Education Press, ISBN: 9787040334838, 2014.
- [34] Ball R S. A treatise on the theory of screws [M]. Cambridge: Cambridge University Press, 1900.
- [35] Dai J S. Finite displacement screw operators with embedded Chasles' motion [J]. Journal of Mechanisms and Robotics, 2012, 4(4): 041002.
- [36] Yang S, Sun T, Huang T, Li Q, Gu D. A finite screw approach to type synthesis of three-DOF translational parallel mechanisms [J]. Mechanism and Machine Theory, 2016, 104: 405-419.
- [37] Sun T, Yang S, Huang T, Dai J S. A way of relating instantaneous and finite screws based on the screw triangle product [J]. Mechanism and Machine Theory, 2017, 108: 75-82.
- [38] Huang C, Chen C M. The linear representation of the screw triangle—a unification of finite and infinitesimal kinematics [J]. Journal of Mechanical Design, 1995, 117(4): 554-560.
- [39] Murray R M, Li Z X, Sastry S S. A mathematical introduction to robotic manipulation [M]. Boca Raton: CRC Press, 1994.
- [40] Hervé J M. The Lie group of rigid body displacements, a fundamental tool for mechanism design [J]. Mechanism and Machine Theory, 1999, 34(5): 719-730.
- [41] Zhang X, López-Custodio P, Dai J S. Compositional submanifolds of prismatic-universal-prismatic and skewed prismatic-revolute-prismatic kinematic chains and their derived parallel mechanisms [J]. Journal of Mechanisms and Robotics, 2018, 10(3): 031001.
- [42] Chai X, Li Q. Analytical mobility analysis of Bennett linkage using geometric algebra [J]. Advances in Applied Clifford Algebras, 2017, 27(3): 2083-2095.
- [43] Perez A, McCarthy J M. Dual quaternion synthesis of constrained robotic systems [J]. Journal of Mechanical Design, 2004, 126(3): 425-435.
- [44] Gan D, Liao Q, Wei S, Dai J S, Qiao S. Dual quaternion-based inverse kinematics of the general spatial $7R$ mechanism [J]. Proceedings of the Institution of Mechanical Engineers, Part C: Journal of Mechanical Engineering Science, 2008, 222(8): 1593-1598.
- [45] Leclercq G, Lefèvre P, Blohm G. 3D kinematics using dual quaternions: theory and applications in neuroscience [J]. Frontiers in Behavioral Neuroscience, 2013, 7: 7.
- [46] Hegedüs G, Schicho J, Schröcker H P. Bond theory and closed $5R$ linkages [C]. Latest Advances in Robot Kinematics, Springer, 2012: 221-228.

- [47] Hegedüs G, Schicho J, Schröcker H P. The theory of bonds: a new method for the analysis of linkages [J]. *Mechanism and Machine Theory*, 2013, 70: 407-424.
- [48] Nawratil G. Introducing the theory of bonds for Stewart Gough platforms with self-motions [J]. *Journal of Mechanisms and Robotics*, 2013, 6(1): 011004.
- [49] Hegedüs G, Li Z, Schicho J, Schröcker H P. The theory of bonds II: closed 6R linkages with maximal genus [J]. *Journal of Symbolic Computation*, 2015, 68: 167-180.
- [50] Chablat D, Kong X, Zhang C. Kinematics, workspace and singularity analysis of a parallel robot with five operation modes [J]. *Journal of Mechanisms and Robotics*, 2018.
- [51] Aspragathos N A, Dimitros J K. A comparative study of three methods for robot kinematics [J]. *IEEE Transactions on Systems, Man, and Cybernetics, Part B (Cybernetics)*, 1998, 28(2): 135-145.
- [52] Selig J M. *Geometrical methods in robotics* [M]. Springer Science & Business Media, 2013.
- [53] Cui L, Dai J S. Axis constraint analysis and its resultant 6R double-centered overconstrained mechanisms [J]. *Journal of Mechanisms and Robotics*, 2011, 3(3): 031004.
- [54] Gogu G. Bifurcation in constraint singularities and structural parameters of parallel mechanisms [J]. *Meccanica*, 2011, 46(1): 65-74.
- [55] Gosselin C, Angeles J. Singularity analysis of closed-loop kinematic chains [J]. *IEEE Transactions on Robotics and Automation*, 1990, 6(3): 281-290.
- [56] Zlatanov D, Bonev I A, Gosselin C M. Constraint singularities of parallel mechanisms [C]. *Proceedings of the 2002 IEEE International Conference on Robotics & Automation*, Washington, DC, 2002.
- [57] Li Q, Chai X, Wu C. Singularity analysis of a 3-RPS parallel manipulator using geometric algebra [J]. *Chinese Journal of Mechanical Engineering*, 2015, 28(6): 1204-1212.
- [58] Yao H, Chen Q, Chai X, Li Q. Singularity analysis of 3-RPR parallel manipulators using geometric algebra [J]. *Advances in Applied Clifford Algebras*, 2017, 27(3): 2097-2113.
- [59] Ma J, Chen Q, Yao H, Chai X, Li Q. Singularity analysis of the 3/6 Stewart parallel manipulator using geometric algebra [J]. *Mathematical Methods in the Applied Sciences*, 2018.
- [60] Jha R, Chablat D, Rouillier F, Moroz G. Workspace and singularity analysis of a Delta like family robot [C]. *Robotics and Mechatronics*. Springer, Cham, 2016: 121-130.

- [61] Ben-Horin P, Shoham M, Caro S, Chablat D, Wenger P. SinguLab-a graphical user interface for the singularity analysis of parallel robots based on Grassmann-Cayley algebra [C]. *Advances in Robot Kinematics: Analysis and Design*, Springer Netherlands, 2008: 49-58.
- [62] Kanaan D, Wenger P, Caro S, Chablat D. Singularity analysis of lower mobility parallel manipulators using Grassmann-Cayley algebra [J]. *IEEE Transactions on Robotics*, 2009, 25(5): 995-1004.
- [63] Caro S, Moroz G, Gayral T, Chablat D, Chen C. Singularity analysis of a six-dof parallel manipulator using Grassmann-Cayley algebra and Gröebner bases [C]. *Brain, Body and Machine*, Springer, Berlin, Heidelberg, 2010: 341-352.
- [64] Gan D, Dai J S. Geometry constraint and branch motion evolution of 3-PUP parallel mechanisms with bifurcated motion [J]. *Mechanism and Machine Theory*, 2013, 61: 168-183.
- [65] Wang Y X, Wang Y M. Configuration bifurcations analysis of six degree-of-freedom symmetrical Stewart parallel mechanisms [J]. *Journal of Mechanical Design*, 2005, 127(1): 70-77.
- [66] Lee C C, Herve J M. A novel discontinuously movable six-revolute mechanism [C]. *Proceedings of the 2009 ASME/IFTOMM International Conference on Reconfigurable Mechanisms and Robots*, IEEE, 2009: 58-62.
- [67] Li Q, Hervé J M. Parallel mechanisms with bifurcation of Schoenflies motion [J]. *IEEE Transactions on Robotics*, 2009, 25(1): 158-164.
- [68] Zhang K, Dai J S, Fang Y. Constraint analysis and bifurcated motion of the 3PUP parallel mechanism [J]. *Mechanism and Machine Theory*, 2012, 49: 256-269.
- [69] Gogu G. Branching singularities in kinematotropic parallel mechanisms [C]. *Computational kinematics*, Springer, Berlin, Heidelberg, 2009: 341-348.
- [70] Chen Y, You Z. An extended Myard linkage and its derived 6R linkage [J]. *Journal of Mechanical Design*, 2008, 130(5): 052301.
- [71] Song C Y, Chen Y, Chen I M. A 6R linkage reconfigurable between the line-symmetric Bricard linkage and the Bennett linkage [J]. *Mechanism and Machine Theory*, 2013, 70: 278-292.
- [72] Song C Y, Chen Y. Multiple linkage forms and bifurcation behaviours of the double-subtractive-Goldberg 6R linkage [J]. *Mechanism and Machine Theory*, 2012, 57: 95-110.
- [73] Song C, Chen Y. A special Wohlhart's double-Goldberg 6R linkage and its multiple operation forms among 4R and 6R linkages [C]. *Advances in Reconfigurable Mechanisms and Robots I*, Springer, London, 2012: 45-52.
- [74] Zhang K, Dai J S. A kirigami-inspired 8R linkage and its evolved

- overconstrained $6R$ linkages with the rotational symmetry of order two [J]. *Journal of Mechanisms and Robotics*, 2014, 6(2): 021007.
- [75] Zhang K, Dai J S. Trifurcation of the evolved Sarrus-motion linkage based on parametric constraints [C]. *Advances in Robot Kinematics*, Springer International Publishing, 2014: 345-353.
- [76] Qin Y, Dai J S, Gogu G. Multi-furcation in a derivative queer-square mechanism [J]. *Mechanism and Machine Theory*, 2014, 81: 36-53.
- [77] Aimedee F, Gogu G, Dai J S, Bouzgarrou C, Bouton N. Systematization of morphing in reconfigurable mechanisms [J]. *Mechanism and Machine Theory*, 2016, 96: 215-224.
- [78] Zhang K, Müller A, Dai J S. A novel reconfigurable $7R$ linkage with multifurcation [C]. *Advances in Reconfigurable Mechanisms and Robots II*, Springer, Cham, 2016: 15-25.
- [79] He X, Kong X, Chablat D, Caro S, Hao G. Kinematic analysis of a single-loop reconfigurable $7R$ mechanism with multiple operation modes [J]. *Robotica*, 2014, 32(7): 1171-1188.
- [80] Pellegrino S. Structural computations with the singular value decomposition of the equilibrium matrix [J]. *International Journal of Solids and Structures*, 1993, 30(21): 3025-3035.
- [81] Chen Y, You Z, Tarnai T. Threefold-symmetric Bricard linkages for deployable structures [J]. *International Journal of Solids and Structures*, 2005, 42(8): 2287-2301.
- [82] Gan W W, Pellegrino S. Numerical approach to the kinematic analysis of deployable structures forming a closed loop [J]. *Proceedings of the Institution of Mechanical Engineers, Part C: Journal of Mechanical Engineering Science*, 2006, 220(7): 1045-1056.
- [83] Kumar P, Pellegrino S. Computation of kinematic paths and bifurcation points [J]. *International Journal of Solids and Structures*, 2000, 37(46-47): 7003-7027.
- [84] Dai J S, Huang Z, Lipkin H. Mobility of overconstrained parallel mechanisms [J]. *Journal of Mechanical Design*, 2006, 128(1): 220-229.
- [85] Gan D, Dai J S, Liao Q. Constraint analysis on mobility change of a novel metamorphic parallel mechanism [J]. *Mechanism and Machine Theory*, 2010, 45(12): 1864-1876.
- [86] Gan D, Dai J S, Dias J, Seneviratne L. Unified kinematics and singularity analysis of a metamorphic parallel mechanism with bifurcated motion [J]. *Journal of Mechanisms and Robotics*, 2013, 5(3): 031004.
- [87] Chen Y, Chai W H. Bifurcation of a special line and plane symmetric Bricard linkage [J]. *Mechanism and Machine Theory*, 2011, 46(4): 515-533.

- [88] Ionescu T G. Terminology for mechanisms and machine science [J]. *Mechanism and Machine Theory*, 2003, 38(7-10): 597-1112.
- [89] Baker J E. A comparative survey of the Bennett-based, 6-revolute kinematic loops [J]. *Mechanism and Machine Theory*, 1993, 28(1): 83-96.
- [90] Myard F E. Contribution à la géométrie des systèmes articulés [J]. *Bulletin de la Société Mathématique de France*, 1931, 59: 183-210.
- [91] You Z, Chen Y. *Motion structures: deployable structural assemblies of mechanisms* [M]. CRC Press, 2014.
- [92] Goldberg M. New five-bar and six-bar linkages in three dimensions [J]. *Transactions of ASME*, 1943, 65: 649-661.
- [93] Wohlhart K. Merging two general Goldberg $5R$ linkages to obtain a new $6R$ space mechanism [J]. *Mechanism and Machine Theory*, 1991, 26(7): 659-668.
- [94] Song C Y, Chen Y. A spatial $6R$ linkage derived from subtractive Goldberg $5R$ linkages [J]. *Mechanism and Machine Theory*, 2011, 46(8): 1097-1106.
- [95] Chen Y, You Z. Spatial $6R$ linkages based on the combination of two Goldberg $5R$ linkages [J]. *Mechanism and Machine Theory*, 2007, 42(11): 1484-1498.
- [96] Song C Y, Chen Y. A family of mixed double-Goldberg $6R$ linkages [J]. *Proceedings of the Royal Society A: Mathematical, Physical and Engineering Science*, 2012, 468(2139): 871-890.
- [97] Waldron K J. Hybrid overconstrained linkages [J]. *Journal of Mechanisms*, 1968, 3(2): 73-78.
- [98] Yu H C, Baker J E. On the generation of new linkages from Bennett loops [J]. *Mechanism and Machine Theory*, 1981, 16(5): 473-485.
- [99] Bricard R. Mémoire sur la théorie de l'octaèdre articulé [J]. *J Math Pures Appl*, 1897, 3: 113-150. (English translation by E. A. Coutsias, 2010, e-print, <http://arxiv.org/abs/1203.1286>)
- [100] Bricard R. *Leçons de cinématique* [M]. Paris: Gauthier-Villars, 1926.
- [101] Bennett G T. Deformabl octahedra [J]. *Proceedings of the London Mathematical Society*, 1912, 2(1): 309-343.
- [102] Lee C C. On the generation synthesis of movable octahedral $6R$ mechanisms [C]. *ASME Design Engineering Technical Conferences and Computers in Engineering Conference*, Irvine, CA, 1996: 18-22.
- [103] Baker J E. Limiting positions of a Bricard linkage and their possible relevance to the cyclohexane molecule [J]. *Mechanism and Machine Theory*, 1986, 21(3): 253-260.
- [104] Chai W H, Chen Y. The line-symmetric octahedral Bricard linkage and its structural closure [J]. *Mechanism and Machine Theory*, 2010, 45(5): 772-779.

- [105] Baker J E. On Bricard's doubly collapsible octahedron and its planar, spherical and skew counterparts [J]. *Journal of the Franklin Institute*, 1995, 332(6): 657-679.
- [106] Baker J E. On the skew network corresponding to Bricard's doubly collapsible octahedron [J]. *Proceedings of the Institution of Mechanical Engineers, Part C: Journal of Mechanical Engineering Science*, 2009, 223(5): 1213-1221.
- [107] Lu S, Zlatanov D, Ding X, Zoppi M, Guest S D. Folding type III Bricard linkages [C]. *Proceedings of the 14th IFToMM World Congress, Taipei, Taiwan*, 2015: 455-462.
- [108] Lu S, Zlatanov D, Ding X, Zoppi M, Guest S D. A network of type III Bricard linkages [C]. *Proceedings of the ASME 2015 International Design Engineering Technical Conferences and Computers and Information in Engineering Conference*, American Society of Mechanical Engineers, 2015: V05CT08A043.
- [109] Lu S, Zlatanov D, Ding X, Zoppi M, Guest S D. Reconfigurable chains of bifurcating type III Bricard linkages [C]. *Advances in Reconfigurable Mechanisms and Robots II*, Springer, Cham, 2016: 3-14.
- [110] Goldberg M. A six-plate linkage in three dimensions [J]. *The Mathematical Gazette*, 1974, 58(406): 287-289.
- [111] Yu H C. The deformable hexahedron of Bricard [J]. *Mechanism and Machine Theory*, 1981, 16(6): 621-629.
- [112] Wohlhart K. The two types of the orthogonal Bricard linkage [J]. *Mechanism and Machine Theory*, 1993, 28(6): 809-817.
- [113] Baker J E, Wohlhart K. On the single screw reciprocal to the general line-symmetric six-screw linkage [J]. *Mechanism and Machine Theory*, 1994, 29(1): 169-175.
- [114] Song C Y, Chen Y, Chen I M. Kinematic study of the original and revised general line-symmetric Bricard $6R$ linkages [J]. *Journal of Mechanisms and Robotics*, 2014, 6(3): 031002.
- [115] López-Custodio P C, Dai J S, Rico J M. Branch reconfiguration of Bricard linkages based on toroids intersections: line-symmetric case [J]. *Journal of Mechanisms and Robotics*, 2018, 10(3): 031003.
- [116] Baker J E. An analysis of the Bricard linkages [J]. *Mechanism and Machine Theory*, 1980, 15(4): 267-286.
- [117] Phillips J. *Freedom in machinery* [M]. Cambridge University Press, 2007.
- [118] Baker J E. The single screw reciprocal to the general plane-symmetric six-screw linkage [J]. *Journal for Geometry Graphics*, 1997, 1(1): 5-12.
- [119] Li Z, Schicho J. A technique for deriving equational conditions on the Denavit-Hartenberg parameters of $6R$ linkages that are necessary for movability [J].

- Mechanism and Machine Theory, 2015, 94: 1-8.
- [120] Deng Z, Huang H, Li B, Liu R. Synthesis of deployable/foldable single loop mechanisms with revolute joints [J]. Journal of Mechanisms and Robotics, 2011, 3(3): 031006.
- [121] Huang H, Deng Z, Qi X, Li B. Virtual chain approach for mobility analysis of multiloop deployable mechanisms [J]. Journal of Mechanical Design, 2013, 135(11): 111002.
- [122] Kong X. Type synthesis of single-loop overconstrained 6R spatial mechanisms for circular translation [J]. Journal of Mechanisms and Robotics, 2014, 6(4): 041016.
- [123] Viquerat A D, Hutt T, Guest S D. A plane symmetric 6R foldable ring [J]. Mechanism and Machine Theory, 2013, 63: 73-88.
- [124] Qi X, Huang H, Miao Z, Li B, Deng Z. Design and mobility analysis of large deployable mechanisms based on plane-symmetric Bricard linkage [J]. Journal of Mechanical Design, 2017, 139(2): 022302.
- [125] Zhang K, Dai J S. Geometric constraints and motion branch variations for reconfiguration of single-loop linkages with mobility one [J]. Mechanism and Machine Theory, 2016, 106: 16-29.
- [126] López-Custodio P C, Dai J S, Rico J M. Branch reconfiguration of Bricard linkages based on toroids intersections: plane-symmetric case [J]. Journal of Mechanisms and Robotics, 2018, 10(3): 031002.
- [127] Sarrus P T. Note sur la transformation des mouvements rectilignes alternatifs, en mouvements circulaires, et reciproquement, comptes. rendus [J]. Académie des Sciences, Paris, 1853, 36: 1036.
- [128] Baker J E. Displacement-closure equations of the unspecialised double-Hooke's-joint linkage [J]. Mechanism and Machine Theory, 2002, 37(10): 1127-1144.
- [129] Bennett G T. The parallel motion of Sarrut and some allied mechanisms [J]. The London, Edinburgh, and Dublin Philosophical Magazine and Journal of Science, 1905, 9(54): 803-810.
- [130] Zhang K, Dai J S. Screw-system-variation enabled reconfiguration of the Bennett plano-spherical hybrid linkage and its evolved parallel mechanism [J]. Journal of Mechanical Design, 2015, 137(6): 062303.
- [131] Altmann P G. Communications to Grodzinski P, M'Ewen E. Link mechanisms in modern kinematics [J]. Proceedings of the Institution of Mechanical Engineers, 1954, 168(1): 877-896.
- [132] Wohlhart K. A new 6R space mechanism [C]. Proceedings of the 7th World Congress on the Theory of Machines and Mechanisms, Sevilla, Spain. 1987:

17-22.

- [133] Mavroidis C, Roth B. Analysis and synthesis of overconstrained mechanisms [C]. Proceedings of the 1994 ASME Design Technical Conferences, Minneapolis, New York, 1994: 115-133.
- [134] Dietmaier P. A new 6R space mechanism [C]. Proceedings of the 9th World Congress on the Theory of Machines and Mechanisms, Milano, Italy. 1995: 52-56.
- [135] Peraza-Hernandez E A, Hartl D J, Malak Jr R J, Lagoudas D C. Origami-inspired active structures: a synthesis and review [J]. Smart Materials and Structures, 2014, 23(9): 094001.
- [136] Miura K. Map fold a la Miura style, its physical characteristics and application to the space science [J]. Research of Pattern Formation, 1994: 77-90.
- [137] Miura K. Triangles and quadrangles in space [C]. Proceedings of the 50th Symposium of the International Association for Shell and Spatial Structures, Valencia, 2009.
- [138] Zirbel S A, Lang R J, Thomson M W, Sigel D A, Walkemeyer P E, Trease B P, Magleby S P, Howell L L. Accommodating thickness in origami-based deployable arrays [J]. Journal of Mechanical Design, 2013, 135(11): 111005.
- [139] Morgan J, Magleby S P, Howell L L. An approach to designing origami-adapted aerospace mechanisms [J]. Journal of Mechanical Design, 2016, 138(5): 052301.
- [140] Wilson L, Pellegrino S, Danner R. Origami sunshield concepts for space telescopes [C]. Proceedings of the 54th AIAA/ASME/ASCE/AHS/ASC Structures, Structural Dynamics, and Materials Conference, 2013: 1594.
- [141] Debnath S, Fei L J. Origami theory and its applications: a literature review [J]. World Academy of Science, Engineering and Technology, 2013: 1131-1135.
- [142] Reis P M, Jiménez F L, Marthelot J. Transforming architectures inspired by origami [J]. Proceedings of the National Academy of Sciences, 2015, 112(40): 12234-12235.
- [143] Lee T U, Gattas J M. Geometric design and construction of structurally stabilized accordion shelters [J]. Journal of Mechanisms and Robotics, 2016, 8(3): 031009.
- [144] Belke C H, Paik J. Mori: a modular origami robot [J]. IEEE/ASME Transactions on Mechatronics, 2017, 22(5): 2153-2164.
- [145] Zhakypov Z, Belke C, Paik J. Tribot: A deployable, self-righting and multi-locomotive origami robot [C]. IEEE International Conference on Intelligent Robots and Systems (IROS), 2017.
- [146] Kuribayashi K, Tsuchiya K, You Z, Tomus D, Umemoto M, Ito T, Sasaki M. Self-deployable origami stent grafts as a biomedical application of Ni-rich TiNi

- shape memory alloy foil [J]. *Materials Science and Engineering: A*, 2006, 419(1-2): 131-137.
- [147] Miyashita S, Guitron S, Ludersdorfer M, Sung C R, Rus D. An untethered miniature origami robot that self-folds, walks, swims, and degrades [C]. *Proceedings of the 2015 IEEE International Conference on Robotics and Automation (ICRA)*, 2015: 1490-1496.
- [148] Miyashita S, Guitron S, Yoshida K, Li S, Damian D D, Rus D. Ingestible, controllable, and degradable origami robot for patching stomach wounds [C]. *Proceedings of the 2016 IEEE International Conference on Robotics and Automation (ICRA)*, 2016: 909-916.
- [149] Guitron S, Guha A, Li S, Rus D. Autonomous locomotion of a miniature, untethered origami robot using hall effect sensor-based magnetic localization [C]. *Proceedings of the 2017 IEEE International Conference on Robotics and Automation (ICRA)*, 2017: 4807-4813.
- [150] Salerno M, Zhang K, Menciassi A, Dai J S. A novel 4-DOF origami grasper with an SMA-actuation system for minimally invasive surgery [J]. *IEEE Transactions on Robotics*, 2016, 32(3): 484-498.
- [151] Johnson M, Chen Y, Hovet S, Xu S, Wood B, Ren H, Tokuda J, Tse Z T H. Fabricating biomedical origami: a state-of-the-art review [J]. *International Journal of Computer Assisted Radiology and Surgery*, 2017, 12(11): 2023-2032.
- [152] Lang R J. *Twists, tilings, and tessellations: mathematical methods for geometric origami* [M]. Boca Raton: CRC Press, 2017.
- [153] Huffman D A. Curvature and creases: a primer on paper [J]. *IEEE Transactions on Computers*, 1976 (10): 1010-1019.
- [154] Miura K. *Proposition of pseudo-cylindrical concave polyhedral shells* [M]. Institute of Space and Aeronautical Science, University of Tokyo, 1969.
- [155] Barreto P T. Lines meeting on a surface: the “Mars” paperfolding [C]. *Proceedings of the 2nd International Meeting of Origami Science and Scientific Origami*, 1997: 323-331.
- [156] Miura K. Method of packaging and deployment of large membranes in space [J]. *The Institute of Space and Astronautical Science Report*, 1985, 618: 1.
- [157] Xie R, Li J, Chen Y. The graded origami structures [C]. *ASME 2015 International Design Engineering Technical Conferences and Computers and Information in Engineering Conference*. American Society of Mechanical Engineers, 2015: V05BT08A026.
- [158] Tachi T. Generalization of rigid foldable quadrilateral mesh origami [C]. *Proceedings of the 50th Symposium of the International Association for Shell and Spatial Structures*, Valencia, 2009.

- [159] Evans T A, Lang R J, Magleby S P, Howell L L. Rigidly foldable origami gadgets and tessellations [J]. *Royal Society Open Science*, 2015, 2(9): 150067.
- [160] Mitani J. *3D Origami Art* [M]. Boca Raton: CRC Press, 2016.
- [161] Evans T A, Lang R J, Magleby S P, Howell L L. Rigidly foldable origami twists [J]. *Origami*, 2015, 6: 119-130.
- [162] Turner N, Goodwine B, Sen M. A review of origami applications in mechanical engineering [J]. *Proceedings of the Institution of Mechanical Engineers, Part C: Journal of Mechanical Engineering Science*, 2016, 230(14): 2345-2362.
- [163] Yoshimura Y. On the mechanism of buckling of a circular cylindrical shell under axial compression [J]. *National Advisory Committee for Aeronautics Technical Memorandum*, 1955.
- [164] Resch R D, Christiansen H. The design and analysis of kinematic folded plate systems [C]. *Proceedings of IASS Symposium on Folded Plates and Prismatic Structures*, 1970.
- [165] Randlett S. *The art of origami* [M]. Faber & Faber, 1961.
- [166] Peng R, Ma J, Chen Y. Rigid foldability of triangle-twist origami pattern and its derived 6R linkage [C]. *Proceedings of the ASME 2017 International Design Engineering Technical Conferences and Computers and Information in Engineering Conference*, American Society of Mechanical Engineers, 2017: V05BT08A057.
- [167] Tachi T, Masubuchi M, Iwamoto M. Rigid origami structures with vacuumatics: geometric considerations [C]. *Proceedings of the IASS-APCS Seoul, Korea*, 2012.
- [168] Qiu C, Zhang K, Dai J S. Repelling-screw based force analysis of origami mechanisms [J]. *Journal of Mechanisms and Robotics*, 2016, 8(3): 031001.
- [169] Goldberg M. Polyhedral linkages [J]. *National Mathematics Magazine*, 1942, 16(7): 323-332.
- [170] Oborn P. *Al bahr towers: the abu dhabi investment council headquarters* [M]. John Wiley & Sons, 2014.
- [171] Onal C D, Wood R J, Rus D. An origami-inspired approach to worm robots [J]. *IEEE/ASME Transactions on Mechatronics*, 2013, 18(2): 430-438.
- [172] Fang H, Zhang Y, Wang K W. Origami-based earthworm-like locomotion robots [J]. *Bioinspiration & Biomimetics*, 2017, 12(6): 065003.
- [173] Lee D Y, Kim J S, Kim S R, Koh J S, Cho K J. The deformable wheel robot using magic-ball origami structure [C]. *Proceedings of the ASME 2013 International Design Engineering Technical Conferences and Computers and Information in Engineering Conference*, American Society of Mechanical Engineers, 2013: V06BT07A040.

- [174] Li S, Vogt D M, Rus D, Wood R J. Fluid-driven origami-inspired artificial muscles [J]. *Proceedings of the National Academy of Sciences*, 2017: 201713450.
- [175] Hull T. On the mathematics of flat origamis [J]. *Congressus Numerantium*, 1994: 215-224.
- [176] Hull T. The combinatorics of flat folds: a survey [C]. *Third International Meeting of Origami Science*, 2002: 29-38.
- [177] Bern M, Hayes B. The complexity of flat origami [C]. *SODA*, 1996, 96: 175-183.
- [178] Schneider J. Flat-foldability of origami crease patterns [J]. *Swathmore College*, December, 2004, 10.
- [179] Tachi T. Freeform variations of origami [J]. *Journal for Geometry and Graphics*, 2010, 14(2): 203-215.
- [180] Watanabe N, Kawaguchi K. The method for judging rigid foldability [J]. *Origami*, 2009, 4: 165-174.
- [181] Hull T. *Project origami: activities for exploring mathematics* [M]. AK Peters/CRC Press, 2006.
- [182] Wu W, You Z. Modelling rigid origami with quaternions and dual quaternions [J]. *Proceedings of the Royal Society of London A: Mathematical, Physical and Engineering Sciences*, 2010: rspa20090625.
- [183] Cai J, Zhang Y, Xu Y, Zhou Y, Feng J. The foldability of cylindrical foldable structures based on rigid origami [J]. *Journal of Mechanical Design*, 2016, 138(3): 031401.
- [184] Cai J, Liu Y, Ma R, Feng J, Zhou Y. Nonrigidly foldability analysis of Kresling cylindrical origami [J]. *Journal of Mechanisms and Robotics*, 2017, 9(4): 041018.
- [185] Liu S, Chen Y, Lu G. The rigid origami patterns for flat surface [C]. *Proceedings of the ASME 2013 International Design Engineering Technical Conferences and Computers and Information in Engineering Conference*, American Society of Mechanical Engineers, 2013: V06BT07A039.
- [186] Arkin E M, Bender M A, Demaine E D, Demaine M L, Mitchell J S B, Sethia S, Skiena S S. When can you fold a map? [J]. *Computational Geometry*, 2004, 29(1): 23-46.
- [187] Song J, Chen Y, Lu G. Axial crushing of thin-walled structures with origami patterns [J]. *Thin-Walled Structures*, 2012, 54: 65-71.
- [188] Han J, Yamazaki K, Nishiyama S. Optimization of the crushing characteristics of triangulated aluminum beverage cans [J]. *Structural and Multidisciplinary Optimization*, 2004, 28(1): 47-54.

- [189] Kresling B, Abel J F. Natural twist buckling in shells: from the Hawkmoth's bellows to the deployable Kresling-pattern and cylindrical miuraori [C]. Proceedings of the 6th International Conference on Computation of Shell and Spatial Structures, John F. Abel and J. Robert Cooke, eds., Ithaca, 2008.
- [190] Nojima T. Modelling of folding patterns in flat membranes and cylinders by origami [J]. JSME International Journal Series C Mechanical Systems, Machine Elements and Manufacturing, 2002, 45(1): 364-370.
- [191] Tachi T. One-DOF cylindrical deployable structures with rigid quadrilateral panels [C]. Proceedings of the 50th Symposium of the International Association for Shell and Spatial Structures, Valencia, 2009.
- [192] Tachi T. Freeform rigid-foldable structure using bidirectionally flat-foldable planar quadrilateral mesh [J]. Advances in Architectural Geometry, 2010, 2010: 87-102.
- [193] Schenk M, Guest S D. Geometry of Miura-folded metamaterials [J]. Proceedings of the National Academy of Sciences, 2013, 110(9): 3276-3281.
- [194] Yasuda H, Yein T, Tachi T, Miura K, Taya M. Folding behaviour of Tachi-Miura polyhedron bellows [J]. Proceedings of the Royal Society A: Mathematical, Physical and Engineering Science, 2013, 469(2159): 20130351.
- [195] Ma J, You Z. Modelling of the waterbomb origami pattern and its applications [C]. Proceedings of the ASME 2014 International Design Engineering Technical Conferences and Computers and Information in Engineering Conference, American Society of Mechanical Engineers, 2014: V05BT08A047.
- [196] Tachi T. Rigid-foldable thick origami [J]. Origami, 2011, 5: 253-264.
- [197] Edmondson B J, Lang R J, Magleby S P, Howell L L. An offset panel technique for thick rigidly foldable origami [C]. Proceedings of the ASME 2014 International Design Engineering Technical Conferences and Computers and Information in Engineering Conference, American Society of Mechanical Engineers, 2014: V05BT08A054.
- [198] Ku J S, Demaine E D. Folding flat crease patterns with thick materials [J]. Journal of Mechanisms and Robotics, 2016, 8(3): 031003.
- [199] Lang R J, Tolman K A, Crampton E B, Magleby S P, Howell L L. A review of thickness-accommodation techniques in origami-inspired engineering [J]. Applied Mechanics Reviews, 2018, 70(1): 010805.
- [200] Sareh S, Rossiter J. Kirigami artificial muscles with complex biologically inspired morphologies [J]. Smart Materials and Structures, 2012, 22(1): 014004.
- [201] Virk K, Monti A, Trehard T, Marsh M, Hazra K, Boba K, Remillat C D L, Scarpa F, Farrow I R. SILICOMB PEEK Kirigami cellular structures: mechanical response and energy dissipation through zero and negative stiffness

- [J]. *Smart Materials and Structures*, 2013, 22(8): 084014.
- [202] Nojima T, Saito K. Development of newly designed ultra-light core structures [J]. *JSME International Journal Series A: Solid Mechanics and Material Engineering*, 2006, 49(1): 38-42.
- [203] Scarpa F, Ouisse M, Collet M, Saito K. Kirigami auxetic pyramidal core: mechanical properties and wave propagation analysis in damped lattice [J]. *Journal of Vibration and Acoustics*, 2013, 135(4): 041001.
- [204] Saito K, Agnese F, Scarpa F. A cellular kirigami morphing wingbox concept [J]. *Journal of Intelligent Material Systems and Structures*, 2011, 22(9): 935-944.
- [205] Lamoureux A, Lee K, Shlian M, Forrest S R, Shtein M. Dynamic kirigami structures for integrated solar tracking [J]. *Nature Communications*, 2015, 6: 8092.
- [206] Wu C, Wang X, Lin L, Guo H, Wang Z L. Paper-based triboelectric nanogenerators made of stretchable interlocking kirigami patterns [J]. *ACS Nano*, 2016, 10(4): 4652-4659.
- [207] Winder B G, Magleby S P, Howell L L. Kinematic representations of pop-up paper mechanisms [J]. *Journal of Mechanisms and Robotics*, 2009, 1(2): 021009.
- [208] Streinu I, Whiteley W. Single-vertex origami and spherical expansive motions [C]. *Japanese Conference on Discrete and Computational Geometry*, Springer, Berlin, Heidelberg, 2004: 161-173.
- [209] Xi Z, Lien J M. Folding rigid origami with closure constraints [C]. *Proceedings of the ASME 2014 International Design Engineering Technical Conferences and Computers and Information in Engineering Conference*. American Society of Mechanical Engineers, 2014: V05BT08A052.
- [210] Wang K, Chen Y. Folding a patterned cylinder by rigid origami [J]. *Origami*, 2011, 5: 265-276.
- [211] Zhang X, Chen Y. Mobile assemblies of Bennett linkages from four-crease origami patterns [J]. *Proceedings of the Royal Society A: Mathematical, Physical and Engineering Science*, 2018, 474(2210): 20170621.
- [212] Wei G, Dai J S. Origami-inspired integrated planar-spherical overconstrained mechanisms [J]. *Journal of Mechanical Design*, 2014, 136(5): 051003.
- [213] Zhang K, Fang Y, Fang H, Dai J S. Geometry and constraint analysis of the three-spherical kinematic chain based parallel mechanism [J]. *Journal of Mechanisms and Robotics*, 2010, 2(3): 031014.
- [214] Zhang K, Dai J S. Reconfiguration of the plane-symmetric double-spherical 6R linkage with bifurcation and trifurcation [J]. *Proceedings of the Institution of Mechanical Engineers, Part C: Journal of Mechanical Engineering Science*, 2016, 230(3): 473-482.

- [215] Cipra B. Proving a link between logic and origami [J]. *Science*, 1998, 279(5352): 804-805.
- [216] Frenzel, T, Kadic, M, Wegener, M. Three-dimensional mechanical metamaterials with a twist [J]. *Science*, 2017, 358 (6366): 1072-1074.

Appendix

A. Entries of Closure Equations of the Plane-symmetric Bricard Linkages

In general case:

(1, 3):

$$\begin{aligned} & \sin \theta_1 (\cos \alpha \sin \gamma \sin \theta_2 \sin \theta_3 - \cos \alpha \cos \beta \sin \gamma \cos \theta_2 \cos \theta_3 \\ & + \sin \alpha \sin \beta \sin \gamma \cos \theta_3 - \cos \alpha \sin \beta \cos \gamma \cos \theta_2 - \sin \alpha \cos \beta \cos \gamma) \\ & = (1 + \cos \theta_1) (\sin \gamma \cos \theta_2 \sin \theta_3 + \cos \beta \sin \gamma \sin \theta_2 \cos \theta_3 + \sin \beta \cos \gamma \sin \theta_2) \end{aligned}$$

(1, 4):

$$\begin{aligned} & \sin \theta_1 [c (\cos \alpha \sin \theta_2 \cos \theta_3 + \cos \alpha \cos \beta \cos \theta_2 \sin \theta_3 - \sin \alpha \sin \beta \sin \theta_3) \\ & + b \cos \alpha \sin \theta_2 - R_3 \cos \alpha \sin \beta \cos \theta_2 - R_2 \sin \alpha - R_3 \sin \alpha \cos \beta] \\ & = (1 + \cos \theta_1) [c (\cos \theta_2 \cos \theta_3 - \cos \beta \sin \theta_2 \sin \theta_3) + b \cos \theta_2 + a + R_3 \sin \beta \sin \theta_2] \end{aligned}$$

(3, 1):

$$\begin{aligned} & (1 + \cos \theta_4) (\sin \alpha \sin \theta_2 \cos \theta_3 + \sin \alpha \cos \beta \cos \theta_2 \sin \theta_3 + \cos \alpha \sin \beta \sin \theta_3) \\ & = \sin \theta_4 [\cos \gamma (\sin \alpha \sin \theta_2 \sin \theta_3 - \sin \alpha \cos \beta \cos \theta_2 \cos \theta_3 - \cos \alpha \sin \beta \cos \theta_3) \\ & + \sin \gamma (\sin \alpha \sin \beta \cos \theta_2 - \cos \alpha \cos \beta)] \end{aligned}$$

When $\theta_1 = \pi$,

(2, 3):

$$\begin{aligned} & \cos \alpha \sin \gamma \sin \theta_2 \sin \theta_3 - \cos \alpha \cos \beta \sin \gamma \cos \theta_2 \cos \theta_3 + \sin \alpha \sin \beta \sin \gamma \cos \theta_3 \\ & - \cos \alpha \sin \beta \cos \gamma \cos \theta_2 - \sin \alpha \cos \beta \cos \gamma = 0 \end{aligned}$$

(2, 4):

$$\begin{aligned} & c (\cos \alpha \sin \theta_2 \cos \theta_3 + \cos \alpha \cos \beta \cos \theta_2 \sin \theta_3 - \sin \alpha \sin \beta \sin \theta_3) \\ & + b \cos \alpha \sin \theta_2 - R_3 \cos \alpha \sin \beta \cos \theta_2 - R_2 \sin \alpha - R_3 \sin \alpha \cos \beta = 0 \end{aligned}$$

When $\theta_2 = \theta_6 = \pi$,

(1, 3):

$$\begin{aligned} & \sin \theta_1 (\cos \alpha \cos \beta \sin \gamma \cos \theta_3 + \sin \alpha \sin \beta \sin \gamma \cos \theta_3 + \cos \alpha \sin \beta \cos \gamma \\ & - \sin \alpha \cos \beta \cos \gamma) = -\sin \gamma \sin \theta_3 (1 + \cos \theta_1) \end{aligned}$$

(1, 4):

$$\begin{aligned} & \sin \theta_1 [-c \cos \alpha \cos \beta \sin \theta_3 - c \sin \alpha \sin \beta \sin \theta_3 + R_3 \cos \alpha \sin \beta \\ & - R_2 \sin \alpha - R_3 \sin \alpha \cos \beta] = (1 + \cos \theta_1) (-c \cos \theta_3 - b + a) \end{aligned}$$

When $\theta_3 = \theta_5 = \pi$,

(1, 3):

$$\sin \theta_1 (\cos \alpha \cos \beta \sin \gamma \cos \theta_2 - \sin \alpha \sin \beta \sin \gamma - \cos \alpha \sin \beta \cos \gamma \cos \theta_2 - \sin \alpha \cos \beta \cos \gamma) = (1 + \cos \theta_1)(-\cos \beta \sin \gamma \sin \theta_2 + \sin \beta \cos \gamma \sin \theta_2)$$

(1, 4):

$$\sin \theta_1 [-c \cos \alpha \sin \theta_2 + b \cos \alpha \sin \theta_2 - R_3 \cos \alpha \sin \beta \cos \theta_2 - R_2 \sin \alpha - R_3 \sin \alpha \cos \beta] = (1 + \cos \theta_1)(-c \cos \theta_2 + b \cos \theta_2 + a + R_3 \sin \beta \sin \theta_2)$$

When $\theta_4 = \pi$,

(1, 3):

$$\begin{aligned} & \sin \theta_1 (\cos \alpha \sin \gamma \sin \theta_2 \sin \theta_3 - \cos \alpha \cos \beta \sin \gamma \cos \theta_2 \cos \theta_3 \\ & + \sin \alpha \sin \beta \sin \gamma \cos \theta_3 - \cos \alpha \sin \beta \cos \gamma \cos \theta_2 - \sin \alpha \cos \beta \cos \gamma) \\ & = (1 + \cos \theta_1)(\sin \gamma \cos \theta_2 \sin \theta_3 + \cos \beta \sin \gamma \sin \theta_2 \cos \theta_3 + \sin \beta \cos \gamma \sin \theta_2) \end{aligned}$$

(1, 4):

$$\begin{aligned} & \sin \theta_1 [c(\cos \alpha \sin \theta_2 \cos \theta_3 + \cos \alpha \cos \beta \cos \theta_2 \sin \theta_3 - \sin \alpha \sin \beta \sin \theta_3) \\ & + b \cos \alpha \sin \theta_2 - R_3 \cos \alpha \sin \beta \cos \theta_2 - R_2 \sin \alpha - R_3 \sin \alpha \cos \beta] \\ & = (1 + \cos \theta_1)[c(\cos \theta_2 \cos \theta_3 - \cos \beta \sin \theta_2 \sin \theta_3) + b \cos \theta_2 + a + R_3 \sin \beta \sin \theta_2] \end{aligned}$$

(3, 2):

$$\begin{aligned} & \cos \gamma (\sin \alpha \sin \theta_2 \sin \theta_3 - \sin \alpha \cos \beta \cos \theta_2 \cos \theta_3 - \cos \alpha \sin \beta \cos \theta_3) \\ & + \sin \gamma (\sin \alpha \sin \beta \cos \theta_2 - \cos \alpha \cos \beta) = 0 \end{aligned}$$

Résumé

Le mécanisme constitue un sujet central dans les recherches en ingénierie mécanique, où divers mécanismes sont conçus comme des composants mécaniques afin de réaliser les mouvements souhaités. Le mécanisme spatial est un mécanisme dans lequel le mouvement est décrit en trois dimensions. En tant que sous-ensemble des mécanismes spatiaux, le mécanisme sphérique représente un mécanisme dans lequel tous les points mobiles se déplacent le long des courbes qui reposent sur des sphères concentriques. Il existe un type particulier de mécanisme, appelé comme mécanisme sur-contraint, qui ne répond pas au critère de mobilité de Grübler-Kutzbach. Il est mobile en raison des propriétés géométriques des liaisons. Il a été largement utilisé dans le domaine des structures dans l'ingénierie aérospatiales, principalement grâce à la rigidité structurelle, la simplicité de sa construction et la fiabilité de fonctionnement. La cinématique est l'étude de la géométrie du mouvement dans les mécanismes sans tenir compte des forces agissant sur ces derniers. La cinématique des mécanismes spatiaux est beaucoup plus complexe que celle-ci des mécanismes plans puisqu'elle produit des mouvements plus compliqués. Les études qui en sont faites permettent de mieux comprendre le mouvement des mécanismes spatiaux qui constitue la base de la conception, de l'analyse dynamique et du contrôle des mécanismes.

De plus, l'origami, art oriental très ancien qui consiste à produire des structures complexes en 2D ou 3D en pliant une feuille de papier plane, a récemment connu un fort développement dans divers domaines de l'ingénierie. Les applications fortes de l'ingénierie d'origami nouvellement formée comprennent les panneaux solaires, les réflecteurs d'antennes de satellites, les métamatériaux, les facettes mobiles, les appareils reconfigurables, les appareils à résistance aux chocs, les endoprothèses en origami, les automates et les robots, etc. Bien que le mouvement de la structure de l'origami soit utilisé dans ces domaines, peu de recherches ont été faites sur la propriété cinématique du type d'origami, en raison de la complexité et du multi-degré de liberté du mouvement d'origami. Une exception est Miura-ori, dont le mouvement est relativement simple et son analyse cinématique a été largement utilisée pour révéler les propriétés mécaniques, telles que le coefficient de Poisson et la rigidité. Puisque la plupart des matériaux d'ingénierie adoptés pour construire des structures d'origami et des métamatériaux sont relativement rigides, un sous-ensemble d'origami qui permet un mouvement continu entre les états pliés et non pliés le long des plis prédéterminés sans étirement ni flexion des facettes a attiré l'attention.

Du point de vue du mécanisme, les plis de l'origami peuvent être considérés comme des liaisons pivot et les facettes de papier sont comme les pièces qui forment la liaison. Un vertex avec tous les plis intersectés au sommet est cinématiquement

équivalent à un mécanisme sphérique. Ensuite, le pli multi-sommet peut être modélisé comme un réseau de mécanismes sphériques, et sa pliabilité rigide peut être jugée par des approches cinématiques. Cependant, dans la plupart des applications d'ingénierie, l'épaisseur du matériau ne peut pas simplement être ignorée. Pour plier des panneaux épais, une approche a été proposée récemment, où l'assemblage de mécanismes sphériques pour l'origami de la feuille de zéro-épaisseur est remplacé par un assemblage de mécanismes spatiaux sur-contraints. Par conséquent, le travail sur la cinématique des mécanismes sphériques et des mécanismes spatiaux sur-contraints contribue à l'analyse du mouvement de l'origami rigide, ce qui facilite davantage les applications d'ingénierie des modèles d'origami.

Le but de cette thèse est de conduire une analyse cinématique des mécanismes spatiaux basés sur la méthode matricielle D-H et de l'appliquer pour explorer le comportement rigide de pliabilité et de mouvement des modèles d'origami.

Dans ce processus, la pliabilité rigide du motif origami en torsion triangulaire est d'abord examinée sur la base de la cinématique du réseau de mécanismes $4R$ sphériques et de nouveaux mécanismes $6R$ sur-contraints dérivés par la technique du kirigami. Ensuite, la cinématique du mécanisme de Bricard $6R$ plan-symétrique est analysée et ses variations de bifurcation sont discutées. Après cela, les résultats sont appliqués pour étudier le pliage symétrique de l'origami de la waterbomb à six plis à panneau épais, qui est modélisé sous la forme d'un réseau de mécanismes de Bricard $6R$ plan-symétriques. Le comportement de mouvement de sa tessellation correspondante de feuille de zéro-épaisseur est démontré par un réseau de mécanismes $6R$ sphériques. Enfin, le comportement de mouvement de la forme cylindrique fermée de l'origami de la waterbomb est analysé à travers une étude paramétrique, en le modélisant comme un réseau fermé de mécanismes $6R$ sphériques. Les principaux résultats sont résumés comme suit.

- **Pliabilité rigide de l'origami en torsion triangulaire généralisée et de ses mécanismes $6R$ sur-contraints dérivés**

La torsion triangulaire est un modèle d'origami avec trois sommets de quatre-pli, qui se compose d'un triangle central et de trois paires de plis rayonnant de chaque côté du triangle. Grâce à son grand taux de déploiement /packaging et à sa propriété de pliage par torsion, il présente un grand potentiel dans la conception de structures pliantes bioniques. Cependant, les travaux existants se concentrent sur le cas où le triangle central est un triangle équilatéral ou le cas avec seulement des paires de plis parallèles, qui limitent la pliabilité rigide et les applications de la torsion triangulaire. En supprimant ces contraintes sur la torsion triangulaire, on peut en obtenir un cas général, représenté sur la figure 1.

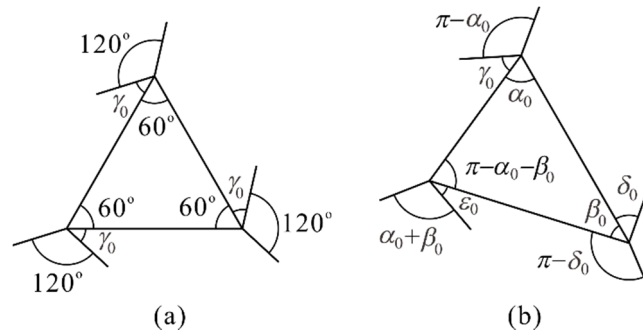


FIGURE 1 (a) Une torsion triangulaire habituelle, (b) une torsion triangulaire généralisée

Dans le 3^{ème} chapitre, la pliabilité rigide et le comportement de mouvement de la torsion triangulaire sont analysés. Basé sur l'équivalence cinématique entre origami rigides et mécanismes sphériques, le modèle peut être traité comme un réseau de mécanismes $4R$ sphériques. Les matrices D-H sont utilisées pour analyser la cinématique du mécanisme $4R$ sphérique à chaque sommet, puis la pliabilité rigide est discutée en utilisant les conditions de compatibilité. On trouve que la torsion triangulaire ne peut pas être pliée de manière rigide que lorsqu'au moins une paire de plis n'est pas parallèle et que la condition de compatibilité de l'angle de secteur est trouvée.

Puisque la pliabilité rigide d'un modèle d'origami peut varier selon le changement de l'assignation de Montagne-Vallée (Mountain-Valley pli (M-V)), tous les schémas possibles d'affectation M-V pour le modèle d'origami de torsion triangulaire généralisée devraient être trouvés. Les critères pour déterminer les schémas de l'assignation M-V sont les conditions de pliage à plat d'un sommet à quatre plis. Pour que le modèle soit plié en feuille plate, les conditions suivantes doivent être remplies: 1) la somme des angles alternatifs sur le sommet pliable est de 180 degrés, 2) la différence entre le nombre de plis de montagne et les plis de vallée devrait être égal à deux, et 3) les deux plis autour de l'angle de secteur minimum doivent être de l'opposé de la montagne ou de la vallée, tandis que les deux plis autour de l'angle de secteur maximal sont de la même affectation. Avec ces conditions, 32 schémas d'assignations M-V sont trouvés. En éliminant les cas dupliqués dus à la vue et à la rotation, il existe 12 types distincts d'assignation M-V pour le modèle d'origami en torsion triangulaire représenté sur la figure 2, dont la pliabilité rigide est analysée. On trouve que seulement huit schémas d'assignations M-V sont rigoureusement pliables. Il est à noter que pour une affectation M-V donnée de la torsion triangulaire dans ces huit types, la pliabilité rigide dépend aussi du choix des paramètres géométriques. Le boîtier rigide pliable peut devenir un boîtier non rigide en modifiant les paramètres géométriques. Par conséquent, nous pouvons concevoir une torsion de triangle rigide ou non-rigide en choisissant

l'affectation M-V et les paramètres géométriques appropriés selon nos besoins.

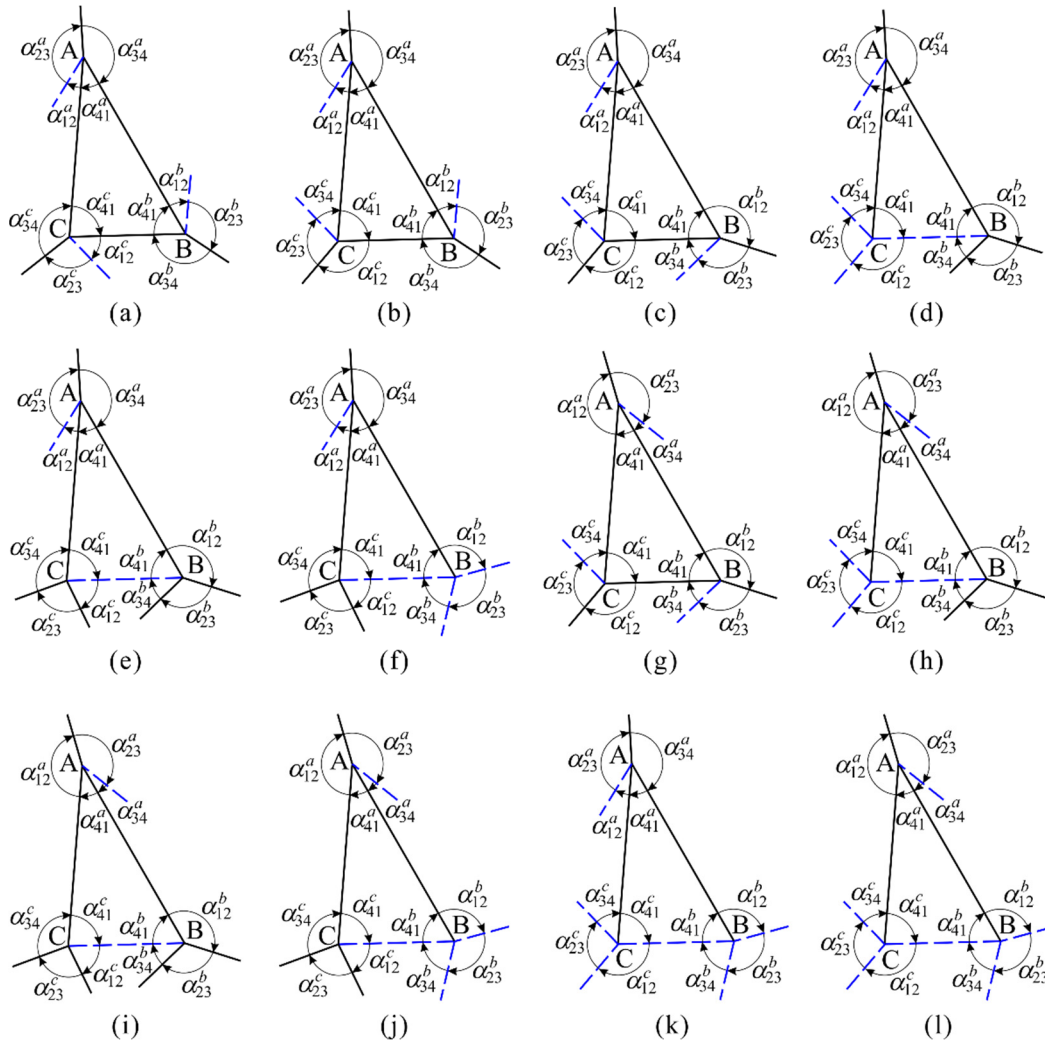


FIGURE 2 Douze schémas uniques d'affectation M-V pour le modèle d'origami de torsion triangulaire généralisée

Lors de l'analyse de la propriété cinématique du réseau correspondant de mécanismes $4R$ sphériques d'un motif d'origami à torsion triangulaire pliable de manière rigide, on constate que les sommets du triangle central restent toujours dans un seul plan au cours du mouvement. Ainsi, le triangle central peut être retiré sans affecter le mouvement du motif, représenté sur la figure 3. Ensuite, on obtient un modèle de torsion triangulaire pour le motif de kirigami, qui correspond à un mécanisme spatial $6R$ sur-contraint, représenté sur la figure 4.

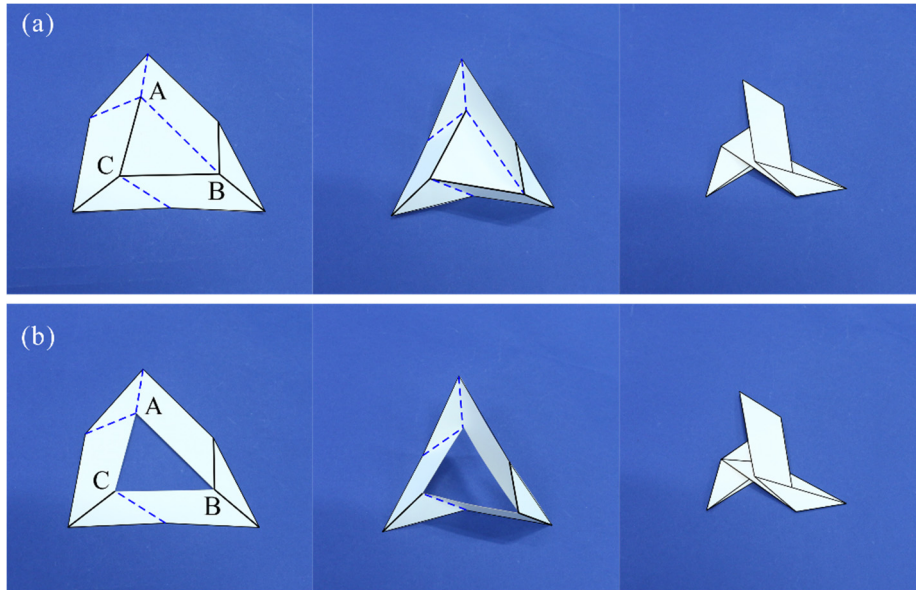


FIGURE 3 Modèles de torsion triangulaire physique pour (a) un motif origami, et (b) un motif de kirigami

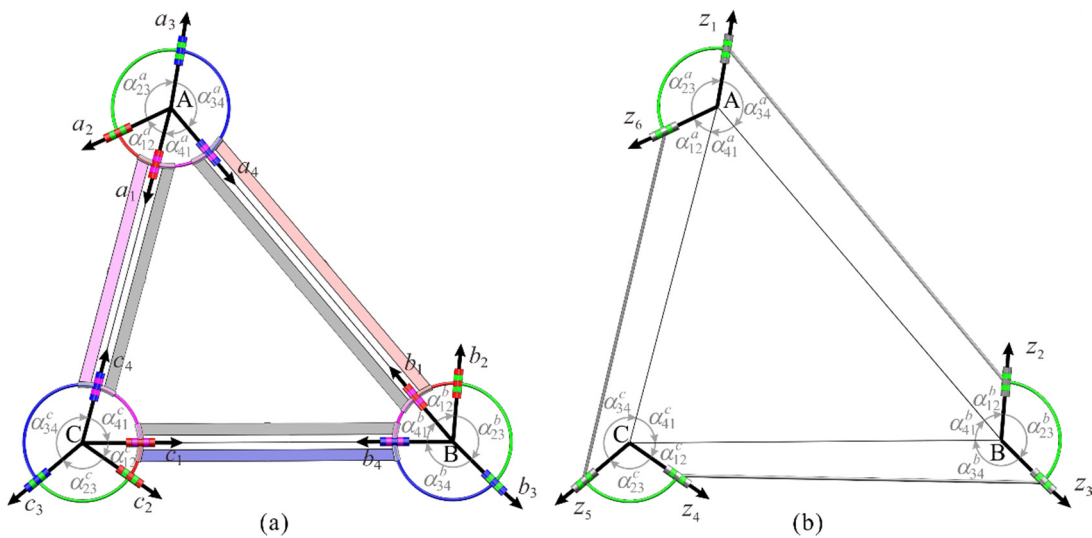


FIGURE 4 Mécanismes équivalents de la torsion triangulaire généralisée pour (a) un motif origami, et (b) un motif de kirigami

En analysant les paramètres géométriques et le mouvement du mécanisme $6R$ dérivée, une version du mécanisme de Bricard octaédrique doublement écrasable est obtenue à partir du modèle de papier de torsion triangulaire où chaque paire de plis se recoupe, représenté sur la figure 5(a). Un nouveau type de mécanisme $6R$ sur-contraint est dérivé quand une seule paire de plis est parallèle, représenté sur la figure 5(b), dont les conditions géométriques et les équations de fermeture sont données.

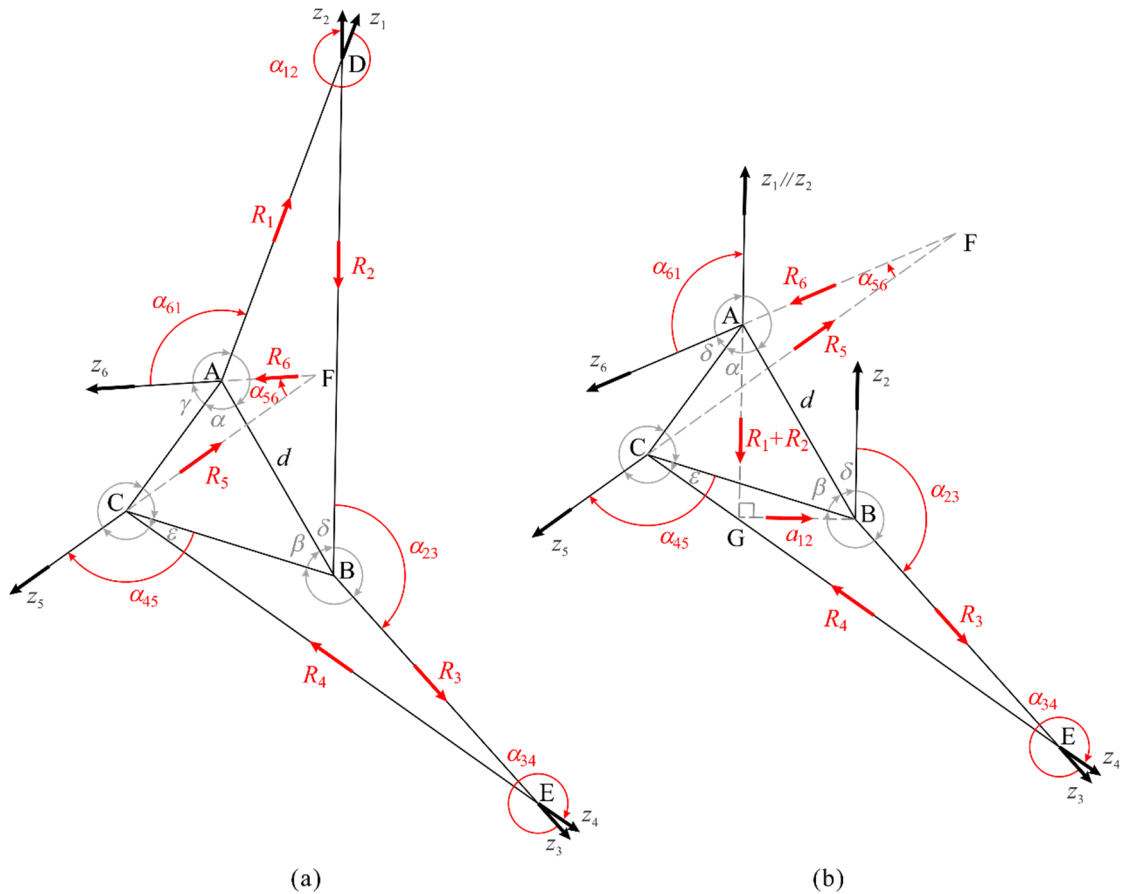


FIGURE 5 Diagrammes schématiques des mécanismes $6R$ sur-contraints dérivés quand (a) chaque paire de plis se recoupe, et (b) une seule paire de plis est parallèle

L'analyse d'origami en torsion triangulaire montre un bon accord avec la méthode d'analyse cinématique proposée de l'origami rigide basée sur les mécanismes spatiaux. Il ouvre une nouvelle façon de construire des mécanismes sur-contraints avec une seule boucle fermée à partir d'un réseau de mécanismes sphériques, qui peut être facilement étendu à d'autres types de modèles d'origami.

- **Analyse cinématique et bifurcation du mécanisme de Bricard plan-symétrique**

En tant que mécanisme $6R$ classique et sur-contraint, le mécanisme de Bricard à symétrie plane a été appliquée dans la conception de structures déployables en raison de sa rigidité structurelle et de sa fiabilité. En raison de la propriété de symétrie, le mécanisme de Bricard $6R$ symétrique a tendance à avoir des comportements de bifurcation compliqués, qui devraient être évités dans l'application de structures déployables, mais pourrait être utilisé dans la conception de mécanismes reconfigurables. Par conséquent, il est très important de réaliser l'analyse de la cinématique et de la bifurcation du mécanisme de Bricard plan-symétrique dans sa configuration générale.

Dans le 4^{ème} chapitre, les conditions cinématiques et de bifurcation du mécanisme de Bricard plan-symétrique général sont analysées en utilisant la méthode traditionnelle D-H, représenté sur la figure 6. Un ensemble d'équations de fermeture du contour du mécanisme de Bricard symétrique est dérivé sous des formes explicites. Les propriétés cinématiques du mécanisme dans diverses conditions géométriques sont comparées, y compris le nombre de branches de mouvement, les courbes cinématiques et les comportements de mouvement. En fixant une ou deux des variables cinématiques à 180 degrés, plusieurs mécanismes 5R / 4R sont dérivés, dont les conditions géométriques sont données.

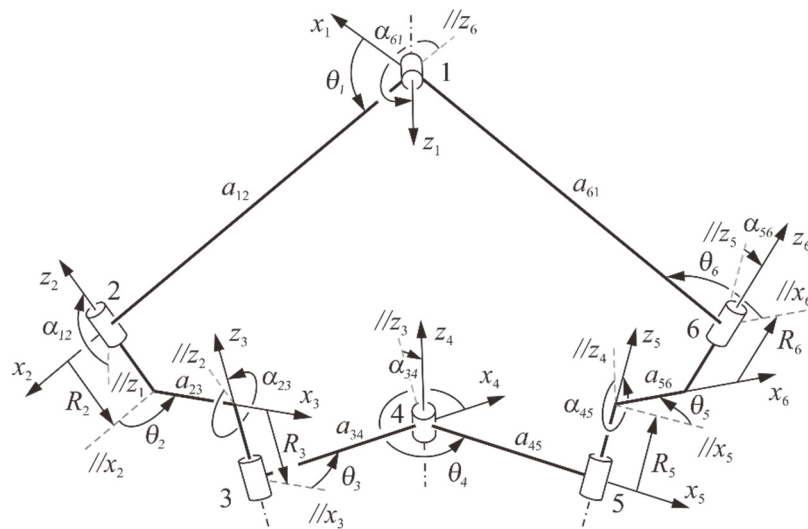


FIGURE 6 Paramètres D-H du mécanisme de Bricard à symétrie plane

Différents cas de bifurcation des mécanismes de Bricard symétriques planes et leurs conditions géométriques correspondantes sont discutées sur la base des solutions explicites et des mécanismes 5R/4R dégénérés. La bifurcation du mécanisme de Bricard plan-symétrique dans un mécanisme de Bennett est proposée, qui établit une connexion entre les familles de mécanismes de Bricard et de Bennett. Selon les différentes conditions géométriques, il existe deux types de bifurcation entre le mécanisme de Bricard à symétrie plane et le mécanisme de Bennett, représenté sur les figures 7 et 8. La condition géométrique d'existence du mécanisme de Bricard symétrique avec deux branches de mouvement 6R est trouvée et l'équation de mouvement des deux branches est dérivée-voir la figure 9. Un modèle physique qui peut reconfigurer entre deux branches de mouvement sans collision est conçu, représenté sur la figure 10. En outre, une version spéciale du mécanisme de Bricard plan-symétrique avec bifurcation entre la configuration non-symétrique (mécanisme double balancier à quatre barres) et des chaînes cinématiques équivalentes est découverte.

Avec l'étude approfondie de la cinématique et de la bifurcation du mécanisme plan-symétrique de Bricard, nous pouvons éviter la bifurcation en concevant

correctement les paramètres géométriques ou en profitant de la bifurcation pour concevoir des mécanismes reconfigurables. Il est bien adapté pour être appliqué dans des géométries d'origami rigides.

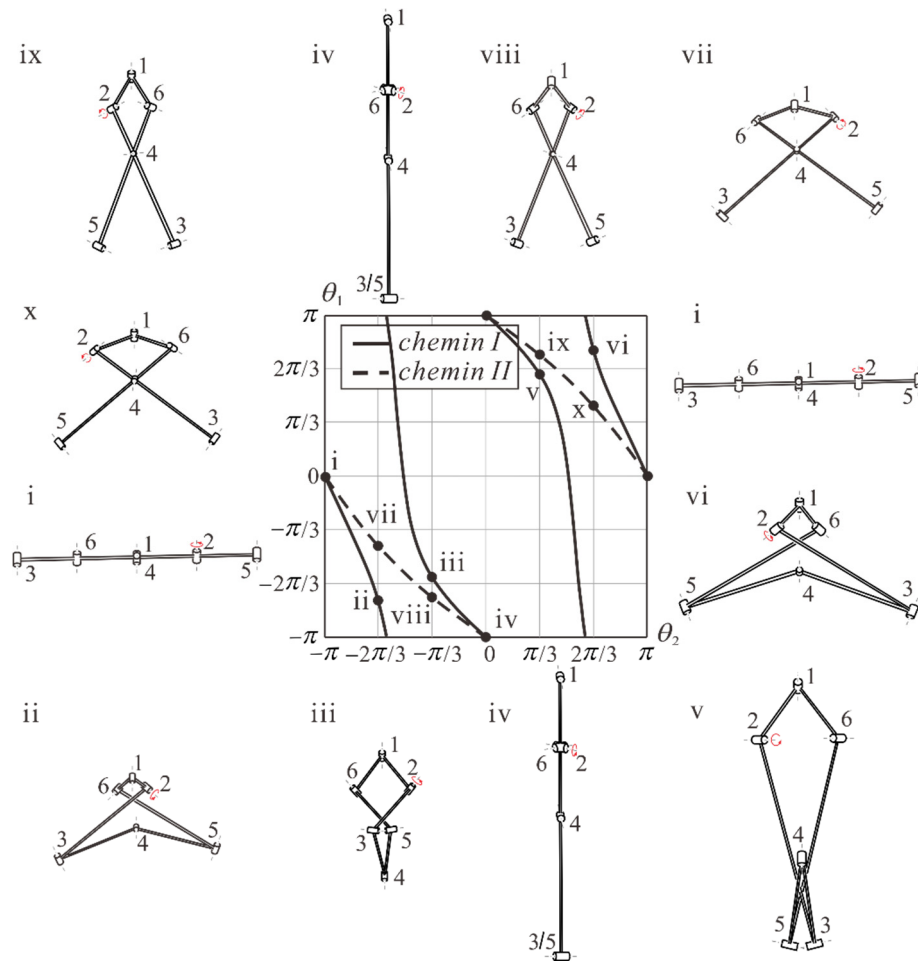


FIGURE 7 Bifurcation entre le mécanisme de Bricard plan-symétrique et le mécanisme de Bennett quand $\theta_3 = \theta_5 = \pi$

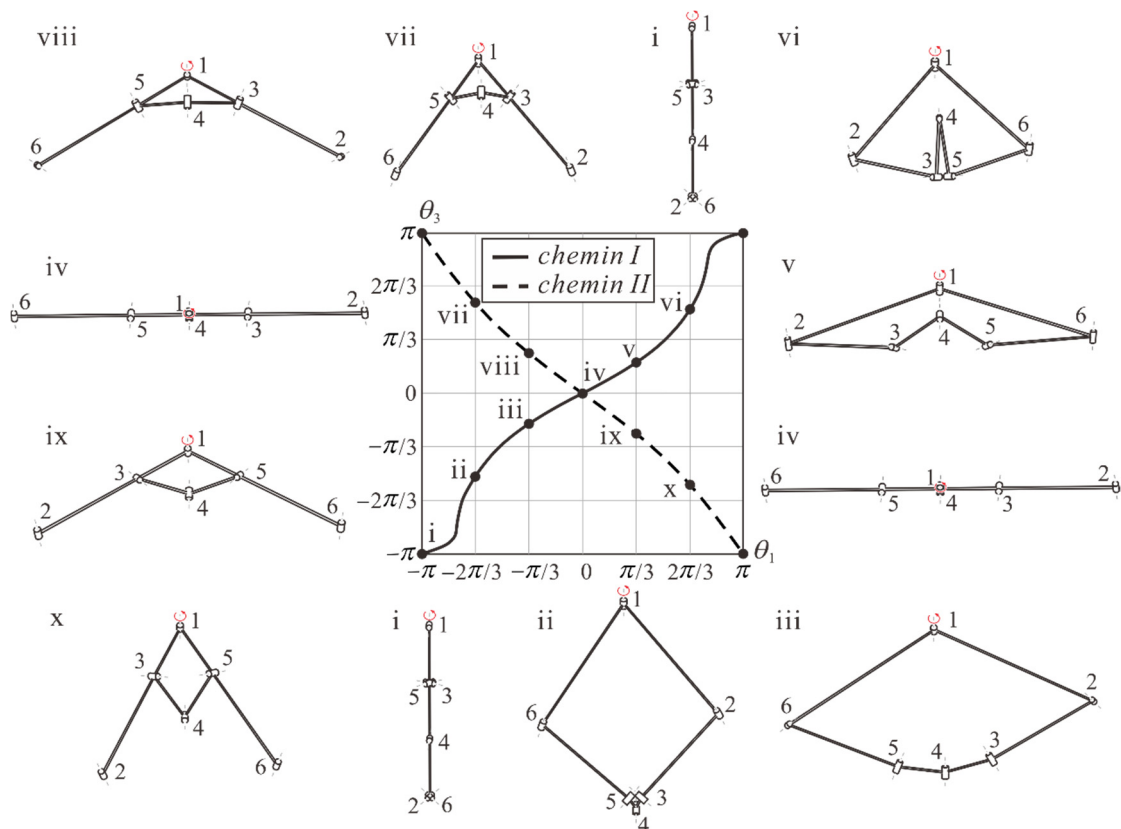


FIGURE 8 Bifurcation entre le mécanisme de Bricard plan-symétrique et le mécanisme de Bennett quand $\theta_2 = \theta_6 = \pi$

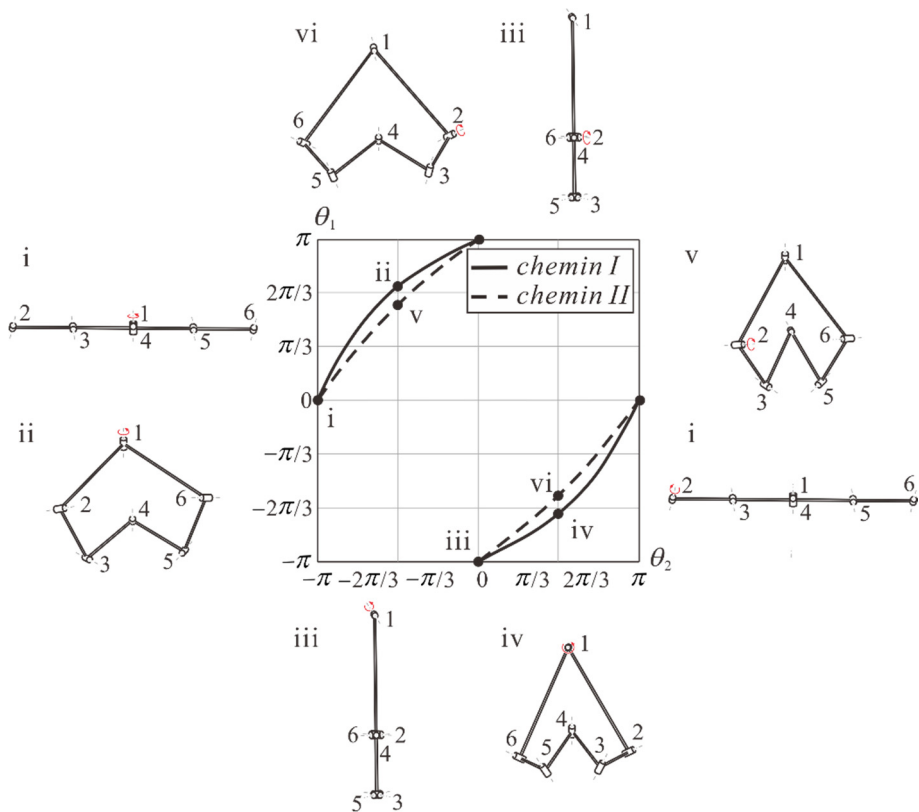


FIGURE 9 Bifurcation entre deux branches de mouvement 6R

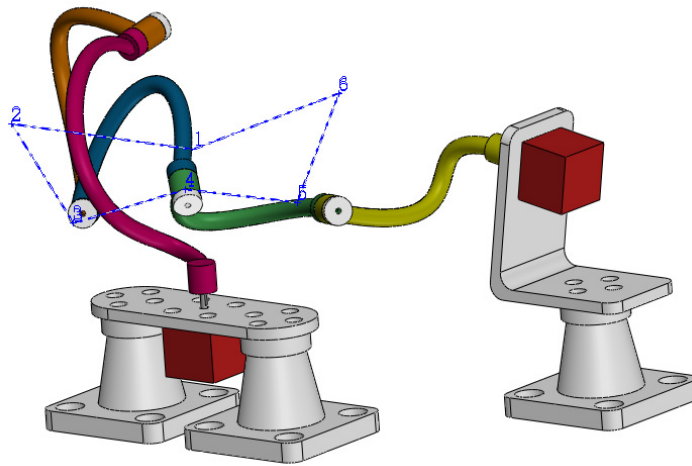


FIGURE 10 Un mécanisme de Bricard plane-symétrique avec deux branches de mouvement $6R$ sans collision

- **Pliage symétrique d'origami de la waterbomb pliable à plat**

L'origami traditionnel de la waterbomb, produit à partir d'un modèle constitué d'une série de sommets où se rencontrent six plis, est l'un des modèles d'origami les plus utilisés. La base de la waterbomb (bombe à eau) à six plis comprend quatre plis de vallée en diagonale et deux plis de montagne colinéaires, représenté sur la figure 11. Puisqu'il a un grand rapport déployé/plié entre les configurations complètement expansées et complètement pliées, il est applicable pour plier des structures déployables telles que des toits pliables et des panneaux solaires.

Dans l'origami rigide, un sommet à six plis peut être considéré comme un mécanisme $6R$ sphérique, qui a généralement trois degrés de liberté. Par conséquent, le modèle de la waterbomb a plusieurs degrés de liberté, et son mouvement est compliqué. Le pliage symétrique est souvent préféré dans la plupart des travaux de recherche ou dans les applications. Il est réalisé en le contraignant avec des conditions symétriques et en contrôlant ensuite le mouvement pour atteindre un état plat pliable idéal.

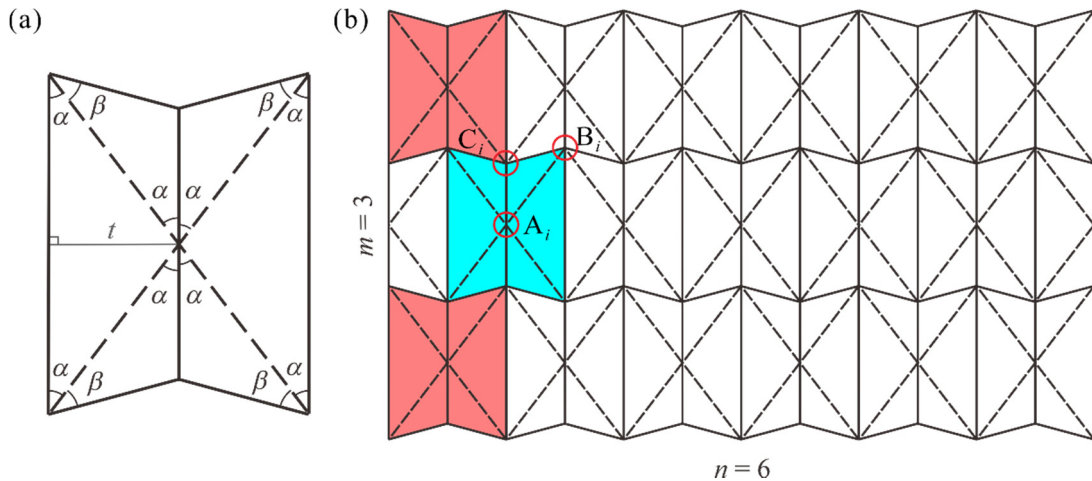


FIGURE 11 (a) La base de la waterbomb à six plis, et (b) le motif d'origami de la waterbomb formé par la combinaison des bases

Dans le 5^{ème} chapitre, la méthode d'analyse de l'origami rigide basée sur la cinématique spatiale est étendue de zéro-épaisseur à panneau épais des formes d'origami, et le pliage symétrique de l'origami est analysé. En supposant que chaque base de waterbomb ait un comportement de mouvement identique pendant le processus, on peut considérer que le modèle est constitué de deux types des sommets, l'un ayant la symétrie par rapport à une droite et par rapport à un plan, et l'autre ayant seulement la symétrie plane. L'origami à waterbomb de zéro-épaisseur correspond donc à un réseau de mécanismes sphériques $6R$ symétriques planes, tandis que la forme à panneau épais correspond à un réseau de mécanismes de Bricard symétriques planes. Considérant les conditions compatibles entre chaque sommet, les équations cinématiques des origamis à waterbomb avec des feuilles à zéro-épaisseur et des panneaux épais sont mises en place.

L'étude paramétrique sur l'origami de la waterbomb est menée pour révéler ses comportements de mouvement des formes à zéro-épaisseur et à panneau épais, tels que le mouvement à deux étages représenté sur la figure 12 et l'interférence pendant le processus de mouvement représenté sur la figure 13. La comparaison détaillée sur le comportement cinématique de mouvement des formes à zéro-épaisseur et à panneau épais pour différents paramètres est donnée dans le tableau 1. En comparant leurs comportements de mouvement, on trouve que le pliage symétrique de l'origami de la waterbomb avec des feuilles à zéro-épaisseur et des panneaux épais est équivalent et possède un DOF. Il y a toujours deux chemins de pliage pour l'origami de la waterbomb à zéro-épaisseur, quels que soient les paramètres géométriques pris. La différence est de savoir si le chemin de pliage est lisse ou non. Cependant, l'origami de la waterbomb à panneau épais n'a que deux chemins de pliage dans des conditions géométriques spécifiques représenté sur la figure 14, ce qui correspond à la bifurcation du mécanisme

de Bricard à symétrie plane. Ceci est dû au fait que l'épaisseur a fourni des contraintes géométriques supplémentaires.

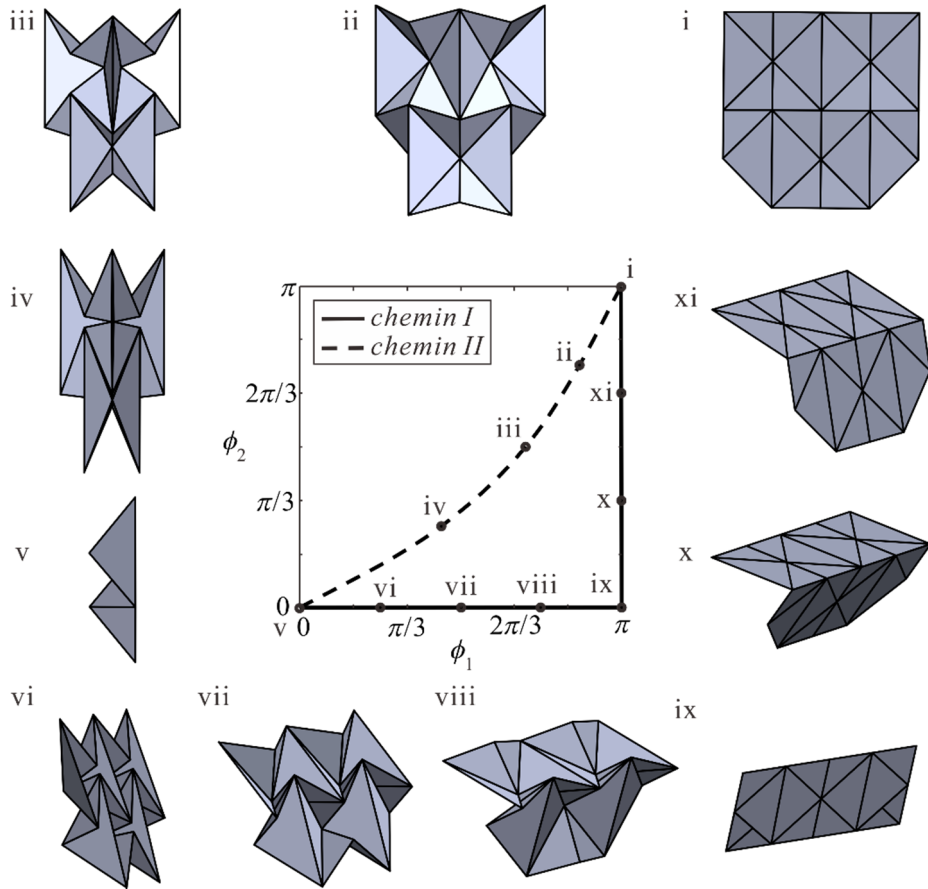


FIGURE 12 Chemins de pliage et configurations pour l'origami à waterbomb de zéro-épaisseur avec le mouvement à deux étapes du chemin I

En dépit du fait que l'origami à panneau épais est né d'un origami existant de feuille de zéro-épaisseur, il a un certain nombre d'avantages sur son précurseur. Premièrement, la structure origami à panneaux épais est un assemblage mobile de mécanismes de Bricard sur-contraint avec un seul DOF, et donc aucune contrainte supplémentaire n'est requise pour maintenir son mouvement symétrique. Cela pourrait être un grand avantage pour les applications d'ingénierie, car son système de contrôle pourrait devenir beaucoup plus simple et fiable. Deuxièmement, en général, l'origami de la tessellation à la waterbomb pour une feuille de zéro-épaisseur a une singularité cinématique quand elle est plate et entièrement compacte. Cependant, pour les origamis à panneaux épais, la singularité n'apparaît que lorsqu'une épaisseur très spécifique est choisie. Une sélection appropriée de l'épaisseur des panneaux permet d'obtenir un origami de la waterbomb à panneau épais pour réaliser un pliage compact sans bifurcations. La trajectoire unique est certainement très souhaitable pour la plupart des applications pratiques. En outre, non seulement la tessellation à waterbomb pour les

panneaux épais permet de plier la structure de manière compacte, mais un côté de la surface expansée est également complètement plat, ce qui permet au modèle d'origami de la waterbomb d'être directement applicable dans l'ingénierie.

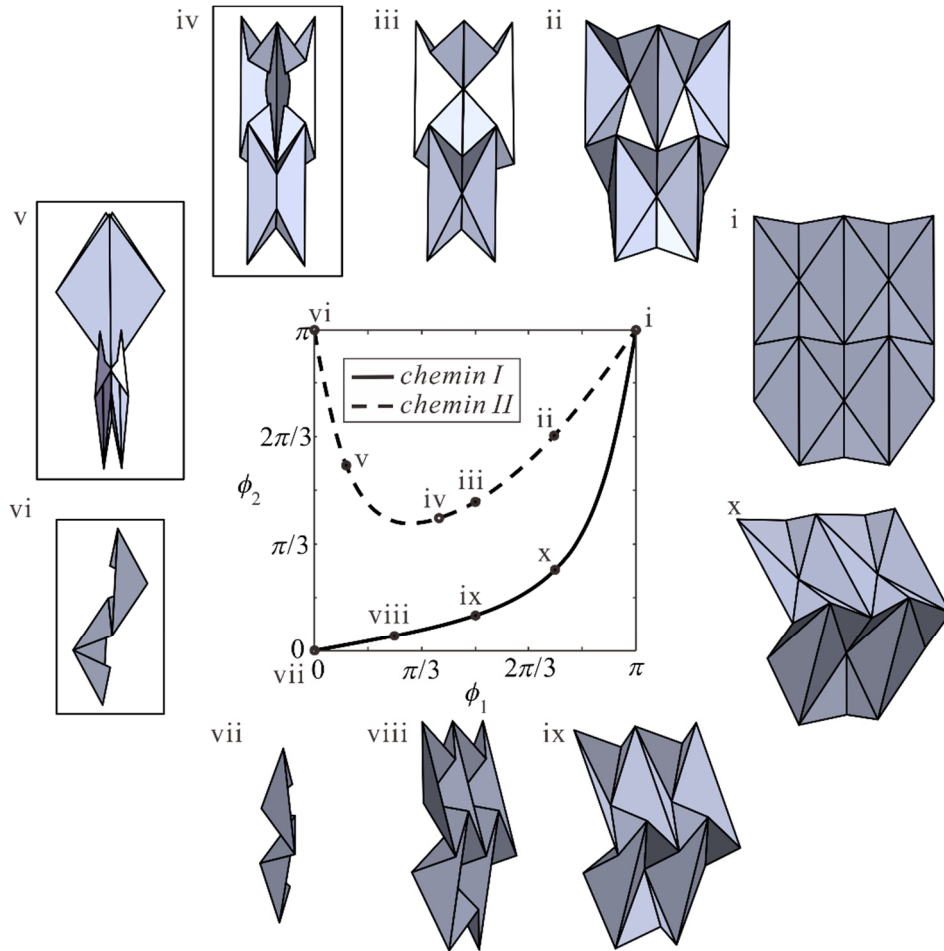


FIGURE 13 Chemins de pliage et configurations pour l'origami à waterbomb de zéro-épaisseur avec l'interférence du chemin II

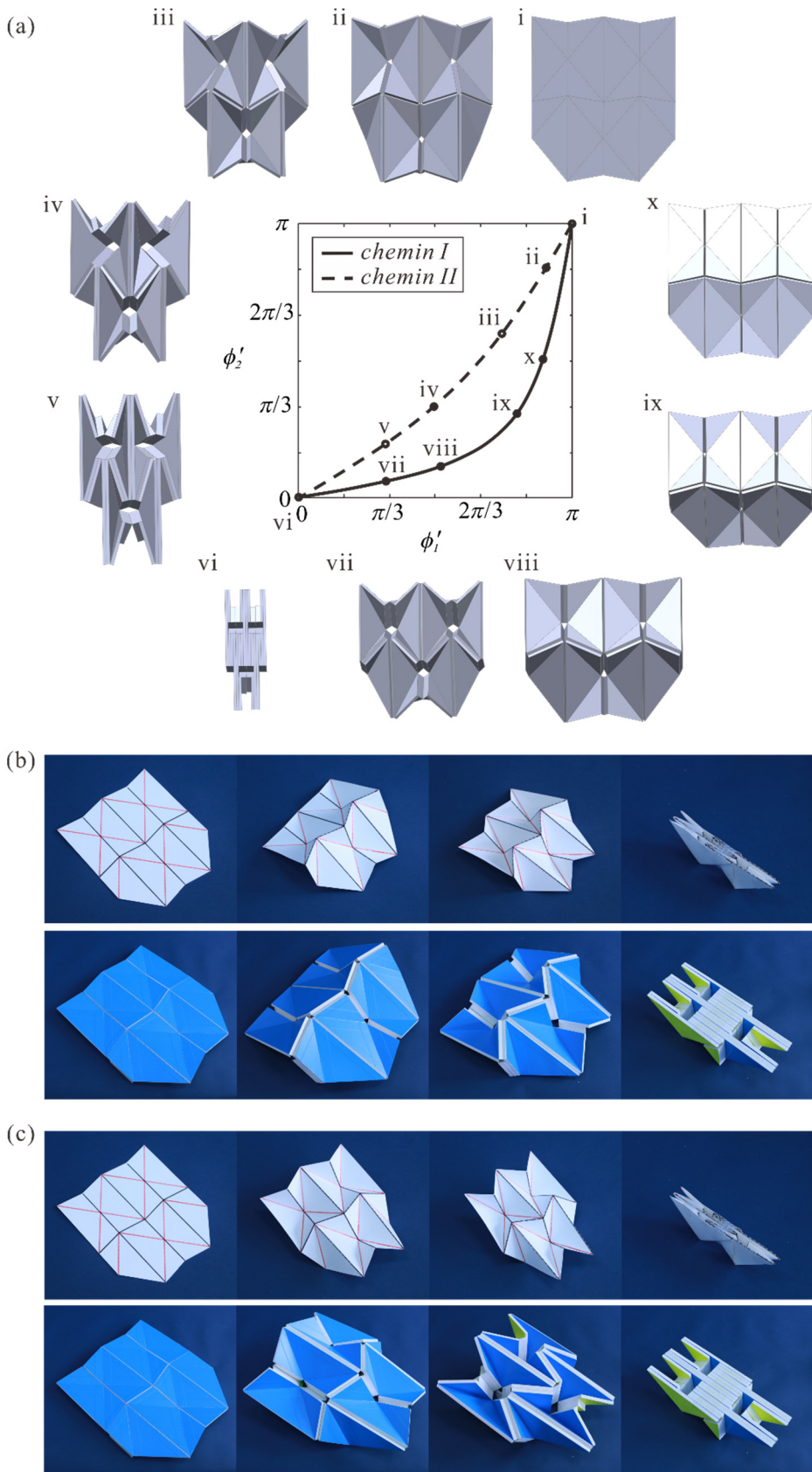


FIGURE 14 Séquence de pliage pour des motifs avec $\alpha = \beta = 2\pi/9$ et $\mu = 1$. (a) Deux chemins de pliage existent; modèles physiques de forme à zéro-épaisseur (en haut) et à panneaux épais qui se replient le long de (b) le chemin I et (c) le chemin II.

Tableau 2 Le comportement cinématique de l'origami de la waterbomb des formes à zéro-épaisseur et à panneau épais avec différents paramètres

Conditions géométriques	Chemins de pliage	L'origami de la waterbomb à zéro-épaisseur	L'origami de la waterbomb à panneau épais
$\alpha + \beta < \frac{\pi}{2}$	$\alpha = \beta$	<i>chemin I</i>	lisse
		<i>chemin II</i>	lisse
	$\alpha \neq \beta$	<i>chemin I</i>	lisse
		<i>chemin II</i>	bloqué
$\alpha + \beta = \frac{\pi}{2}$	$\alpha = \beta$	<i>chemin I</i>	le mouvement à deux étages
		<i>chemin II</i>	lisse
	$\alpha \neq \beta$	<i>chemin I</i>	le mouvement à deux étages
		<i>chemin II</i>	bloqué
$\alpha + \beta > \frac{\pi}{2}$	$\alpha = \beta$	<i>chemin I</i>	bloqué
		<i>chemin II</i>	bloqué alors que le chemin du sommet B est lisse
	$\alpha \neq \beta$	<i>chemin I</i>	bloqué
		<i>chemin II</i>	bloqué

• **Le tube de la waterbomb**

Lorsque les deux côtés verticaux du modèle de la waterbomb pliable à plat sont joints, un tube de la waterbomb est formé, représenté sur la figure 15. Il a été largement utilisé dans les domaines de l'ingénierie, notamment le stent origami médical déployable, les robots de locomotion semblables à des vers et des vers de terre, le robot à roues déformables, les muscles artificiels hautement efficaces, etc. Dans toutes les applications mentionnées ci-dessus, le tube de la waterbomb subit seulement une

dilatation/contraction radiale, accompagnée de l'extension/raccourcissement dans la direction axiale. Malgré la large application, le comportement de mouvement du tube de la waterbomb est resté ambigu et sa cinématique doit être étudiée plus profondément.

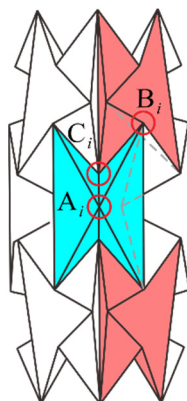


FIGURE 15 Le tube de la waterbomb généralisée

Dans le 6^{ème} chapitre, le mouvement de pliage d'un tube de la waterbomb généralisée sous la symétrie longitudinale et circonférentielle est analysé. Le comportement rigide de pliabilité et de mouvement du tube ainsi que ses conditions géométriques correspondantes sont étudiés par analyse cinématique et étude paramétrique.

Différent du boîtier pliable à plat, le tube est composé de trois types des sommets. Compte tenu de la symétrie circonférentielle, chaque sommet peut être considéré comme un mécanisme sphérique $6R$ symétrique plan pendant le mouvement de contraction. En conséquence, le tube entier correspond à un réseau fermé de mécanismes sphériques $6R$ symétriques plans, qui a deux DOF. Pour un tube de la waterbomb avec un nombre impair de rangées, le sommet à six plis dans la rangée du milieu est un mécanisme sphérique $6R$ symétrique par rapport à une droite et par rapport à un plan sous la symétrie longitudinale, qui contraint davantage le DOF à un. Pour le tube de la waterbomb avec un nombre pair de rangées, les bases dans les deux rangées adjacentes au plan équatorial ont un mouvement identique, ce qui rend la structure rigide pliable avec une DOF dans ce cas. En outre, la plage du mouvement rigide est déterminée par la configuration entièrement serrée de la rangée du milieu et par la configuration la plus étendue de la rangée d'extrémité.

Avec l'étude paramétrique, on voit que le tube plié peut subir des comportements différents, dont la condition de déclenchement peut être déterminée en utilisant la méthode d'analyse cinématique proposée de l'origami rigide sous les conditions géométriques spécifiées. Par exemple, certains tubes sont capables d'origami rigide pur représenté sur la figure 16, tandis que d'autres subiront une déformation structurelle entre des mouvements d'origami rigides représenté sur la figure 17, et la condition de transition est trouvée. La configuration de rayon uniforme du tube est rapportée. En

combinant avec le mouvement de l'origami pliable de la waterbomb, l'existence et le nombre de configurations de rayon uniforme sont discutés.

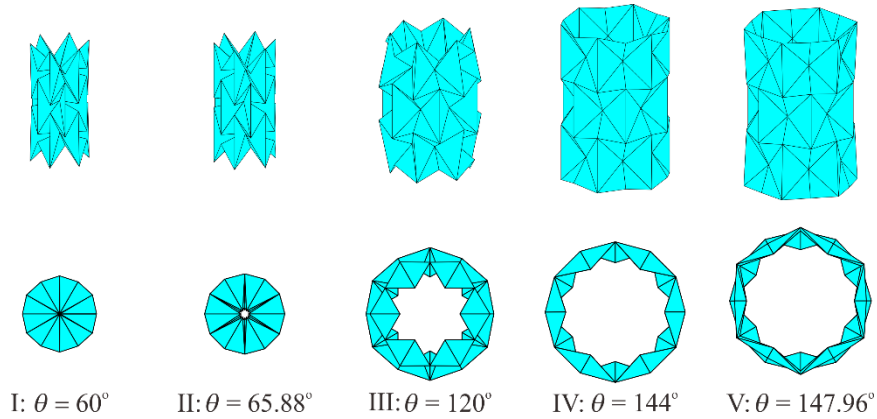


FIGURE 16 Vues 3D et projetées d'un tube de la waterbomb avec un mouvement rigide pur

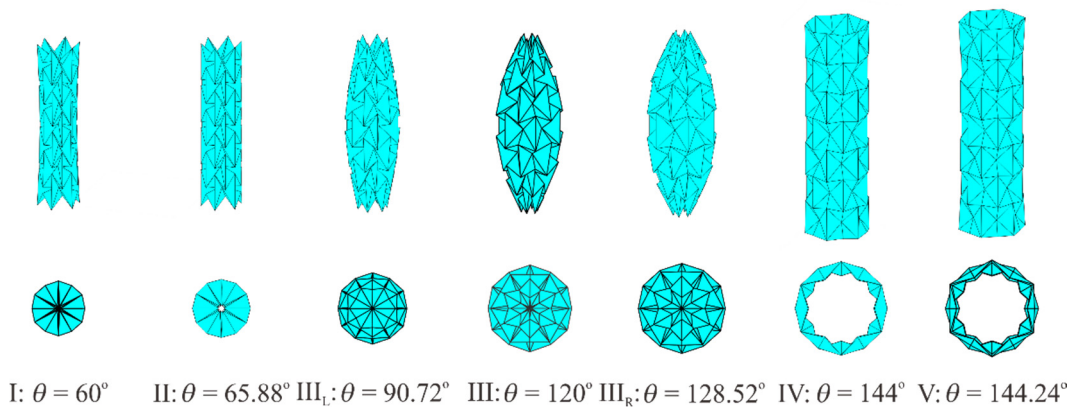


FIGURE 17 Vues 3D et projetées d'un tube de la waterbomb avec une déformation structurelle entre des mouvements rigides

En outre, en prenant en considération l'effet du nombre de rangées sur le mouvement, on découvre le profil ondulatoire du tube de la waterbomb, représenté sur la figure 18. La portée d'un tel profil et sa relation avec les paramètres géométriques sont révélées. Un tube plus court peut également être obtenu en tronquant un certain nombre de rangées d'un long tube. La bifurcation entre le mouvement d'un tube tronqué et celui d'un tube à un nombre pair de rangées est découverte à la configuration de rayon uniforme.

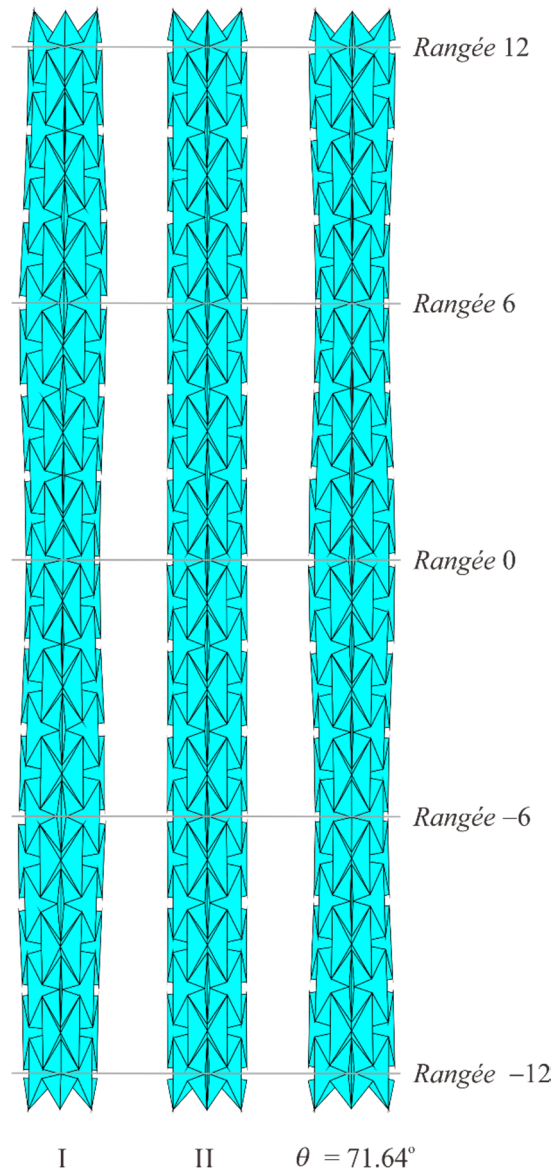


FIGURE 18 Le profil ondulatoire du tube de la waterbomb

En outre, un mouvement de torsion a été trouvé dans certains tubes de la waterbomb spécifiques, représenté sur la figure 19. La rigidité du pliage par torsion a été explorée. Grâce à une analyse cinématique détaillée, la condition suffisante et nécessaire d'un mouvement de torsion rigide a été révélée dans le cas de la symétrie par rapport à une droite et par rapport à un plan à la fin de la contraction. Il indique que le mouvement de torsion rigide ne se produit que sur le tube de la waterbomb avec un nombre impair de rangées. En effectuant l'analyse cinématique, les équations de mouvement du tube de la waterbomb sont dérivées en considérant la base dans la rangée torsadée comme un mécanisme sphérique $6R$ symétrique par rapport à une droite. On trouve que les bases des autres rangées restent en symétrie plane. Dans la perspective cinématique, la transition entre la contraction et le mouvement de torsion est une

bifurcation, où le point de bifurcation est la configuration entièrement comprimée.

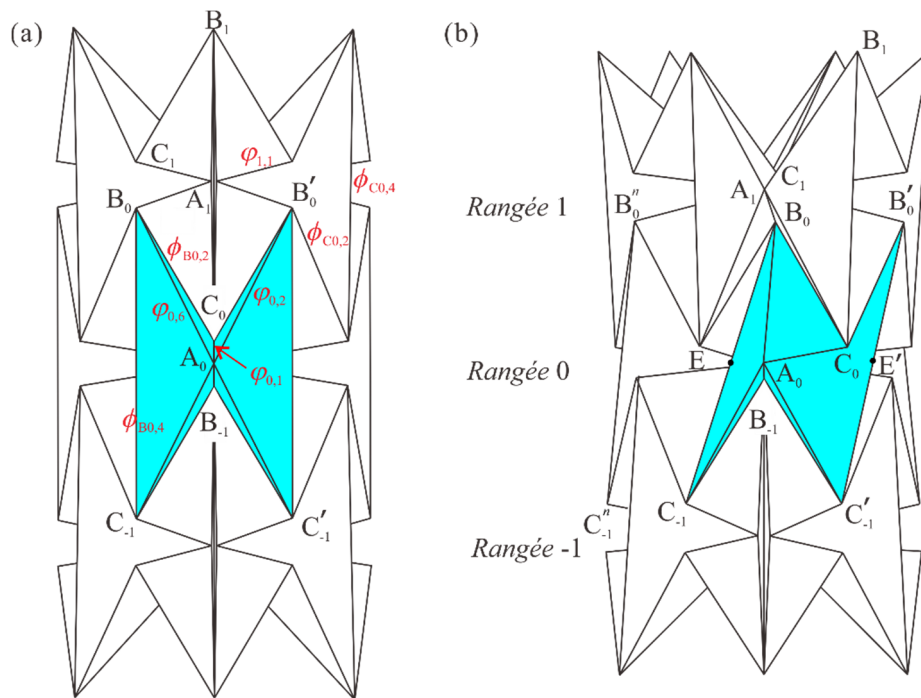


FIGURE 19 Le mouvement de torsion du tube de la waterbomb

En outre, l'existence et la plage de mouvement de torsion rigide dans différentes conditions géométriques sont explorées. L'angle de torsion par déformation axiale et sa relation avec les paramètres géométriques du tube pendant le mouvement de torsion rigide sont révélés, représenté sur la figure 20. L'état géométrique du tube de la waterbomb spécial où la configuration entièrement serrée est exactement la configuration de rayon uniforme, est trouvé. Dans ce cas, le tube peut avoir un mouvement de torsion rigide à n'importe quelle rangée, et il peut bifurquer à des chemins différents à la configuration de rayon uniforme, représenté sur la figure 21. En outre, les comportements des mouvements de torsion non-rigides sont étudiés. Les résultats expérimentaux montrent l'amélioration de la rigidité du tube avec apparition du mouvement de torsion continu, représenté sur la figure 22.

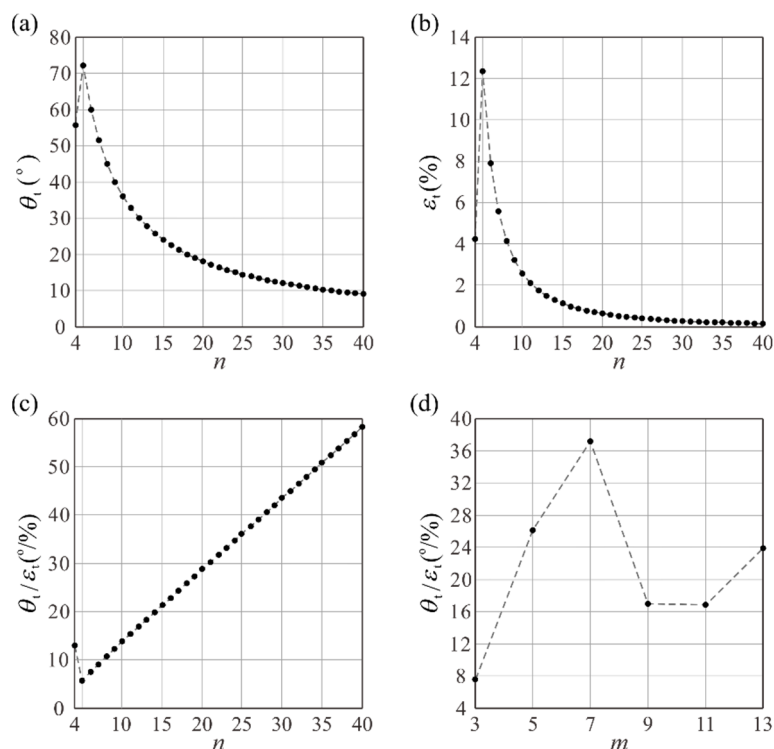


FIGURE 20 L'angle de torsion par déformation axiale et sa relation avec les paramètres géométriques du tube pendant le mouvement de torsion rigide

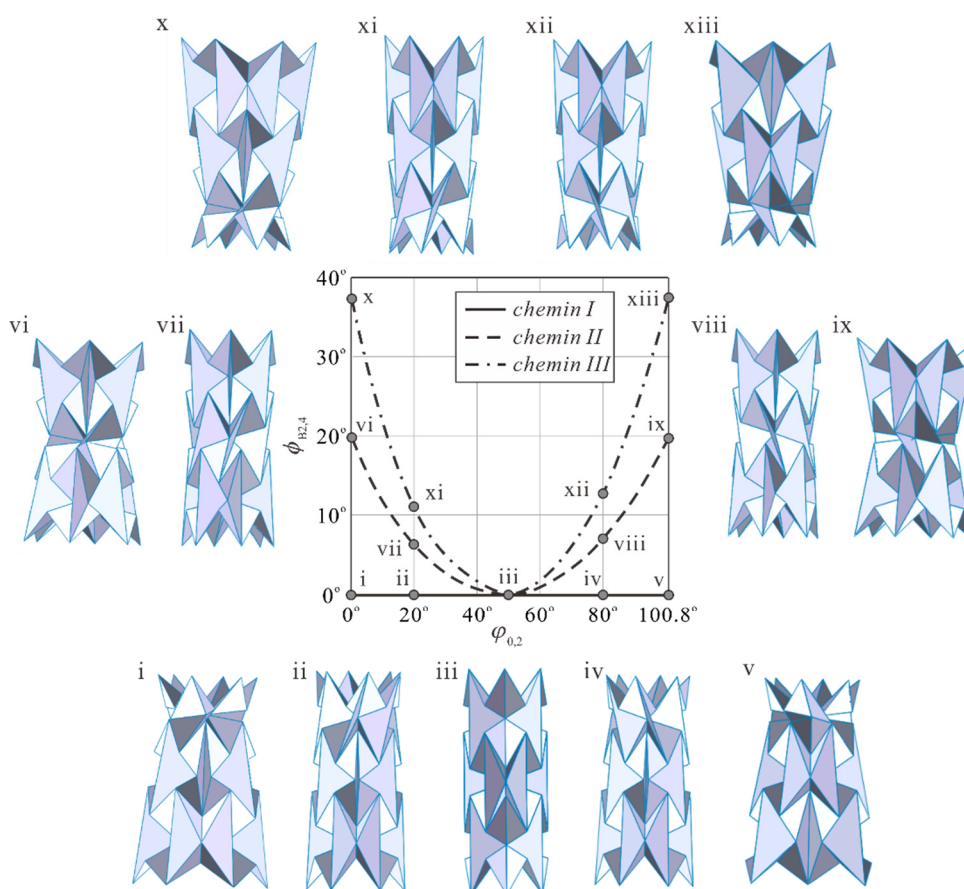


FIGURE 21 Bifurcation pendant le mouvement de torsion du tube de la waterbomb

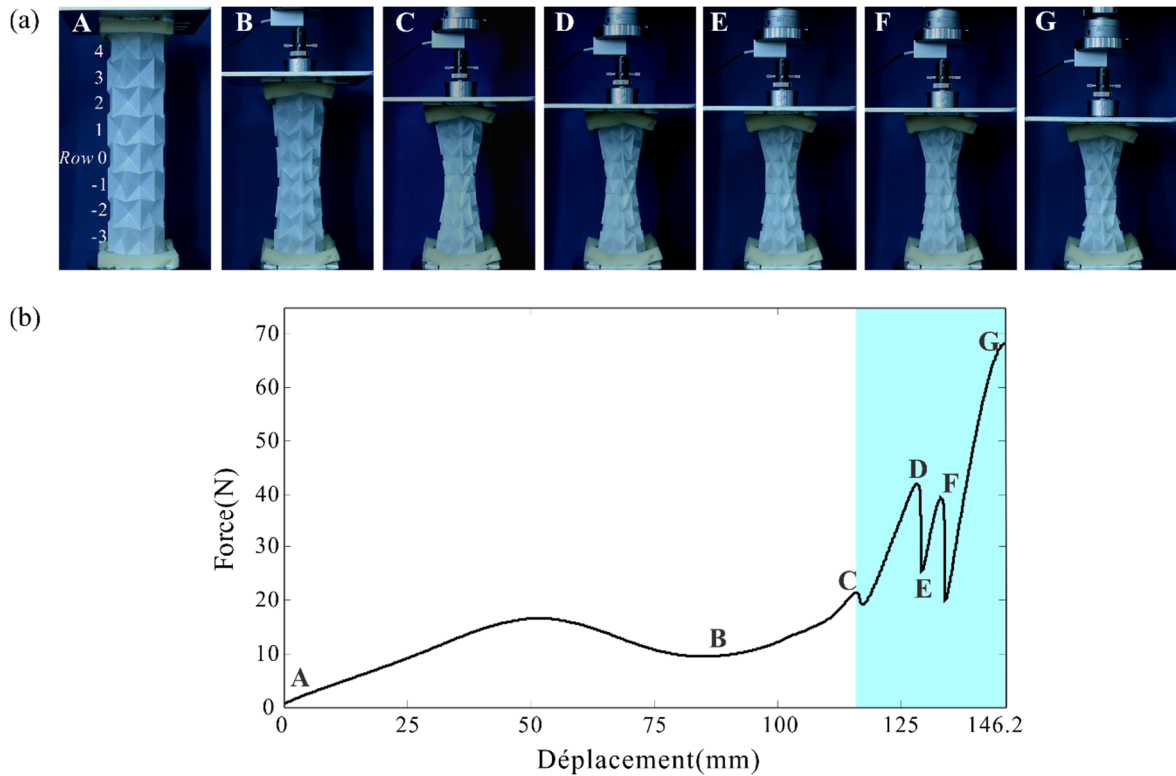


FIGURE 22 Expérience de compression axiale du tube de la waterbomb

L'étude des propriétés cinématiques du tube à waterbomb basée sur la cinématique du réseau fermé de mécanismes sphériques $6R$ révèle la relation interne entre le comportement du mouvement et les paramètres géométriques, ce qui pose les bases de la conception de structures d'origami avec divers comportements ajustés par les paramètres géométriques de mouvement. Les résultats fourniront une base solide pour l'exploitation complète de cet objet origami ancien mais fascinant pour créer de nouvelles structures de changement de forme ainsi que des métamatériaux mécaniques programmables et ajustables.

• Remarques Finales

La thèse se concentre sur une thématique de croisement entre la théorie du mécanisme et la science de l'origami. Elle explore la cinématique des mécanismes spatiaux et ses applications aux origamis rigides, allant de l'assemblage mobile de mécanismes $4R$ sphériques aux mécanismes $6R$ spatiaux sur-contraints, puis à l'assemblage mobile de mécanismes $6R$ sphériques et de mécanismes $6R$ spatiaux sur-contraints, et finalement au réseau en boucle fermée de mécanismes $6R$ sphériques. Ces études aident à approfondir la compréhension de la cinématique des mécanismes spatiaux et du mouvement rigide de l'origami, et à jeter les bases des applications techniques des mécanismes spatiaux et des motifs d'origami rigides.

Le travail de cette thèse porte principalement sur l'étude théorique des mécanismes spatiaux et des origamis rigides. Il nous fournit plusieurs sujets à explorer plus loin, qui comprend la réalisation de prototype physique, la validation expérimentale et les applications d'ingénierie de ces mécanismes et des modèles d'origami comme indiqué ci-dessous.

Tout d'abord, les applications potentielles et les adaptations du modèle d'origami à torsion triangulaire pliable dans la tessellation en tant qu'unité modulaire, ou dans la conception de structures déployables bioniques et de robots origami doivent être explorées. La cinématique du réseau de mécanismes $4R$ sphérique peut être davantage utilisée pour analyser la pliability rigide des autres modèles d'origami existants tels que les torsions hexagonales, ou pour générer de nouveaux modèles d'origami. La méthode proposée pour générer un mécanisme spatial sur-contraint à partir du réseau de mécanismes sphériques par la technique d'origami peut être étendue à d'autres types de modèles d'origami pour imaginer de nouveaux mécanismes.

Deuxièmement, le comportement de bifurcation du mécanisme de Bricard plan-symétrique peut être utilisé dans la conception de mécanismes reconfigurables. La cinématique du mécanisme de Bricard plan-symétrique peut être appliquée à d'autres types de modèles d'origami à panneau épais composés de sommets à six plis, tels que le motif en losange et le motif Resch, etc. Plus de travail en matière de modèle de la waterbomb peut également être fait sur ses applications d'ingénierie telles que les panneaux solaires.

Troisièmement, les dispositifs d'ingénierie tubulaires à base de la waterbomb et les métamatériaux à rigidité programmable et de forme contrôlable peuvent être conçus sur la base du cas rigide ou non rigide du tube. Profitant du profil ondulatoire, un robot ver peut être conçu. La stratégie de contrôle pour maintenir la symétrie ou accomplir la transition entre la multitude de comportements de la waterbomb doit être recherchée pour faciliter ses applications. L'analyse sur le tube d'origami à panneau épais peut également être réalisée en même temps que le réseau tubulaire de mécanismes spatiaux sur-contraints.

MOTS-CLÉS: Cinématique; Origami rigide; Mécanisme sphérique; Mécanisme spatial sur-contraint; Mécanisme de Bricard à symétrie plane; Bifurcation; Origami de la waterbomb; Origami à panneau épais.

Publications and Research Projects during PhD's Study

Papers:

- [1] Feng H, Ma J, Chen Y, You Z. Twist of tubular mechanical metamaterials based on waterbomb origami [J]. Scientific Reports, 2018, 8(1): 9522.
- [2] Feng H, Peng R, Ma J, Chen Y, Rigid foldability of generalized triangle twist origami pattern and its derived 6R linkages [J]. Journal of Mechanisms and Robotics, 2018, 10(5): 051003-051003-13.
- [3] Feng H, Chen Y, Dai J, Gogu G. Kinematic study of the general plane-symmetric Bricard linkage and its bifurcation variations [J]. Mechanism and Machine Theory, 2017, 116: 89-104.
- [4] Chen Y, Feng H, Ma J, Peng R, You Z. Symmetric waterbomb origami [J]. Proceedings of the Royal Society A-Mathematical, Physical and Engineering Sciences, 2016, 472: 20150846. (Journal cover paper)
- [5] Song C Y, Feng H, Chen Y, Chen I-M, Kang R. Reconfigurable mechanism generated from the network of Bennett linkages [J]. Mechanism and Machine Theory, 2015, 88: 49-62.
- [6] Feng H, Kang R, Chen Y. Workspace analysis of a reconfigurable mechanism generated from the network of Bennett linkages [C]. Proceedings of the 3rd IEEE/IFTOMM International Conference on Reconfigurable Mechanisms and Robots, Beijing, China, 20-22 July 2015.
- [7] Ma X, Feng H, Dai J. Bifurcation condition and parameter design of three reconfigurable mobility-one single loop linkages based on double points of kinematic curves [J]. Journal of Mechanisms and Robotics, Under Review.
- [8] Ma J, Chen Y, Feng H, Hou D, Gattas J, You Z. A unified kinematic framework for rigid-foldable waterbomb origami, Ready to submit.
- [9] Feng H, Ma J, Chen Y, You Z. Rigid-foldability of the generalized waterbomb tube, Ready to submit.

Research Projects Participated in:

- [1] The Excellent Young Scientists Fund, National Natural Science Foundation of China, Kinematics of Mechanism and Motion Structures (Grant No. 51422506)
- [2] The National Natural Science Foundation General Program, Essential Design Theory Research of the Deployable Structures in the Reconfigurable Robots (Grant No. 51275334)

- [3] Tianjin Research Program of Application Foundation and Advanced Technology, Research on the reconfiguration analysis and synthesis of spatial overconstrained linkages (Grant No. 13JCZDJC26400)

Acknowledgements

First of all, I would like to express my deepest sense of gratitude to my supervisors, Prof. Jian S Dai and Prof. Yan Chen at Tianjin University and Prof. Grigore Gogu at l'Université Clermont-Auvergne, for their constant encouragement and patient guidance throughout my PhD's study. I am extremely grateful to Prof. Jian S Dai for sharing expertise and providing me with numerous exchange opportunities. His requirements of being proficient, professional and perfect in doing research inspired me a lot. I am greatly thankful to Prof. Yan Chen for her constructive suggestions and valuable guidance towards my work and life. I am also very indebted to Prof. Grigore Gogu for his patience, generosity, guidance and help during my research as well as my life in France. All the things I've learned from these supervisors are the valuable lifetime treasures which will continually guide my future work.

I would also like to thank Prof. Qinchuan Li and Dr. Damien Chablat for being my thesis reviewers and providing their valuable comments on my manuscript. I am also thankful to Dr. Chedli Bouzgarrou, Prof. Yimin Song, Prof. Tao Sun and Prof. Shiyu Wang for serving as my committee members. I also want to thank Prof. Zhong You, Dr. Joseph Michael Gattas, Dr. Nicolas Bouton, Dr. Khaled Assad Arrouk and Dr. Nicolas Blanchard for their helpful suggestions on my research.

I am also grateful to Prof. Jiayao Ma for his advices and help on my research, Prof. Rongjie Kang, Prof. Zhibin Song and Ms. Yunyan Wang for their kind help. Appreciation also goes to Mr. Rui Peng, Mr. Xiao Zhang, Mr. Fufu Yang, Mr. Xuesi Ma and Mr. Jeff Lee. Discussions with them deepen my understanding of the research. Moreover, I would like to thank my colleagues in Motion Structure Laboratory, in particular Mr. Zufeng Shang, Mr. Jichao Song, Miss Shixi Zang, Miss Mengyan Shi, Miss Xiaochen Yang, Mr. Xuesong Chen and Mr. Degao Hou for their friendly help.

Special gratitude goes to my close friends, in particular Miss Yanmei Chen, Miss Yu Wang, Miss Qing Feng, Miss Yaqing Song, Mr. Xi Kang, Mr. Shaobin Lan and Miss Yueming Zhu for their friendship and selfless help. Their warm words helped me go through many hard times.

The State Scholarship Fund by China Scholarship Council, the financial support by the National Natural Science Foundation of China (Projects 51275334, 51290293, 51422506, 51535008 and 51721003), by the Ministry of Science and Technology of China (Project 2014DFA70710), and the University PhD Scholarship by Tianjin University are also gratefully acknowledged.

Finally, I would like to express my sincerest thanks to my family for their support, encouragement and love, which provide me with courage to overcome any difficulty during my study.

Kinematics of spatial linkages and its applications to rigid origami

Keywords:

Kinematics; Rigid origami; Spherical linkage; Spatial overconstrained linkage; Plane-symmetric Bricard linkage; Bifurcation; Waterbomb origami; Thick-panel origami.

Abstract:

This dissertation conducts kinematic analysis of spatial linkages ranging from spherical linkages to overconstrained linkages based on the D-H matrix method, and applies it to explore the rigid foldability and motion behaviour of origami patterns. In this process, the rigid foldability of triangle twist origami pattern is firstly examined based on the kinematics of spherical $4R$ linkage network and new overconstrained $6R$ linkages are derived by kirigami technique. Then the kinematics of the plane-symmetric Bricard $6R$ linkage is analyzed and its bifurcation variations are discussed. After that, the results are applied to study the symmetric folding of six-crease thick-panel waterbomb origami, which is modelled as a network of plane-symmetric Bricard $6R$ linkages. The motion behaviour of its corresponding tessellation of zero-thickness sheet is demonstrated by a network of spherical $6R$ linkages. Finally, the motion behaviour of the closed cylindrical form of waterbomb origami is investigated through a parametric study, by means of modelling it as a closed network of spherical $6R$ linkages. These studies help to deepen the understanding of spatial linkage kinematics and rigid origami motion, and lay the foundation for engineering applications of spatial linkages and rigid origami patterns.

La cinématique des mécanismes spatiaux et ses applications à l'origami rigide

Mots-clés:

Cinématique; Origami rigide; Mécanisme sphérique; Mécanisme spatial sur-contraint; Mécanisme de Bricard à symétrie plane; Bifurcation; Origami de la waterbomb; Origami à panneau épais.

Résumé:

La thèse conduit une analyse cinématique des mécanismes spatiaux allant de mécanismes sphériques aux mécanismes spatiaux sur-contraints basés sur la méthode matricielle D-H et l'applique pour explorer le comportement rigide de pliabilité et de mouvement des modèles d'origami. Dans ce processus, la pliabilité rigide du motif origami en torsion triangulaire est d'abord examinée sur la base de la cinématique du réseau de mécanismes $4R$ sphériques et de nouveaux mécanismes $6R$ sur-contraints dérivés par la technique du kirigami. Ensuite, la cinématique du mécanisme de Bricard $6R$ plan-symétrique est analysée et ses variations de bifurcation sont discutées. Après cela, les résultats sont appliqués pour étudier le pliage symétrique de l'origami de la waterbomb à six plis à panneau épais, qui est modélisé sous la forme d'un réseau de mécanismes de Bricard $6R$ plan-symétriques. Le comportement de mouvement de sa tessellation correspondante de feuille de zéro-épaisseur est démontré par un réseau de mécanismes $6R$ sphériques. Enfin, le comportement de mouvement de la forme cylindrique fermée de l'origami de la waterbomb est analysé à travers une étude paramétrique, en le modélisant comme un réseau fermé de mécanismes $6R$ sphériques. Ces études aident à approfondir la compréhension de la cinématique des mécanismes spatiaux et du mouvement rigide de l'origami, et à jeter les bases des applications techniques des mécanismes spatiaux et des motifs d'origami rigides.